The Spin Structure of the Proton at Low Q^2: A Measurement of the Structure Function g_2^p

Chao Gu

Shiyan, Hubei, China

B.S. Peking University, 2009

A Dissertation Presented to the Graduate Faculty

of the University of Virginia in Candidacy for the Degree of

Doctor of Philosophy

Department of Physics

University of Virginia

June, 2016

Abstract

The spin structure of the nucleon has remained as one of the key points of interest in hadronic physics, which has attracted many efforts from both experimentalists and theorists. Quantum Chromodynamics (QCD) is the fundamental theory that describes the strong interaction. It has been verified in the asymptotically free region. However, the non-perturbative confinement of quarks within the nucleon is still not well understood within QCD. In the non-perturbative regime, low-energy effective field theories such as chiral perturbation theory (χPT) provide predictions for the spin structure functions. The neutron spin structure functions, g_1^n and g_2^n, and the proton spin structure function, g_1^p, have been measured over a wide kinematic range and compared with the theoretical predictions. However, the proton spin structure function, g_2^p, remains largely unmeasured.

The E08-027 collaboration successfully performed the first measurement of the inclusive electron-proton scattering in the kinematic range $0.02 < Q^2 < 0.2$ GeV^2. The experiment took place in experimental Hall A at Jefferson Lab in 2012. A longitudinally polarized electron beam with incident energies between 1.1 GeV and 3.3 GeV was scattered from a longitudinally or transversely polarized NH_3 target. Asymmetries and polarized cross-section differences were measured in the resonance region to extract the proton spin structure functions g_2. The results allow us to obtain the generalized spin polarizabilities γ_0 and δ_{LT} and test the Burkhardtt-Cottingham (BC) sum rule. Chiral perturbation theory is expected to work in this kinematic range and this measurement of δ_{LT} will give a benchmark test to χPT calculations. This thesis will discuss preliminary results from the E08-027 data analysis.

Acknowledgments

There have been so many people who provided support and encouragement to me during this long journey to complete this dissertation. I would like to deeply thank everyone providing me with so much help.

First, I would like to thank my thesis advisor, Nilanga Liyanage, who has been such a terrific mentor and friend during the past years. I would not have reach this point without his help and guidiance. My discussions with him were always enjoyable, not only enhanced my physics insight, but also helped me to become independent and to understand how to become a physicist.

I would like to thank my Jefferson Lab supervisor, Jian-ping Chen, who quickly brought me involved in the collabration and enthusiastically answered my questions and help me to better understand the physics behind the experiment. I spent most of my graduate time at Jefferson Lab and I learned a lot from his advices and help, both in research and in everyday life. It was my great privilege to get this chance to work with him.

I would like to thank my thesis committee members: Edward Murphy, Kent Paschke and Xiaochao Zheng for their time in carefully going through this document and providing valuable comments.

I would like to thank Alexandre Camsonne, Jian-Ping Chen, Don Crabb and Karl Slifer for their role as the spokepersons in this experiment. Our experiment experienced many problems. Their delibrate plan guaranteed a promising experiment. I would also like to thank the Hall A collaboration and the JLab target group. Without their efforts, the experiment would not have been a success.

I would like to thank my colleagues, either graduate students or post-docs, for their hard work to ensure the experiment was a success: Toby Badman, Melissa Cummings, Min Huang, Jie Liu, Pengjia Zhu, Ryan Zielinski, Kalyan Allada, Ellie Long, James Maxwell, Vince Sulkosky and Jixie Zhang. Thanks to Jixie for teaching me to build a simulation package and for many valuable discussions on the spectrometer optics study. I would also like to thank Kalyan for teaching me the detector and DAQ setup.

I would like to thank all my friends at University of Virginia and Jefferson Lab. Their friendship made my graduate study an enjoyable experience. They are: Xiaping Tang, Zukai Wang, Yuxiang Zhao, Li Ye, Xiuchang Yang, Yi Qiang, Chaolun Wu, Chunhua Chen, Yuncheng Han, Zhihong Ye, Zongwen Yang, Longwu Ou, Yang Wang, Zhiwen Zhao, He Zhang, He Huang, Kai Jin, Peng Peng, Wei Liu, Jin Huang, Chao Peng, Yawei Zhang, Wei Tang, Siyu Jian, Danning Di, Kondo Gnanvo, Aiwu Zhang, Mei Zhang, Yifei Shi, Luna Yang, Moran Chen, Ryan Duve.

I would like to thank my parents for their persistent support and endless encouragements. It was not easy for them to push me so far away to pursue my dream, but they were always understanding of my decision.

Finally, thanks to my wife Deli Zhu for all her love and support which made all of this possible.

Dedicated to my parents, Fei Ye and Xinqin Guan

Contents

List of Figures

List of Tables

Chapter 1

Introduction

Nucleons, protons and neutrons, belong to the hadronic family of sub-atomic particles. The internal structure of the nucleon remained a mystery untill the 1960s. In the late 1960s, J. Friedman, H. Kendall and R. Taylor used a new high-energy electron beam at SLAC and found that the ratio of the differential cross-section and the Mott cross-section exhibits approximate scaling at large Q^2 [1], demonstration that the nucleon is composed of some point-like particles known as partons. We now know that nucleons are bound states of fundamental particles: quarks and gluons. The quarks interact with each other by exchanging gluons via the strong interaction. Quantum Chromodynamics (QCD) is the fundamental theory that describes the strong interaction. In the high energy region, QCD has been verified by numorous experimental results which have been compared to the perturbative solutions of the QCD Lagrangian. However, the non-perturbative confinement of quarks within the nucleon is still not well understood within QCD. This makes hadronic physics and the study of QCD one of the most fascinating and challenging areas of modern science.

The spin structure of the nucleon has remained as one of the key issues of hadronic physics. Spin is one of the fundamental properties of particles. The investigation of spin began with the experiments of Stern and Gerlach in the early 1920s [2]. Many decades later, the scattering experiments at powerful accelerators provide us the opportunity to begin to answer the question of how the quarks and gluons interact

with each other to produce the spin of the nucleon. All the spin of the nucleon was expected to be carried by the quarks in the naive parton model. However, the first spin structure function experiments at SLAC [3] and CERN [4] showed that the total spin carried by quarks was very small. This puzzling result was known as the "spin crisis". Following this the spin structure of the nucleon became a highly productive area for both experiment and theory. During the past 30 years, many experiments were carried out to study the spin structure of the nucleon at SLAC, CERN, DESY, RHIC, Jefferson Lab (JLab) and other facilities [5]. The purpose of these measurements was to examine how the total spin of the nucleon is distributed among its constituents. The present understanding is that the quarks only carries about 30% of the total nucleon spin; the rest is expected to be carried by the quarks' orbital momentum and by the gluons. Although many experiment and theoretical efforts have been made, there are still many questions remaining along with some new challenges.

The structure of the nucleon is studied primarily through deep inelastic scattering (DIS) experiments which emphasize interaction with individual quarks and gluons at sufficiently high energies. In this asymptoticaly-free regime, the probes have provided a great understanding of how the spin of the nucleon arises from its intrinsic degrees of freedom. However, physicists are not only focused on the DIS region where the internal interaction is relatively weak but also on the resonance region where the quarks and gluons are strongly interacting with each other. Results have become available recently from a new generation of JLab experiments which focused on probing QCD in the non-perturbative and transition regimes. The different energy regimes provide probes with different resolutions, which could be used for a complementary mapping of the strong interaction in the nucleon. The collective behavior of the nucleon constituents could also be retrieved from the low momentum transfer (Q^2) results, in contrast to higher Q^2 where quark-gluon correlations are suppressed and parton-like behavior is observed [6].

The spin structure functions g_1 and g_2 of proton and neutron and their moments have been extracted over a wide kinematic range [7–15]. However, data on the spin structure function g_2 are absent for proton at low energy. Jefferson Lab Hall A

Experiment E08-027 was carried out to provide precise data for the proton g_2 in the low energy region to address intriguing discrepancies between neutron data and sum rule predictions from chiral perturbation theory.

This thesis is organized as follows. Chapters 2 and 3 present the theory to formulate the inclusive scattering experiment. Chapter 4 gives a review of the physics motivation behind E08-027. Chapter 5 discusses the experimental setup at Jefferson Lab Hall A. Chapter 6 gives a detailed discussion about spectrometer optics study and Chapter 7 explains the rest of the data analysis. Chapter 8 presents results and the conclusions.

Chapter 2

Inclusive Electron Scattering

Electron scattering is a well-proven technique to probe the internal structure of the nucleon. The electromagnetic interactions of leptons are well understood and are described by Quantum Electrodynamics (QED). Depending on whether or not the final hadronic system is detected, the electron scattering experiments can be divided into three types: inclusive scattering, semi-inclusive and exclusive scattering. The process of inclusive electron-nucleon scattering, where only the scattered electron is detected, is discussed in this chapter. The relevant kinematic variables, the differential cross-sections and the formulation of inclusive electron scattering are presented.

2.1 Kinematic Variables

The simplest picture of inclusive electron-nucleon scattering is with the one photon exchange approximation, which is shown in Figure 2-1. In this scenario, an electron with four momentum $k_\mu = (E, \vec{k})$ interacts with a hadronic target. In the laboratory frame where the target is at rest, the four momentum of the target nucleon is defined as $P_\mu = (M, \vec{0})$. For inclusive scattering, the final hadronic system is not detected, while the scattered electron is detected with the four momentum $k'_\mu = (E', \vec{k'})$. The angle between $\vec{k}$ and $\vec{k'}$ is the scattering angle θ. The virtual photon exchanged by the electron and the nucleon carries a four-momentum $q_\mu = (k - k')_\mu = (\nu, \vec{q})$. Since the virtual photon is off its mass shell, q_μ satisfies $q^2 \neq 0$.

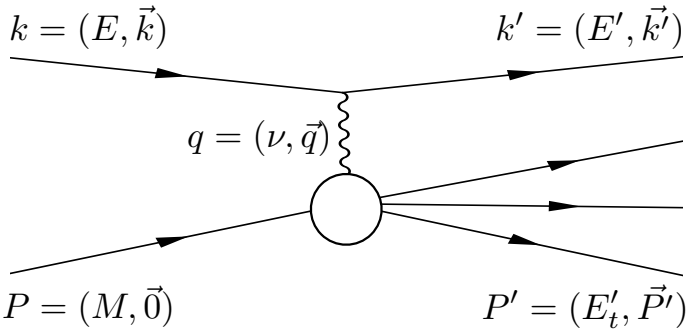

Figure 2-1: Diagram for inclusive electron scattering.

Two independent Lorentz invariants can be constructed from these kinematic variables. The energy transfer $\nu = (P \cdot q)/M$ and the squared four-momentum transfer $q^2 = (k - k')^2$ are chosen to describe the inclusive scattering process [16]. For a space-like virtual photon, $q^2 < 0$, the variable $Q^2 = -q^2$ is used instead of q^2. Since E and E' are always much larger than the electron mass, m_e, in the scattering experiments, the electron mass can be neglected. In this case, ν and Q^2 can be expressed as:

$$\nu = E - E', \tag{2.1}$$

$$Q^2 = 4EE' \sin^2 \frac{\theta}{2}. \tag{2.2}$$

We also refer to the invariant mass of the final hadronic state:

$$W^2 = (P + q)^2 = M^2 + 2M\nu - Q^2. \tag{2.3}$$

For convenience, two dimensionless scalar invariants are commonly used to replace ν and Q^2: the Bjorken scaling variable,

$$x = \frac{Q^2}{2P \cdot q} = \frac{Q^2}{2M\nu}, \tag{2.4}$$

and the fraction of the electron energy loss,

$$y = \frac{P \cdot q}{P \cdot k} = \frac{E - E'}{E}. \tag{2.5}$$

2.2 Cross-Sections and Structure Functions

Consider the inclusive scattering of polarized electrons off polarized nucleons. The differential cross-section for detecting the final electron in the solid angle $\mathrm{d}\Omega$ and in the final energy range $(E',\ E' + \mathrm{d}E)$ in the laboratory frame can be written as [17]:

$$\frac{\mathrm{d}^2\sigma}{\mathrm{d}\Omega\,\mathrm{d}E'} = \frac{\alpha^2}{Q^4}\frac{E'}{E}L_{\mu\nu}W^{\mu\nu}, \tag{2.6}$$

where α is the electromagnetic fine structure constant, $L_{\mu\nu}$ and $W^{\mu\nu}$ are the leptonic and hadronic tensor respectively. Defining the spin four-vector of the initial and final electron as s_μ and s'_μ respectively, the leptonic tensor $L_{\mu\nu}$ is calculable from QED:

$$L_{\mu\nu}(k, s; k's') = \sum_{s'} \bar{u}(k, s)\gamma_\mu u(k', s')\bar{u}(k', s')\gamma_\nu u(k, s), \tag{2.7}$$

where u is the Dirac spinor and $s_\mu = \bar{u}\gamma_\mu\gamma_5 u$. $L_{\mu\nu}$ can be split into symmetric (S) and antisymmetric (A) parts under μ, ν interchange:

$$L_{\mu\nu}(k, s; k') = 2[L^{(S)}_{\mu\nu}(k; k') + iL^{(A)}_{\mu\nu}(k, s; k')], \tag{2.8}$$

with

$$L^{(S)}_{\mu\nu}(k; k') = k_\mu k'_\nu + k'_\mu k_\nu - g_{\mu\nu}(k \cdot k' - m_e^2), \tag{2.9}$$

$$L^{(A)}_{\mu\nu}(k, s; k') = m_e\varepsilon_{\mu\nu\alpha\beta}s^\alpha q^\beta. \tag{2.10}$$

The convention for the Levi-Civita tensor is $\varepsilon_{0123} = +1$.

Due to the lack of knowledge of the hadronic vertex in Figure 2-1, the hadronic tensor $W_{\mu\nu}$ is not yet calculable from first principles. Considering all possible transitions of the nucleon from the ground state $|N(P)\rangle$ to any excited state $|X(P')\rangle$, the

hadronic tensor becomes [18]:

$$W_{\mu\nu}(q;P,S) = \frac{1}{2M}\sum_X \langle N_S(P)|J_\mu(0)|X(P')\rangle\ \langle X(P')|J_\nu(0)|N_S(P)\rangle \cdot (2\pi)^3\delta^4(q+P-P'), \tag{2.11}$$

where $S^\mu = \bar{u}(P)\gamma^\mu\gamma_5 u(P)/2M$ is the hadron spin four-vector and J_μ is the electromagnetic current operator of the nucleon. Using the completeness relations of states $|X\rangle$, the tensor $W_{\mu\nu}$ can be expressed as:

$$W_{\mu\nu}(q;P,S) = \frac{1}{4\pi M}\int \mathrm{d}^4\xi\, e^{iq\cdot\xi}\,\langle N_S(P)|J_\mu(\xi)J_\nu(0)|N_S(P)\rangle\,, \tag{2.12}$$

where ξ is the spatial four-vector.

As in Eq. (2.8), the hadronic tensor can also be split into symmetric and antisymmetric parts:

$$W_{\mu\nu}(q;P,S) = W^{(S)}_{\mu\nu}(q;P) + iW^{(A)}_{\mu\nu}(q;P,S). \tag{2.13}$$

Taking into account the gauge invariance and parity conservation of the electromagnetic interaction, the most general expressions of these terms are [19]:

$$W^{(S)}_{\mu\nu}(q;P) = W_1(\nu,Q^2)\left(\frac{q_\mu q_\nu}{q^2} - g_{\mu\nu}\right) + \frac{W_2(\nu,Q^2)}{M^2}(P_\mu - \frac{P\cdot q}{q^2}q_\mu)(P_\nu - \frac{P\cdot q}{q^2}q_\nu), \tag{2.14}$$

and

$$W^{(A)}_{\mu\nu}(q;P,S) = \varepsilon_{\mu\nu\alpha\beta}q^\alpha\left[G_1(\nu,Q^2)S^\beta + \frac{G_2(\nu,Q^2)}{M^2}(S^\beta P\cdot q - P^\beta S\cdot q)\right], \tag{2.15}$$

where $W_{1,2}(\nu,Q^2)$ and $G_{1,2}(\nu,Q^2)$ are four response functions which describe the internal structure of the nucleon.

From Eqs. (2.6), (2.8) and (2.13), one has:

$$\frac{\mathrm{d}^2\sigma}{\mathrm{d}\Omega\,\mathrm{d}E'}(k,s,P,S;k') = \frac{\alpha^2}{Q^4}\frac{E'}{E}\left[2L^{(S)}_{\mu\nu}W^{\mu\nu}_{(S)} - 2L^{(A)}_{\mu\nu}W^{\mu\nu}_{(A)}\right]. \tag{2.16}$$

The two terms in the brackets can be separately studied by considering different polarizations of the initial electron and the target nucleon. For example, the first term is the usual unpolarized cross-section:

$$\frac{\mathrm{d}^2\sigma^{\mathrm{unp}}}{\mathrm{d}\Omega\,\mathrm{d}E'}(k,P;k') = \frac{1}{4}\sum_{s,S}\frac{\mathrm{d}^2\sigma}{\mathrm{d}\Omega\,\mathrm{d}E'}(k,s,P,S;k') = \frac{\alpha^2}{Q^4}\frac{E'}{E}2L^{(S)}_{\mu\nu}W^{\mu\nu}_{(S)}. \tag{2.17}$$

In the polarized case, the difference of cross-sections for scattering a polarized electron with spin s on a polarized target with spin S and that with spin $-S$ are given by the second term in Eq. (2.16):

$$\frac{\mathrm{d}^2\sigma}{\mathrm{d}\Omega\,\mathrm{d}E'}(k,s,P,-S;k') - \frac{\mathrm{d}^2\sigma}{\mathrm{d}\Omega\,\mathrm{d}E'}(k,s,P,S;k') = \frac{\alpha^2}{Q^4}\frac{E'}{E}4L^{(A)}_{\mu\nu}W^{\mu\nu}_{(A)}. \tag{2.18}$$

In practice, the response functions $W_{1,2}(\nu,Q^2)$ and $G_{1,2}(\nu,Q^2)$ are often replaced by four dimensionless structure functions in terms of the Bjorken variable x and the squared four-momentum transfer Q^2:

$$F_1(x,Q^2) = MW_1(\nu,Q^2), \tag{2.19}$$

$$F_2(x,Q^2) = \nu W_2(\nu,Q^2), \tag{2.20}$$

$$g_1(x,Q^2) = M\nu G_1(\nu,Q^2), \tag{2.21}$$

$$g_2(x,Q^2) = \nu^2 G_2(\nu,Q^2). \tag{2.22}$$

In terms of $F_{1,2}$ and $g_{1,2}$, Eqs. (2.14) and (2.15) becomes

$$\begin{aligned} W^{(S)}_{\mu\nu}(q;P) = {} & \frac{1}{M}\left(\frac{q_\mu q_\nu}{q^2} - g_{\mu\nu}\right)F_1(x,Q^2) \\ & + \frac{1}{\nu M^2}(P_\mu - \frac{P\cdot q}{q^2}q_\mu)(P_\nu - \frac{P\cdot q}{q^2}q_\nu)F_2(x,Q^2), \end{aligned} \tag{2.23}$$

$$W^{(A)}_{\mu\nu}(q;P,S) = \frac{1}{M\nu}\varepsilon_{\mu\nu\alpha\beta}q^\alpha\left[S^\beta g_1(x,Q^2) + (S^\beta - \frac{S\cdot q}{P\cdot q}P^\beta)g_2(x,Q^2)\right]. \tag{2.24}$$

Using Eqs. (2.9), (2.17) and (2.23), the differential cross-section for the inelastic

scattering of unpolarized electron on unpolarized nucleon can be written as:

$$\frac{\mathrm{d}^2\sigma}{\mathrm{d}\Omega\,\mathrm{d}E'} = \sigma_{\mathrm{Mott}}\left[\frac{2}{M}F_1(x,Q^2)\tan^2\frac{\theta}{2} + \frac{1}{\nu}F_2(x,Q^2)\right], \tag{2.25}$$

where σ_{Mott} is the cross-section for scattering an electron off a point-like infinitely heavy target, which can be expressed as:

$$\sigma_{\mathrm{Mott}} = \frac{\alpha^2\cos^2(\theta/2)}{4E^2\sin^4(\theta/2)}. \tag{2.26}$$

For polarized electrons and target, the difference of cross-sections for scattering a polarized electron on polarized targets with opposite spins can be written using Eqs. (2.10), (2.18) and (2.24):

$$\begin{aligned}\frac{\mathrm{d}^2\sigma^{s,S}}{\mathrm{d}\Omega\,\mathrm{d}E'} - \frac{\mathrm{d}^2\sigma^{s,-S}}{\mathrm{d}\Omega\,\mathrm{d}E'} = \frac{8m\alpha^2}{q^4}\frac{E'}{E}\frac{1}{M\nu}\Big\{&[(q\cdot S)(q\cdot s) + Q^2(s\cdot S)]g_1(x,Q^2) \\ &+ \frac{Q^2}{M\nu}[(s\cdot S)(P\cdot q) - (q\cdot S)(P\cdot s)]g_2(x,Q^2)\Big\}.\end{aligned} \tag{2.27}$$

Considering the case that the electron is longitudinally polarized, while the nucleon is polarized along (S) or opposite $(-S)$ with respect to an arbitrary direction $\vec{S}$, the cross-section difference can be expressed in terms of g_1 and g_2 as:

$$\begin{aligned}\frac{\mathrm{d}^2\sigma^{\rightarrow,S}}{\mathrm{d}\Omega\,\mathrm{d}E'} - \frac{\mathrm{d}^2\sigma^{\rightarrow,-S}}{\mathrm{d}\Omega\,\mathrm{d}E'} &= -\frac{4\alpha^2}{Q^2}\frac{E'}{E} \\ &\times \frac{1}{\nu M}\left[(E\cos\alpha + E'\cos\Theta)g_1(x,Q^2) + \frac{2EE'}{\nu}(\cos\Theta - \cos\alpha)g_2(x,Q^2)\right],\end{aligned} \tag{2.28}$$

where α is the angle between the incident electron momentum $\vec{k}$ and the direction of the target polarization $\vec{S}$. Θ is the angle between the outgoing electron momentum $\vec{k'}$ and $\vec{S}$. If ϕ is the azimuthal angle between the scattering plane ($\vec{k}$, $\vec{k'}$) and the polarization plane ($\vec{k}$, $\vec{S}$), $\cos\Theta$ can be expressed as:

$$\cos\Theta = \sin\theta\sin\alpha\cos\phi + \cos\theta\cos\alpha, \tag{2.29}$$

where θ is the scattering angle. See Figure 2-2 for the definitions of the angles α, θ

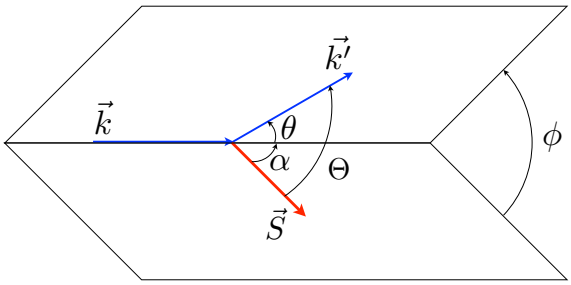

Figure 2-2: Angular relations of polarized electron scattering.

and ϕ.

Therefore, one can derive the cross-section difference for some special values of α. For the case that the target nucleons are longitudinally polarized, $\alpha = 0$ and $\Theta = \theta$ (or $\alpha = \pi$ and $\Theta = \pi - \theta$), the cross-section difference for the electron scattering on the nucleon polarized parallel ($\overrightarrow{\Rightarrow}$, $\alpha = 0$) or anti-parallel ($\overrightarrow{\Leftarrow}$, $\alpha = \pi$) to the initial electron direction (i.e. the electron spin direction since the electron is longitudinal polarized) can be expressed as:

$$\begin{aligned}\frac{\mathrm{d}^2\sigma^{\overrightarrow{\Leftarrow}}}{\mathrm{d}\Omega\,\mathrm{d}E'} - \frac{\mathrm{d}^2\sigma^{\overrightarrow{\Rightarrow}}}{\mathrm{d}\Omega\,\mathrm{d}E'} &= \frac{4\alpha^2 E'}{\nu M Q^2 E}\left[(E + E'\cos\theta)g_1(x,Q^2) + \frac{2EE'}{\nu}(\cos\theta - 1)g_2(x,Q^2)\right] \\ &= \frac{4\alpha^2 E'}{\nu M Q^2 E}\left[(E + E'\cos\theta)g_1(x,Q^2) - 2Mxg_2(x,Q^2)\right]. \qquad (2.30)\end{aligned}$$

If the target nucleons are transversely polarized and the nucleon spin lies in the scattering plane, $\alpha = \pi/2$ and $\phi = 0$ or π, the cross-section difference can be expressed as:

$$\begin{aligned}\frac{\mathrm{d}^2\sigma^{\rightarrow\Uparrow}}{\mathrm{d}\Omega\,\mathrm{d}E'} - \frac{\mathrm{d}^2\sigma^{\rightarrow\Downarrow}}{\mathrm{d}\Omega\,\mathrm{d}E'} &= \frac{4\alpha^2 E'}{\nu M Q^2 E}\left[E'\sin\theta g_1(x,Q^2) + \frac{2EE'}{\nu}\sin\theta g_2(x,Q^2)\right]. \\ &= \frac{4\alpha^2 E'^2}{\nu M Q^2 E}\sin\theta\left[g_1(x,Q^2) + \frac{2E}{\nu}g_2(x,Q^2)\right]. \qquad (2.31)\end{aligned}$$

2.3 Structure Functions in the Parton Model

In the last Section, the hadronic tensor $W_{\mu\nu}$ was written in term of the structure functions $F_{1,2}$ and $g_{1,2}$. One of the important features of the structure functions is

their scaling behavior in the Bjorken limit [20]:

$$Q^2 \to \infty, \text{ and } \nu \to \infty, \text{ with } x = \frac{Q^2}{2M\nu} \text{ fixed.} \tag{2.32}$$

It turns out that to a very good approximation the structure functions are independent of Q^2 and can be written as $F_{1,2}(x)$ and $g_{1,2}(x)$. This phenomenon known as Bjorken scaling was first discovered at the Stanford Linear Accelerator [21].

The parton model of Feynman [22] provides a clear explanation for the Bjorken scaling. Any object with a finite size must have a form factor which introduces some Q^2 dependence. Thus, the fact of Bjorken scaling implies that the nucleon must contain point-like constituents, which are named partons. Since the structure functions are Lorentz invariant, the parton model can be formulated in any frame. For convenience, the infinite momentum frame, where the nucleon is moving with momentum approaching ∞ along the z-direction, is chosen to formulate the parton model. Due to time dilatation, there is no time for interaction between the partons in this frame and the process can be viewed as the incoherent sum of elastic scattering from non-interacting partons, that is: the hadronic tensor $W_{\mu\nu}$ is given in terms of the elementary quark tensor $w_{\mu\nu}$ by [17]:

$$W_{\mu\nu}(q; P, S) = \sum_{i,s} e_i^2 \frac{1}{2P \cdot q} \int_0^1 \frac{\mathrm{d}x'}{x'} \delta(x' - x) n_i(x', s; S) w_{\mu\nu}(x', q, s), \tag{2.33}$$

where the $\sum_i$ runs over quarks and antiquarks, and n_i is the number density of the quark i with charge e_i. Since quarks are point-like particles in the model, the quark tensor $w_{\mu\nu}$ is similar to the lepton tensor $L_{\mu\nu}$.

To evaluate the structure functions from Eq. (2.33), four projection operators are defined as [19]:

$$P_1^{\alpha\beta} \equiv \frac{1}{4} \left[\frac{1}{a} P^\alpha P^\beta - g^{\alpha\beta} \right], \tag{2.34}$$

$$P_2^{\alpha\beta} \equiv \frac{3P \cdot q}{4a} \left[\frac{1}{a} P^\alpha P^\beta - \frac{1}{3} g^{\alpha\beta} \right], \tag{2.35}$$

where $a = (P \cdot q)/2x + M^2$, and

$$P_3^{\alpha\beta} \equiv \frac{(P \cdot q)^2}{bM^2(q \cdot S)} \left[(q \cdot S)S_\lambda + q_\lambda\right] P_\eta \varepsilon^{\alpha\beta\lambda\eta}, \tag{2.36}$$

$$P_4^{\alpha\beta} \equiv \frac{1}{b} \left\{ \left[\frac{(P \cdot q)^2}{M^2} + 2(P \cdot q)x \right] S_\lambda + (q \cdot S)q_\lambda \right\} P_\eta \varepsilon^{\alpha\beta\lambda\eta}, \tag{2.37}$$

where

$$b = -4M \left[\frac{(P \cdot q)^2}{M^2} + 2(P \cdot q)x - (q \cdot S)^2 \right]. \tag{2.38}$$

With these projectors, one has:

$$\begin{aligned} P_1^{\alpha\beta} W_{\alpha\beta} &= F_1, & P_2^{\alpha\beta} W_{\alpha\beta} &= F_2, \\ P_3^{\alpha\beta} W_{\alpha\beta} &= g_1, & P_4^{\alpha\beta} W_{\alpha\beta} &= g_1 + g_2. \end{aligned} \tag{2.39}$$

Applying the projection operator Eqs. (2.34) to (2.37) to Eq. (2.33), one can obtain the relations between the nucleon structure functions and the parton distribution functions:

$$F_1(x) = \frac{1}{2} \sum_i e_i^2 q_i(x), \tag{2.40}$$

$$F_2(x) = x \sum_i e_i^2 q_i(x) = 2xF_1(x), \tag{2.41}$$

$$g_1(x) = \frac{1}{2} \sum_i e_i^2 \Delta q_i(x), \tag{2.42}$$

where $q(x) = q^\uparrow(x) + q^\downarrow(x)$ is the unpolarized parton distribution function, which is the probability of finding a quark carrying the fraction x of the momentum of the nucleon. $\Delta q(x) = q^\uparrow(x) - q^\downarrow(x)$ is the polarized parton distribution function, where $q^\uparrow(x)$ ($q^\downarrow(x)$) is the number density of the quark carrying the fraction x of the momentum of the nucleon when it is aligned parallel (or anti-parallel) to the nucleon spin direction. Eq. (2.41) is a relation between F_1 and F_2 which is also known as the Callan-Gross relation [23].

The transverse polarized structure function $g_2(x)$ is zero in the naive parton model described above. However, if one allows the constituent quarks to have an intrinsic

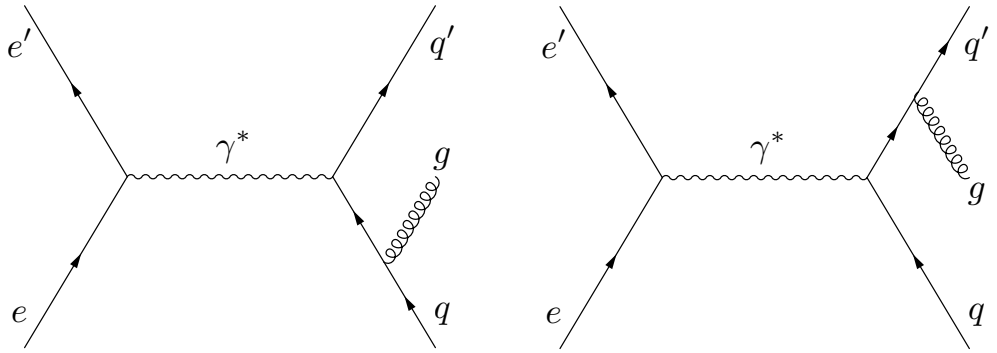

Figure 2-3: Radiating process which cannot be separated from the basic process of electron scattering.

transverse momentum in the nucleon, the value of g_2 can be non-zero. The interpretation of $g_2(x)$ in the naive parton model is not as simple as the other structure functions [18]. It carries the information of the quark-gluon interaction inside the nucleon, which will be introduced in the next chapter.

The scaling behavior of the structure functions is only valid at the Bjorken limit as mentioned at the beginning of this section. At finite Q^2, the Bjorken scaling is only a good approximation since the interaction between quarks can not be ignored. QCD radiative corrections need to be included in the cross-section calculation. Figure 2-3 shows two basic processes which cannot be separated from the major process of electron scattering. In particular, the electron scattering process from a quark cannot be separated from the scattering processes with a soft gluon radiated. As the radiative effects in QED, the soft gluon radiation also gives rise to an infinite cross-section which can be renormalized if all other processes at the same order are included.

This variation of the structure functions with Q^2 is referred to as QCD evolution. After renormalization, the gluon radiative correction gives a logarithmic dependence to the cross-section. Figure 2-4 shows the experimental Q^2-dependence of the proton F_2 structure function for a large range of x [24]. By incorporating the Q^2-dependence into the definition of the parton distributions, the expression of structure functions

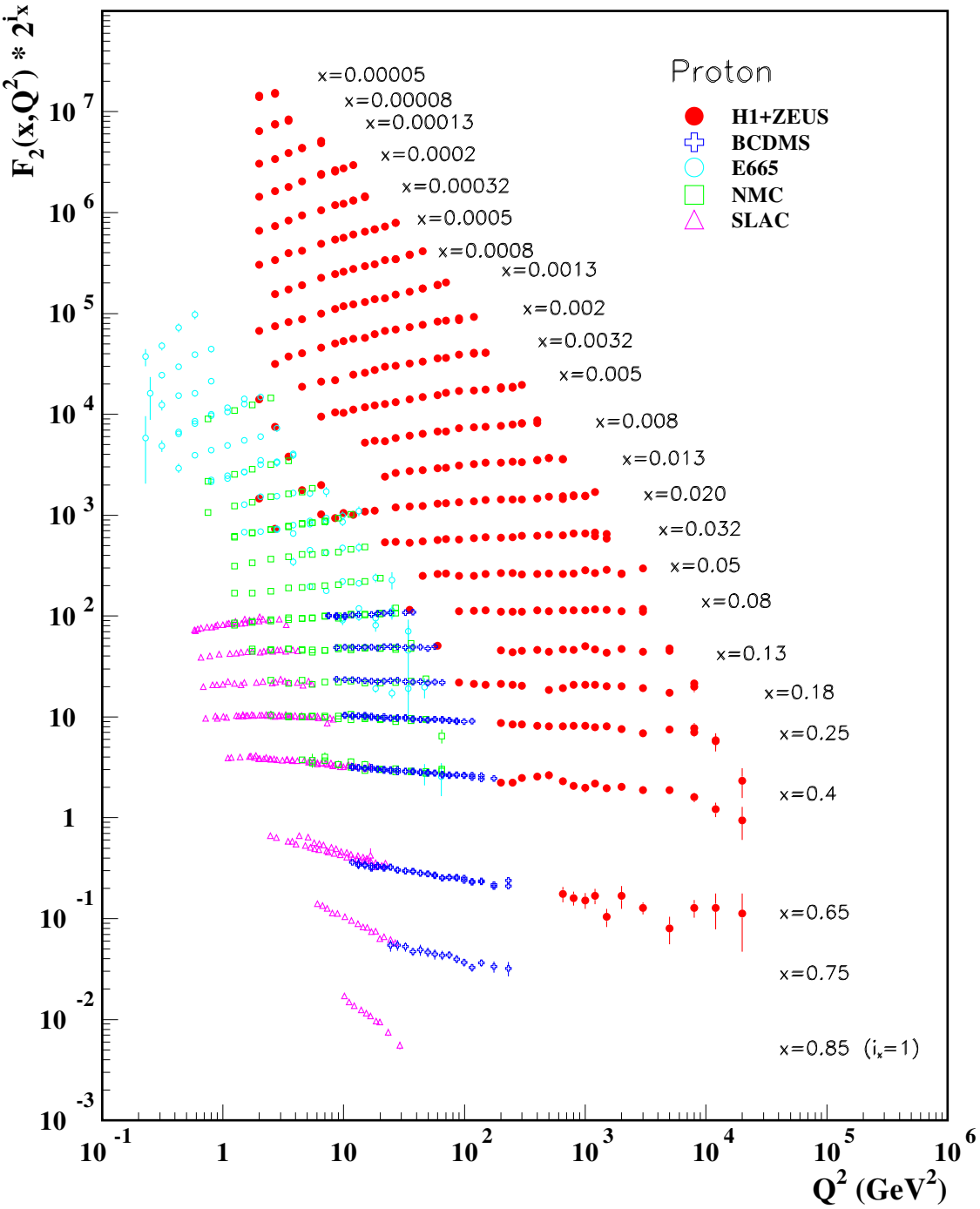

Figure 2-4: The proton structure function F_2^p measured in electromagnetic scattering of electrons and positrons off protons (collider experiments H1 and ZEUS for $Q^2 \geq 2$ GeV^2) and for electrons (SLAC) and muons (BCDMS, E665, NMC) on a fixed target. The data are plotted as a function of Q^2 in bins of fixed x. For the purpose of plotting, F_2^p has been multiplied by 2^{i_x}, where i_x is the number of the x bin, ranging from $i_x = 1$ ($x = 0.85$) to $i_x = 24$ ($x = 0.00005$). Plot reproduced from [24].

can be generalized as:

$$F_1(x, Q^2) = \frac{1}{2} \sum_i e_i^2 q_i(x, Q^2), \tag{2.43}$$

$$g_1(x, Q^2) = \frac{1}{2} \sum_i e_i^2 \Delta q_i(x, Q^2). \tag{2.44}$$

Now $q(x, Q^2)\,\mathrm{d}x$ should be interpreted as the probability of finding a quark in the nucleon with momentum fraction between x and $x+\mathrm{d}x$ when viewed with a resolution determined by Q^2. If one probes the proton at low Q^2, the wavelength is large $(1/\sqrt{Q^2})$ and the spatial resolution is poor. The structure functions is expected to be dominated by the valence quarks at this case. As Q^2 increases, more and more $q\bar{q}$ pairs and gluons can be seen since the resolution becomes better.

The QCD evolution can be calculated from perturbative QCD in the leading order. The Altarelli Parisi, or DGLAP equations developed by Gribov and Lipatov [25], Dokshitzer [26] and Altarelli and Parisi [27] provide a method to calculate the Q^2-dependence of the structure functions. These equations are first-order integro-differential equations. Thus, the parton distributions can be calculated at any Q^2 scale where perturbative QCD applies if the distributions at some particular scale is known.

2.4 Virtual Photon-absorption Cross-Sections: An Alternative Formulation

The previous sections revealed that the inclusive scattering process can be formulated with four structure functions. Before we go further, it is worth introducing an equivalent formulation of the inclusive scattering process in which the cross-section is parameterized in terms of four virtual photon-absorption cross-sections.

2.4.1 Virtual Photon-absorption Cross-Sections

As shown in Figure 2-1, the inclusive scattering process is equivalent to absorption of a virtual photon on a nucleon. In the center of mass (c.m.) frame of the hadronic intermediate state, the four-momentum of the virtual photon is given by $(\omega_\gamma, \vec{k}_\gamma)$, which can be expressed as [28]:

$$\omega_\gamma = \frac{M\nu - Q^2}{W}, \qquad \vec{k}_\gamma = \frac{M}{W}\vec{q}. \tag{2.45}$$

where $|\vec{q}| = \sqrt{\nu^2 + Q^2}$ is the lab photon momentum. Since ω_γ vanishes at $\nu = Q^2/M$ and therefore is inconvenient in the context of the multipole expansion, one can define the "equivalent photon energy" or the virtual photon flux K to replace ω_γ according to Hand's definition [29]:

$$K = K_H = \nu(1 - x) = \frac{W^2 - M^2}{2M}. \tag{2.46}$$

An alternative convention could be Gilman's definition [30]:

$$K = K_G = |\vec{q}| = \sqrt{\nu^2 + Q^2}. \tag{2.47}$$

Eqs. (2.46) and (2.47) reduce to ν for the real photon scattering at $Q^2 = 0$. However, at intermediate Q^2, the photon flux is strongly convention dependent.

The inclusive electron-nucleon scattering can then be parameterized in terms of a flux factor and four partial cross-sections [31]:

$$\frac{\mathrm{d}\sigma}{\mathrm{d}\Omega\,\mathrm{d}E'} = \Gamma_V[\sigma_T + \epsilon\sigma_L - hP_x\sqrt{2\epsilon(1-\epsilon)}\sigma_{LT} - hP_z\sqrt{1-\epsilon^2}\sigma_{TT}], \tag{2.48}$$

where h is the helicity of the longitudinally polarized electron and P_z and P_x denote the components of the target polarization parallel and perpendicular to the virtual photon momentum $\vec{q}$ in the scattering plane of the electron respectively. The ϵ is the

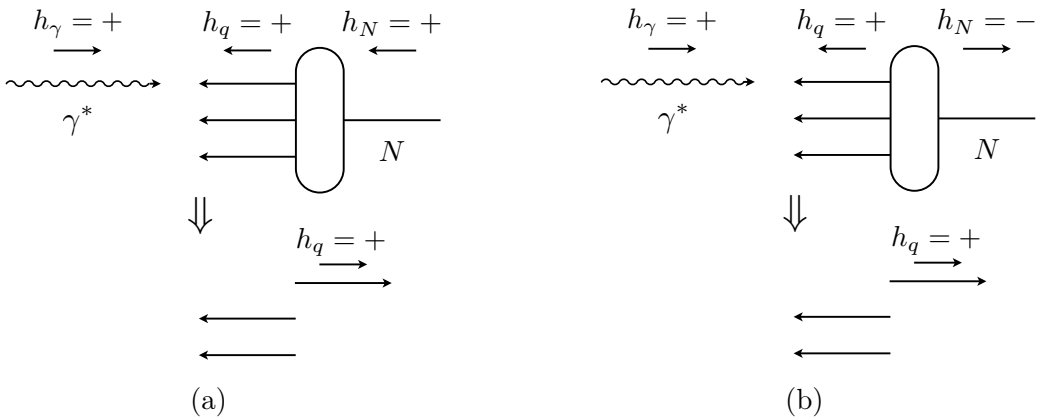

Figure 2-5: The helicity dependent cross-sections for a positive helicity virtual photon ($h_\gamma = +$) to be absorbed by a polarized nucleon (here $h_N = \pm$ means $h_N = \pm 1/2$): (a) $\sigma_{1/2}$ and (b) $\sigma_{3/2}$.

photon polarization and Γ_V is the virtual photon flux factor:

$$\epsilon = \frac{1}{1 + 2(1 + \nu^2/Q^2)\tan^2\theta/2}, \qquad \Gamma_V = \frac{\alpha}{2\pi^2}\frac{E'}{E}\frac{K}{Q^2}\frac{1}{1-\epsilon}.$$

The four partial cross-sections are the transverse (σ_T) and longitudinal (σ_L) cross-sections and two interference terms: the longitudinal-transverse cross-sections (σ_{LT}) and the transverse-transverse cross-sections (σ_{TT}). σ_T and σ_L represent the cross-sections for absorption of transverse and longitudinal virtual photons respectively. σ_L vanishes in the $Q^2 = 0$ (real photon) limit since the real photon is transversely polarized. Therefore, the total photon-absorption cross-section is given by σ_T in the real photon limit. The two spin-flip cross-sections σ_{TT} and σ_{LT} can only be measured by double-polarization experiments.

The partial cross-sections σ_T and σ_{TT} can be expressed in terms of the helicity dependent photo-absorption cross-sections $\sigma_{1/2}$ and $\sigma_{3/2}$. The subscripts refer to the total spin of the photon plus the target nucleon. Figure 2-5 shows the two different situations. These helicity dependent cross-sections are related to σ_T and σ_{TT} through:

$$\sigma_T = \frac{1}{2}(\sigma_{1/2} + \sigma_{3/2}), \qquad \sigma_{TT} = \frac{1}{2}(\sigma_{1/2} - \sigma_{3/2}). \tag{2.49}$$

The relations between the structure functions and the photo-absorption cross-

sections can be written as [18, 32]:

$$\sigma_T = AF_1, \tag{2.50}$$

$$\sigma_L = A\left[\frac{(1+\gamma^2)M}{\gamma^2\nu}F_2 - F_1\right], \tag{2.51}$$

$$\sigma_{TT} = A(g_1 - \gamma^2 g_2), \tag{2.52}$$

$$\sigma_{LT} = A\gamma(g_1 + g_2), \tag{2.53}$$

where $\gamma = Q/\nu$ and $A = 4\pi^2\alpha/MK$.

2.4.2 Compton Scattering

Now consider the elastic real photon scattering process $\gamma(k) + N(P) \to \gamma(k') + N(P')$. The four-momentum of the incident and scattered real photon is $k = (\nu, \vec{k})$ and $k' = (\nu', \vec{k'})$ respectively with $k^2 = k'^2 = 0$. In the laboratory frame, the four-momentum of the nucleon is $P = (M, \vec{0})$. If we denote the scattering angle by θ in the laboratory frame, the energy and momentum conservation gives [18]:

$$\nu' = \frac{\nu}{1 + \frac{\nu}{M}(1 - \cos\theta)}. \tag{2.54}$$

The polarization of the incident and scattered photons can be characterized by two linear polarization vectors ϵ^μ and ϵ'^ν. Due to the transverse nature of real photons, we choose:

$$\begin{aligned} \epsilon^\mu &= (0, \vec{\epsilon}), \quad \vec{k}\cdot\vec{\epsilon} = 0, \\ \epsilon'^\nu &= (0, \vec{\epsilon'}), \quad \vec{k'}\cdot\vec{\epsilon'} = 0. \end{aligned} \tag{2.55}$$

We can choose a coordinate system such that the z-axis coincides with the direction of $\vec{k}$. The polarization vector of a linearly polarized photon can be expressed as the linear combination of two unit vectors:

$$\vec{\epsilon}_x = (1, 0, 0), \quad \vec{\epsilon}_y = (0, 1, 0). \tag{2.56}$$

The circularly polarized photons are given by:

$$\vec{\epsilon}_{\lambda=1} = \frac{1}{\sqrt{2}}(\vec{\epsilon}_x + i\vec{\epsilon}_y), \quad \vec{\epsilon}_{\lambda=-1} = \frac{1}{\sqrt{2}}(\vec{\epsilon}_x - i\vec{\epsilon}_y), \tag{2.57}$$

with $\vec{\epsilon}^{\star}_{\lambda'} \cdot \vec{\epsilon}_{\lambda} = \delta_{\lambda'\lambda}$.

The differential cross-section for real Compton scattering is given by:

$$\frac{\mathrm{d}\sigma}{\mathrm{d}\nu} = \left(\frac{\nu'}{8\pi M\nu}\right)^2 |T_{fi}|^2. \tag{2.58}$$

Using the polarization vectors defined in Eq. (2.55), the transition matrix T_{fi} of real Compton scattering can be written as [18]:

$$T_{fi} = e^2 \epsilon'^{\star\mu} \epsilon^{\nu} T_{\mu\nu}(k', P'; k, P), \tag{2.59}$$

with

$$T_{\mu\nu} = i \int \mathrm{d}^4x \, e^{ik'\cdot x} \, \langle N(P')|\mathcal{T}\{J_\mu(x)J_\nu(0)\}|N(P)\rangle \,, \tag{2.60}$$

here $\mathcal{T}$ is the time-ordering operator.

For forward scattering with $\vec{k'} = \vec{k}$, the forward Compton scattering amplitude can be expressed as [32]:

$$T(\nu, \theta = 0) = \vec{\epsilon}'^{\star} \cdot \vec{\epsilon} f(\nu) + i\vec{\sigma} \cdot (\vec{\epsilon}'^{\star} \times \vec{\epsilon}) g(\nu), \tag{2.61}$$

where $\vec{\sigma}$ are the Pauli spin matrices and $f(\nu)$, $g(\nu)$ represents the spin non-flip and flip amplitudes respectively.

According to the optical theorem, the total photon absorption cross-sections are related to the imaginary part of the forward Compton scattering amplitudes by:

$$\begin{aligned} \mathrm{Im}\, f(\nu) &= \frac{\nu}{8\pi}(\sigma_{1/2}(\nu) + \sigma_{3/2}(\nu)) = \frac{\nu}{4\pi}\sigma_T(\nu), \\ \mathrm{Im}\, g(\nu) &= \frac{\nu}{8\pi}(\sigma_{1/2}(\nu) - \sigma_{3/2}(\nu)) = \frac{\nu}{4\pi}\sigma_{TT}(\nu). \end{aligned} \tag{2.62}$$

The amplitudes $f(\nu)$ and $g(\nu)$ can be expanded in powers of ν via the low energy

theorem (LET) of Low [33] and Gell-Mann and Goldberger [34]:

$$f(\nu) = -\frac{Z^2e^2}{4\pi M} + (\alpha+\beta)\nu^2 + \mathcal{O}(\nu^4), \tag{2.63}$$

$$g(\nu) = -\frac{\kappa^2e^2}{8\pi M^2}\nu + \gamma_0\nu^3 + \mathcal{O}(\nu^5), \tag{2.64}$$

where Z is the charge in the unit of elementary charge, and κ is the anomalous magnetic moment in the unit of nuclear magneton. The leading term of the spin non-flip amplitude gives the classical Thomson scattering result. The $\mathcal{O}(\nu^2)$ term contains information of the internal structure and appears as the sum of the electric and magnetic dipole polarizabilities α and β. The $\mathcal{O}(\nu^3)$ term of the spin flip amplitude is related to the forward spin polarizability γ_0 with information of the spin structure.

By use of the optical theorem, the Kramers-Kronig dispersion relations can be derived for $f(\nu)$ and $g(\nu)$, which gives:

$$\mathrm{Re}\, f(\nu) = f(0) + \frac{\nu^2}{2\pi^2}\mathcal{P}\int_{\nu_0}^{\infty} \mathrm{d}\nu' \, \frac{\sigma_T(\nu')}{\nu'^2 - \nu^2}, \tag{2.65}$$

$$\mathrm{Re}\, g(\nu) = \frac{\nu}{4\pi^2}\mathcal{P}\int_{\nu_0}^{\infty} \mathrm{d}\nu' \, \nu' \frac{\sigma_{1/2}(\nu') - \sigma_{3/2}(\nu')}{\nu'^2 - \nu^2}, \tag{2.66}$$

where $\mathcal{P}$ means the principal value of the integral. ν_0 is introduced to ensure that the integral converges. Thus, the two integrals can be expand as a Taylor series in ν:

$$\mathrm{Re}\, f(\nu) = f(0) + \sum_{n=1}\left(\frac{1}{2\pi^2}\int_{\nu_0}^{\infty} \mathrm{d}\nu' \, \frac{\sigma_T(\nu')}{\nu'^{2n}}\right)\nu^{2n}, \tag{2.67}$$

$$\mathrm{Re}\, g(\nu) = \sum_{n=1}\left(\frac{1}{4\pi^2}\int_{\nu_0}^{\infty} \mathrm{d}\nu' \, \frac{\sigma_{1/2}(\nu') - \sigma_{3/2}(\nu')}{\nu'^{2n-1}}\right)\nu^{2n-1}. \tag{2.68}$$

By comparing Eqs. (2.67) and (2.68) with Eqs. (2.63) and (2.64), we can obtain Baldin's sum rule [35, 36] from the $\mathcal{O}(\nu^2)$ term of spin non-flip amplitude $f(\nu)$:

$$\alpha + \beta = \frac{1}{2\pi^2}\int_{\nu_0}^{\infty} \mathrm{d}\nu' \, \frac{\sigma_T(\nu')}{\nu'^2}. \tag{2.69}$$

From the leading term of the spin flip amplitude $g(\nu)$, we can obtain the Gerasimov-

Drell-Hearn (GDH) sum rule [37, 38]:

$$-2\pi^2\alpha\frac{\kappa^2}{M^2} = \int_{\nu_0}^{\infty} \mathrm{d}\nu' \, \frac{\sigma_{1/2}(\nu') - \sigma_{3/2}(\nu')}{\nu'} \equiv I, \tag{2.70}$$

where $\alpha = e^2/4\pi$ is the fine structure constant. And we can also obtain a relation for the forward spin polarizability [34, 39]:

$$\gamma_0 = \frac{1}{4\pi^2} \int_{\nu_0}^{\infty} \mathrm{d}\nu' \, \frac{\sigma_{1/2}(\nu') - \sigma_{3/2}(\nu')}{\nu'^3}. \tag{2.71}$$

The above discussion could be generalized if we treat the real photon as virtual by replacing k with q ($q^2 \neq 0$). This is known as the double virtual Compton scattering (VVCS). Comparing Eq. (2.60) with Eq. (2.12), we notice that the difference between $T_{\mu\nu}$ and the hadronic tensor $W_{\mu\nu}$ is the time ordering operator $\mathcal{T}$ of the electromagnetic currents. Actually $W_{\mu\nu}$ is related to the forward virtual Compton tensor $T_{\mu\nu}$ by [18]:

$$W_{\mu\nu}(q, P) = \frac{1}{2\pi M} \operatorname{Im} T_{\mu\nu}(q, P; q, P). \tag{2.72}$$

This relation implies that the components of the hadronic tensor, e.g., the structure functions, are related to the forward double VVCS amplitudes by the Kramers-Kronig dispersion relations.

2.4.3 Sum Rules and Spin Polarizabilities

In the previous section, we discussed the formulation of real Compton scattering as well as the moments and sum rules which could be extracted from the dispersion relations of the forward real Compton scattering amplitude. Most of that discussion could be generalized for double virtual Compton scattering. In this case, the virtual photon has a third polarization component in addition to the $\epsilon_\pm$ defined in Eq. (2.57) due to the longitudinal degree of freedom. The longitudinal polarization vector could be defined as:

$$\epsilon_0 = \frac{1}{Q}(|\vec{q}|, 0, 0, q_0), \tag{2.73}$$

where q is the four-momentum of the virtual photon and we have chosen the z-axis in the direction of the photon propagation, i.e.,

$$q = (q_0, 0, 0, |\vec{q}|). \tag{2.74}$$

All three polarization vectors and the momentum are orthogonal in the Lorentz metrics.

The forward real Compton scattering amplitude Eq. (2.61) could be generalized for the VVCS as [32]:

$$\begin{aligned} T(\nu, Q^2, \theta = 0) = \quad & \vec{\epsilon}'^{\star} \cdot \vec{\epsilon} f_T(\nu, Q^2) + f_L(\nu, Q^2) \\ & + i\vec{\sigma} \cdot (\vec{\epsilon}'^{\star} \times \vec{\epsilon}) g_{TT}(\nu, Q^2) + i\vec{\sigma} \cdot [(\vec{\epsilon}'^{\star} - \vec{\epsilon}) \times \hat{q}] g_{LT}(\nu, Q^2). \end{aligned} \tag{2.75}$$

Notice the $f(\nu)$ and $g(\nu)$ has been generalized to $f_T(\nu, Q^2)$ and $g_{TT}(\nu, Q^2)$.

Similar to what we did in the previous section, we can apply the optical theorem to Eq. (2.75) and get the relations between the four amplitudes and the four partial cross-sections of the inclusive scattering in Eq. (2.48), which gives:

$$\begin{aligned} \mathrm{Im}\, f_T(\nu, Q^2) &= \frac{K}{4\pi} \sigma_T(\nu, Q^2), & \mathrm{Im}\, f_L(\nu, Q^2) &= \frac{K}{4\pi} \sigma_L(\nu, Q^2), \\ \mathrm{Im}\, g_{TT}(\nu, Q^2) &= \frac{K}{4\pi} \sigma_{TT}(\nu, Q^2), & \mathrm{Im}\, g_{LT}(\nu, Q^2) &= \frac{K}{4\pi} \sigma_{LT}(\nu, Q^2), \end{aligned} \tag{2.76}$$

where K is the virtual photon flux defined in Eq. (2.46) or Eq. (2.47).

Considering the spin-dependent amplitude g_{TT} and assuming it converges appropriately at high energy, there is an unsubtracted dispersion relation [32]:

$$\mathrm{Re}[g_{TT}(\nu, Q^2) - g_{TT}^{\mathrm{pole}}(\nu, Q^2)] = \frac{\nu}{2\pi^2} \mathcal{P} \int_{\nu_0}^{\infty} \mathrm{d}\nu' \, \frac{K(\nu', Q^2) \sigma_{TT}(\nu', Q^2)}{\nu'^2 - \nu^2}, \tag{2.77}$$

where g_{TT}^{pole} is the elastic contribution. The lower limit of the integration ν_0 is the pion-production threshold. As what we did for real Compton scattering, we could also perform a low energy expansion for the non-pole contribution of g_{TT} similar to

Eq. (2.64):

$$\mathrm{Re}[g_{TT}(\nu,Q^2)-g_{TT}^{\mathrm{pole}}(\nu,Q^2)]=\frac{2\alpha}{M^2}I_A(Q^2)\nu+\gamma_0(Q^2)\nu^3+\mathcal{O}\big(\nu^5\big). \tag{2.78}$$

Comparing Eq. (2.78) and the Taylor expansion of Eq. (2.77), the $\mathcal{O}(\nu)$ term yields a generalized GDH sum rule [31]:

$$\begin{aligned} I_A(Q^2)&=\frac{M^2}{4\pi^2\alpha}\int_{\nu_0}^{\infty}\mathrm{d}\nu\,\frac{K(\nu,Q^2)}{\nu}\frac{\sigma_{TT}(\nu,Q^2)}{\nu},\\ &=\frac{2M^2}{Q^2}\int_0^{x_0}\mathrm{d}x\left\{g_1(x,Q^2)-\frac{4M^2}{Q^2}x^2g_2(x,Q^2)\right\}. \end{aligned} \tag{2.79}$$

The $\mathcal{O}(\nu^3)$ term leads to a generalized form of the forward spin polarizability γ_0:

$$\begin{aligned} \gamma_0(Q^2)&=\frac{1}{2\pi^2}\int_{\nu_0}^{\infty}\mathrm{d}\nu\,\frac{K(\nu,Q^2)}{\nu}\frac{\sigma_{TT}(\nu,Q^2)}{\nu^3},\\ &=\frac{16\alpha M^2}{Q^6}\int_0^{x_0}\mathrm{d}x\,x^2\left\{g_1(x,Q^2)-\frac{4M^2}{Q^2}x^2g_2(x,Q^2)\right\}. \end{aligned} \tag{2.80}$$

The term proportional to g_2 can be dropped when Q^2 is large.

For amplitude g_{LT}, we have an unsubtracted dispersion relation in the form of [32]:

$$\mathrm{Re}[g_{LT}(\nu,Q^2)-g_{LT}^{\mathrm{pole}}(\nu,Q^2)]=\frac{1}{2\pi^2}\mathcal{P}\int_{\nu_0}^{\infty}\mathrm{d}\nu'\,\frac{\nu' K(\nu',Q^2)\sigma_{LT}(\nu',Q^2)}{\nu'^2-\nu^2}. \tag{2.81}$$

The low energy expansion of the non-pole contribution of g_{LT} gives:

$$\mathrm{Re}[g_{LT}(\nu,Q^2)-g_{LT}^{\mathrm{pole}}(\nu,Q^2)]=\frac{2\alpha}{M^2}QI_3(Q^2)\nu+Q\delta_{LT}(Q^2)\nu^2+\mathcal{O}\big(\nu^4\big), \tag{2.82}$$

where the leading term is a sum rule for $I_3(Q^2)$:

$$\begin{aligned} I_3(Q^2)&=\frac{M^2}{4\pi^2\alpha}\int_{\nu_0}^{\infty}\mathrm{d}\nu\,\frac{K(\nu,Q^2)}{\nu}\frac{\sigma_{LT}(\nu,Q^2)}{Q},\\ &=\frac{2M^2}{Q^2}\int_0^{x_0}\mathrm{d}x\left\{g_1(x,Q^2)+g_2(x,Q^2)\right\}, \end{aligned} \tag{2.83}$$

and the $\mathcal{O}(\nu^2)$ gives the generalized longitudinal-transverse polarizability:

$$\begin{aligned}\delta_{LT}(Q^2) &= \frac{1}{2\pi^2}\int_{\nu_0}^{\infty} \mathrm{d}\nu\, \frac{K(\nu,Q^2)}{\nu}\frac{\sigma_{LT}(\nu,Q^2)}{Q\nu^2}, \\ &= \frac{16\alpha M^2}{Q^6}\int_0^{x_0} \mathrm{d}x\, x^2 \left\{g_1(x,Q^2)+g_2(x,Q^2)\right\}.\end{aligned} \tag{2.84}$$

The forward VVCS amplitude $T(\nu, Q^2, \theta = 0)$ can also be written in the form of an one-to-one correspondence with the structure functions [32]:

$$\begin{aligned}T(\nu,Q^2,\theta=0) = \epsilon'^{\star}_{\mu}\epsilon_{\nu}\Bigg\{&\left(\frac{q^\mu q^\nu}{q^2}-g^{\mu\nu}\right)T_1(\nu,Q^2) \\ &+\frac{1}{P\cdot q}(P^\mu-\frac{P\cdot q}{q^2}q^\mu)(P^\nu-\frac{P\cdot q}{q^2}q^\nu)T_2(\nu,Q^2) \\ &+i\varepsilon^{\mu\nu\alpha\beta}\frac{1}{M}q_\alpha S_\beta S_1(\nu,Q^2) \\ &+i\varepsilon^{\mu\nu\alpha\beta}\frac{1}{M^3}q_\alpha(P\cdot qS_\beta - S\cdot qP_\beta)S_2(\nu,Q^2)\Bigg\},\end{aligned} \tag{2.85}$$

where P^μ and S^μ are the four momentum and the spin vector of the nucleon and T_1, T_2, S_1, S_2 are four VVCS amplitudes which is covariant under Lorentz transform.

Since we only discussed te spin-flip amplitudes g_{TT} and g_{LT} in this section, we will focus on S_1 and S_2, which can be expressed as a linear combination of g_{TT} and g_{LT}:

$$\begin{aligned}S_1(\nu,Q^2) &= \frac{\nu M}{\nu^2+Q^2}\left(g_{TT}(\nu,Q^2)+\frac{Q}{\nu}g_{LT}(\nu,Q^2)\right), \\ S_2(\nu,Q^2) &= -\frac{M^2}{\nu^2+Q^2}\left(g_{TT}(\nu,Q^2)-\frac{\nu}{Q}g_{LT}(\nu,Q^2)\right).\end{aligned} \tag{2.86}$$

We can construct unsubtracted dispersion relations for S_1 and S_2 with a similar procedure as g_{LT} and g_{TT}.

For amplitude S_1, the low energy expansion has the form:

$$\begin{aligned}&\mathrm{Re}[S_1(\nu,Q^2)-S_1^{\mathrm{pole}}(\nu,Q^2)] = \\ &\qquad\frac{2\alpha}{M^2}I_1(Q^2)+\left[\frac{2\alpha}{MQ^2}(I_A(Q^2)-I_1(Q^2))+M\delta_{LT}(Q^2)\right]\nu^2+\mathcal{O}\big(\nu^4\big),\end{aligned} \tag{2.87}$$

where the leading term leads to a sum rule:

$$\begin{aligned} I_1(Q^2) &\equiv \frac{2M^2}{Q^2}\int_0^{x_0} \mathrm{d}x\, g_1(x,Q^2) \\ &= \frac{M^2}{4\pi^2\alpha}\int_{\nu_0}^{\infty} \mathrm{d}\nu\, \frac{K(\nu,Q^2)}{\nu^2+Q^2}\left\{\sigma_{TT}(\nu,Q^2)+\frac{Q}{\nu}\sigma_{LT}(\nu,Q^2)\right\}, \end{aligned} \tag{2.88}$$

which reduces to the GDH sum rule at $Q^2 = 0$ (real photon limit). $I_1(Q^2)$ has a limit at large Q^2:

$$I_1(Q^2) \to (2M^2/Q^2)\Gamma_1(Q^2), \qquad Q^2 \to \infty, \tag{2.89}$$

where

$$\Gamma_1(Q^2) \equiv \int_0^1 \mathrm{d}x\, g_1(x,Q^2). \tag{2.90}$$

Here the Γ_1 is the first moment of structure function g_1. The Bjorken sum rule [40, 41] gives a prediction of the isovector combination $\Gamma_1^p - \Gamma_1^n$ with the QCD radiative corrections [42]:

$$\begin{aligned} \Gamma_1^p - \Gamma_1^n &= \frac{1}{6} g_A \\ &\times \left\{1 - \left(\frac{\alpha_S(Q^2)}{\pi}\right) - 3.5833\left(\frac{\alpha_S(Q^2)}{\pi}\right)^2 - 20.2153\left(\frac{\alpha_S(Q^2)}{\pi}\right)^3 + \cdots\right\}, \end{aligned} \tag{2.91}$$

where g_A is the axial-vector coupling constant. At $Q^2 = 5$ GeV^2, Eq. (2.91) gives $\Gamma_1^p - \Gamma_1^n = 0.182 \pm 0.005$ if only the three light quark flavors are considered. The next-to-leading order fit to global g_1 data gives $\Gamma_1^p - \Gamma_1^n = 0.176 \pm 0.003 \pm 0.007$ [43], in agreement with the theoretical calculation.

The unsubtracted dispersion relations of the amplitude S_2 lead to the Burkhardt-Cottingham sum rule. Assume the high energy behavior of this amplitude is given by $S_2 \to \nu^{\alpha_2}$ with $\alpha_2 < -1$ when $\nu \to \infty$, there should be a dispersion relation for νS_2. By subtracting the dispersion relation of νS_2 from the dispersion relation of S_2 multiplied by ν, we could get a "super-convergence relation" [44]:

$$\int_0^1 \mathrm{d}x\, g_2(x,Q^2) = 0. \tag{2.92}$$

This indicates that the elastic and the inelastic contributions to the first moment of g_2 should cancel for any value of Q^2. The elastic and inelastic contributions to the integral can be separated, thus the BC sum rule can be expressed as:

$$I_2(Q^2) \equiv \frac{2M^2}{Q^2}\int_0^{x_0} \mathrm{d}x\, g_2(x,Q^2) = \frac{1}{4}F_P(Q^2)(F_D(Q^2)+F_P(Q^2)), \tag{2.93}$$

where F_P is the Pauli form factor and F_D is the Dirac form factor. The integral I_2 can also be written in terms of the photon-absorption cross-sections and the Sachs form factor G_E and G_M:

$$\begin{aligned} I_2(Q^2) &= \frac{M^2}{4\pi^2\alpha}\int_{\nu_0}^{\infty}\frac{K(\nu,Q^2)}{\nu^2+Q^2}\left\{-\sigma_{TT}(\nu,Q^2)+\frac{\nu}{Q}\sigma_{LT}(\nu,Q^2)\right\} \\ &= \frac{1}{4}\frac{G_M(Q^2)(G_M(Q^2)-G_E(Q^2))}{1+\tau}, \end{aligned} \tag{2.94}$$

with $\tau = Q^2/4M^2$.

Chapter 3

Theoretical Methods

The internal structure of the nucleon can be parameterized by unpolarized and polarized structure functions as described in Chapter 2. In this chapter, some of the most common theoretical methods to calculate the Q^2 evolution of the structure functions will be discussed. We will give special emphasis to the chiral perturbation theory which is expected to be applicable in the low Q^2, the region covered in E08-027.

3.1 Chiral Perturbation Theory

3.1.1 Chiral Symmetry

QCD is a type of quantum field theory called non-abelian gauge theory of colored quarks and gluons. The complete QCD Lagrangian is [45]:

$$\mathcal{L}_{\mathrm{QCD}} = \sum_f \bar{q}_f (i\not{D} - m_f) q_f - \frac{1}{4}\mathcal{G}^{\alpha}_{\mu\nu}\mathcal{G}^{\mu\nu}_{\alpha}, \tag{3.1}$$

where $\mathcal{G}$ is the field strength tensor and q is the quark spinor. The summation is taken over all six quark flavors.

One particular important concept in QCD is asymptotic freedom, which refers to the fact that the coupling strength decreases for increasing momentum transfer Q^2. Asymptotic freedom allows a perturbative approach at high energies for QCD

by expanding in powers of the strong interaction coupling constant $\alpha_s(Q^2)$. However, for low energy interactions ($Q^2 < 1$ GeV^2), the coupling constant $\alpha_s(Q^2)$ is of order one, which makes the expansion approach no longer valid.

The masses of the three light quarks u, d and s are small compared to typical masses of light hadrons, like the ρ meson (770 MeV) or the proton (938 MeV). For a massless fermion, the chirality or handedness is identical to the particle's helicity $h = \vec{\sigma}\cdot\vec{p}/|\vec{p}|$, where $\vec{\sigma}$ are the Pauli spin matrices and $\vec{p}$ is the particle's momentum. In the limit where the light quark masses vanish, the left-handed and right-handed quark fields are decoupled from each other in the QCD Lagrangian. We could introduce the left and right handed quark fields:

$$q_{L,R} = \frac{1}{2}(1 \mp \gamma_5)q. \tag{3.2}$$

and rewrite the QCD Lagrangian as [46]:

$$\mathcal{L}^0_{\text{QCD}} = \sum_{f=u,d,s} (\bar{q}_{R,f} i \not{D} q_{R,f} + \bar{q}_{L,f} i \not{D} q_{L,f}) - \frac{1}{4}\mathcal{G}^{\alpha}_{\mu\nu}\mathcal{G}^{\mu\nu}_{\alpha}. \tag{3.3}$$

The Lagrangian $\mathcal{L}^0_{\text{QCD}}$ exhibits a global $\text{U}(3)_L \times \text{U}(3)_R$ symmetry, which is referred as chiral symmetry.

The chiral symmetry can be decomposed to a $\text{SU}(3)_L \times \text{SU}(3)_R \times \text{U}(1)_V$ symmetry [46]. Here the $\text{U}(1)_V$ symmetry is connected to baryon number conservation, where quarks and antiquarks are assigned the baryon numbers $B = 1/3$ and $B = -1/3$ respectively. Mesons and baryons can be distinguished with their baryon numbers $B = 0$ or $B = 1$.

On the other side, although the theory admits the $\text{SU}(3)_L \times \text{SU}(3)_R$ symmetry, the ground state of QCD does not have the full symmetry. Consider the linear combinations of the 16 generators of the group $G = \text{SU}(3)_L \times \text{SU}(3)_R$, $Q^a_V = Q^a_R + Q^a_L$ and $Q^a_A = Q^a_R - Q^a_L$, $a = 1, \cdots, 8$, the generators Q^a_V form a Lie algebra corresponding to a $\text{SU}(3)_V$ subgroup H of the G. In the chiral limit, the ground state is necessarily invariant under H [47], i.e., the eight generators Q^a_V annihilate the ground state.

However, if we apply Q_A^a to an arbitrary state of a given multiplet with well-defined parity, we would obtain a degenerate state of opposite parity since the axial generators Q_A^a have negative parity [46]. This assumes that hadrons should have a partner of the same mass but with opposite parity. Such a parity doubling is not observed in the real hadron spectrum, which means that the ground state is not invariant under the full symmetry group G, i.e., Q_A^a do not annihilate the ground state. In other words, the chiral symmetry is spontaneously broken to the flavor group $\mathrm{SU}(3)_V$.

Goldstone's theorem requires that each generator which does not annihilate the ground state is associated with a Goldstone boson [48, 49]. Thus, the eight generators Q_A^a imply the existence of eight massless Goldstone bosons with negative parity and baryon number zero which transform as an octet under $\mathrm{SU}(3)_V$. In nature, the eight lightest hadrons, including the pions $(\pi^{\pm}, \pi^0)$, the kaons $(K^{\pm}, K^0, \bar{K}^0)$ and the eta (η), compose an octet which qualifies for these Goldstone bosons. The mass of these bosons are interpreted as a result of the explicit symmetry breaking due to the non-zero quark mass.

3.1.2 Chiral Effective Field Theory

At low-energy limit, it is impractical to directly deal with quarks and gluons since the relevant degrees of freedom in QCD at low-energy region are composite hadrons. An effective field theory is constructed to approximate the QCD in the low-energy limit which still reproduces the basic QCD symmetries and spontaneous symmetry breaking patterns.

The basic idea of an effective field theory is to treat the active, light particles as collective degrees of freedom, while the heavy particles as frozen and static sources [18]. An effective Lagrangian $\mathcal{L}_{\text{eff}}$ is constructed to describe the dynamics which incorporates all symmetries of the underlying fundamental theory.

Thus, the QCD Lagrangian Eq. (3.1) is split into a symmetric part, $\mathcal{L}^0_{\text{QCD}}$, and a symmetry breaking part $\mathcal{L}'_{\text{QCD}}$ to construct this effective Lagrangian:

$$\mathcal{L}^{\text{eff}}_{\text{QCD}} = \mathcal{L}^0_{\text{QCD}} + \mathcal{L}'_{\text{QCD}}, \tag{3.4}$$

where

$$\mathcal{L}'_{\rm QCD} = -\sum_f \bar{q}_f m_f q_f \tag{3.5}$$

is considered as a perturbation to the $\mathcal{L}^0_{\rm QCD}$.

The effective Lagrangian should be able to represent the same low-energy expansion as QCD itself. Any matrix element or scattering amplitude derived from this effective Lagrangian is organized as a low-energy expansion in powers of energies and momenta (generically denoted as p) of the interacting particles. Although the symmetry breaking mass term can be treated perturbatively, the convergence radius is often quite limited. However, many rigorous statements can still be made within the limit. This framework for the expansion of the effective field theory is called chiral perturbation theory (χPT) [50].

3.1.3 Chiral Perturbative Theory for Baryons

Chiral Perturbation Theory provides a systematic method to discuss the interaction of Goldstone bosons with each other and with the external fields, which has been discussed in many theoretical works such as [51, 52]. The baryons have also been included into the scheme as well [53]. Consider the transition matrix elements with only a single baryon in the initial and final states, we can describe many static properties such as masses or magnetic moments, form factors as well as some more complicated processes, such as pion-nucleon scattering, Compton scattering, pion photo-production etc with the help of the χPT. However, the presence of the baryons creates a complication. The low-energy expansion corresponds to an expansion in pion loops. The baryon mass does not vanish in the chiral limit and is comparable to the chiral scale $\Lambda_\chi \simeq 1$GeV, and thus only baryon three-momenta can be considered small [54]. This implies that there is no guarantee that the small-momentum expansion is an exact one-to-one corresponding to the one-loop graphs. Theorists have considered two main approaches to deal with this complication: Heavy Baryon χPT (HBχPT) [55, 56] and Relativistic Baryon χPT (RBχPT) [57].

Heavey Baryon χPT :

The baryons are considered as very heavy in the HBχPT approach. This allows for a consistent power counting scheme as an expansion in the inverse powers of the baryon mass. The troublesome baryon mass term can be eliminated in this case. However the expansion in the ratio of pion to nucleon masses m_π/M_N is not expected to converge very fast [54].

Relativistic Baryon χPT :

The heavy baryon χPT suffers from a deficiency that the standard low energy expansion in powers of meson momenta and light quark masses in general only converges in part of the low energy region. The problem is generated by a set of higher order graphs involving insertions in nucleon lines [58]. The non-relativistic expansion in HBχPT causes the problem and it does not occur in the relativistic formulation of the effective theory. This relativistically invariant formulation can extract the infrared singularities of the various one loop graphs occurring in the χPT series. This procedure can be viewed as a novel method of regularization, where any dimensionally regularized one-loop integral can be split into an infrared singular and a regular part depending on a particular choice of Feynman parameterization. The low-energy constants absorb the contribution from the regular part while non-trivial results are obtained from the chiral expansion of the infrared part. The result agrees with the one obtained with HBχPT if the chiral expansion of the one-loop integrals converge.

Both HBχPT and RBχPT have been used to study the spin-dependent structure functions and their moments [59–62]. The theoretical effects in these works are limited to the two flavor case of the u and d quarks. Typically the Q^2-dependence of the Compton amplitudes is studied in the chiral limit, which can be connected to the spin structure functions via Kramers-Kronig dispersion relations as mentioned in Section 2.4.

One more thing needs to be mentioned is the contribution from the resonances. The resonances are expected to have significant contributions to the Compton amplitudes, especially from the $\Delta(1232)$ resonance. Ideally one would like to include the contribution from the Δ as a dynamical degree of freedom in the effective Lagrangian. However, an effective field theory formulation for the relativistic pion-nucleon-delta system does not exist. Thus, the contribution from Δ can only be done systematically in the heavy baryon scheme treating the nucleon-delta mass splitting as an additional small parameter [63]. The Δ contribution is estimated by calculating relativistic Born graphs, which are dependent on a few experimental parameters that are not well-known. Another important resonance contribution which is less pronounced is due to the vector mesons [62]. Ref. [64] discusses the procedure to include the degrees of freedom of the vector mesons.

3.2 Operator Product Expansion

The Operator Product Expansion (OPE) was originally introduced by Wilson in 1969 as an attempt to provide direct QCD predictions for the moments of the structure functions via sum rules [65]. The method is model-independent and the main results depend only on some general results from Quantum Field Theory.

As mentioned in Section 2.4.2, the hadronic tensor $W_{\mu\nu}$ of the inclusive electron-nucleon scattering is related to the forward virtual Compton tensor $T_{\mu\nu}$. At the Bjorken limit, where the Q^2 and $p \cdot q$ are both large - typically greater than 2 GeV^2, the Fourier transform in Eq. (2.60) is dominated by the behavior $x^2 \to 0$. The OPE is the ideal tool to deal with such problems [18].

The OPE allows the evaluation of products of operators by separating the perturbative part of the product from the non-perturbative part. For example, the product of the two operators $\mathcal{O}_a(x)\mathcal{O}_b(0)$ can be expressed as a sum over local operators in the limit $x \to 0$ [66]:

$$\mathcal{O}_a(x)\mathcal{O}_b(0) = \sum_i C_{ab,i}(x)\mathcal{O}_i(0), \tag{3.6}$$

where C_{ab} are the Wilson coefficient functions. Because of the asymptotic freedom feature of QCD, the coupling constant is small at short distances. Thus the Wilson coefficient functions can be calculated perturbatively in the limit $x \to 0$.

In practice, the momentum space version of the operator product is more commonly used:

$$\int \mathrm{d}^4 x e^{iq\cdot x} \mathcal{O}_a(x)\mathcal{O}_b(0). \tag{3.7}$$

The limit $x \to 0$ forces $q \to \infty$ in the Fourier transform of the Operator Product Expansion of Eq. (3.6), which can be expressed in terms of the coefficient functions that depend on q:

$$\lim_{q\to\infty} \int \mathrm{d}^4 x e^{iq\cdot x} \mathcal{O}_a(x)\mathcal{O}_b(0) = \sum_i C_{ab,i}(q)\mathcal{O}_i(0). \tag{3.8}$$

This expansion will be valid when q is much larger than the typical hadronic mass scale Λ_{QCD}.

The local operators used in OPE are quark and gluon operators with arbitrary dimension d and spin n. With this notation, an operator with dimension d and spin n can be written as:

$$\mathcal{O}_{n,d}^{\mu_1\cdots\mu_n}, \tag{3.9}$$

where $\mathcal{O}$ is symmetric and traceless in $\mu_1 \cdots \mu_n$. The matrix elements of $\mathcal{O}$ of a hadron are proportional to

$$\frac{\mathcal{S}[p^{\mu_1}\cdots p^{\mu_n}]}{M^{2+n-d}} \tag{3.10}$$

for a vector operator, and to

$$\frac{\mathcal{S}[s^{\mu_1}p^{\mu_2}\cdots p^{\mu_n}]}{M^{2+n-d}} \tag{3.11}$$

for an axial operator. Here $\mathcal{S}$ symmetries the Lorentz indices. The power of M is decided by dimensional analysis. A detailed dimensional analysis gives that the contribution of the operator $\mathcal{O}$ to $W_{\mu\nu}L^{\mu\nu}$ is of order [66]:

$$x^{-n}\left(\frac{M}{Q}\right)^{\tau-2}, \tag{3.12}$$

where $\tau \equiv d - n$ is defined as the "twist". At large Q^2, the most important operator in the OPE are those with the twist-2, since higher twists are suppressed by increasing powers of M/Q. Thus higher twist contributions are expected to be more important for low Q^2. The reliable parts of the parton model can be mapped onto an OPE analysis in which the leading twist is related to the amplitude for scattering off asymptotically free quarks and the higher twists arise from the quark-gluon interaction and the quark mass effects.

3.2.1 Operator Product Expansion Analysis of g_2

When we discussed the structure functions in the parton model in Section 2.3, we claimed that the g_2 structure function does not have a simple interpretation in the naive parton model. The most reliable method to explore the g_2 structure function is OPE. Light quark mass effects are suppressed by m/Q in F_1 or g_1 but they are important in g_2 where they enter as $\mathcal{O}(m/\Lambda_{\rm QCD})$ [67].

In analogy to the hadron tensor, the forward virtual Compton scattering amplitude $T_{\mu\nu}$ in Eq. (2.60) can be decomposed to [68]:

$$T_{\mu\nu}(q;P,S) = T^{(S)}_{\mu\nu}(q;P) + iT^{(A)}_{\mu\nu}(q;P,S), \tag{3.13}$$

$$T^{(S)}_{\mu\nu}(q;P) = -g_{\mu\nu}T_1(\nu,Q^2) + \frac{P_\mu P_\nu}{M^2}T_2(\nu,Q^2) + q^\mu \text{ or } q^\nu \text{ terms}, \tag{3.14}$$

$$T^{(A)}_{\mu\nu}(q;P,S) = \frac{\varepsilon_{\mu\nu\alpha\beta}q^\alpha S^\beta}{M^2}A_1(\nu,Q^2) + \frac{\varepsilon_{\mu\nu\alpha\beta}q^\alpha(\nu S^\beta - q\cdot S P^\beta)}{M^4}A_2(\nu,Q^2). \tag{3.15}$$

From Eq. (2.72), the relation between $T_{\mu\nu}$ and the hadronic tensor is $W_{\mu\nu} = T_{\mu\nu}/2\pi M$. Thus, by comparing the imaginary part of $T_{\mu\nu}$ and the hadronic tensor, we can get:

$$g_1(x,Q^2) = \frac{\nu}{2\pi M^2}\,\mathrm{Im}\,A_1(\nu,Q^2), \quad g_2(x,Q^2) = \frac{\nu^2}{2\pi M^4}\,\mathrm{Im}\,A_2(\nu,Q^2). \tag{3.16}$$

We could define

$$\alpha_1(x,Q^2) = \frac{\nu}{M^2}A_1(\nu,Q^2), \quad \alpha_2(x,Q^2) = \frac{\nu^2}{M^4}A_2(\nu,Q^2). \tag{3.17}$$

for convenience. The Kramers-Kronig dispersion relations of $\alpha_1(x,Q^2)$ and $\alpha_1(x,Q^2)$ can be written as [68]:

$$\begin{aligned}\alpha_1(\omega,Q^2) &= \frac{2\omega}{\pi}\int_1^\infty \frac{\mathrm{d}\omega'}{\omega'^2-\omega^2}\,\mathrm{Im}\,\alpha_1(\omega',Q^2),\\ \alpha_2(\omega,Q^2) &= \frac{2\omega^3}{\pi}\int_1^\infty \frac{\mathrm{d}\omega'}{\omega'^2(\omega'^2-\omega^2)}\,\mathrm{Im}\,\alpha_2(\omega',Q^2),\end{aligned} \tag{3.18}$$

where $\omega = 1/x$. Replacing $\alpha_{1,2}$ in Eq. (3.18) with $g_{1,2}$ and expanding the right side in Taylor series gives the dispersion relations between $\alpha_{1,2}$ and $g_{1,2}$:

$$\begin{aligned}\alpha_1(x,Q^2) &= \frac{4}{x}\sum_{n=0,2,4,\ldots}\left(\frac{1}{x^n}\right)\int_0^1 \mathrm{d}y\, y^n g_1(y,Q^2),\\ \alpha_2(x,Q^2) &= \frac{4}{x^3}\sum_{n=0,2,4,\ldots}\left(\frac{1}{x^n}\right)\int_0^1 \mathrm{d}y\, y^{n+2} g_2(y,Q^2).\end{aligned} \tag{3.19}$$

$T_{\mu\nu}$ could also be calculated via Operator Product Expansion. The calculation result gives us the expressions for the $\alpha_1(x,Q^2)$ and $\alpha_1(x,Q^2)$ as a series of $1/x$ [68]:

$$\alpha_1(x,Q^2)+\alpha_2(x,Q^2) = \sum_{n=0,2,4,\ldots}\frac{a_n+nd_n}{n+1}\frac{1}{x^{n+1}}, \tag{3.20}$$

$$\alpha_2(x,Q^2) = \sum_{n=2,4,\ldots}\frac{n(d_n-a_n)}{n+1}\frac{1}{x^{n+1}}, \tag{3.21}$$

where a_n are the twist-2 and d_n are the twist-3 matrix elements of the quark and gluon operators. By comparing Eqs. (3.20) and (3.21) with Eq. (3.19), we can get an infinite set of moment sum rules for the structure function g_1 and g_2:

$$\int_0^1 \mathrm{d}x\, x^n g_1(x,Q^2) = \frac{1}{4}a_n, \quad n=0,2,4,\ldots, \tag{3.22}$$

$$\int_0^1 \mathrm{d}x\, x^n g_2(x,Q^2) = \frac{1}{4}\frac{n}{n+1}(d_n-a_n), \quad n=2,4,\ldots. \tag{3.23}$$

The symmetry of the system under charge conjugation selects only even moments out in the above relations.

Eq. (3.22) connects g_1 with the twist-2 matrix element a_n. If we replace the a_n

with the corresponding moments of g_1, the leading twist terms cancel, and we get:

$$\int_0^1 \mathrm{d}x\, x^{n-1} \left(g_1(x,Q^2) + \frac{n}{n-1} g_2(x,Q^2) \right) = \frac{1}{4} d_{n-1}, \quad n \geq 3. \tag{3.24}$$

If we only consider the leading twist effect and set the twist-3 d_n terms to be 0, we can get:

$$\int_0^1 \mathrm{d}x\, x^{n-1} [g_1(x,Q^2) + g_2(x,Q^2)] = \int_0^1 \mathrm{d}x\, x^{n-1} \frac{1}{n} g_1(x,Q^2). \tag{3.25}$$

Notice that the left hand side and the right hand side are both in the form of Mellin Transform. Using the convolution property of integral transforms and the fact that $1/n$ is the Mellin transform of unity [69], Eq. (3.25) can be inverted as:

$$g_1(x,Q^2) + g_2(x,Q^2) = \int_x^1 \frac{\mathrm{d}y}{y} g_1(y,Q^2). \tag{3.26}$$

This relation is referred as the Wandzura-Wilczek relation [70]:

$$g_2^{\mathrm{WW}}(x,Q^2) = -g_1(x,Q^2) + \int_x^1 \frac{\mathrm{d}y}{y} g_1(y,Q^2), \tag{3.27}$$

which shows that the leading twist part of g_2 is determined completely by g_1 and can be interpreted by the parton model.

With the Wandzura-Wilczek relation, the g_2 structure function can be separated into leading and higher-twist components, which can be expressed as:

$$g_2(x,Q^2) = g_2^{\mathrm{WW}}(x,Q^2) + \bar{g}_2(x,Q^2), \tag{3.28}$$

where

$$\int_0^1 \mathrm{d}x\, x^n \bar{g}_2(x,Q^2) = \frac{n}{4(n+1)} d_n, \quad n = 2,4,\ldots. \tag{3.29}$$

The higher-twist part $\bar{g}_2$ can also be separated as [71]:

$$g_2(x,Q^2) = -\int_x^1 \frac{\partial}{\partial y} \left[\frac{m_q}{M} h_T(y,Q^2) + \zeta(y,Q^2) \right] \frac{\mathrm{d}y}{y}. \tag{3.30}$$

There are three contributions to the structure function g_2 [6]:

1. g_2^{WW}: The leading twist-2 term, which depends only on g_1;

2. h_T: Arises from the quark transverse polarization distribution. Also twist-2, this term is suppressed by the smallness of the quark mass;

3. ζ: The twist-3 part which arises from quark-gluon interactions.

The g_2^{WW} defined by the Wandzura-Wilczek relation is not a good approximation to g_2 at low Q^2 since the higher twist contribution can not be ignored. At typical Jefferson Lab kinematics, g_2 strongly deviates from its leading twist behavior which gives g_2 a unique sensitivity to higher twist, i.e. interaction-dependent effects in QCD [68].

Chapter 4

Physics Motivation

In previous chapters, we have discussed the unpolarized and polarized structure functions and their relations to the parton model. These structure functions have been extracted over a wide kinematic range during the past 40 years. However, data on the spin structure function g_2 at low energy are still lacking. Jefferson Lab Experiment E08-027 will provide precise g_2 data for the proton in the resonance region and extract the generalized longitudinal-transverse polarizability δ_{LT}. δ_{LT} is expected to be a good test for the Chiral Perturbation Theory, as mentioned in Section 3.1. In addition, the g_2 data in the low Q^2 region could be used to provide a test of the Burkhardt-Cottingham (BC) sum rule. In this chapter, we will first give an overview of previous experiments of structure function measurements. The generalized longitudinal-transverse polarizability δ_{LT} and the BC sum rule will be discussed as the major motivation of E08-027. The low Q^2 g_2 data will also help to improve the precision of the hyperfine structure calculation of hydrogen, which will also be discussed in this chapter.

4.1 Existing g_2 Data

In Section 2.2, the relations between the spin structure functions and the cross-sections have been given as Eqs. (2.30) and (2.31). To extract the spin structure functions g_1 and g_2, one natural way is to measure the cross-section differences, which

are defined as:

$$\Delta\sigma_{\parallel} = \mathrm{d}\sigma^{\rightleftarrows} - \mathrm{d}\sigma^{\rightrightarrows}, \tag{4.1}$$

$$\Delta\sigma_{\perp} = \mathrm{d}\sigma^{\rightarrow\Uparrow} - \mathrm{d}\sigma^{\rightarrow\Downarrow}, \tag{4.2}$$

where the single arrow and the double arrow indicate the polarization of the electrons and the target respectively: $\rightleftarrows$ and $\rightrightarrows$ means the target is longitudinal polarized, $\rightarrow\Uparrow$ and $\rightarrow\Downarrow$ means the target is transversely polarized. The second method is to measure the asymmetries which typically have reduced systematic uncertainty. The longitudinal asymmetry $A_{\parallel}$ and transverse asymmetry $A_{\perp}$ can be defined straightforwardly:

$$A_{\parallel} = \frac{\mathrm{d}\sigma^{\rightleftarrows} - \mathrm{d}\sigma^{\rightrightarrows}}{\mathrm{d}\sigma^{\rightleftarrows} + \mathrm{d}\sigma^{\rightrightarrows}} = \frac{\Delta\sigma_{\parallel}}{2\,\mathrm{d}\sigma_{\mathrm{unpol}}}, \tag{4.3}$$

$$A_{\perp} = \frac{\mathrm{d}\sigma^{\rightarrow\Uparrow} - \mathrm{d}\sigma^{\rightarrow\Downarrow}}{\mathrm{d}\sigma^{\rightarrow\Uparrow} + \mathrm{d}\sigma^{\rightarrow\Downarrow}} = \frac{\Delta\sigma_{\perp}}{2\,\mathrm{d}\sigma_{\mathrm{unpol}}}. \tag{4.4}$$

From the photon-absorption cross-sections formulation discussed in Section 2.4.1, we could define two more asymmetries via Eqs. (2.50) to (2.53):

$$A_1 = \frac{\sigma_{TT}}{\sigma_T} = \frac{g_1 - \gamma^2 g_2}{F_1}, \tag{4.5}$$

$$A_2 = \frac{\sigma_{LT}}{\sigma_T} = \frac{\gamma(g_1 + g_2)}{F_1}, \tag{4.6}$$

where $\gamma = Q/\nu$.

One can measure the longitudinal and transverse cross-section differences $\sigma_{\parallel}$ and $\sigma_{\perp}$ to extract g_2. As an alternative way, it is also possible to measure the asymmetries $A_{\parallel}$, $A_{\perp}$ or A_1, A_2 and combine with existing F_1 results to extract g_2.

SLAC represented the earliest results for g_2 structure function in the DIS region [72]. During the same time, the SMC group at CERN used deep inelastic muon-nucleon scattering to extract the g_1 and g_2 structure functions for a proton target [73]. Since g_2 is relatively small, more statistics are always required to extract it than for the extraction of g_1. Thus, some of the experiments like the SLAC E155x [74]

focused on transversely polarized targets to achieve enough statistics and extracted g_2 using existing g_1 or A_1 data. The most recent results came from Jefferson Lab, where several experiments have collected a large amount of data covering a wide Q^2 range with a high intensity polarized electron beam. These JLab measurements covered both DIS and resonance regions.

The most precise DIS measurement results of g_2 for proton and deuteron targets were represented by SLAC E155x [74]. The kinematic range was $0.02 \leq x \leq 0.8$ and $0.7 \leq Q^2 \leq 20$ GeV^2. The SLAC E143 [75] and E155 [74] also contributed to the g_2 measurement of proton. The g_2 results from SLAC E143, E155 and E155x are shown in Figure 4-1. The solid curve in the figure represents the g_2^{WW} calculation results using g_1 data. The curve shows that the measurement and the leading twist

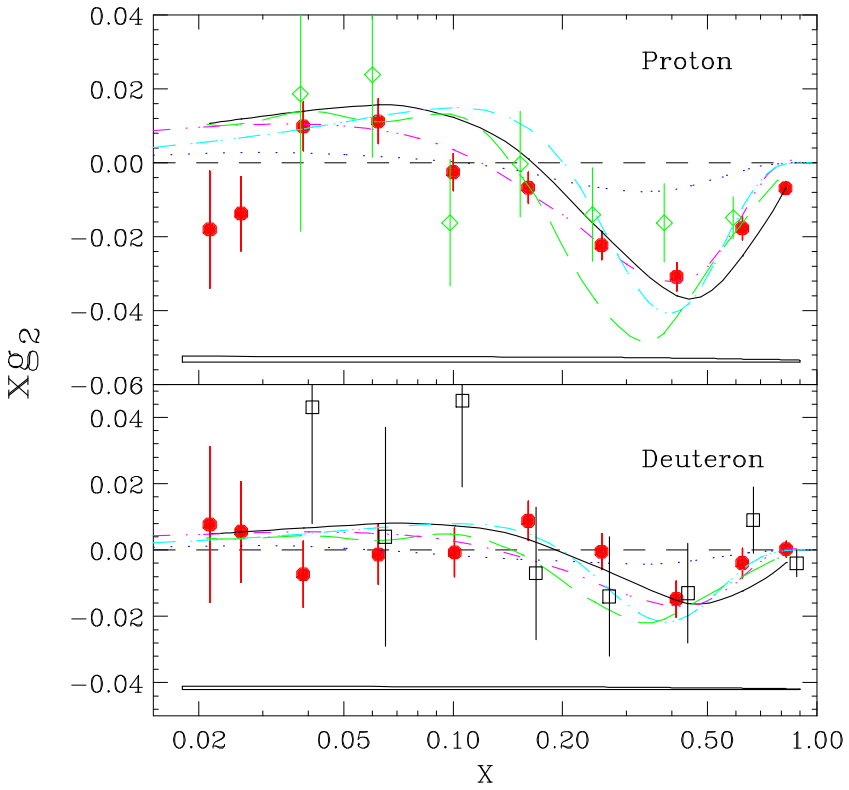

Figure 4-1: xg_2 data from E155x [74] (solid circle), E143 [75] (open diamond) and E155 [74] (open square). The g_2^{WW} calculation result at the average Q^2 of E155x is also shown as the solid line as well as some model estimations from Stratmann [76] (dash-dot), Song [77] (dot), Weigel and Gamberg [78] (short dash) and Wakamatsu [79] (long dash). Plot reproduced from [74].

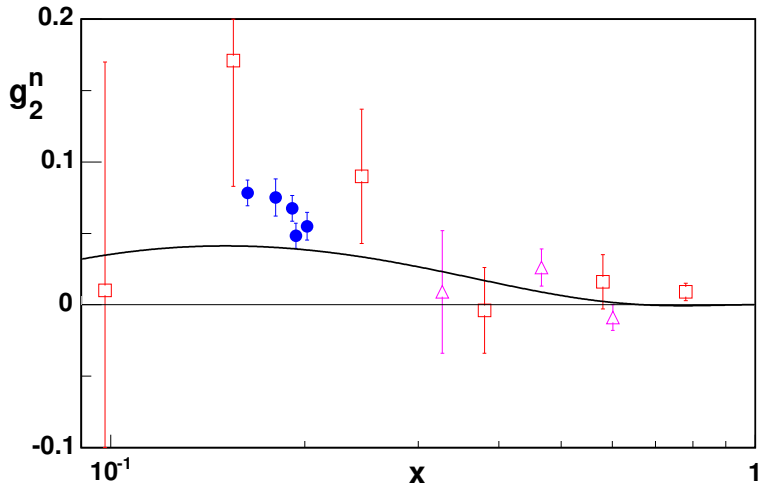

Figure 4-2: xg_2^n data from E97-103 [80] (solid circle), E99-117 [81] (open triangle) and E155 [74] (open square). The solid curve shows $g_2^{\rm WW}$ calculation at $Q^2 = 1.0$ GeV^2. Plot reproduced from [80].

estimation are consistent. However, the large error bars do not exclude the possible higher-twist effects.

As mentioned above, JLab also measured the g_2 structure function in the DIS region. The JLab E97-103 measured g_2 for neutrons and reported a two standard deviation difference from the leading twist expectation of g_2^n [80]. The Q^2 coverage of this experiment is $0.58 < Q^2 < 1.36$ GeV^2 at $x \approx 0.2$. Figure 4-2 shows the xg_2^n results from JLab E97-103 [80], E99-117 [81] and SLAC E155 [74]. The figure clearly represents the deviation between the experimental results and the leading twist estimation.

From the discussion in Section 3.1.3, we know that the quark-gluon interaction has a stronger effect in the resonance region. The first experiment to measure g_2 in the resonance region was the SLAC E143, at $Q^2 = 0.5$ GeV^2 and 1.2 GeV^2 [75]. However the error bars were large for this measurement. JLab E94-010 collected a large amount of data to extract the neutron g_2 structure function at low Q^2 [8]. The structure function g_2 was extracted from the longitudinal and transverse cross-section differences of a polarized ^{3}He target. The results of ^{3}He g_2 are shown in Figure 4-3, which shows a significant deviation from the $g_2^{\rm WW}$ estimation.

The Resonance Spin Structure (RSS) collaboration in JLab Hall B measured the

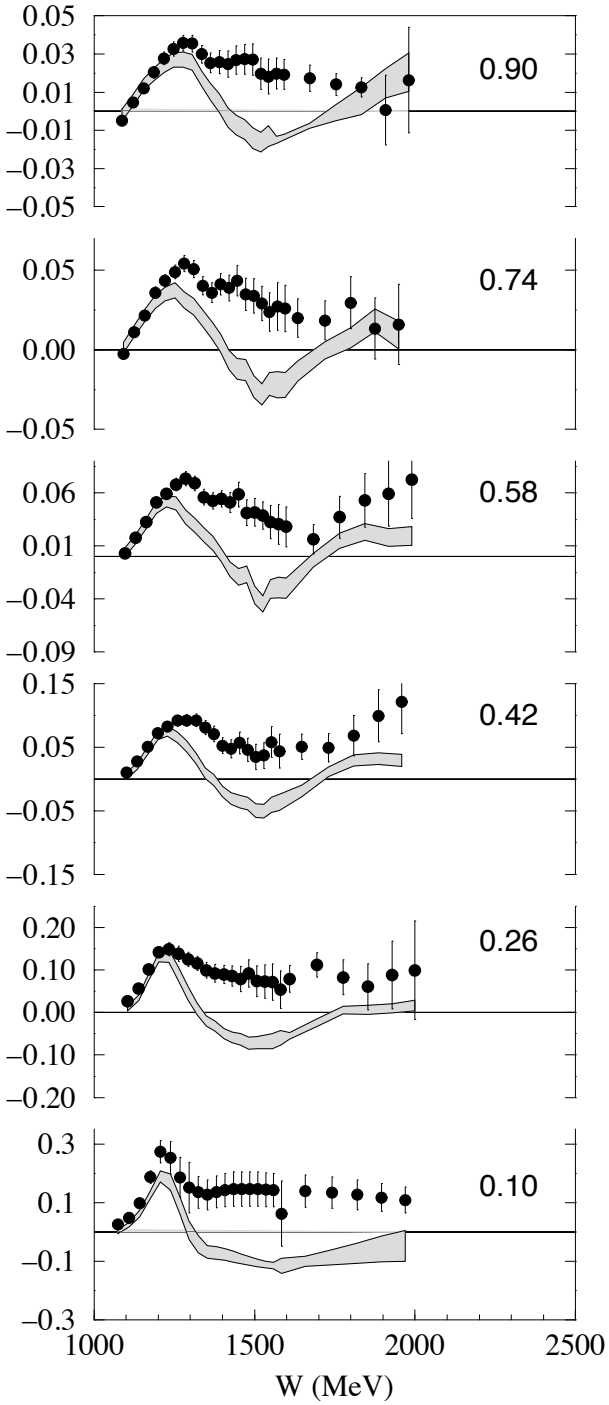

Figure 4-3: ^{3}He g_2 data from E94-010. The constant Q^2 values are indicated in GeV^2 in each panel. The grey bands represent the $g_2^{\rm WW}$ expectations at each corresponding Q^2 value. Plot reproduced from [8].

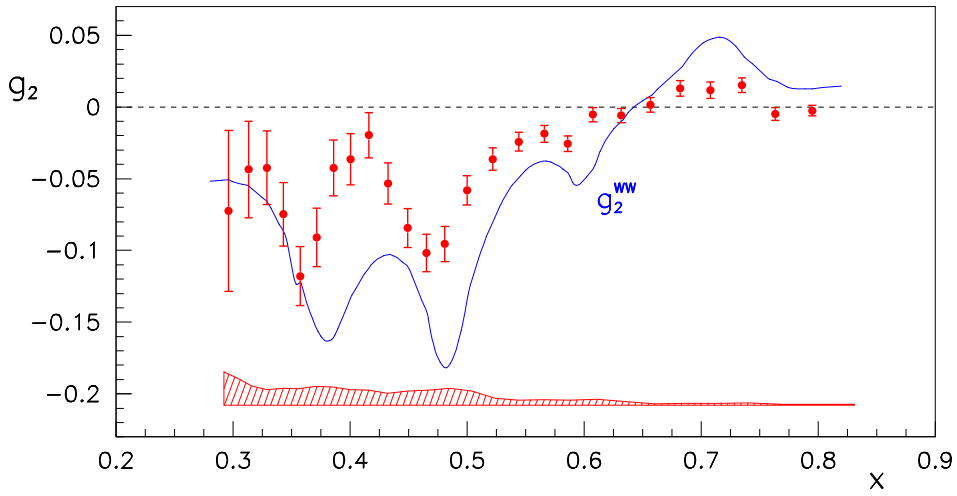

Figure 4-4: Proton g_2 data from RSS experiment compared with the g_2^{WW} expectations at $Q^2 = 1.3$ GeV^2. Plot reproduced from [10].

proton g_2 structure function at $Q^2 = 1.3$ GeV^2 [10]. Currently this is the lowest Q^2 measurement of g_2^p. The results are shown in Figure 4-4. The leading twist behavior is clearly insufficient to describe the data.

4.2 Existing Data for Spin Polarizabilities

From the discussion in Section 2.4, we know that the nucleon polarizabilities are fundamental observables that characterize nucleon structure. The electric and magnetic polarizabilities α and β describe the response of a nucleon to an external electromagnetic field. Real photon Compton scattering experiments were performed to measure these two quantities since they are related to the spin non-flip forward Compton scattering amplitude [82, 83]. The forward spin polarizability γ_0 is associated with the spin flip amplitude. It has been measured at MAMI (Mainz) with a circularly polarized photon beam on a longitudinally polarized proton target [84].

In the previous section, we have discussed that these polarizabilities could be generalized in VVCS. The generalized polarizabilities defined in Eqs. (2.80) and (2.84) have an extra $1/\nu^2$ weighting in the integrand compared to the corresponding leading moments. Thus, the contribution of the large-ν region to these integrals are suppressed by this weight. With this suppression effect, the generalized spin polarizabil-

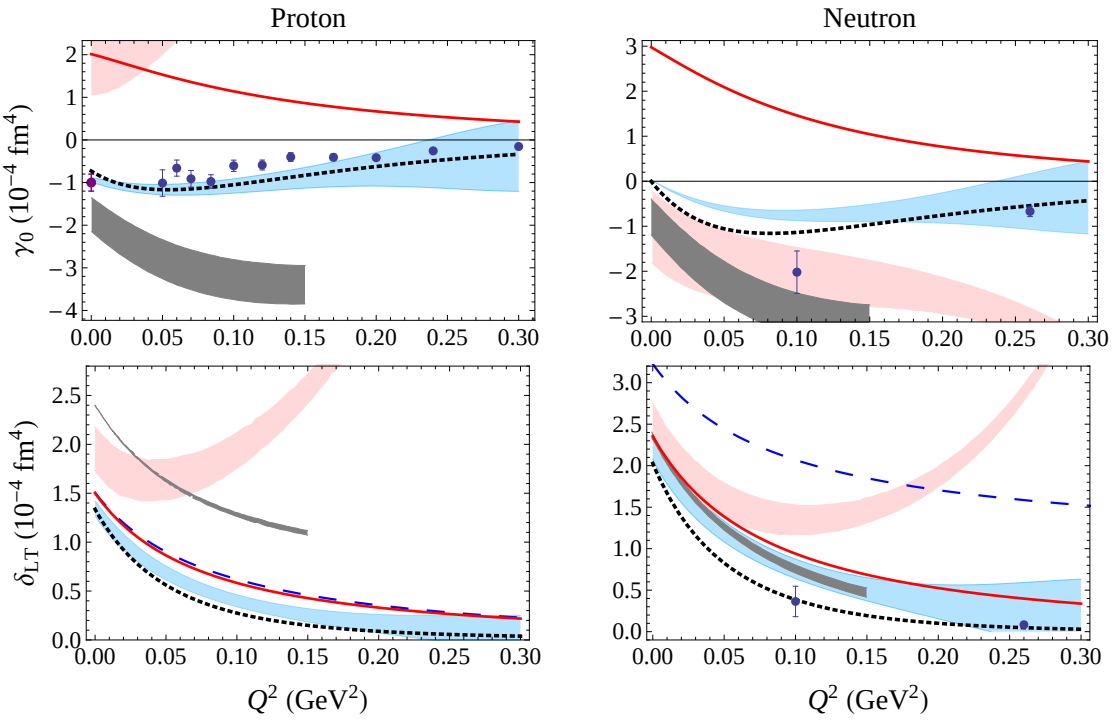

Figure 4-5: Generalized spin polarizability γ_0 and δ_{LT} of proton and neutron. The neutron data are from E94-010 experiment [9]. The proton data at $Q^2 = 0$ (purple dot) are from ELSA [85], and at finite Q^2 (blue dots) from EG1 experiment at JLab [86]. The blue dashed line is the HBχPT calculation [61], off the scale in the upper panels. The red bands shows the IR version of RBχPT calculation [62]. The grey bands are the first RBχPT calculation from Ref. [87]. The red solid lines and blue bands shows the most recent LO and NLO RBχPT calculations respectively [88]. Black dotted lines represents the empirical evaluation using the Mainz online partial-wave analysis of meson electroproduction (MAID). Plot reproduced from [88].

ities become a perfect tool to probe the nucleon structure in the chiral perturbation region. The generalized polarizabilities have been evaluated with next-to-leading order (NLO) χPT calculations at low Q^2 [61, 62]. As mentioned in Section 3.1.3, the nucleon resonances, especially the Δ resonance, play an important role in the χPT calculations. Ref. [62] and [61] have pointed out that the generalized longitudinal polarizability δ_{LT} is insensitive to the Δ resonance compare with the generalized forward spin polarizability γ_0. The effects from the Δ resonance contribution are expected to be important in γ_0 but are supposed to largely cancel in δ_{LT}.

The experimental results compared with the χPT calculations are shown in Figure 4-5. The first results of neutron $\gamma_0(Q^2)$ and $\delta_{LT}(Q^2)$ were obtained from JLab

Hall A E94-010 [9] (blue dots in the neutron panels). The data are compared with a HBχPT calculation [61] (blue dashed line) and an infrared-regularized (IR) version of RBχPT calculation [62] (red bands) which is relativisitic but has an unphysical analytic structure. At the lowest Q^2 point, the IR version of RBχPT calculation of γ_0 including the resonance contributions agrees with the experimental result from E94-010 for neutron. But there are discrepancies between the HBχPT calculation of γ_0 and the experimental result even at the lowest Q^2 point. For δ_{LT}, both the HBχPT calculation and the IR version of RBχPT calculation indicates a significant disagreement with the data, which is known as the "δ_{LT} puzzle". Since the δ_{LT} is insensitive to the Δ resonance contribution, it is believed that δ_{LT} is a more suitable testing base for the χPT compare with γ_0. A first RBχPT calculation (with no unphysical analytical structure) from Ref. [87] shows that it agrees much better than the HBχPT and the IR version of the RBχPT for γ_0 (grey bands). The most recent calculation from Ref. [88] using LO and NLO RBχPT shows that the δ_{LT} data agrees with their NLO calculation (blue bands). The neutron γ_0 and δ_{LT} data in Figure 4-5 is obtained from the JLab E94-010. The proton δ_{LT} data is required to complete the comparison. This is one of the major physics motivation of the JLab E08-027.

4.3 Burkhardt-Cottingham Sum Rule

In Section 2.4.3, we have discussed the dispersion relations for the covariant spin-dependent VVCS amplitudes S_2. The dispersion relations for S_2 and νS_2 lead to a sum rule for g_2 which is valid for all Q^2 [44]:

$$\Gamma_2(Q^2) = \int_0^1 \mathrm{d}x\, g_2(x, Q^2) = 0. \tag{4.7}$$

The existence of the dispersion relation of νS_2 requires $S_2 \to \nu^{\alpha_2}$ with $\alpha_2 < -1$ when $\nu \to \infty$. Thus, the convergence condition of the integral leads to $g_2(x, Q^2) \to x^{\tilde{\alpha}_2}$ with $\tilde{\alpha}_2 > -1$ when $x \to 0$, which means that g_2 must exhibit Regge behavior at low x and does not exhibit a delta function singularity at $x = 0$ [67].

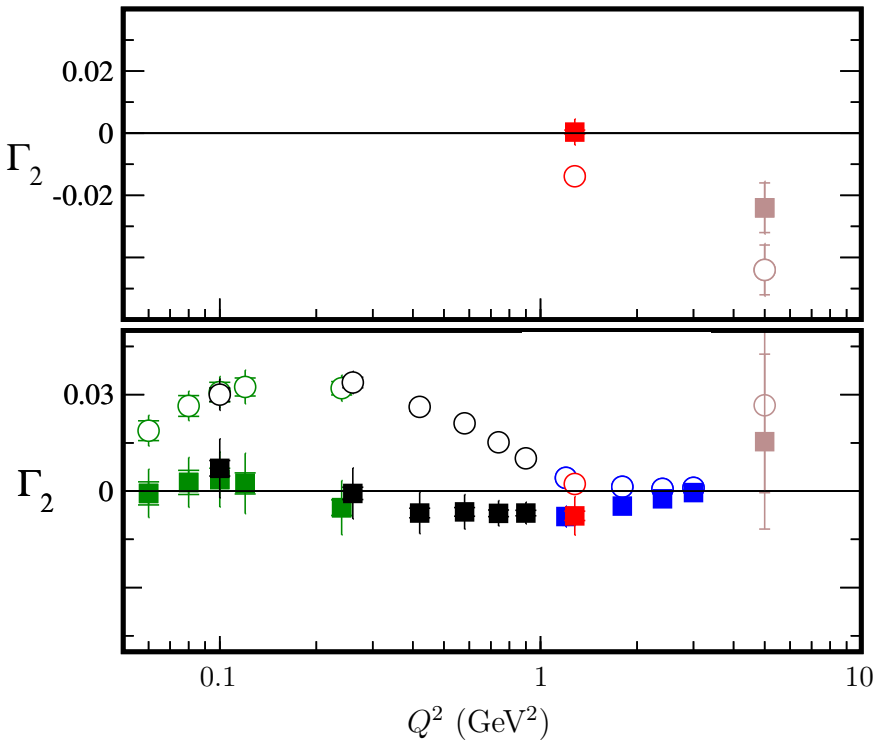

Figure 4-6: The verification of the BC sum rule from JLab Hall C experiment RSS (red) and Hall A experiments E94-010 [8] (black), E97-110 (green) and E01-012 (blue), together with SLAC E155x [74] (brown). The open circles are the measured values and the solid squares are the total moments including the elastic and estimated contributions from high energy region. The data from experiments RSS and E97-110 are still preliminary. Plot reproduced from [89].

The first measurement of the moment Γ_2 is the SLAC E155, which included the result of proton, deuteron and neutron. JLab Hall A has collected a large amount of data to extract the BC integral of neutron over a wide kinematic range in several experiments: E94-010 [8], E97-110 and E01-012. Since it is impossible to cover the full integral range, the full $(0 < x < 1)$ integral is evaluated using the elastics form factors for the elastic contribution, and assuming $g_2 = g_2^{\mathrm{WW}}$ in the very low-x region. The full integral exhibits a significant cancellation of the inelastic (resonance and DIS) and elastic contributions. The neutron data agrees with the BC sum rule prediction within uncertainty.

On the other hand, the proton BC integral deviated from zero by three standard deviations in SLAC E155x [75]. E155x covered the x range from 0.02 to 0.8 and its Q^2

coverage $0.8-8.2$ GeV^2 was averaged to 5 GeV^2. JLab experiment RSS also measured the BC integral for proton which covered $W < 1.910$ MeV at $Q^2 \approx 1.3$ GeV^2. The preliminary result agrees with the BC sum rule prediction within the experimental error. The experimental results for verification of the BC sum rule are summarized in Figure 4-6.

4.4 Proton Hyperfine Structure

The hydrogen hyperfine splitting has been measured to a relative accuracy of 10^{-13} according to the discussion in Ref. [90]:

$$\Delta E = 1420.4057517667(9)\text{MHz}. \tag{4.8}$$

This value could be calculate in QED. ΔE can be expressed in terms of the so-called Fermi energy E_F which is the leading order contribution to the ground state hyperfine splitting as $\Delta E = (1+\delta)E_F$, where the correction δ is given by:

$$\delta = 1 + (\delta_{\text{QED}} + \delta_R + \delta_{\text{small}}) + \Delta_S. \tag{4.9}$$

Here the δ_{QED} represents the QED radiative correction which has been calculated to very high accuracy. The δ_R accounts the recoil effects and the δ_{small} term contains all other small corrections such as the weak interaction correction.

The Δ_S term in Eq. (4.9) represents the proton structure correction which has the largest uncertainty. Δ_S is conventionally split into two terms:

$$\Delta_S = \Delta_Z + \Delta_{\text{pol}}, \tag{4.10}$$

where Δ_Z can be determined from elastic scattering [91] and Δ_{pol} contains the contributions from excited proton [92, 93]:

$$\Delta_{\text{pol}} = \frac{\alpha m_e}{\pi g_p m_p}(\Delta_1 + \Delta_2), \tag{4.11}$$

where Δ_1 involves the Pauli form factor and the g_1 structure function, and Δ_2 only depends on the g_2 structure function:

$$\Delta_2 = -24m_p^2 \int_0^\infty \frac{\mathrm{d}Q^2}{Q^4} B_2(Q^2), \tag{4.12}$$

where

$$B_2(Q^2) = \int_0^{x_{\mathrm{th}}} \mathrm{d}x\, \beta_2(\tau) g_2(x, Q^2). \tag{4.13}$$

and

$$\beta_2(\tau) = 1 + 2\tau - 2\sqrt{\tau(\tau+1)}, \tag{4.14}$$

with $\tau = \nu^2/Q^2$ and x_{th} is the pion production threshold.

Δ_1 could be determined with data but to evaluate Δ_2 physicists still heavily rely on models since proton g_2 data are still lacking. The Q^2 weighting in Eq. (4.12) indicates that Δ_2 is dominated by the contribution at low Q^2 [90]. Thus, precision data of proton g_2 at low Q^2 is needed to evaluate Δ_2.

Chapter 5

The Experiment

E08-027 was conducted in Hall A at Thomas Jefferson National Accelerator Facility (Jefferson Lab or JLab) from March to May, 2012. The experiment was a precise measurement of the inclusive polarized cross-section for electron scattering from protons. The main goal of this experiment is to extract the proton spin-dependent structure function g_2 in the resonance region with $0.02 < Q^2 < 0.20$ GeV^2 [6]. The measured g_2^p data will allow us to extract the longitudinal-transverse spin polarizability δ_{LT} for the proton to perform a benchmark test of χPT predictions and to test the BC sum rule as we already discussed in Chapter 4.

During E08-027, a longitudinally polarized electron beam was scattered from a transversely polarized proton target to measure the transverse polarized cross-section differences $\Delta\sigma_\perp$. The Hall A High Resolution Spectrometers (HRS) were used to detect the scattered electrons at an angle of 5.77°. The $\Delta\sigma_\perp$ data were combined with the longitudinal polarized cross-section differences $\Delta\sigma_\parallel$ from JLab Hall B EG4 experiment [94] in the same kinematic region to extract the proton g_2 structure function. The $\Delta\sigma_\parallel$ data was also collected in E08-027 with a longitudinally polarized proton target at a 2.254 GeV incident beam energy to verify the EG4 data.

The data were acquired in four different beam energies between 1.157 and 3.350 GeV and two different target field strength configurations (2.5 T and 5.0 T). The kinematic coverage of each setting is shown in Figure 5-1. Only those settings with the transverse target field are included in the figure. Since the minimum scatter-

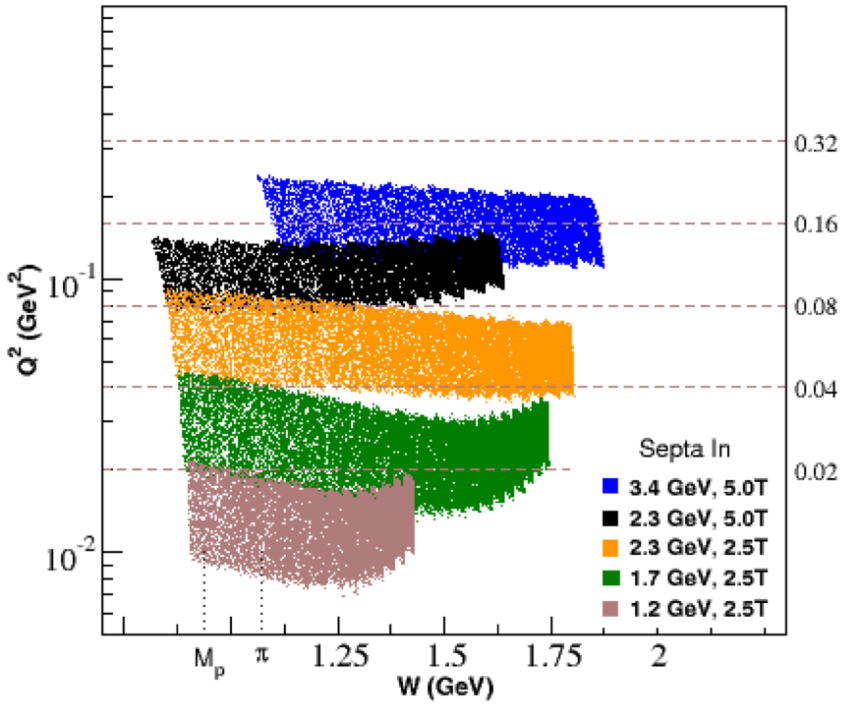

Figure 5-1: Kinematic coverage of E08-027. The legend shows the beam energy and target field strength for each setting. Plot reproduced from [6].

	Beam Energy (GeV)	Field Strength (T)	Field Angle	Septum
1	2.254	0.0	N/A	48-48-16
2	2.254	2.5	90°	48-48-16
3	2.254	2.5	90°	40-32-16
4	1.710	2.5	90°	40-00-16
5	1.157	2.5	90°	40-00-16
6	2.254	5.0	0°	40-00-16
7	2.254	5.0	90°	40-00-16
8	3.350	5.0	90°	40-00-16

Table 5.1: Beam energy and target field configurations for E08-027. The septum configuration is also listed in this table. During the experiment, the spectrometers were set at 5.77°.

ing angle limit of the HRS is 12.5° [95], a septum magnet was installed in front of the spectrometer pair to bend the ≈5.77° scattered electrons into the HRS. Unfortunately, portions of the septum magnet coils were burned twice during the experiment,

which led to three different septum configurations. The experiment configurations are summarized in Table 5.1.

The polarized proton in E08-027 was provided by a frozen ammonia target. The Dynamic Nuclear Polarization (DNP) process was used to polarize the target. Beam current was limited to 50 nA during the experiment to reduce the depolarization of the target. However, the standard Hall A beamline electronics were not designed to work with such low beam currents. For E08-027, new beam current monitors, beam position monitors and chicane were used to accommodate the target. These will be presented in Section 5.2.

This chapter will discuss the electron beam, the Hall A beamline components, the polarized ammonia target and the HRS system.

5.1 The Electron Accelerator

5.1.1 Continuous Electron Beam Accelerator Facility

The superconducting radio-frequency Continuous Electron Beam Accelerator Facility (CEBAF) at JLab consists of a polarized electron source, an injector, two linacs, two recirculation arcs and extraction elements to send the beam into three experimental halls: A, B and C * [96]. Figure 5-2 is a sketch of the CEBAF accelerator.

Once the electron beam is generated, it is injected into the accelerator after an initial acceleration to 45 MeV. A Wien filter is used at the injector to set the polarization angle of the electrons. The precession of the electrons is taken into account to assure that the electrons are longitudinally polarized when they reach the experimental halls. As shown in Figure 5-2, the main acceleration part is composed of two anti-parallel linacs linked by nine recirculation arcs for up to five passes. Each linac can be used to accelerate electrons for all passes since the electrons are ultra-relativistic and travel at almost the same speed. At the end of the second linac, the beam can either enter the recirculation arc to be accelerated one more pass or be

*Following the 12 GeV upgrade of Jefferson lab, which was carried out after this experiment, a fourth experimental hall, Hall D, was added.

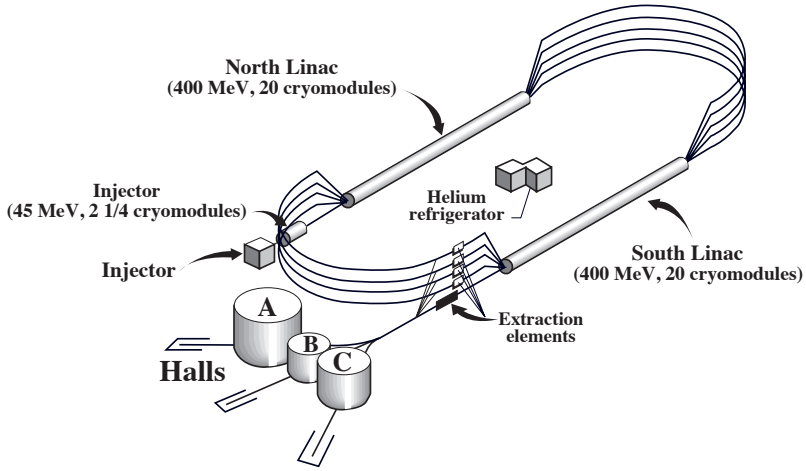

Figure 5-2: Sketch of the CEBAF accelerator during the 6GeV era. The beam travels once through the North and South linacs with each recirculation, when part of it could be extracted to any of the three Halls. The linac energies shown are for operation at 4 GeV; at 6 GeV each linac operates at 600 MeV. Plot reproduced from [97].

extracted into the experimental halls.

CEBAF can provide electron beams at different but correlated energies to three experimental halls simultaneously. Although the accelerator was originally designed to be operated with a maximum beam energy around 4 GeV, the maximum achieved beam energy reached nearly 6 GeV with the state-of-art superconducting radio-frequency technologies. The maximum total beam current available among the three halls is 200 μA. The current can be split arbitrarily between three inter-leaved 499 MHz bunches. Each of the bunches can then be peeled off to send beam to one of the halls [96]. CEBAF has provided electron beams at 1-150 μA for experimental Hall A and C and 1-100 nA for experimental Hall B since 2000.

5.1.2 Beam Helicity

At Jefferson Lab, the polarized electron beam is produced by illuminating a GaAs photocathode with circularly polarized photons [97]. The beam helicity needs to be reversed to measure helicity-dependent observables like the cross-section differences in E08-027. The spin of the photo-emitted electron is correlated to the circular polarization state of the photon. It can be either aligned parallel (1 or +) or anti-

parallel (0 or -) to the electron momentum direction, which are the two helicity states of the electron. Thus the beam helicity can be reversed by changing the polarization state of the light.

A programmable logic generator known as the Helicity Control Board is installed at the injector to control the helicity of the electron beam [98]. It generates a logic signal known as the Helicity Flip signal to control the polarity of the high voltage of the Pockels Cell on the Laser Table in the injector. The Pockels Cell is a crystal that acts as a quarter-wave retardation plate when a high voltage is applied on it. Flipping the polarity of the high voltage of the Pockels Cell changes the circular polarization state of the laser and hence changes the helicity of the electron beam [99]. Since there is no mechanical movement, the Pockels Cell can be used to provide relatively fast reversal of the beam helicity. Normally, the beam helicity is flipped at 30 Hz. However during E08-027, the helicity was flipped at 960.02 Hz to be compatible with other experimental halls.

The actual sequence of the beam helicity is a series of identical length helicity windows in which helicity is stable. See Figure 5-3. To minimize the low frequency systematic uncertainty, the helicity signal always shows up in some symmetric multi-window patterns, like a double-window Pair or a four-window Quartet. For example, the helicity sequence in a Quartet pattern can either be $(+--+)$ or $(-++-)$ so

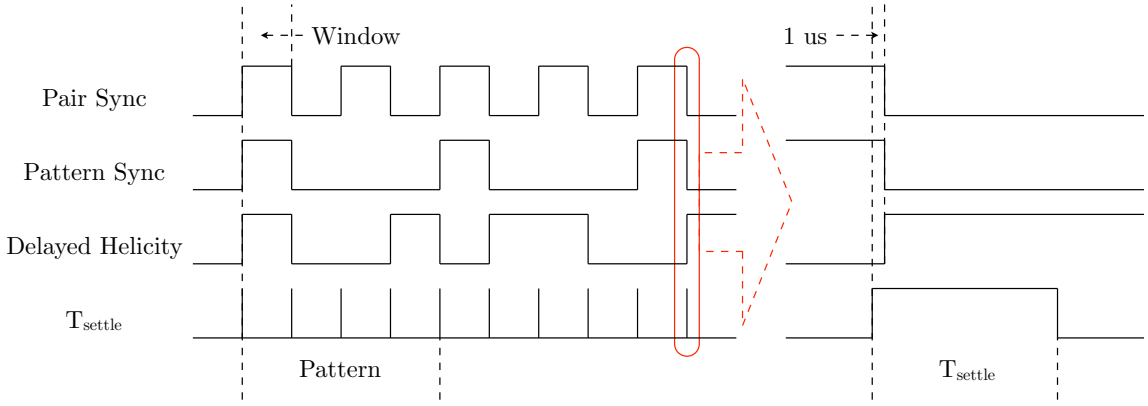

Figure 5-3: Helicity signals received by experiment DAQ. The right side shows the time sequence of these signals, notice that the T_{settle} signal is 1 μs prior to the other three to avoid misalignment.

any linear background is cancelled out.

The helicity of the first window of each pattern is determined by a pseudo-random generator in the Helicity Control Board. Any correlation between the helicity of the beam and other data acquisition (DAQ) components is removed by using this pseudo-random generator. To minimize any other possible systematic effects, the helicity signal received by experiment DAQ is delayed by 8 helicity windows. However, the actual helicity of the incident electrons can still be extracted since the pseudo-random algorithm is fully known.

Due to the non-zero response time of the Pockels Cell to the HV change, the helicity during the transition time between two helicity windows is not stable. A $\mathrm{T_{settle}}$ signal is generated to deal with this problem. This signal is composed by a T_{settle} part and a T_{stable} part. $T_{\mathrm{settle}} + T_{\mathrm{stable}}$ equals to the time length of a helicity window and the T_{settle} is chosen to be slightly longer than the transition time of the Pockels Cell.

Aside from the Delayed Helicity and the $\mathrm{T_{settle}}$ signal, the experiment DAQ also receives two more signals from the Helicity Control Board. The Pattern Sync signal indicates the start of a helicity pattern with a logic 1 and remains 0 in other helicity windows. The Pair Sync signal begins with a logic 1 at the first window of a helicity pattern and then toggles between 0 and 1. These two signals are useful to help predicting the actual helicity. Figure 5-3 shows the relations of these signals and their time sequence.

The helicity scheme generated by the Helicity Control Board can be varied. During E08-027, the helicity pattern was set to be Quartet. The T_{settle} and T_{stable} was set to 70 μs and 971.65 μs respectively so the helicity reversal rate is 960.02 Hz. However the typical DAQ rate of E08-027 was $5 \sim 6$ kHz. The existing helicity decoder to extract the actual helicity from the Delayed Helicity signal did not work at this DAQ rate. A new helicity decoder was designed for E08-027. The algorithm and the test of this new helicity decoder is discussed in Appendix A.

An insertable half-wave plate (IHWP) located upstream of the Pockels cell could also be used to reverse the beam helicity manually. Insertion of the half-wave plate

was performed several times per day to check and to help cancel the helicity dependent systematic effects.

5.2 Hall A Beamline

As we mentioned at the beginning of this chapter, beam current of E08-027 was limited to 50 nA due to the depolarization effect of the target. Thus new beam current monitors (BCMs) and beam position monitors (BPMs) which could work at very low beam currents were used in this experiment to accommodate the target. To further reduce the depolarization effect, a pair of slow rasters were installed in Hall A for the first time to spread the beam over the target uniformly. Since the strong transverse target field would bend the incident and the scattered electrons, two chicane dipole magnets were installed in Hall A upstream of the target to compensate the effect of the target field. A local beam dump was also installed downstream of the target to stop the electron beam when it could not reach the standard beam dump of Hall A due to the effect of the target field. Figure 5-4 is a schematic diagram indicating major experimental components of E08-027. These new instruments will be presented in this section.

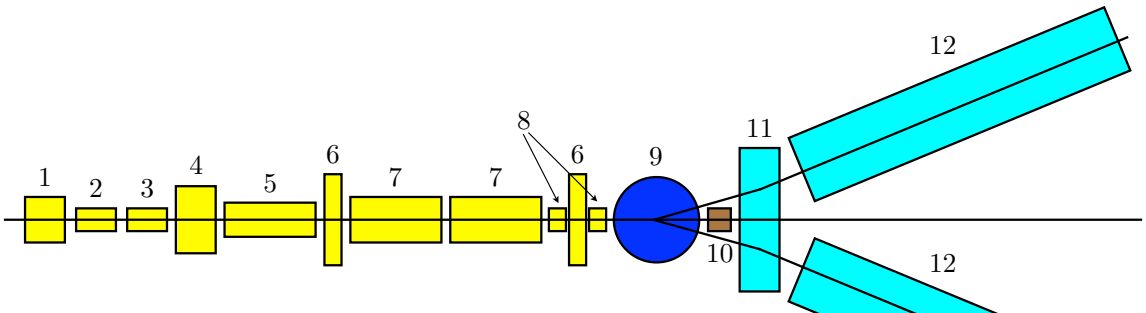

1. Beam current monitor
2. Fast raster
3. Slow raster
4. Tungsten calorimeter
5. Moller polarimeter
6. Harps
7. Chicanes
8. Beam position monitors
9. Polarized NH_3 target
10. Local beam dump
11. Septum magnet
12. High resolution spectrometers

Figure 5-4: Schematic diagram of the experiment components.

5.2.1 Beam Energy Measurement

During E08-027, the beam energy was measured by the Arc method [95]. The idea of the Arc measurement is that the radius of the circular movement of an electron in a magnetic field depends on the field strength and the momentum of the electron. It measures the deflection of the beam in the arc section of the beamline, see Figure 5-5. The momentum of the beam P can then be related to the integral of the magnitude of the magnetic field B of the eight dipoles and the net bend angle θ through the arc sections [101]:

$$P = k\frac{\int \vec{B} \times \mathrm{d}\vec{l}}{\theta} \tag{5.1}$$

where $k = 0.299792$ GeV·rad·T^1·m^1/c. The Arc method relies on two simultaneous measurements. One is for the actual bend angle of the arc, and the magnetic field integral $B\,\mathrm{d}l$ of the eight dipoles in the arc based on a reference magnet measurement. The Arc energy measurement provides an absolute measurement to the 2×10^{-4} GeV level.

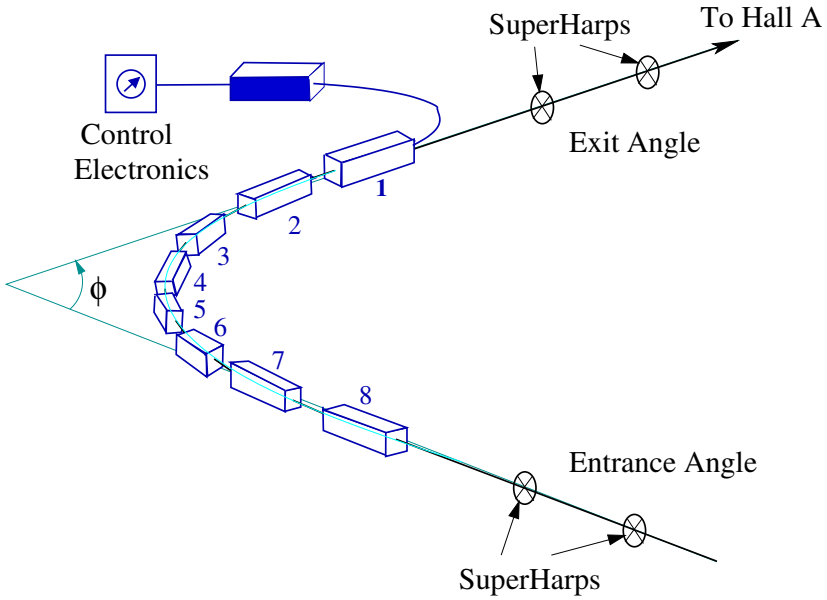

Figure 5-5: Diagram of the arc section of the Hall A beamline. Plot reproduced from [100].

5.2.2 Beam Current Measurement

The beam current is measured by two Beam Current Monitors (BCMs). The BCMs used in E08-027 are two stainless steel cylindrical high-Q ($\approx$3000) waveguides (cavities) that are tuned to the frequency of the beam (1497 MHz) [95]. The output voltage signals of the two cavities are proportional to the beam current. The BCM system is composed of two cavities which are located $\approx$23 m upstream from the target center, an Unser monitor and a BCM receiver which converts the raw signals to be compatible with the DAQ system.

Since the standard RMS-to-DC converter of the BCM system [102] did not work at low beam current, a new BCM receiver designed by the JLab instrumentation group to improve the signal-to-noise (S/N) ratio in an environment with beam current from several nano-ampere to several micro-ampere [103]. The receiver is composed of an analog part, which converts the radiofrequency (RF) signal from the cavities to the intermediate frequency (IF) signal and amplify it, and a digital part, which provides several digital filters to reduce the S/N ratio.

The RF signal with a frequency $\omega = 1497$ MHz (same as beam) is mixed multiplicatively with a sinusoidal $\omega' = 1452$ MHz signal from a local oscillator. Thus the mixed signal could be decomposed to a high frequency component with frequency $\omega + \omega'$ and a low frequency component with frequency $\omega - \omega' = 45$ MHz. The high frequency signal is filtered out.

The 45 MHz intermediate frequency signal is amplified twice and is digitized by an analog-to-digital convertor (ADC). Two digital filters are applied to the digital signal, which can achieve higher stop-band attenuation, faster transition and higher efficiency. The cut-off frequency of the filter is set to 10.4 kHz for the BCM receiver to achieve enough S/N ratio. After the filter, the digital signal is converted back to a 0$\sim$10 V analog signal to match the input of the existed Hall A DAQ system. A voltage-to-frequency module in the DAQ system converts the voltage signal to the frequency signal and is counted by the scalers.

Usually the BCMs are calibrated with the Faraday cup in the injector. The Unser

monitor located between two RF cavities could also be used to give a cross-check of the Faraday cup calibration result. However, both methods can not work at low beam currents. Therefore a tungsten calorimeter [104] was installed to calibrate our BCMs with the heating effect of the electron beam.

During the calibration, the beam is incident to the tungsten block in the calorimeter. All the electrons are stopped by the tungsten causing the temperature of the block to increase during the beam. The tungsten block is held in a vacuum chamber to minimize heat loss. The relation between the total charge Q and the increased temperature ΔT is:

$$Q = e \cdot \frac{K_{\mathrm{W}} \cdot \Delta T}{E_{\mathrm{Beam}}}, \tag{5.2}$$

where E_{Beam} is the beam energy, and the K_{W} is the heat capacity of the tungsten. K_{W} of the tungsten block used in the experiment was measured before the experiment, which is 8555.5±50 J/K [105].

Once the Q for a calibration run is known, the scaler readout is calibrated via the formula:

$$N = (C \cdot I + C_0) \cdot t, \tag{5.3}$$

where N is the BCM scaler reading, C is the calibration constant and C_0 is the pedestal value of the BCM.

The uncertainty of the calibration could arise from the uncertainty of the beam energy, the temperature and the heat capacity of the tungsten as well as the effect from heat loss. The uncertainty of the beam energy measurement at Hall A is at the 2×10^{-4} level [106]. The uncertainties of the temperature sensors are 12.5 mK [107]. The uncertainty of the tungsten heat capacity is 50 J/K. The Hall A calorimeter thermal and mechanical design assures that the heat loss is at ≈0.2% level if the measurement takes less than 20 minutes [104]. Combining all of these effects, one could get the uncertainty of the calibration to be 0.7% on the beam current.

Since the beam current is measured by two cavities independently, the difference between the upstream and downstream BCM could be used to estimate the uncertainty of the BCM readout. The relative differences between the two BCMs are

below 0.7% for 90% of the runs. See Ref. [108] for detailed discussions of the BCM calibration and the uncertainty estimation.

5.2.3 Beam Position Measurement

Two Beam Position Monitors (BPMs) located 95.5 cm and 69.0 cm upstream from the target center were used to determine the position and direction of the beam at the target center. Each BPM contains four wire antennas parallel to the beam direction, which are placed symmetrically around the beam pipe in a vacuum chamber. When the beam passes through the BPM system, a signal is induced in each antenna. The size of each induced signal is inversely proportional to the distance from that antenna to the beam [109]. Figure 5-6 shows the structure of a BPM. With the assumption that the chamber is long enough so that the edge effect could be neglected and the antenna did not influence the electric field inside the chamber, the amplitude of the signal received by each antenna can be expressed as [110]:

$$\varphi_i = \varphi_0 I \frac{R^2 - \rho^2}{R^2 + \rho^2 - 2R\rho\cos(\theta_i - \theta_0)}, \tag{5.4}$$

where i is one of four antennas u_+, u_-, v_+ and v_-, φ_0 is a constant related to the geometry of the BPM chamber and the output resistance, I is the beam current, R is the radius of the BPM chamber, ρ is the radial position of the beam and $\theta_i - \theta_0$ is the angle difference between the antenna and the beam in a polar coordinates.

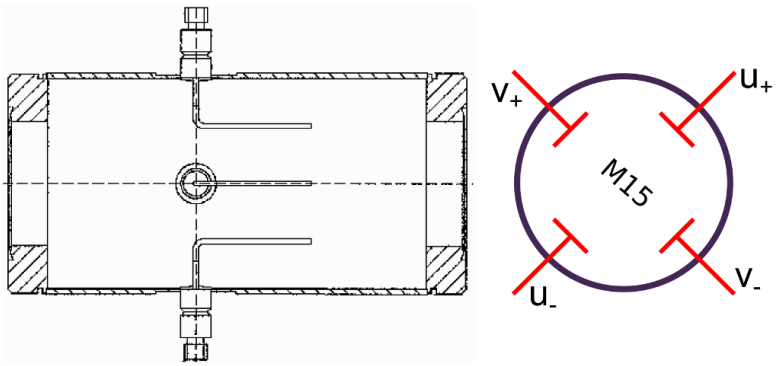

Figure 5-6: Diagram of the BPM.

The beam position u and v could be extracted in the BPM local coordinates. The u_+ and u_- antennas define the $\hat{u}$ axis of this coordinate system and the v_+ and v_- antennas define the $\hat{v}$ axis. If $u^2 + v^2 \ll R^2$, the beam position can be expressed as:

$$W \approx \frac{R}{2} D_W, \tag{5.5}$$

with

$$D_W = \frac{R}{2} \frac{\varphi_{W_+} - \varphi_{W_-}}{\varphi_{W_+} + \varphi_{W_-}}. \tag{5.6}$$

Here W denotes u or v. Since the beam is circularly rastered with a diameter of 2 cm in E08-027 and the radius of the BPM chamber R is only 1.73 cm, Eq. (5.5) is no longer valid, and the beam position must be calculated via a corrected formula:

$$W = R D_W \left(\frac{1}{D^2} - \frac{1}{D} \sqrt{\frac{1}{D^2} - 1} \right), \tag{5.7}$$

with $D^2 = D_u^2 + D_v^2$.

Like the BCMs, the BPM system also contains a receiver which collects and sends the signal to the DAQ system. As mentioned in Section 5.2.2, the original receiver did not work at low beam currents, thus a new BPM receiver was designed by the JLab instrumentation group [103] to be compatible with beam current as low as 50 nA. The output signal of the receiver is sent to a 13-bit fastbus ADC with an integration time of 50 ns which is triggered by a detected event. The BPM receiver shares the same design with the BCM receiver, but the cut-off frequency of the digital filter of the BPM receiver is set to 175 Hz to increase the S/N ratio and reach the required resolution. This leads to a 1/175 s delay of the beam position signal. There is also a $\approx$4 μs delay as the processing time of the electronics. Since the beam is spread by a 25 kHz fast raster, the BPM could not provide the beam position event by event due to the time delay effect. Thus the BPM is only used to measure the center of the raster pattern, the raster information is combined with the BPM readout to provide the beam position for each event. The magnet current of the rasters is calibrated to get the absolute values of the deviations with respect to the center of the raster pattern.

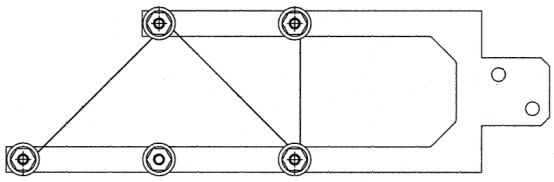

Figure 5-7: Diagram of the harp.

The details of the rasters used in the experiment will be discussed in Section 5.2.5.

The BPMs are calibrated with two superharps. One harp is installed between the 2 BPMs and the other one is installed upstream of the upstream chicane magnet. Figure 5-7 shows a schematic diagram of the harp. The harp consists of three wires with a thickness of 50 μm which are fixed to a chassis controlled by a step motor [111]. The original position of each wire is surveyed with a precision level of 0.1 mm. During the calibration, the harp is moved into the beam pipe by the step motor. The wires are scanned by the electron beam resulting showers of particles which can be detected. The absolute beam position could be calculated with the recorded wire signal and the survey result. Meanwhile the beam position is also measured with BPMs. By comparing the BPM readout and the harp wire signal, the BPMs can be calibrated.

The BPMs only measure the beam position at their own locations. Usually the beam positions at BPMs could be linearly projected to the target location to retrieve the beam positions at the target. However, the transverse target field in E08-027 breaks the linear projection. A simulation package was constructed to trace the movement of the incident electrons in the target field. The beam trajectories generated by the simulation package are used to fit a set of transport functions which could transport the beam positions at two BPMs to the spatial coordinates and the incident angles of the beam at the target location. These transport functions are used to calculate the beam position at the target location.

The uncertainty of the final beam position at the target location arises from several sources such as the uncertainty of the harp calibration constant, the survey data and the pedestal value of the electronics. The final uncertainty of the beam position is

1∼2 mm, while the uncertainty of the incident angle is 1∼2 mrad. See Ref. [112] for detailed discussion of the BPM calibration and the uncertainty estimation.

5.2.4 Beam Polarization

The polarization of the electron beam was measured by the Møller polarimeter [95, 113] during E08-027. The polarimeter uses polarized Møller scattering, in which polarized electron beam scatters off polarized atomic electrons in a magnetized ferromagnetic foil $\vec{e}^- + \vec{e}^- \rightarrow e^- + e^-$, to measure the beam polarization. Figure 5-8 shows a sketch of the Møller polarimeter. The polarimeter is composed of three quadrupoles and a dipole. The detector system consists of scintillators and lead-glass calorimeter modules.

The Møller scattering cross-section can be expressed in terms of the beam polar-

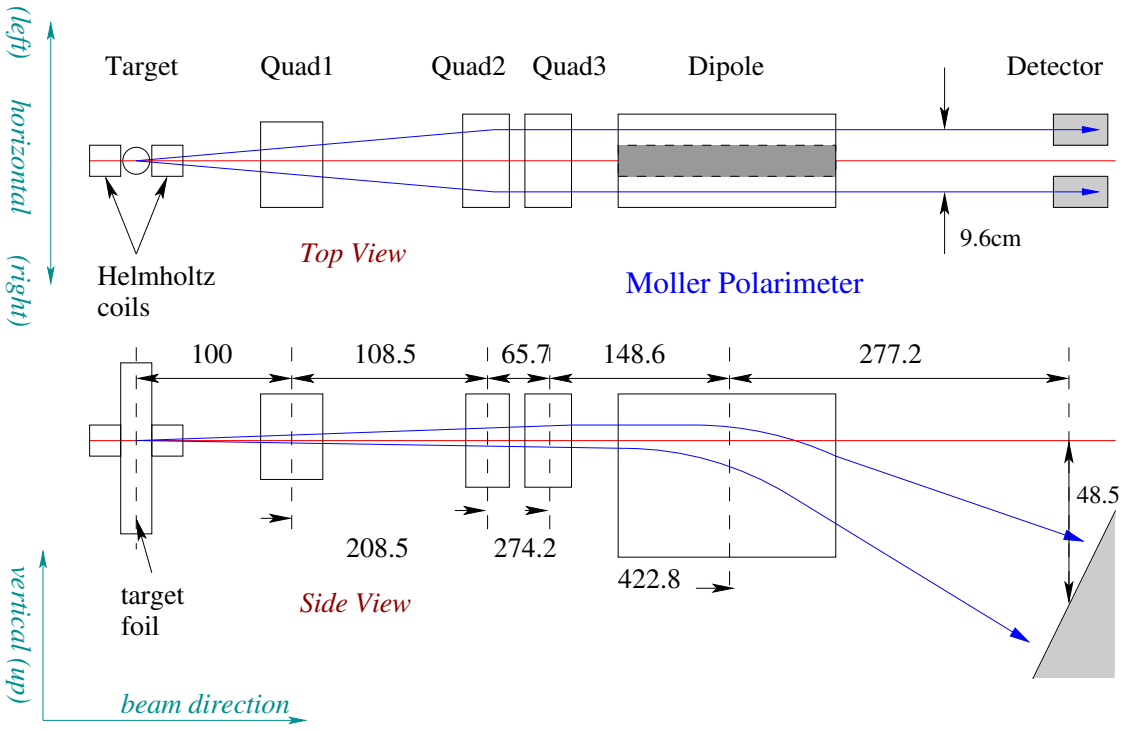

Figure 5-8: Schematic diagram of the Møller polarimeter. Plot reproduced from [100].

ization P^i_{beam} and target polarization P^i_{target} [95]:

$$\sigma = \sigma_0 \left[1 + \sum_{i=x,y,z} A_{ii} P^i_{\text{beam}} P^i_{\text{target}} \right], \tag{5.8}$$

where i is the projection direction of the polarization, and σ_0 is the unpolarized Møller cross-section. The coordinate system is defined such that the beam direction is along the z-axis and the y-axis is perpendicular to the scattering plane. The A_{ii} are the analyzing powers which can be expressed as:

$$A_{zz} = -\frac{\sin^2\theta_{\text{cm}} \cdot (7 + \cos^2\theta_{\text{cm}})}{(3 + \cos^2\theta_{\text{cm}})^2}, \tag{5.9}$$

$$A_{xx} = -A_{yy} = -\frac{\sin^4\theta_{\text{cm}}}{(3 + \cos^2\theta_{\text{cm}})^2}, \tag{5.10}$$

where θ_{cm} is the scattering angle in the center-of-mass frame. Since the beam is longitudinally polarized, the corresponding analyzing power is A_{zz}, which reaches its maximum value of 7/9 when θ_{cm} =90°. The polarized Møller cross-sections are less sensitive to the transverse polarization and the data with opposite target transverse polarization could be averaged to cancel the transverse contributions.

During the experiment, a pair of asymmetries are measured at two target angles of about ±20° with respect to the beam in the horizontal plane, and the average is taken to cancel the transverse contributions as mentioned above. Here asymmetries are measured rather than cross-sections since the asymmetry is a ratio of cross-sections, thus most of the systematic uncertainties related to the cross-section measurement cancel out when taking the ratio.

The beam longitudinal polarization is measured as:

$$P_{\text{beam}} = \frac{1}{P_{\text{target}} \cos\theta_{\text{target}} \langle A_{zz} \rangle} \times \frac{N_+ - N_-}{N_+ - N_-}, \tag{5.11}$$

where N_+ and N_- are the detected events with opposite orientations of beam polarization. The average analyzing power $\langle A_{zz} \rangle$ is calculated with a Monte-Carlo simultion of the Møller polarimeter. Nine measurements were taken during the experiment, which

	Date	Polarization and Statistical Error (%)	Systematic Error (%)
1	03/03/2012	79.91±0.20	±1.7
2	03/30/2012	80.43±0.46	±1.7
3	03/30/2012	79.89±0.58	±1.7
4	04/10/2012	88.52±0.30	±1.7
5	04/23/2012	89.72±0.29	±1.7
6	05/04/2012	83.47±0.57	±1.7
7	05/04/2012	81.82±0.59	±1.7
8	05/04/2012	80.40±0.45	±1.7
9	05/15/2012	83.59±0.31	±1.7

Table 5.2: Summary of the Møller measurement result. Table reproduced from [114].

were scheduled during beam unavailable periods or during a configuration change in the accelerator. The Møller measurement results are shown in Table 5.2. The statistical accuracy is typically 0.2% as discussed in Ref. [95]. There is a ≈1.7% relative systematic uncertainty dominated by the knowledge of the foil polarization [113].

5.2.5 New Instruments

Raster System

The target used in E08-027 is a polarized NH_3 target, which will be described in Section 5.3. It was operated at ≈1 K and would depolarize if the target material was heated by the electron beam. Thus the beam position must be moved constantly to avoid localized overheating of the target material. A uniform distribution of beam on the target was achieved by moving the beam position with time-varying dipole magnetic fields. These dipoles were referred to as rasters.

Two raster systems, the fast raster and the slow raster, were installed at ≈17 m upstream from the target center. The fast raster is a standard Hall A beamline component, which consists of two dipole magnets. Both of the dipoles were driven by the same current in a triangular waveform with a frequency of 25 kHz. The beam position was moved by the dipole fields in $\hat{x}$ and $\hat{y}$ directions, respectively, and formed

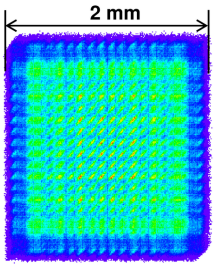

Figure 5-9: Fast raster pattern. The plot is produced from the magnet current signal.

a 2 mm × 2 mm rectangular pattern. The shape of the fast raster pattern is shown in Figure 5-9.

The target cell of E08-027 is a cylinder with ≈25 mm diameter. Thus the fast raster is not enough to spread the beam uniformly on to the whole target. A slow raster was installed in Hall A immediately downstream of the fast raster. The slow raster also consists of two dipole magnets, however the drive current of the dipoles is not in triangular waveform. The waveform used in the slow raster was generated from a dual-channel function-generator:

$$I_x = I_x^{\max} f(t^{\frac{1}{2}}) \sin(\omega t), \tag{5.12}$$

$$I_y = I_y^{\max} f([t + t_0]^{\frac{1}{2}}) \cos(\omega t), \tag{5.13}$$

for the $\hat{x}$ and $\hat{y}$ directions, respectively. Here the $I_x^{\max}$ and $I_y^{\max}$ are the maximum amplitude. Eqs. (5.12) and (5.13) are parametric equations of a circle which is modulated by a function $f(t^{\frac{1}{2}})$ to generate a uniform circular pattern [115], up to ≈20 mm diameter for E08-027. The amplitude modulation (AM) function $f(t^{\frac{1}{2}})$ is a periodic piecewise function with frequency $1/T$, which can be expressed as (in the first period):

$$f(t) = \begin{cases} t^{\frac{1}{2}}, & \text{if } 0 \le t < T/4, \\ (T/2 - t)^{\frac{1}{2}}, & \text{if } T/4 \le t < T/2, \\ -(t - T/2)^{\frac{1}{2}}, & \text{if } T/2 \le t < 3T/4, \\ -(T - t)^{\frac{1}{2}}, & \text{if } 3T/4 \le t < T. \end{cases} \tag{5.14}$$

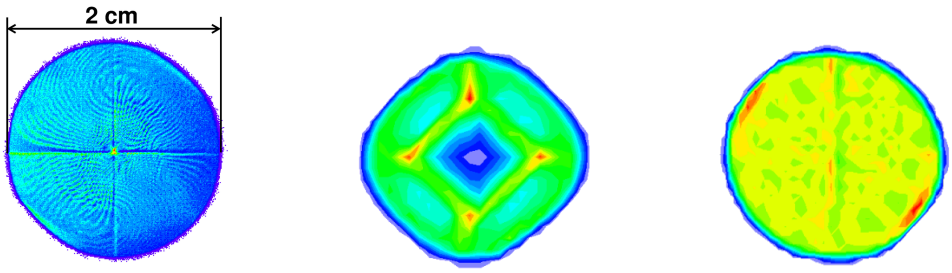

(a) Slow raster magnet current distribution.

(b) Slow raster pattern with $t_0 \neq 0$.

(c) Slow raster pattern with $t_0 = 0$.

Figure 5-10: Slow raster pattern. Here (a) is produced from the magnet current distribution, (b) and (c) are produced from the BPM readout of the slow raster pattern with different t_0 settings.

The t_0 in Eq. (5.13) is the phase difference between the AM functions in the $\hat{x}$ and $\hat{y}$ directions. Figure 5-10 indicates the effect of t_0.

During E08-027, the frequency ω in Eqs. (5.12) and (5.13) was 99.412 Hz. The frequency $1/T$ of the AM function was set to 30 Hz. The phase difference t_0 was manually adjusted to be 0. As shown in Figure 5-10b, a non-zero t_0 could cause a non-uniform pattern. Thus, t_0 was carefully minimized during the experiment to avoid the non-uniformity. The pattern of the beam was relatively uniform after the adjustment as shown in Figure 5-10c.

Chicane Magnets

The strong transverse magnetic field in the target region influences the electron beam. The direction of the magnetic field was pointing to the left of the beam if looking along the downstream direction. According to the right-hand rule, the electron beam would be deflected downwards in the target field. Two chicane magnets were placed in front of the target and the BPMs to provide an upward incident angle for the electron beam when it reaches the center of the target. Figure 5-11 shows the effects of the chicane magnets and the target field on the electron beam. The first chicane magnet, installed 5.92 m upstream from the target center, bent the beam downwards. The second chicane magnet, installed 2.66 m upstream from the target center, bent the beam back towards the target but at an angle to compensate for

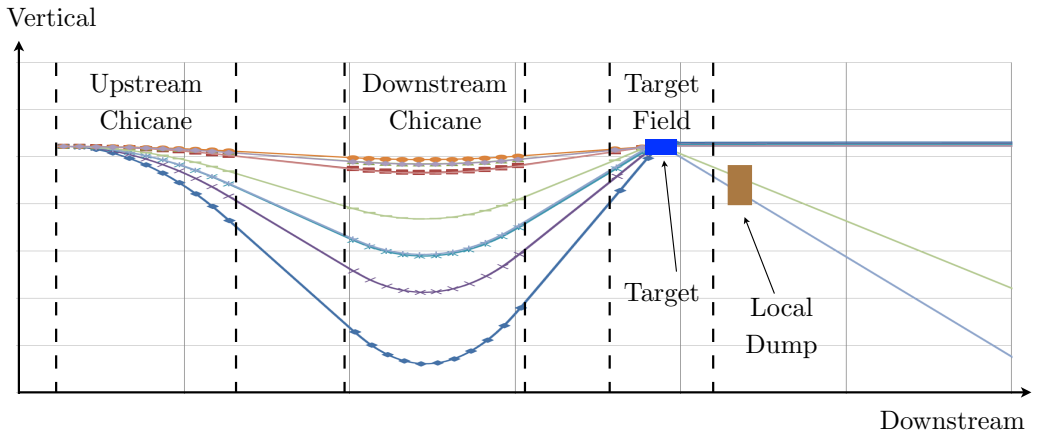

Figure 5-11: Schematic diagram of the effects of the chicane magnets and the target field on the electron beam. The trajectories are marked with different colors for different beam energy and target field configuration. Notice the diagram does not reflect the actual scale of each component.

further bending from the target field. The vertical position of the chicane magnets was adjusted according to the beam energy and the target field configuration during the experiment such that when the beam hit the target, its direction is parallel to the beamline.

Local Beam Dump

As seen in Figure 5-11, most of the beam trajectories exit the target field region horizontally (in these cases the target field strength is 2.5 T), and could reach the Hall A beam dump. However, the chicane magnets could not bend the beam to the Hall A beam dump for those configurations with the 5.0 T transverse target field due to the limited installation space for the chicane magnets. Since the beam current was quite low for this experiment, a local beam dump which consisted of a series of tungsten and copper plates was used to stop the beam which could not reach the Hall A beam dump. The local beam dump was installed 0.64 m downstream of the center of the polarized target as shown in Figure 5-11. The local beam dump worked well during the experiment and successfully protected the electronics in the experimental hall from high radiation background.

5.3 Polarized NH_3 Target

In E08-027, a polarized ammonia NH_3 target was used to provide the polarized proton target. Since the nucleons in the nitrogen nuclei are not coupled with the electrons, they would not be polarized by the Dynamic Nuclear Polarization (DNP) method. This target has been successfully used for several JLab experiments prior to E08-027. The target has demonstrated a high proton polarization up to 90% with a 5.0 T target field. The 5.0 T target field was used in E08-027 and a new 2.5 T configuration was operated in this experiment for the first time.

5.3.1 Dynamic Nuclear Polarization

The DNP method is used to polarize the hydrogen nuclei in a NH_3 target. Zeeman effect tells us that a spin non-zero particle located in a strong magnetic field is polarized spontaneously. If the magnetic moment of the particle is μ and the spin is $1/2$, the ground state of this particle splits to two sublevels with energy $E_0 + \mu B$ and $E_0 - \mu B$, respectively. The population of these two sublevels follows Maxwell-Boltzmann statistics:

$$N(E_0 \pm \mu B) = N(E_0) \exp\left(-\frac{\pm \mu B}{k_B T}\right), \tag{5.15}$$

where k_B is the Boltzmann constant and T is the temperature of the system. Thus the spontaneous polarization of the material is:

$$P_{\mathrm{TE}} = \frac{\exp\left(\frac{\mu B}{k_B T}\right) - \exp\left(-\frac{\mu B}{k_B T}\right)}{\exp\left(\frac{\mu B}{k_B T}\right) + \exp\left(-\frac{\mu B}{k_B T}\right)} = \tanh\left(\frac{\mu B}{k_B T}\right). \tag{5.16}$$

where TE stands for thermal equilibrium and we refer to this polarization as the thermal polarization. The magnetic moment of the electron is approximately $\mu_{\mathrm{B}} \equiv e\hbar/2m_e$ and the magnetic moment of the proton is only $1.521 \times 10^{-3}\mu_{\mathrm{B}}$ due to the mass difference. From Eq. (5.16), we know that the thermal polarization of a sample of electrons is above 90% but the proton's thermal polarization is only ≈2.5% for

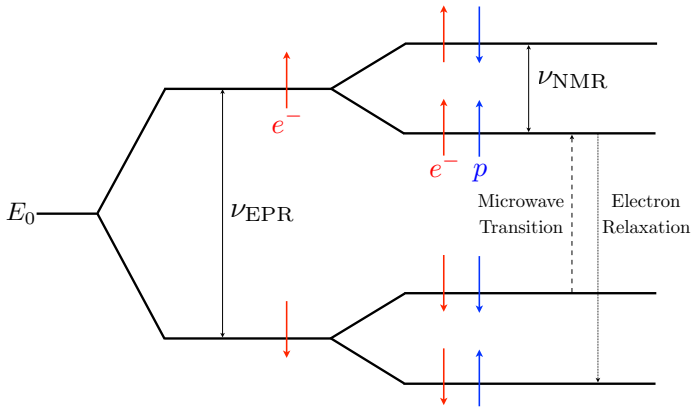

Figure 5-12: Electron-proton spin coupling interaction diagram.

the 1 K temperature and 2.5 T magnetic field, the typical target configuration in E08-027.

The thermal polarization of the proton is not enough for carring out spin-structure experiments. Thus the DNP method is developed to enhance the polarization by transferring the electron polarization to the nucleon via the electron-proton spin coupling [116, 117]. The Hamiltonian of this system can be written as:

$$H = \vec{\mu_e} \cdot \vec{B} + \vec{\mu_p} \cdot \vec{B} + H_{\mathrm{ss}}, \tag{5.17}$$

where μ_e and μ_p are the magnetic moments of the electron and proton, respectively, and the H_{ss} arises from the interaction between the electron and proton. The ground state of this system split to four sublevels as shown in Figure 5-12, corresponding to the four spin combinations of the electron and the proton. A microwave generator can be used to flip the proton spin and electron spin together if the frequency is carefully tuned at $\nu_{\mathrm{EPR}} - \nu_{\mathrm{NMR}}$ to polarize the proton parallel to the field direction (or $\nu_{\mathrm{EPR}} + \nu_{\mathrm{NMR}}$ for an opposite direction). Here the ν_{EPR} is the electron paramagnetic resonance (EPR) frequency and ν_{NMR} is the proton nuclear magnetic resonance (NMR) frequency. Since the relaxation time of electrons is only a few milliseconds, the polarized electron is relaxed to the lowest ground state and can be used to polarize a new proton. The relaxation time of protons is tens of minutes so the polarization of protons could be kept if we pump the microwave continuously.

5.3.2 Target Setup

The NH_3 target system used in E08-027 is shown in Figure 5-13. The original 5 T Oxford superconducting magnet was burned before the experimentand could not be used. Fortunately, an alternate magnet from Hall B was identified as a suitable replacement. Because of the power and construction limit of the chicane magnets, a 2.5 T field configuration was used in addition to the original 5.0 T magnetic field to reach the minimum possible Q^2 with this magnet. The magnetic field must be uniform in order for the DNP process to be efficient. The nonuniformity of the field is less than 10^{-4} over the volume of the material which is a cylinder with ≈2 cm diameter and ≈2 cm length [118]. The open geometry of the magnet allows the beam to pass through in both longitudinal and transverse configurations. The magnet is superconducting and is maintained at 4 K with a reservoir of liquid helium.

The target stick can be seen in Figure 5-14. The stick contains two NH_3 cells, a

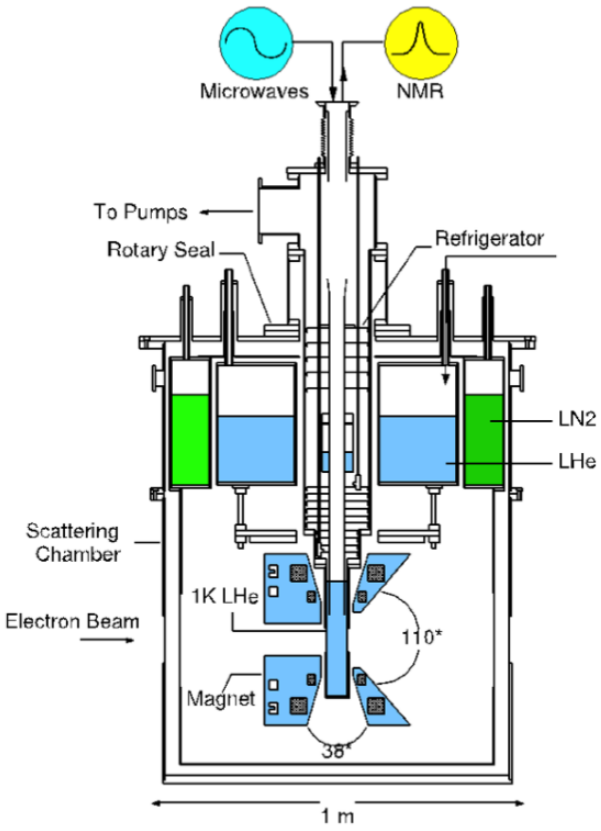

Figure 5-13: Diagram of the polarized NH_3 target system.

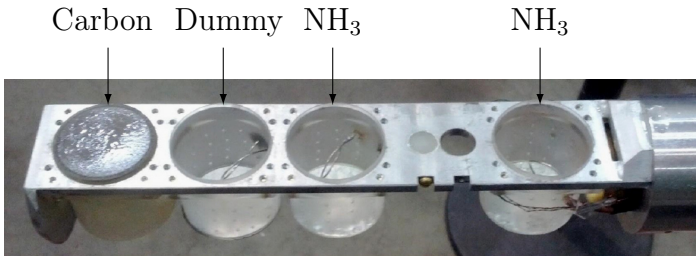

Figure 5-14: The end of the target insert. A carbon foil cell, a "dummy" cell and two NH_3 cells are installed in the stick from left to right. And a carbon disk and a polyethylene disk are installed in the holes between two NH_3 cells.

carbon foil cell, a "dummy" cell and two small disk targets made with carbon and polyethylene respectively. The NH_3 cells are filled with solid NH_3 beads and are covered with aluminum foils. A short Cu-Ni capillary coil is installed in the cell for NMR measurement. The dummy cell is identical to the NH_3 cells which also includes aluminum foils and the NMR coil, but does not contain any NH_3 beads. During the experiment, the end of the target stick is immersed in a container full of liquid helium, which is refered as the target "nose". A ^{4}He evaporation refrigerator was used to cool down the target and maintain its temperature at 1.1 K with 3 W microwave power [118].

The selection of NH_3 as the target material is due to several reasons. It has been proved that NH_3 is capable of reaching 90% polarization in a 5 T magnetic field. And it can be polarized within 30 minutes or less, which is very fast compare to other materials. Solid NH_3 also holds up very well against radiation damage which could reduce the polarization rapidly. The radiation can produce additional radicals that reduce the relaxation time of the proton.

On the other hand, radicals in the target material can also allow the material to polarize faster. The NH_3 beads are irradiated with a 10 MeV linear accelerator at the National Institute of Standards and Technology (NIST) before the experiment in order to produce a few additional radicals in the material. The irradiation causes the solid NH_3 beads to become a deep purple color, as seen in Figure 5-15. The number of radicals in the material must be carefully balanced: they can speed up

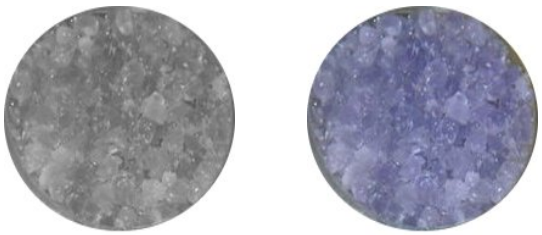

(a) Unirradiated. (b) Irradiated.

Figure 5-15: NH_3 beads before and after irradiation.

the DNP process, but they also increase the speed of the proton depolarization. The DNP process becomes inefficient when the target is exposed in the electron beam long enough with the amount of radicals exceeding the tolerance. To counteract this effect, the target material can be heated up to force the radicals to recombine, which is referred to as the "annealing" of the target. During E08-027, the beam current was limited to 50 nA, and the target was annealed periodically. However, there is a limit to how many times the material can be annealed, thus the NH_3 beads still need to be replaced several times during the experiment.

Microwaves are necessary to drive the spin transitions. The microwave generator contains an Extended Interaction Oscillator (EIO) tube to generate the microwave. The microwaves are then carried via waveguides to a horn close to the target cell. The optimal frequency of the microwave radiation is not a constant value due to the radiation damage, thus the frequency need to be tweaked throughout the experiment.

5.3.3 Target Polarization Measurement

The polarization is measured via the NMR method. An LCR circuit with resonance frequency equal to the Larmor frequency of the proton is used as the NMR circuit [119]. The power lost or gained in the circuit can be measured via the quality factor (Q-factor) of the circuit by a Q-meter. The response of the target material to a radiofrequency irradiation is described by its magnetic susceptibility $\chi(\omega) = \chi'(\omega) - i\chi''(\omega)$, where $\chi'(\omega)$ and $\chi''(\omega)$ are the dispersive and absorptive part of the susceptibility respectively. The polarization P of the target is related to the

absorptive part of the susceptibility $\chi(\omega)$ [120]:

$$P = K \int_0^\infty \chi''(\omega)\, \mathrm{d}\omega\,, \tag{5.18}$$

where K is a constant containing the properties of the NMR system. The NMR circuit has inductance L_C and resistance r_C itself, and the inductive coupling between the material and the coil changes the impedance of the circuit to:

$$Z_C = r_C + i\omega L_C(1 + 4\pi\eta\chi(\omega)), \tag{5.19}$$

where η is the filling factor of the coil. The circuit is driven by an RF generator which sweeps through a range of frequencies around the Larmor resonance of the circuit.

The output complex voltage $V(\omega, \chi)$ is proportional to the impedance of the circuit (Eq. (5.19)). The NMR signal is composed with $V(\omega, \chi)$, together with the Q-meter response in the absence of χ, $V(\omega, 0)$, which is always referred as the "Q-curve". The Q-curve is measured by setting the target field so that the Larmor frequency is outside the range of the frequency scan of the Q-meter. The two signals are subtracted and the real part of the voltage is selected out by electronics, which gives the NMR signal $S(\omega)$:

$$S(\omega) = \mathrm{Re}[V(\omega, \chi) - V(\omega, 0)] \approx \chi''(\omega). \tag{5.20}$$

Combining Eqs. (5.16), (5.18) and (5.20), the polarization P can be calibrated in terms of the thermal polarization P_{TE} and the ratio of the integral of two NMR signals S_{TE} and S_{enh}, where S_{TE} is the NMR signal at thermal equilibrium and S_{enh} is the NMR signal under microwave irradiation (when the target is polarized):

$$P = \frac{\int_0^\infty S_{\mathrm{enh}}(\omega)\, \mathrm{d}\omega}{\int_0^\infty S_{\mathrm{TE}}(\omega)\, \mathrm{d}\omega} P_{\mathrm{TE}}. \tag{5.21}$$

Figure 5-16 shows the raw voltage signal and the NMR signal.

The S_{TE} curve is measured several times during the experiment, which is referred to as the TE measurement. For each different NH_3 sample, the numbers of the TE

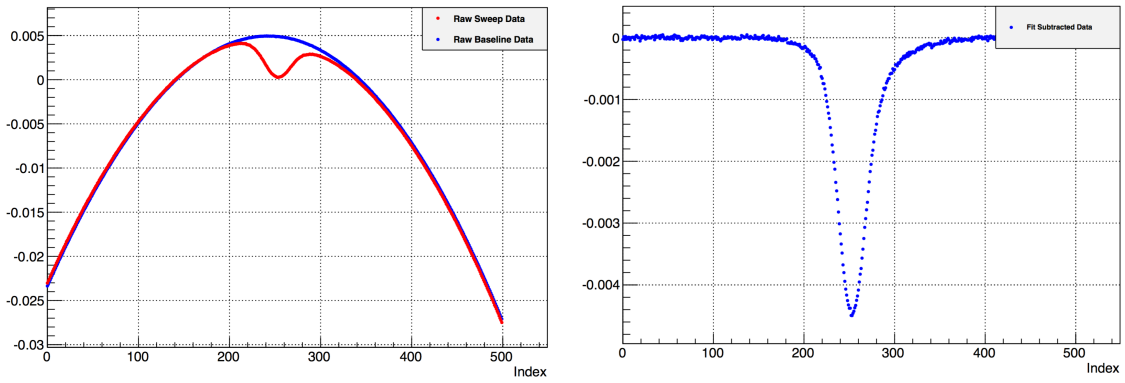

(a) The raw signal (red) and the baseline signal (Q-curve signal, blue).

(b) NMR signal after the subtraction.

Figure 5-16: An example of the target NMR signals. The x-axis index is proportional to the frequency of the RF generator.

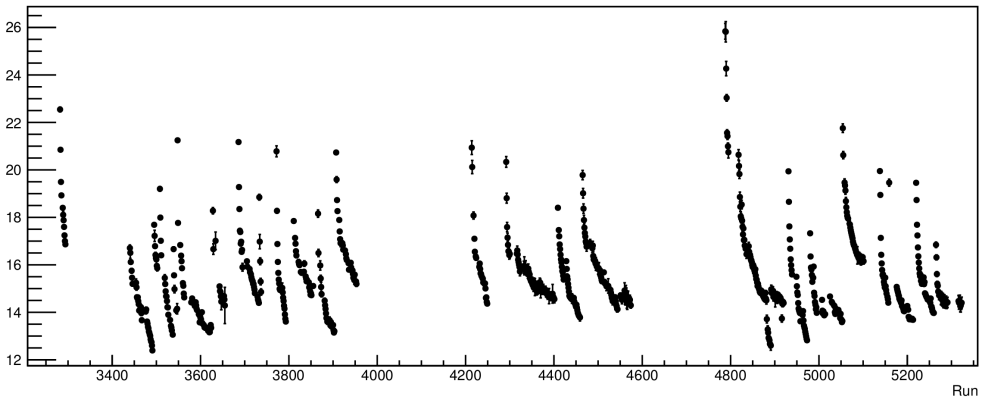

(a) 2.5T target field configuration.

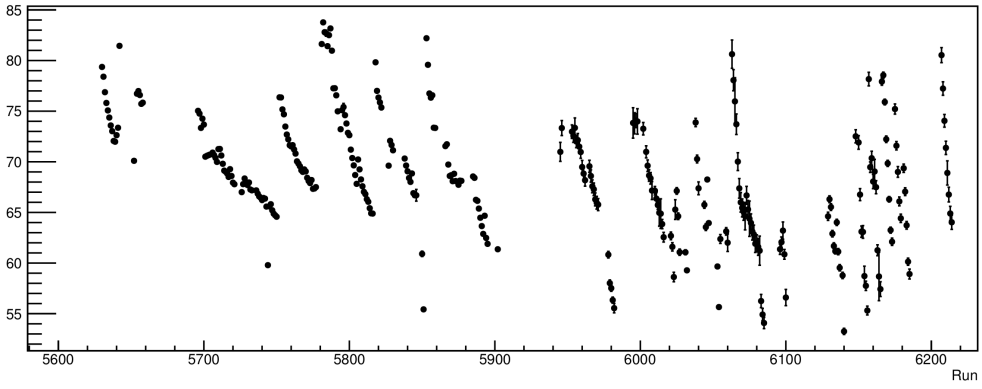

(b) 5.0T target field configuration.

Figure 5-17: Target polarization results during the experiment. Plot reproduced from [121].

measurements varied from 1 to 8 measurements, depending on the time available. The polarization was then calculated via Eq. (5.21) on a run-by-run basis. Figure 5-17 shows the final polarization results. An average polarization of 70% and 15% was seen for the 5.0 T and 2.5 T configurations of the target field, respectively.

The uncertainty of the polarization measurement arises from two major reasons. One is the uncertainty of the NMR signal. The other one is the uncertainty in the magnetic field and temperature readings, which contribute to the P_{TE} polarization calculation. The target polarization uncertainty is still being finalized. The current result is that the relative uncertainty of the target polarization is $\approx$1.2% for the NH_3 samples with 8 TE measurements, which is the best case. For the worst case with only one TE measurement, the relative uncertainty of the target polarization is $\approx$3.0% [121].

5.4 Hall A High Resolution Spectrometers

E08-027 uses the two standard Hall A high resolution spectrometers (HRS) to detect the scattered electrons [95]. The two HRSs are nearly identical, and are referred to as HRS-L (left arm) and HRS-R (right arm) respectively. The main characteristics of HRS are summarized in Table 5.3. Both arms contain three quadrupoles and a dipole magnet in a QQDQ configuration as illustrated in Figure 5-18. The Q1, Q2 and Q3 are three superconducting quadrupoles to provide focusing: Q1 focuses in the vertical plane and Q2 and Q3 in the transverse plane. The momentum of the electrons that reach the detector package are determined by the superconducting dipole with a momentum resolution at the 10^{-4} level. The electrons are bent by the dipole magnet by an angle of 45° in the vertical direction.

5.4.1 Septum Magnet

E08-027 measured the scattered electrons at an angle of $\approx$5.77°. However, the HRS have a minimum achievable angle of 12.5°, that is mainly because the Q1 magnet would hit the beam pipe if the spectrometer is moved to a smaller angle. During

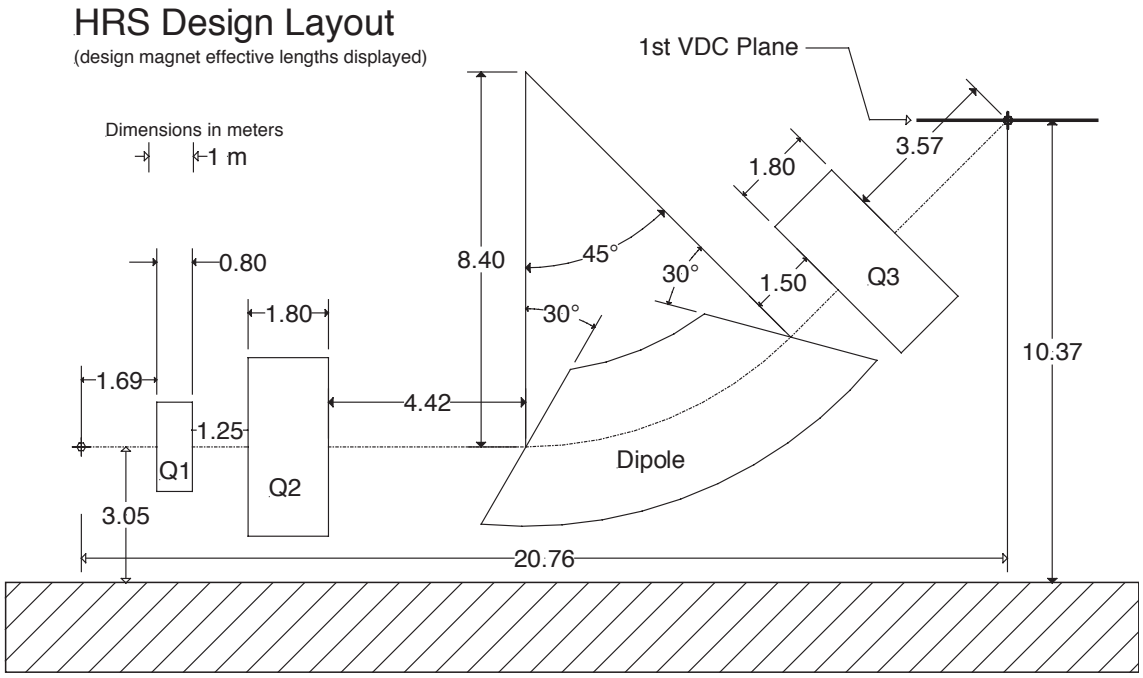

Figure 5-18: Magnet configuration for HRS. Also shown is the location of the first VDC tracking detector. Figure reproduced from [95].

Bending angle	45°
Optical length	23.4 m
Momentum range	0.3∼4.0 GeV/c
Momentum acceptance	±4.5%
Momentum resolution	1×10^{-4}
Angular range (HRS-L)	12.5°∼150°
Angular range (HRS-R)	12.5°∼130°
Angular acceptance (horizontal)	±30 mrad
Angular acceptance (vertical)	±60 mrad
Angular resolution (horizontal)	0.5 mrad
Angular resolution (vertical)	1.0 mrad
Solid angle at $\delta = 0$, $y_0 = 0$	6 msr
Transverse length acceptance	±5 cm
Transverse position resolution	1 mm

Table 5.3: The characteristics of the standard Hall A spectrometers. Table reproduced from [95].

the experiment, a pair of septum magnets was used to allow both spectrometers to reach angles down to 5.77° [6]. The septum magnet pair was located in front of the Q1 entrence of the HRS and horizontally bent the electrons with scattering angle ≈5.77° into the spectrometer located at 12.5°. The coils of the septum magnet burned twice during the experiment, which led to three different septum configurations. The detailed configurations are listed in Table 5.1.

5.4.2 Detector Package

The detector package of the HRS is in a shielding hut together with the DAQ electronics at the end of the magnet group. The standard layout of the detector package is shown in Figure 5-19. The trajectory and the momentum of the scattered particle is determined by a pair of vertical drift chambers. Then the particles pass through a pair of plastic scintillator planes which generate the trigger for DAQ system. A gas Cherenkov detector and a set of lead glass calorimeters (pion rejectors in HRS-L, shower and pre-shower in HRS-R) are used for particle identification (PID). The main difference between the two arms is in the second layer of the calorimeters. The lead-glass blocks are aligned perpendicular to the particle trajectories in the left arm, whereas in the right arm the blocks in the second layer are oriented parallel to the trajectories.

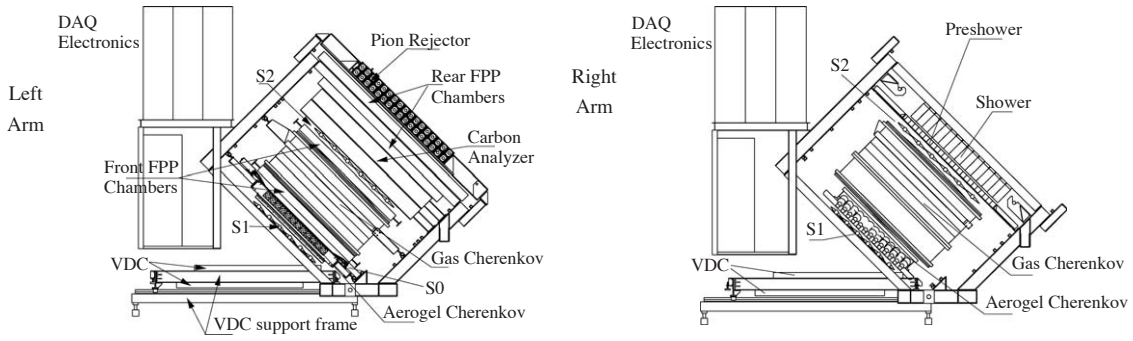

(a) Left arm. (b) Right arm.

Figure 5-19: Detector package of HRS. Note that only the VDC, scintillators (S1 and S2), gas Cherenkov detector and the calorimeters (pion rejectors in HRS-L, shower and pre-shower in HRS-R) were used during E08-027. Figure reproduced from [95].

Vertical Drift Chambers

The vertical drift chambers (VDC) in each spectrometer consists of two VDC chambers, each composed of two wire planes in a UV configuration [122] as shown in Figure 5-20. The U and V planes are orthogonal and lie in the laboratory horizontal plane. They are inclined at an angle of 45° with respect to the dispersive direction of the dipole. Each plane contains 368 sense wires, spaced 4.24 mm apart. The upper and lower VDC chambers are separated by about 335 mm. The spectrometer focal plane is referred as the first wire plane (U1) that the particles traverse through. The concept of the focal plane is important to the spectrometer optics study which will be discussed in detail in Chapter 6.

The chambers are filled with a gas mixture of argon (62%) and ethane (38%). Argon provides the ionizing medium while ethane absorbs the photons produced from ionization. The electric field of the VDCs is shaped by gold-plated mylar planes powered at -4 kV. Ionized electrons drift along the electric field lines and rapidly accelerate towards the wire when they are close to a wire, producing a shower of secondary ionizations. The approaching avalanche of electrons induces a signal on

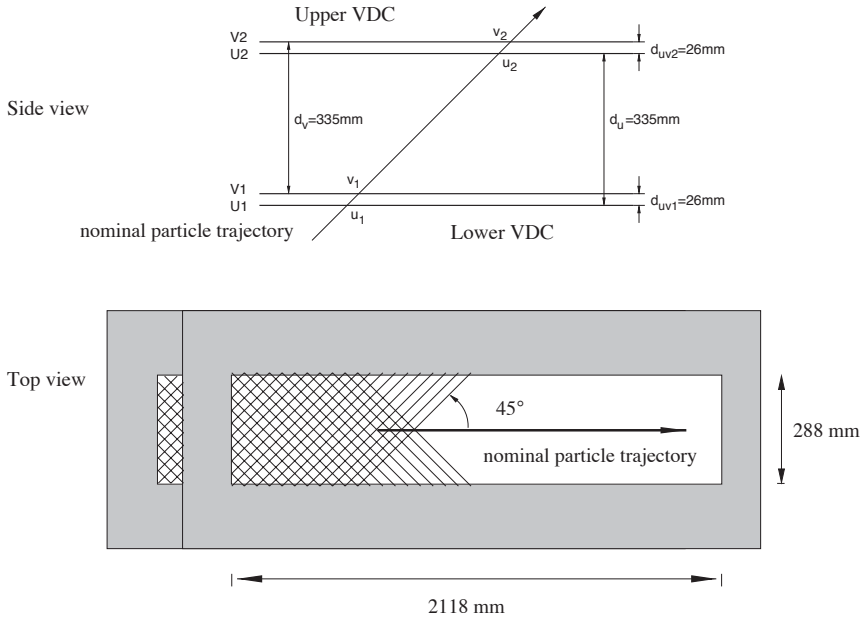

Figure 5-20: Schematic diagram of the Hall A vertical drift chambers. Plot reproduced from [95].

the wire.

By design, the electrons that travel across the VDCs with an angle of 45° will fire four to six wires per plane. This provides an accurate reconstruction of the particle's trajectory. The trajectories are reconstructed with the timing information provided by time-to-digital converters (TDCs) which are connected to the wires. The timing information can be used to determine the drift distance for each wire. The cross-over point is then determined via a linear fit of drift distances versus the wire position. The position and angular resolution of the focal plane are approximately 100 μm and 0.5 mrad, respectively.

Scintillator Planes

Two plastic scintillator planes (S1 and S2m) separated by 2 m are used to form the trigger for the DAQ system. Both planes are made of overlapping paddles of plastic scintillators [95]. The S1 plane has 6 paddles and the S2m plane consists of 12 paddles. Each paddle is monitored by a pair of photomultiplier tubes (PMTs), one at each end. The timing resolution for each plane is about 0.3 ns.

The main trigger (referred as T3 for HRS-L and T1 for HRS-R) is formed as:

- A paddle in S1 is defined to be fired if there are signals from both its left and right PMTs;
- A paddle in S2m is defined to be fired if there are signals from both its left and right PMTs;
- One S1 paddle and one S2m paddle are both fired within a specified timing window.

A secondary trigger (referred as T4 and T2 for left and right arm, respectively) is used to monitor the scintillator efficiency. The efficiency trigger is exclusive to T1(or T3) trigger and is formed by requiring either one S1 paddle or one S2m paddle to be fired as well as a signal from the gas Cherenkov detector. The T2 and T4 triggers represent possibly good events but one of the scintillator planes failed to detect.

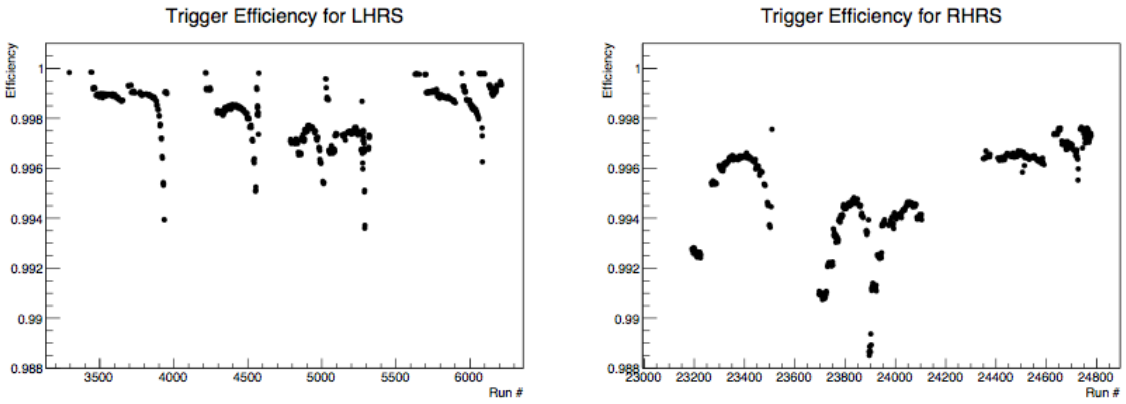

Figure 5-21: Trigger efficiencies of HRS, calculated using Eq. (5.23). Plot reproduced from [123].

The triggers are sent to the trigger supervisor (TS) to determine if the event should be sent to the DAQ system. The DAQ has a deadtime and cannot record every event if the event rate is high. The fraction of events which the DAQ records is called the livetime LT, which is determined by the deadtime DT as $LT = 1 - DT$. The DAQ deadtime can be decreased by scaling the incoming events with a prescale factor ps at the TS which means that only 1 of every ps events fed to the TS is sent to the DAQ system. The livetime depends on the event type and helicity state. It can be calculated by the number of triggers accepted by the DAQ system, $NT_{\rm acc}$, and the total number of triggers input to the TS, NT, which is recorded by scalers (The scalers are treated as deadtime-less):

$$LT^{\pm} = \frac{ps \cdot NT^{\pm}_{\rm acc}}{NT}, \tag{5.22}$$

The trigger efficiency $\eta_{\rm T}$ is defined as:

$$\eta_{\rm T} = \frac{NT_{\rm main}}{NT_{\rm main} + NT_{\rm eff}}, \tag{5.23}$$

where the $NT_{\rm main}$ are the total number of the T1 (or T3) trigger and $NT_{\rm eff}$ are the total number of the T2 (or T4) trigger described above. The trigger efficiency results are shown in Figure 5-21. Overall, the efficiencies are greater than 99.1% [123]. Some substructure can be seen in the data, for example, the trigger efficiency at lower

momenta tends to drop off. However, it is still safe to conclude that the correction to the cross-sections from the trigger efficiency is less than 1%.

Gas Cherenkov Detector

The speed of light in a medium is always lower than the speed of light in vacuum. The ratio between the two speeds is the index of refraction (n), which is a characteristic of the medium. Although the speed of light in the vacuum is the upper limit of the velocity of a particle, the velocity of a high energy particle may exceed the speed of light in a medium, $v > c/n$. A charged particle disrupts the local electromagnetic field when it travels through the medium. When the particle is traveling fast enough, the disturbance accumulates in the medium due to the limited response speed (speed of light in the medium), thus the energy contained in this disturbance radiates as a coherent shockwave, known as Cherenkov radiation [124]. The wave is emitted in a cone. Figure 5-22 shows the geometry of the Cherenkov radiation. The threshold for the production of Cherenkov radiation is given by:

$$\beta c \geq \frac{c}{n}, \tag{5.24}$$

where $\beta = v/c$ is the velocity of the particle in unit of c. Since the speed threshold to produce Cherenkov radiation is $\beta \geq 1/n$, the momentum threshold is therefore dependent on the mass of the particle:

$$p_{\text{thr}} = m_0 \gamma v = m_0 \frac{c}{\sqrt{n^2 - 1}}. \tag{5.25}$$

In the detector package of HRS, a gas Cherenkov detector [125] is sandwiched between the two scintillator planes. The detector is filled with carbon dioxide gas with index of refraction $n = 1.00041$. From Eq. (5.25), the momentum threshold for electrons is 0.018 GeV/c, whereas the threshold for pions is 4.87 GeV/c. Thus, the Cherenkov detector can be used to identify the electrons and pions for momentum between 0.018 and 4.87 GeV/c.

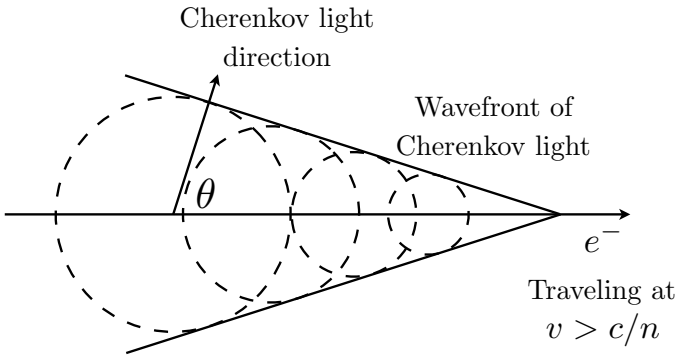

Figure 5-22: Geometry of the Cherenkov radiation. The angle θ is given by $\cos\theta = 1/n\beta$.

The detector has a path length of 1.5 m. Ten spherical mirrors are installed to focus the Cherenkov light onto 10 PMTs. The signals from the PMTs are sent to ADCs and are summed together, representing the total radiation produced by that particle. However, pions can cause a sizable background when they interact with materials in the detector causing secondary electrons. These background events are removed with the aid of a lead-glass calorimeter.

Electromagnetic Calorimeter

When a high energy particle traverses through a dense material, an electromagnetic cascade of photons and electron-positron pairs is generated [124]. The light produced by the cascade is linearly proportional to the energy deposited in the material and can be detected by PMTs.

The calorimeters of the left and right arm of HRS are slightly different in construction [95], see Figure 5-23. The HRS-L calorimeter is composed of two layers of lead-glass blocks, each made of thirty-four blocks, oriented perpendicular to the particle trajectory. The blocks in the first layer are 14.5 cm×14.5 cm×30 cm while the blocks in the second layer are 14.5 cm×14.5 cm×35 cm. On HRS-R, the first layer of the calorimeter contains 48 10 cm×10 cm×35 cm lead-glass blocks which are oriented perpendicular to the particle trajectory, whereas the second layer is composed of 80 14.5 cm×14.5 cm×35 cm blocks which are oriented parallel to the particle trajectory. The major difference between the HRS-L and HRS-R calorimeters is that the HRS-R

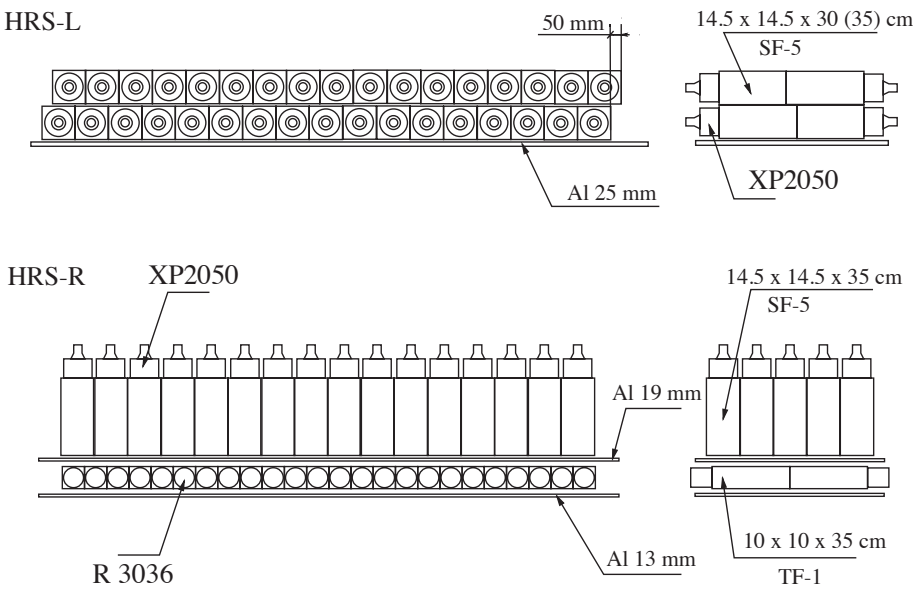

Figure 5-23: The electromagnetic calorimeters in the HRS. Plot reproduced from [95].

calorimeter is a total energy absorber, which means the scattered electrons will deposit all of their energies in the calorimeter since it is thick enough, while the HRS-L calorimeter is not a full energy absorber because of the thinner length.

Chapter 6

Spectrometer Optics Study

In Chapter 5, we have introduced the experimental setup of E08-027. The strong transverse target field and the septum field makes the reconstruction of the kinematics of the scattered electrons, i.e., the spectrometer optics study, to be a challenge.

In the usual optics study procedure, the HRS is considered as an identical pair of magnetic spectrometers, each of which contains three quadrupoles and a dipole magnet in a QQDQ configuration as mentioned in the previous chapter. An optics matrix is introduced to represent the effect of the magnets configuration. Using this optics matrix, the kinematic variables of the scattered particles at the interaction point can be reconstructed from the signals recorded in the detectors. The optics matrix elements are determined through an established optics calibration procedure. They have been optimized over the full momentum ranges of both spectrometers and have been tested and shown to be stable.

During E08-027, a pair of septum magnets were used to bend the electrons with scattering angles $\approx 5.77^\circ$ into the minimum spectrometer angle 12.5° of the HRS. The optics study for HRS with septum was first performed during E97-110 [126]. In E97-110, the optics matrix was re-optimized with the septum magnet added into the QQDQ magnets configuration. The basic optimization procedure was almost the same as the normal optics calibration procedure of the HRS. This procedure is preserved in E08-027, and thus the optics matrix method is used to describe the joint effect of the septum magnet and the HRS magnets.

In addition to the septa magnets, the optics calibration procedure needs to be modified to accommodate the effect from the strong transverse magnetic field of the polarized NH_3 target. For E08-027, this was done by separating the motion of the scattered electron into two parts: the motion in the target field region, which can be calculated using the equation of motion of charged particles in the magnetic field, and the motion out of the target field region, which is described by the optics matrix. The optics study procedure and the corresponding reconstruction procedure were adjusted following this idea. In this chapter, we will summarize the procedure of the spectrometer optics study for E08-027.

6.1 Coordinate Systems

In this section, an overview of the target and focal plane coordinate systems used in the spectrometer optics study is presented. More details can be found in Ref. [127]. All coordinate systems are Cartesian unless otherwise stated. Note that in this section all references to angular coordinates should be considered as referring to the tangent of the angle.

6.1.1 Hall Coordinate System (HCS)

The origin of the HCS is at the center of the Hall A, which is defined to be the intersection point of the beam and the vertical axis of the target. The $\hat{z}$ axis is along the beam line and points downstream, the $\hat{y}$ axis is vertically up, and the $\hat{x}$ axis is horizontal and pointing to the left if looking along $\hat{z}$ and upright along $\hat{y}$, see Figure 6-1.

6.1.2 Target Coordinate System (TCS)

Each of the two spectrometers has its own TCS. The $\hat{z}_{\rm tg}$ axis of the TCS is defined by the central ray of the sieve collimator for a given spectrometer which is the line perpendicular to the plane of the sieve slit passing through the center point of the

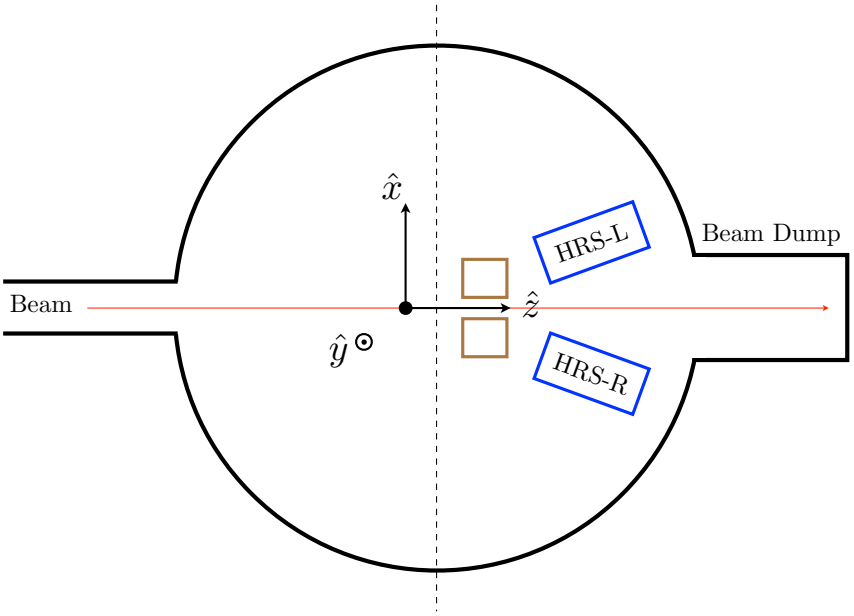

Figure 6-1: Hall coordinate system (top view).

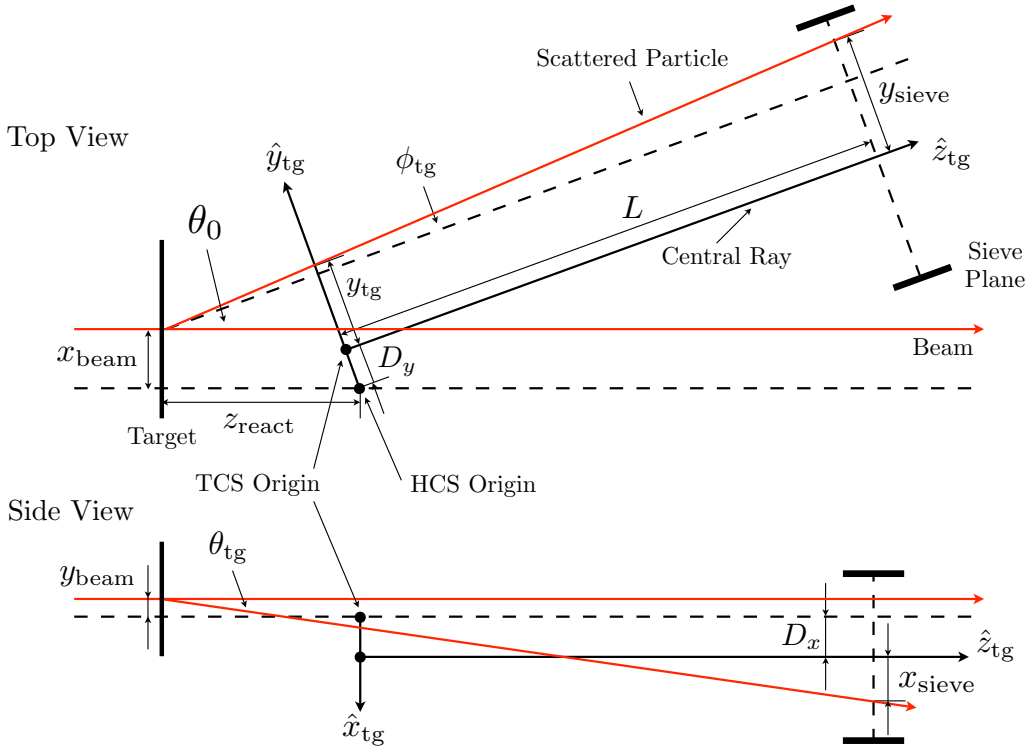

Figure 6-2: Target coordinate system (top and side views). θ_0 is the spectrometer central angle, L is the distance from the sieve slit to the TCS origin, D_x and D_y are the vertical and horizontal deviations of the spectrometer central ray to the HCS origin.

central sieve slit hole. The $\hat{z}_{\rm tg}$ points away from the target towards the spectrometer and $\hat{x}_{\rm tg}$ is vertically down. Thus $\hat{y}_{\rm tg}$ is pointing to the left if looking along the $\hat{z}_{\rm tg}$ direction. Ideally, the $\hat{z}_{\rm tg}$ axis should pass through the hall center if the spectrometer points directly to the hall center and the sieve slit is perfectly centered. In this ideal case, the origin of the TCS coincides with the origin of the HCS. However, the origin of the TCS typically deviates from the hall center. The deviation can be measured by surveying the spectrometer pointing. The angle between $\hat{z}_{\rm tg}$ of the TCS and the $\hat{z}$ of the HCS is defined as the central angle θ_0 of the spectrometer.

The kinematics of each scattering event is expressed as four variables in the TCS: the out-of-plane angle $\theta_{\rm tg}$ and the in-plane $\phi_{\rm tg}$ angle with respect to the central ray are given by $\mathrm{d}x/\mathrm{d}z$ and $\mathrm{d}y/\mathrm{d}z$ in the TCS; $y_{\rm tg}$ is given by the y coordinate of the intersection point of the scattered particles's trajectory and the $z_{\rm tg} = 0$ plane. The fourth variable δ is related to the momentum of the scattered particle:

$$\delta = \frac{P - P_0}{P_0}, \tag{6.1}$$

where P is the measured momentum of a particle and P_0 is the central momentum setting of HRS and septum [127]. The scattering angle of the scattered particle can be calculated from the TCS variables:

$$\theta_{\rm scat} = \arccos\left(\frac{\cos(\theta_0) - \phi_{\rm tg}\sin(\theta_0)}{\sqrt{1 + \theta_{\rm tg}^2 + \phi_{\rm tg}^2}}\right), \tag{6.2}$$

where θ_0 is the spectrometer certral angle. A diagram of the TCS as well as its relations with the HCS for the left arm is shown in Figure 6-2.

6.1.3 Detector Coordinate System (DCS)

The coordinates of the detected particles are measured by the VDCs, as described in Chapter 5. The origin of the DCS is given by the intersection point of wire 184 of the VDC1 U1 plane and the perpendicular projection of wire 184 in the VDC1 V1 plane onto the VDC1 U1 plane. $\hat{z}_{\rm det}$ is perpendicular to the VDC plane pointing

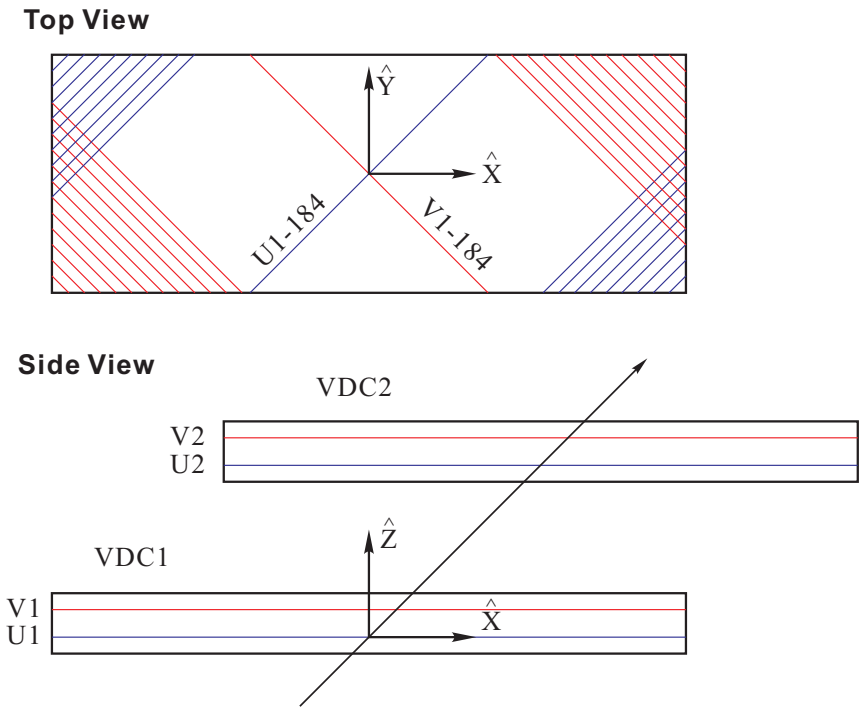

Figure 6-3: Detector coordinate system (top and side views). The intersection point of the wire 184 of the U1 plane and the perpendicular projection of wire 184 of the V1 plane onto the U1 plane is shown in the top view. Plot reproduced from [128].

vertically up, and the $\hat{x}_{\rm det}$ is parallel to the long symmetry axis of the lower VDC pointing downstream. Thus the $\hat{y}_{\rm det}$ is parallel to the short symmetry axis of the lower VDC. See Figure 6-3. When a particle is detected, two spatial coordinates $x_{\rm det}$, $y_{\rm det}$ and two angular coordinates $\theta_{\rm det} \equiv {\rm d}x_{\rm det}/{\rm d}z_{\rm det}$, $\phi_{\rm det} \equiv {\rm d}y_{\rm det}/{\rm d}z_{\rm det}$ are calculated in this coordinate system.

6.1.4 Transport Coordinate System (TRCS) at the Focal Plane

The TRCS at the focal plane is given by rotating the DCS around the y axis by 45° clockwise if viewing along y axis. Ideally, the $\hat{z}_{\rm tra}$ coincides with the central ray of the spectrometer. Typically, it is used to transport the DCS to the focal plane coordinate system. The TRCS coordinates of an event can be calculated from the DCS coordinates by:

$$x_{\rm tra} = x_{\rm det}\cos(\rho_0)(1 + \theta_{\rm tra}\tan(\rho_0)), \tag{6.3}$$

$$\theta_{\text{tra}} = \frac{\theta_{\text{det}} + \tan(\rho_0)}{1 - \theta_{\text{det}} \tan(\rho_0)}, \tag{6.4}$$

$$y_{\text{tra}} = y_{\text{det}} + \sin(\rho_0)\phi_{\text{tra}} x_{\text{det}}, \tag{6.5}$$

$$\phi_{\text{tra}} = \frac{\phi_{\text{det}}}{\cos(\rho_0)(1 - \theta_{\text{det}} \tan(\rho_0))}, \tag{6.6}$$

where $\rho_0 = -45°$.

6.1.5 Focal Plane Coordinate System (FCS)

The FCS is a rotated coordinate system with its z axis always parallel to the local central ray, which is defined as the trajectory of a particular particle with $\theta_{\text{tg}} = \phi_{\text{tg}} = 0$ in the TCS for each relative momentum. This coordinate system is generated by rotating the DCS clockwise around its y axis by the angle ρ between the local central ray and the z axis of the DCS. See Figure 6-4. Because of the focusing of the HRS magnet system, particles with the same scattering momentum will be focused at the focal plane, which means the relative momentum to the central momentum of the spectrometer is approximately a function of x_{tra}. Therefore, the rotating angle ρ is a function of x_{tra}. As a result, the dispersive angle θ_{fp} is small for all points across the focal plane in this rotated coordinate system, thus the expansion of the optics matrix will converge faster during the calibration, which will greatly simplify the optimizing procedure. The FCS coordinates of an event can be calculated form the DCS and

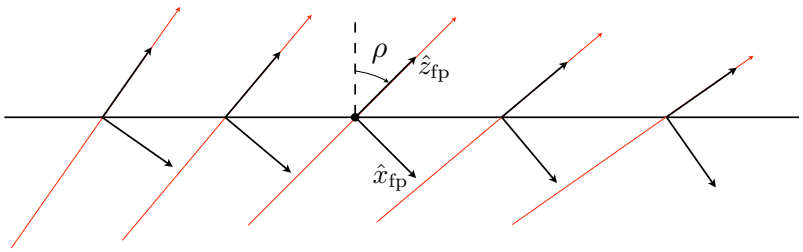

Figure 6-4: Focal plane coordinate system. The red trajectories are the local certral rays with $\theta_{\text{tg}} = \phi_{\text{tg}} = 0$.

TRCS coordinates by:

$$x_{\rm fp} = x_{\rm tra} \tag{6.7}$$

$$\theta_{\rm fp} = \frac{\theta_{\rm det} + \tan(\rho)}{1 - \theta_{\rm det}\tan(\rho)} \tag{6.8}$$

$$y_{\rm fp} = y_{\rm tra} - \sum_i C^y_{i000} x^i_{\rm fp} \tag{6.9}$$

$$\phi_{\rm fp} = \frac{\phi_{\rm det} - \sum_i C^p_{i000} x^i_{\rm fp}}{\cos(\rho)(1 - \theta_{\rm det}\tan(\rho))}, \tag{6.10}$$

where $\tan(\rho) = \sum C^t_{i000} x^i_{\rm fp}$. The coefficients C^t_{i000}, C^y_{i000} and C^p_{i000} also include corrections for the systematic offsets due to misalignment of VDC packages.

6.2 Optimization Procedure

6.2.1 Optics Matrix

As mentioned above, the DCS coordinates $x_{\rm det}$, $\theta_{\rm det}$, $y_{\rm det}$, $\phi_{\rm det}$ are directly measured with the VDC package. The optics matrix method allows a unique one-to-one mapping between these variables and the TCS variables, $x_{\rm tg}$, $\theta_{\rm tg}$, $y_{\rm tg}$, $\phi_{\rm tg}$ and δ.

During the optics calibration, the $x_{\rm tg}$ is effectively set at zero, therefore the unknowns at the target are reduced to four: δ, $\theta_{\rm tg}$, $y_{\rm tg}$, $\phi_{\rm tg}$. Thus, the optics matrix can be expressed as (in a first-order approximation):

$$\begin{pmatrix} \delta \\ \theta \\ y \\ \phi \end{pmatrix}_{\rm tg} = \begin{pmatrix} \langle\delta|x\rangle & \langle\delta|\theta\rangle & 0 & 0 \\ \langle\theta|x\rangle & \langle\theta|\theta\rangle & 0 & 0 \\ 0 & 0 & \langle y|y\rangle & \langle y|\phi\rangle \\ 0 & 0 & \langle\phi|y\rangle & \langle\phi|\phi\rangle \end{pmatrix} \begin{pmatrix} x \\ \theta \\ y \\ \phi \end{pmatrix}_{\rm fp} . \tag{6.11}$$

In practice, the matrix takes a more complicated form: a set of tensors D_{jkl}, T_{jkl}, Y_{jkl} and P_{jkl}, which are polynomials of $x_{\rm fp}$, links the FCS coordinates to TCS

coordinates for each target variables. For example:

$$\theta_{\rm tg} = \sum_{j,k,l} T_{jkl} \theta_{\rm fp}^{j} y_{\rm fp}^{k} \phi_{\rm fp}^{l}, \tag{6.12}$$

$$T_{jkl} = \sum_{i} C_{ijkl}^{T} x_{\rm fp}^{i}, \tag{6.13}$$

where C_{ijkl}^{T} are the optics matrix elements for $\theta_{\rm tg}$. Similar expressions can be written for δ, $y_{\rm tg}$ and $\phi_{\rm tg}$. The summation over i, j, k and l is carried out and optimized up to the third order. The main purpose of the optimization procedure is to determine all optics matrix elements using dedicated optics calibration data, described in the next section.

6.2.2 Matrix Optimization without Target Field

The optics optimization procedure is always performed on a set of data with wide coverage on the entire acceptance of the spectrometer, which includes δ for momentum, $\theta_{\rm tg}$ and $\phi_{\rm tg}$ for solid angle and $y_{\rm tg}$ for reaction position. The target variables δ, $\theta_{\rm tg}$, $y_{\rm tg}$ and $\phi_{\rm tg}$ for the calibration data set has to be precisely known. This requirement can be fulfilled by using survey results combined with a sieve-slit collimator for $\theta_{\rm tg}$ and $\phi_{\rm tg}$ and a foil target for $y_{\rm tg}$ and some well-known physics process like elastic scattering for δ as explained in this section.

To calibrate $\theta_{\rm tg}$, $\phi_{\rm tg}$ and $y_{\rm tg}$, a fixed energy electron beam with a point-like profile is incident on a set of foil target. The target foils are aligned along the beam line to cover the $y_{\rm tg}$ acceptance. Therefore, the HCS coordinates $x_{\rm beam}$ and $y_{\rm beam}$ of the interaction point can be determined by BPM, and the z coordinate $z_{\rm react}$ can be determined by the survey result of the target foil. On the other side, a sieve slit collimator is placed before the entrance of the spectrometer (if there is a septum magnet, it is placed before the entrance of the septum magnet). A figure of the sieve slit used in E08-027 is shown in Figure 6-5. The sieve has holes that are arranged in a grid pattern with well-defined horizontal and vertical coordinates $x_{\rm sieve}$ and $y_{\rm sieve}$ (in TCS) covering the angular acceptance. The in-plane angle $\phi_{\rm tg}$ and the out-of-plane

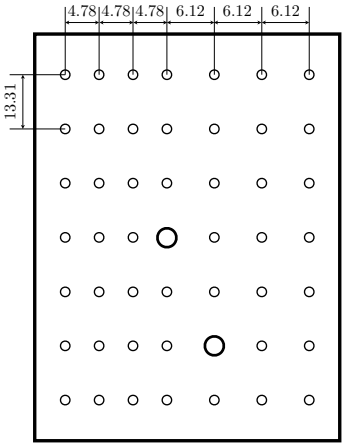

Figure 6-5: Geometric configuration of the sieve slit used during E08-027. The dimensions are in mm. The two large holes are used to determine the orientation of the sieve slit. The diameters are 1.4 mm and 2.7 mm for the normal holes and the large holes, respectively.

angle $\theta_{\rm tg}$ for each hole can be expressed as:

$$\theta_{\rm tg} = \frac{x_{\rm sieve} + D_x + y_{\rm beam}}{L - z_{\rm react}\cos(\theta_0) - x_{\rm beam}\sin(\theta_0)}, \tag{6.14}$$

$$\phi_{\rm tg} = \frac{y_{\rm sieve} + D_y - x_{\rm beam}\cos(\theta_0) + z_{\rm react}\sin(\theta_0)}{L - z_{\rm react}\cos(\theta_0) - x_{\rm beam}\sin(\theta_0)}, \tag{6.15}$$

where θ_0 is the spectrometer central angle, L is the distance from the sieve slit to the TCS origin and the D_x and D_y are the vertical and horizontal deviations of the spectrometer central ray from the HCS origin, respectively, see Figure 6-2. L, D_x and D_y can be determined by surveying the spectrometer. The spectrometer central angle θ_0 can be calculated from the geometries of the sieve slit and the target or by performing a pointing measurement using the energy deviation between the elastic peaks of two different nuclei [129]. Precise determination of $\theta_{\rm tg}$ and $\phi_{\rm tg}$ is important because they determine the scattering angle via Eq. (6.2). With $\theta_{\rm tg}$ and $\phi_{\rm tg}$ known from Eqs. (6.14) and (6.15), the spatial coordinates $x_{\rm tg}$ and $y_{\rm tg}$ can be expressed as:

$$x_{\rm tg} = x_{\rm sieve} - L\theta_{\rm tg}, \tag{6.16}$$

$$y_{\rm tg} = y_{\rm sieve} - L\phi_{\rm tg}. \tag{6.17}$$

To calibrate δ, some well-known physics process can be used to determine the momentum of the detected particle. Take elastic scattering as example, the scattering momentum can be expressed as:

$$P(M,\theta) = E' = \frac{E}{1 + E/M(1 - \cos(\theta))}, \tag{6.18}$$

where E is the beam energy, M is the target mass and θ is the scattering angle. Therefore, the target variable δ can be obtained from the calculated P and the spectrometer central momentum P_0 by Eq. (6.1). To cover the acceptance range of δ of the HRS, several different P_0 values are used during the data collection to perform a so-called "delta scan". The energy loss of the scattered electrons due to the radiative effect when the electrons pass through the target material is considered as a correction to δ.

As described above, the target variables $\theta_{\rm tg}$, $y_{\rm tg}$, $\phi_{\rm tg}$ and δ calculated from survey results (Eqs. (6.14) to (6.17)) or elastic scattering conditions (Eq. (6.18)) are assumed to be the true value of the events in the data set collected with the sieve slit or elastic scattering. The optics matrix elements are then obtained by the minimizing of the aberration functions:

$$\Delta(W) = \sum_s \left[\frac{\sum_{ijkl} C^W_{ijkl} x^i_{\rm fp} \theta^j_{\rm fp} y^k_{\rm fp} \phi^l_{\rm fp} - W^0}{\sigma^s_W} \right]^2, \tag{6.19}$$

where s is the total number of the events measured for optics calibration, W can be any target variables δ, $\theta_{\rm tg}$, $y_{\rm tg}$ or $\phi_{\rm tg}$ and W_0 is the corresponding reference variable calculated from survey results and the elastic condition. A C++ package based on the Hall A Analyzer [130] is developed to do this optimization, which is adopted from N. Liyanage's original code [127] for ESPACE [131]. The core of this package is the MIGRAD algorithm in the TMinuit package of ROOT [132]. The magnetic field simulation package SNAKE is used to generate an initial optics matrix for the optimization. This initial optics matrix accounts for the effects of the HRS magnets and the septum magnet. The package also contains a script for users to select events

for optimization and some test scripts to compare the survey calculations with the reconstructed target variables.

6.2.3 Target Field Effect

As mentioned in Section 5.3, the field used to polarize the NH_3 target is provided by a superconducting magnet, formed by a pair of Helmholtz coils. The field map of these coils has been directly calculated using the Biot-Savart law using the current density distribution of these coils. To estimate the uncertainty of this calculation, a measurement of the target field was performed during the experiment. The results indicate that the relative uncertainty of this field map is less than 1.2% over the whole field region. The details of the field map are discussed in Appendix B. The field map is calculated under the 5.0 T case and is scaled by 0.5 for the 2.5 T configuration.

The most important step during the optimization procedure in Section 6.2.2 is to determine the target plane variables for events collected during calibration runs. If there is no target field, the calculation of these variables only involves the linear projection between the sieve and the target and is straight forward. However, the linear projection is broken by the target field since the trajectory of the scattered electron is now a curve in the presence of this field.

A simulation package was developed to study the behavior of the scattered electrons in the target field. In order to do this, the equation of motion of the scattered electrons is integrated in the target field. The package uses the Runge-Kutta-Nystrom (RKN) method to do the integration. The trajectory of the electrons is approximated by chords in the integration method. For each chord, the deviation between its middle point and the real curve is also estimated by RKN method. The step size of the integration is adjusted dynamically to limit the integration uncertainty to $\leq$0.5 mm.

The trajectory of the scattered electron is also affected by the radiation effects when target field exists. The momentum of the electron decreases during the motion due to the energy loss. If there is no target field, the linear projection would not be influenced by the decreased momentum, but the curved trajectory of the scattered electron in the presence of the target field might change. This effect is also calculated

in the simulation package. More details of the radiation effects can be found in reference [133].

With the help of the simulation package, the motion of the scattered electron in the target field region can be isolated. Since the field strength drops to less than 10 Gauss by the middle of the sieve slit, the sieve slit is taken as the edge of the target field region. Thus, the motion is separated into two parts: the first segment is from the interaction point to the sieve slit, where the trajectory can be calculated from the equation of motion, and the second segment is from the sieve slit to the focal plane, which can be described by the optics matrix.

6.2.4 Matrix Optimization Revised

The original optimization procedure had to be modified due to the presence of the target field. The reference values W_0 in Eq. (6.19) can not be directly calculated from the survey results in this case. The new reference values are determined using the simulation package. The procedure to calculate new reference values involves the following steps:

1. Select an elastic event, determine the coordinates of its interaction point (x_{react}, y_{react}, z_{react}) and the coordinates of the sieve hole which it passes through (x_{sieve}, y_{sieve});

2. Randomly generate a pair of scattering angles in TCS (θ_{test}, ϕ_{test}) and use Eqs. (6.2) and (6.18) to calculate the momentum P_{elastic} of the elastically scattered electron with this scattering angle;

3. Set (x_{beam}, y_{beam}, z_{react}) as start point and set P_{elastic} and (θ_{test}, ϕ_{test}) as the magnitude and direction of the momentum respectively, use the simulation package to generate a trajectory from the start point to sieve slit, assuming the coordinates of the intersection point of this trajectory and the sieve slit are (x_{drift}, y_{drift});

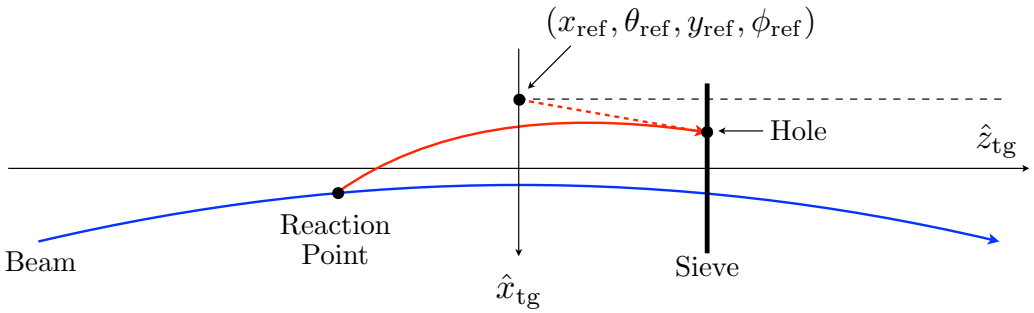

Figure 6-6: Determine the new reference values for the optics optimization with simulation. The red trajectory is determined in step 3 and 4.

4. Compare ($x_{\rm drift}$, $y_{\rm drift}$) with ($x_{\rm sieve}$, $y_{\rm sieve}$), calculate the new test scattering angle:

$$\theta_{\rm test}^{\rm new} = \theta_{\rm test}^{\rm old} + \frac{(x_{\rm drift} - x_{\rm sieve})/L}{2}, \tag{6.20}$$

$$\phi_{\rm test}^{\rm new} = \phi_{\rm test}^{\rm old} + \frac{(y_{\rm drift} - y_{\rm sieve})/L}{2}, \tag{6.21}$$

   where L is the distance from the sieve slit to the TCS origin;

5. Repeat step 3 and 4 until the deviation between the simulated point ($x_{\rm drift}$, $y_{\rm drift}$) and the actual sieve hole position ($x_{\rm sieve}$, $y_{\rm sieve}$) is less than the preset tolerance;

6. The trajectory obtained in the final step passes the interaction point and the same sieve hole as the electron passes, step 3 assures it simulates an elastic electron. Thus it is the ideal trajectory for this particular event. If the coordinates of this trajectory at its intersection point with the sieve slit is defined as ($x_{\rm drift}$, $\theta_{\rm drift}$, $y_{\rm drift}$, $\phi_{\rm drift}$), the new reference values for the optimization can be obtained by projecting them to the target plane linearly, see Figure 6-6:

$$x_{\rm ref} = x_{\rm drift} - L\theta_{\rm drift}, \qquad \theta_{\rm ref} = \theta_{\rm drift}, \tag{6.22}$$

$$y_{\rm ref} = y_{\rm drift} - L\phi_{\rm drift}, \qquad \phi_{\rm ref} = \phi_{\rm drift}. \tag{6.23}$$

Once the new reference values are determined, the same algorithm in Section 6.2.2 can be used to do the optimization. A set of Python scripts is added into the original

optimization package to calculate the reference values from the survey results with the simulation package. The optimization package is also updated to replace the linear-projected reference values with the new values from the simulation.

6.3 Experimental Technique and Results

6.3.1 Required Data

Table 5.1 summarizes the beam energy and the target field configuration for all kinematic settings. Unfortunately, the septum magnet coils for the right arm of the HRS burned twice during the experiment. Some turns of the coils in the septum were bypassed to fix it, which led to three different septum configurations. They are labeled by the number of the coil turns: "48-48-16" for the original septum, "40-32-16" for the septum burned once and "40-00-16" for the worst case. The septum configuration for each kinematic setting is listed in the septum column of Table 5.1.

The polarized NH_3 target need to be cooled down to 1K in a liquid He (LHe) bath. The LHe container is a cylinder and the diameter is only 42.0 mm. The length of the target is limited by the LHe container to only 28.3 mm along z axis in the HCS. As mentioned in Section 6.2.2, a set of foil targets is generally used to cover the $y_{\rm tg}$ acceptance. But at 5.77°, the typical position resolution of $y_{\rm tg}$, ≈1 mm [95], is magnified by a factor of 10 in the position along the beam line (z axis in the HCS), which means that the multiple foils installed in the 28.3 mm target cell can not be easily distinguished by the spectrometer. Thus, only one carbon foil is used to collect optics data and we can only optimize δ, $\theta_{\rm tg}$ and $\phi_{\rm tg}$. The BPM readout is used to determine y_{tg} instead without optics calibration. The thickness of the carbon foil was 40 mil (1.016 mm) for settings 1-5 in Table 5.1 and 125 mil (3.175 mm) for the other settings. The foil locations along the beam direction ($z_{\rm react}$ in Eqs. (6.14) and (6.15)) was -13.6 mm for settings 1-5 in Table 5.1 and -12.5 mm for the other settings. To reduce the radiation effect, the LHe in the LHe container was vapored and pumped out when collecting the optics data.

The sieve slit used to take optics data is shown in Figure 6-5. There are 49 holes in a 7×7 grid pattern with two holes larger than the others. The large holes are used to determine the orientation of the image of the sieve slit. The horizontal distance between the four columns closest to the beam is larger than the distance between the other three columns. This can also be used to determine the orientation in the image. The survey information of the sieve slit was used to calculate the offsets of the central hole from its ideal positions. The x_{sieve} and y_{sieve} for each sieve hole is calculated from these offsets and the relative position to the center of the sieve slit. As calculated from the survey result [134, 135], the horizontal offset D_y is 0.0 mm and the vertical offset D_x is -0.2 mm.

The beam position x_{beam} and y_{beam} is determined by BPMs. The details of the calibration of the BPMs can be found in reference [136]. Because of the target field, the beam is not a straight line in this experiment. The incident angle of the beam at the target can be obtained from the BPM readouts, which can be expressed as the polar angle θ_{beam} and the azimuthal angle ϕ_{beam} in the HCS. The scattering angle is the angle between the incident beam and the trajectory of the scattered electron, which can be calculated via two auxiliary vectors. The vector describing the beam direction is:

$$\vec{A} = (\sin(\theta_{\text{beam}})\cos(\phi_{\text{beam}}),\ \sin(\theta_{\text{beam}})\sin(\phi_{\text{beam}}),\ \cos(\theta_{\text{beam}})), \tag{6.24}$$

while the vector corresponding to the scattered electron is:

$$\vec{B} = (\phi_{\text{tg}}\cos(\theta_0) + \sin(\theta_0),\ -\theta_{\text{tg}},\ \cos(\theta_0) - \phi_{\text{tg}}\sin(\theta_0)), \tag{6.25}$$

and the scattering angle is determined as:

$$\cos\theta_{\text{scat}} = \frac{\vec{A}\cdot\vec{B}}{|\vec{A}||\vec{B}|}, \tag{6.26}$$

where θ_{beam} and ϕ_{beam} are the azimuthal angles of the incident angle of the beam and θ_{tg} and ϕ_{tg} are the tangents of the corresponding angles to keep consistent with the

definition in the TCS. Eqs. (6.24) to (6.26) replace Eq. (6.2) when the beam has an incident angle.

Delta scan was performed by setting P_0 at $\pm 3\%$, $\pm 2\%$, $\pm 1\%$ and 0% of the elastic momentum for each configuration except for the one with 3.350 GeV beam energy. In this paticular setting, the elastic scattered electrons can not pass through the septum magnet even if the septum current is set to its upper limit. Since only one foil of carbon target is used in the experiment, the $y_{\rm tg}$ coverage of the optics calibration was limited. Thus, the incident beam position was adjusted manually by a few millimeters to perform a beam position scan to increase the $y_{\rm tg}$ coverage. Assuming that the original beam position is (0,0), beam position scan is performed at (0, ± 4 mm) and (± 4 mm,0).

6.3.2 Optimization Results

The optics matrix was optimized for each beam energy and target field configurations listed in Table 5.1 except for 3.350 GeV. The procedure discussed in Section 6.2.4 was followed. In this section, the event selection and optimization results are discussed. The data collected with the 1.710 GeV beam energy and 2.5 T transverse target field is taken as an example.

The spectrometer central angle needs to be determined before the matrix calibration. As mentioned in Section 6.2.2, the pointing measurement is considered to be more accurate than a survey for the spectrometer central angle determination, since most of the systematic uncertainty can cancel out when considering the difference of the elastic peak. However, in this experiment, although the carbon and the LHe can be used to perform a pointing measurement, the systematic error can not cancel completely due to the fact that the center of the liquid helium region could not be determined accurately. Thus, the survey method was chosen to determine the spectrometer central angle. The result is summarized in Table 6.1. More details about the central angle calibration can be found in Ref. [137].

Before the optics study, the initial matrix generated by SNAKE as mentioned in Section 6.2.2 was used to reconstruct the target variables of the optics data. These

Arm	Central Angle (rad)
HRS-L	0.1007±0.0007
HRS-R	0.1009±0.0007

Table 6.1: Spectrometer central angles.

target variables were used to make cuts. The data need to be selected by applying several different kinds of cut. Although the carbon foil data is relatively clean, it can still be diluted by electrons scattered from the windows on the target chamber. These events can be removed by applying a foil cut on $y_{\rm tg}$ or a cut on the focal plane variable $y_{\rm fp}$ since only one foil was used. The focal plane cut and $y_{\rm tg}$ cut are shown in Figure 6-7, which were chosen empirically. After the foil cut was made, a set of cuts on target variable $\theta_{\rm tg}$ and $\phi_{\rm tg}$ was made for each hole in the sieve slit. And for each sieve hole, a cut on relative momentum δ was made to select the elastic events. Since $y_{\rm tg}$ acceptance is covered by the beam position scan instead of using multiple foils of target, a beam position cut on $x_{\rm beam}$ and $y_{\rm beam}$ was also performed to select data with the proper beam position. The cut definition process was repeated for each delta scan and beam position scan configurations. Each cut was assigned with an identification number and saved to a separate file.

The optimization package uses the saved cuts to select events. The FCS coordi-

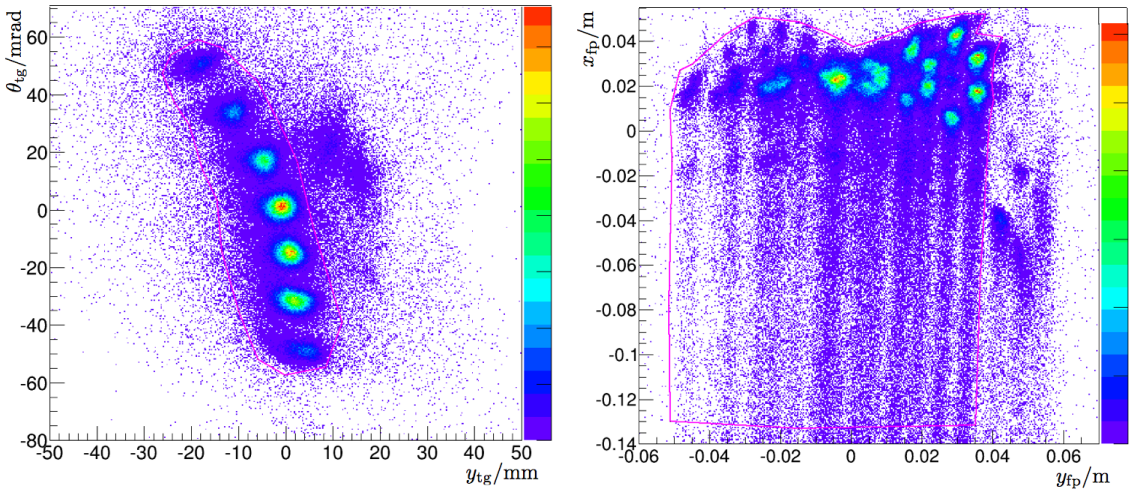

Figure 6-7: The foil cut (left) and the focal plane cut (right).

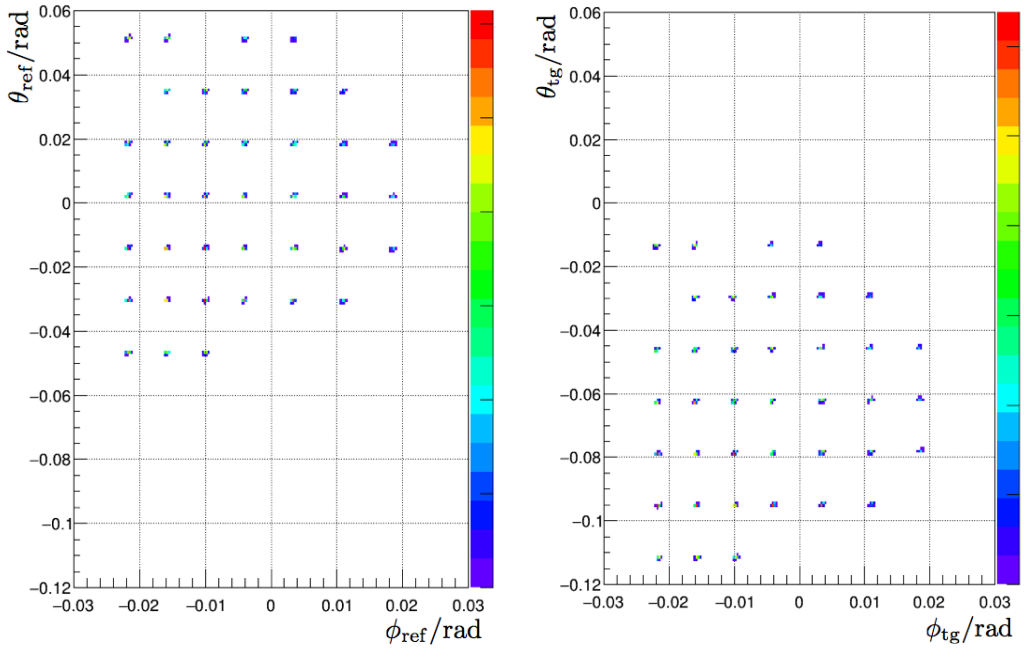

Figure 6-8: The reference values of $\theta_{\rm tg}$ and $\phi_{\rm tg}$ for optimization (left) and the corresponding actual target plane angle at the reaction point (right). The difference between the two panels is due to the target field, which was determined from the simulation described in Section 6.2.3.

nates, positions and angles of the beam and the identification number of the cut for selected events are recorded into a ASCII file. The script mentioned in Section 6.2.4 uses the file as an input to calculate the reference values for optimization, and append the reference values to the focal plane variables for each event in the file. For example, the reference values of $\theta_{\rm tg}$ and $\phi_{\rm tg}$ for 1.710 GeV configuration is shown in the left panel of Figure 6-8. The focal plane variables and the reference values are read by the updated optimization program from the file to optimize the optics matrix.

The angular components of the optics matrix are optimized first. The optimized matrix is used to reconstruct the target variables. The sieve pattern is generated by the projection of the reconstructed $\theta_{\rm tg}$ and $\phi_{\rm tg}$ from the interaction point to the sieve slit plane. The sieve pattern for the 1.710 GeV data is shown in Figure 6-9. The nominal position of the sieve holes are indicated by the cross points of the grids in the plots.

Next step is the momentum calibration. As shown in Section 6.2.2, the momentum

of an elastically scattered electron depends on the scattering angle. Since the sieve slit covers a wide angle range, the scattering angles of the electrons passing through different sieve holes are different. The elastic peak is broadened due to this effect, which influences the resolution of the optimization. Thus, a new variable is defined

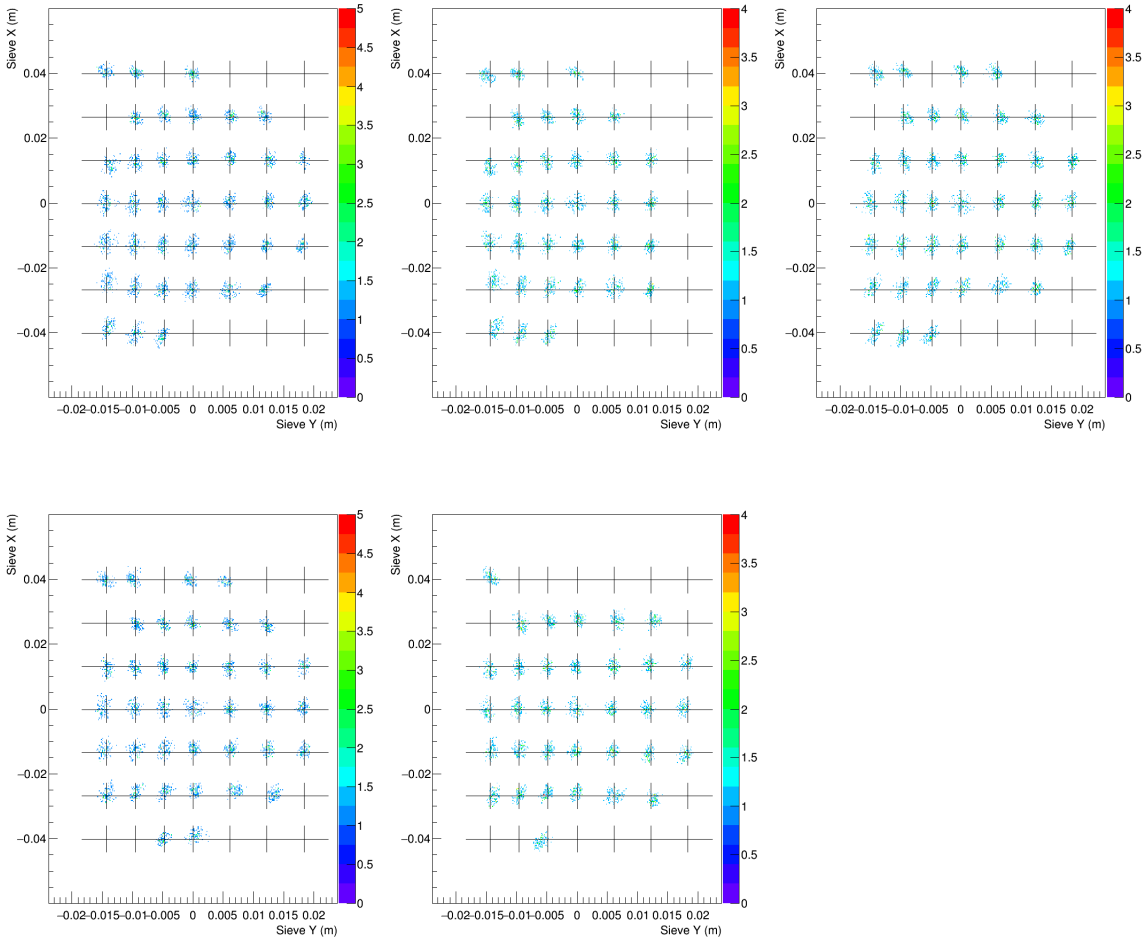

Figure 6-9: Sieve Pattern for 1.710 GeV data. The patterns of different delta scans are shown in separate plots. The three plots in the top row is delta scans with spectrometer central momenta (P_0) setting to +3% (left), +2% (center) and 0% (right) of the elastic momentum, the bottom row is delta scans with P_0 setting to −2% (left) and −3% (center). The cross points of the grids in the plots are used to indicate the actual positions of the sieve holes. The good agreement between the hole images and the grid indicates the angles $\theta_{\rm tg}$ and $\phi_{\rm tg}$ have been calibrated well.

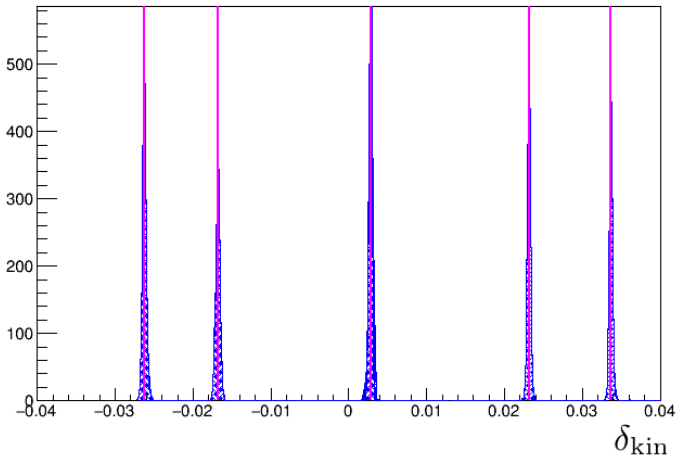

Figure 6-10: The δ_{kin} calibration results for 1.710 GeV data. The peaks in the plot are the reconstructed δ_{kin} from different delta scan configurations, summed over all sieve holes. Starting from the left, the spectrometer central momenta are +3%, +2%, 0%, −2% and −3% of the elastic momentum respectively. The magenta lines in the plots indicate the actual value of the δ_{kin}.

to remove the angular dependence of δ:

$$\delta_{\text{kin}} = \delta - \frac{P(M,\ \theta) - P(M,\ \theta_0)}{P_0}, \tag{6.27}$$

where θ_0 is the spectrometer central angle and θ is the scattering angle. The second term on the right hand side of Eq. (6.27) is defined as δ_{corr}:

$$\delta = \delta_{\text{kin}} + \delta_{\text{corr}}(M, \theta). \tag{6.28}$$

δ_{corr} only depends on the target material and the scattering angle. In practice, δ_{corr} is calculated with the survey result and the beam positions before the optimization starts. During the optimization, the saved δ_{corr} can be used to convert δ to δ_{kin} with almost no additional computing cost. Momentum δ_{kin} for events from different sieve holes can then be optimized together. The δ_{kin} calibration results for 1.710 GeV data are shown in Figure 6-10. The nominal positions of the δ_{kin} are indicated by magenta lines for each delta scan configuration.

In this section, only the optimization results for 1.710 GeV configuration is shown as an example. However the optimization was performed for all kinematic settings and

	Left Arm	Right Arm
$\delta_{\rm res}$	1.5×10^{-4}	2.4×10^{-4}
$\theta_{\rm res}$ (mrad)	1.6	1.6
$\phi_{\rm res}$ (mrad)	1.0	0.8

Table 6.2: Summary of the optics performance without target field. $\delta_{\rm res}$, $\theta_{\rm res}$ and $\phi_{\rm res}$ are resolutions in δ, θ and ϕ, respectively.

HRS	Beam Energy (GeV)	Field Strength (T)	Field Angle	Septum	$\delta_{\rm res}$	$\theta_{\rm res}$ (mrad)	$\phi_{\rm res}$ (mrad)
L	2.254	2.5	90°	48-48-16	2.0×10^{-4}	1.7	1.7
L	2.254	2.5	90°	40-32-16	2.2×10^{-4}	1.8	1.8
L	1.710	2.5	90°	40-00-16	2.4×10^{-4}	2.4	1.5
L	1.157	2.5	90°	40-00-16	3.2×10^{-4}	2.1	1.3
L	2.254	5.0	0°	40-00-16	2.2×10^{-4}	1.6	1.2
R	2.254	2.5	90°	48-48-16	1.8×10^{-4}	1.6	1.2
R	2.254	2.5	90°	40-32-16	2.5×10^{-4}	2.2	1.8
R	1.710	2.5	90°	40-00-16	2.3×10^{-4}	2.7	1.7
R	1.157	2.5	90°	40-00-16	3.4×10^{-4}	1.9	1.5

Table 6.3: Summary of optics performance with the target field. Here "L" and "R" stand for the left arm and right arm of the HRS. $\delta_{\rm res}$, $\theta_{\rm res}$ and $\phi_{\rm res}$ are resolutions in δ, θ and ϕ, respectively.

the optics data without target field was optimized as well with the normal procedure to verify the HRS performance. The resolutions of the optics matrix without the target field is summarized in Table 6.2 and the resolutions of the optics matrix with target field is summarized in Table 6.3. Here the resolution is evaluated via:

$$f^W_{\rm res} = \sqrt{\frac{1}{N}\sum_{s=1}^{N}(W_s - W^0_s)^2}, \tag{6.29}$$

where W are calculated with optics matrix, W_0 are the reference values and N is the total number of the events used in the optimization. See Ref. [138] for more plots of the optimization results for each setting listed in Table 5.1.

6.4 Reconstruction Procedure

Since the final purpose of the optics study is to reconstruct the kinematic variables for each event, the reconstruction procedure is included as part of the optics study. If there is no target field, the Hall A Analyzer is designed to read the optics matrix and calculate the target plane variables directly for each event [130] and no additional process is required. However, this is not the case with the target field.

Following the logic in Section 6.2.4, the reconstruction procedure can also be completed in two steps. The first step is to reconstruct the coordinates of the intersection point of the scattered electron and the sieve slit plane, which can be obtained from the focal plane variables with the optimized optics matrix. The second step is to determine the trajectory of the electron from the sieve slit plane to the target with the simulation package. The detailed procedure to reconstruct kinematic variables involve the following steps:

1. Select an event, apply the optics matrix to the focal plane coordinates ($x_{\rm fp}$, $\theta_{\rm fp}$, $y_{\rm fp}$, $\phi_{\rm fp}$) to calculate the relative momentum δ and the effective target angles $\theta_{\rm eff}$ and $\phi_{\rm eff}$ at the target plane, which is the $z = 0$ plane in TCS. In practice, this step is performed by the Hall A Analyzer;

2. Calculate the effective beam positions $x_{\rm eff}$ and $y_{\rm eff}$ in TCS from the actual beam positions provided by BPMs with the target field simulation described

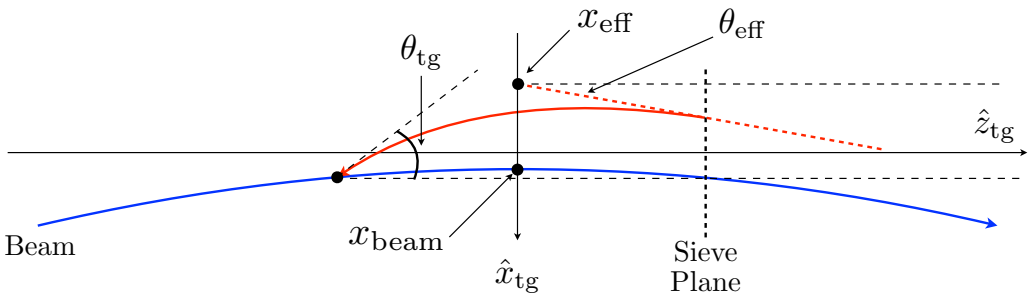

Figure 6-11: Reconstruction of the target kinematic variables. Here $\theta_{\rm eff}$ is reconstrcted by the optics matrix from the focal plane variable. The red dot line shows the linear projection to the sieve slit plane and the read solid line indicates the trojectory generated by the simulation package, which gives us the real target variable $\theta_{\rm tg}$. The detailed procudure is discussed in this section.

later. Combine with the angles obtained in step 1, the effective target variables are (x_{eff}, θ_{eff}, y_{eff}, ϕ_{eff});

3. Perform a linear projection of (x_{eff}, θ_{eff}, y_{eff}, ϕ_{eff}) to the sieve slit plane, which is the $z = L$ plane in TCS, to obtain (x_{proj}, θ_{proj}, y_{proj}, ϕ_{proj});

4. Set (x_{proj}, y_{proj}, $z_{\text{proj}} = L$) as the start point and set the δ and (θ_{proj}, ϕ_{proj}) as the magnitude and direction of the momentum respectively, use the simulation package to generate a trajectory from the start point to the target plane in TCS, which gives the target variables (x_{tg}, θ_{tg}, y_{tg}, ϕ_{tg}) of the selected event.

The effective beam positions x_{eff} and y_{eff} used in step 2 is generated by adding a correction to actual position, x_{beam} and y_{beam}, of the scattered electron. The correction

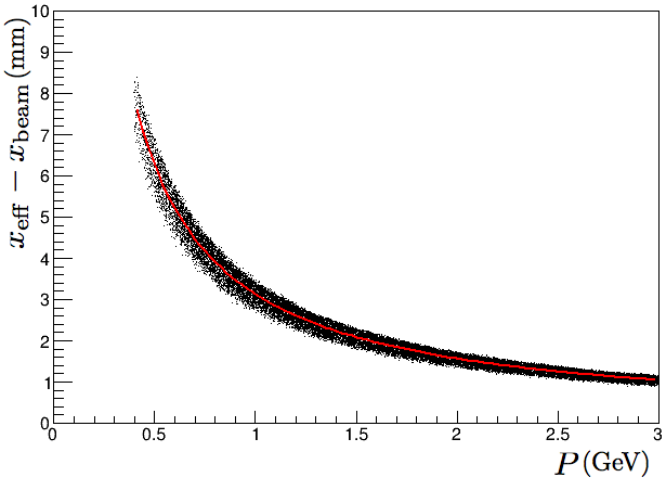

Figure 6-12: The relation between $x_{\text{eff}} - x_{\text{beam}}$ and the momentum of the scattered electron from the simulation. The red curve is the fit result of the function in Eq. (6.30).

HRS	Field	C_0^x (mm)	C_1^x (mm·GeV/c)	C_0^y (mm)	C_1^y (mm·GeV/c)
Left	2.5 T at 90°	0.00	3.14	-0.09	0.22
Left	5.0 T at 0°	0.00	-0.75	0.16	-0.40
Left	5.0 T at 90°	-0.04	6.34	-0.35	0.86
Right	2.5 T at 90°	0.00	3.13	0.09	-0.21
Right	5.0 T at 0°	0.00	0.76	-0.15	0.34
Right	5.0 T at 90°	-0.05	6.37	0.35	-0.85

Table 6.4: Fit parameters of the effective beam position correction.

is defined as $x_{\text{eff}} - x_{\text{beam}}$, which is plotted in Figure 6-12 for 2.5 T transverse target field setting as an example. Since the target in this experiment is short, the $x_{\text{eff}} - x_{\text{beam}}$ term is dominated by the deviation of the linear projection from the actual trajectory. The deviation shows a strong correlation with the momentum P of the scattered electron due to the target field. The simulated $x_{\text{eff}} - x_{\text{beam}}$ values can be fit as a function of P:

$$x_{\text{eff}} - x_{\text{beam}} = C_0 + C_1/P. \tag{6.30}$$

Similar expressions can be written for y_{eff} and y_{beam}. The fit is performed for all three target field configurations on both spectrometers. The fit parameters are summarized in Table 6.4.

A Python script was developed to calculate the kinematic variables following the procedure described above. The original reconstruction script based on the Hall A analyzer is included in this script as a preprocessor of the data.

Chapter 7

Analysis

For E08-027, asymmetries and unpolarized cross-sections are measured to extract the polarized cross-section differences for inclusive electron scattering between a longitudinally polarized electron beam and a transversely polarized NH_3 target. In this chapter, I will give an overview of the analysis of the necessary inputs to extract the polarized cross-section differences.

7.1 Asymmetries and Cross-Sections

To extract the asymmetries $A_\parallel$ and $A_\perp$ defined in Eqs. (4.3) and (4.4), we first calculate the raw asymmetries using the number of events within the $\pm$ helicity state:

$$A_{\text{raw}} = \frac{\frac{N^+}{LT^+Q^+} - \frac{N^-}{LT^-Q^-}}{\frac{N^+}{LT^+Q^+} + \frac{N^-}{LT^-Q^-}}, \tag{7.1}$$

where $N^\pm$ is the number of events, $LT^\pm$ is the DAQ livetime (Section 5.4.2) and $Q^\pm$ is the charge in the $\pm$ helicity state respectively (Section 5.2.2).

The physics asymmetries and the raw asymmetries are related through the expression:

$$A_{\parallel,\perp}^{\text{phys}} = \frac{A_{\parallel,\perp}^{\text{raw}}}{f P_b P_t}, \tag{7.2}$$

where f is the dilution factor due to the unpolarized materials in the target, P_b is the

beam polarization (Section 5.2.4) and P_t is the target polarization (Section 5.3.3).

Due to the radiation effect, we need to make radiative corrections to Eq. (7.2) to retrieve Born asymmetries:

$$A_{\parallel,\perp}^{\text{Born}} = A_{\parallel,\perp}^{\text{phys}} + \Delta A_{\text{RC}}^{\text{ext}} + \Delta A_{\text{RC}}^{\text{int}}, \tag{7.3}$$

where $\Delta A_{\text{RC}}^{\text{ext}}$ and $\Delta A_{\text{RC}}^{\text{int}}$ are the external and internal radiative corrections respectively. The Born asymmetries need to be retrieved from the data to be compared with theoretical results.

The raw unpolarized cross-section can be expressed in terms of measurable quantities as:

$$\sigma_0^{\text{raw}} = \frac{\dfrac{ps \cdot N_{\text{acc}}}{LT \cdot \eta_{\text{det}}}}{\dfrac{Q}{e} \cdot \rho \cdot \Delta Z} \cdot \frac{1}{\Delta\Omega \Delta E'}, \tag{7.4}$$

where

- N_{acc} is the number of detected electrons within the acceptance and the particle identification cuts, recorded by the DAQ system (Section 5.4.2);
- ps is the prescale factor for the DAQ system;
- LT is the DAQ livetime (Section 5.4.2);
- η_{det} is the product of all hardware and cut efficiencies;
- Q is the total charge read by BCMs, e is the electron charge;
- ρ is the target density;
- ΔZ is the target length seen by the spectrometer;
- $\Delta\Omega$, $\Delta E'$ are the solid angle acceptance and the momentum acceptance.

The contribution from materials other than hydrogen in the target must be removed from the raw cross-section:

$$\sigma_0^{\text{phys}} = \sigma_0^{\text{raw}} \cdot f, \tag{7.5}$$

where f is the dilution factor. The unpolarized Born cross-section can be determined after applying the external and internal radiative corrections:

$$\sigma_0^{\text{Born}} = \sigma_0^{\text{phys}} + \Delta\sigma_{\text{RC}}^{\text{ext}} + \Delta\sigma_{\text{RC}}^{\text{int}}. \tag{7.6}$$

The cross-section differences can be expressed as the product of the physics asymmetries and the unpolarized cross-sections:

$$\Delta\sigma_{\parallel,\perp}^{\text{phys}} = 2A_{\parallel,\perp}^{\text{phys}} \cdot \sigma_0^{\text{phys}}. \tag{7.7}$$

The cross-section differences also need to be corrected for the radiative effects to be compared with theoretical results.

7.2 Detector Efficiencies

The detector efficiency η_{det} in Eq. (7.4) contains several different contributions:

$$\eta_{\text{det}} = \eta_{\text{VDC}} \cdot \eta_{\text{T}} \cdot \eta_{\text{PID}}, \tag{7.8}$$

where η_{VDC} is the VDC efficiency, η_{T} is the trigger efficiency and the η_{PID} is the particle identification cut (PID) efficiency determined by the performance of the Cherenkov detector and the lead-glass calorimeters and the cuts applied. The trigger efficiency η_{T} has been discussed in Eq. (5.23). In this section, we will discuss VDC efficiency and the PID efficiency.

7.2.1 VDC Efficiency

The efficiency of the VDCs is defined as:

$$\eta_{\text{VDC}} = \frac{N_{\text{good}}}{N_{\text{total}}}, \tag{7.9}$$

where N_{good} is the number of the events with at least one track reconstructed by VDC and verified with the calorimeter, and N_{total} is the number of total accepted events.

Under normal conditions, each detected particle leaves only one track in the HRS detectors. However, multi-track events can occur when several particles pass through the wire chambers simultaneously or due to noise. Only events with a single track are kept in the cross-section analysis for convenience, thus the results needs to be corrected for the efficiency due to the presence of multi-track events, which is defined as:

$$\eta_{\text{multitrack}} = \frac{N_{\text{onetrack}}}{N_{\text{total}}}, \tag{7.10}$$

where N_{onetrack} is the number of the events with only one track reconstructed by VDC. The fraction of multi-track events was small when the event rate is low. However, the fraction of multi-track events reached 30% in some kinematic settings of E08-027. Figure 7-1 shows the proportion of single-track events for both arms of HRS.

The energy deposited in the calorimeters for each track is examined carefully to determine whether there is at least one good track reconstructed by VDC for each multi-track event. We can expect a multi-track event to have at least one good track if the energy deposited by one of the tracks in this event is approximately the central momentum of the spectrometer P_0. If there are two or more tracks deposited energy $\approx P_0$, the distance between the tracks are examined to determine whether there is a good track or not. After careful examination of multi-track events, the uncertainty

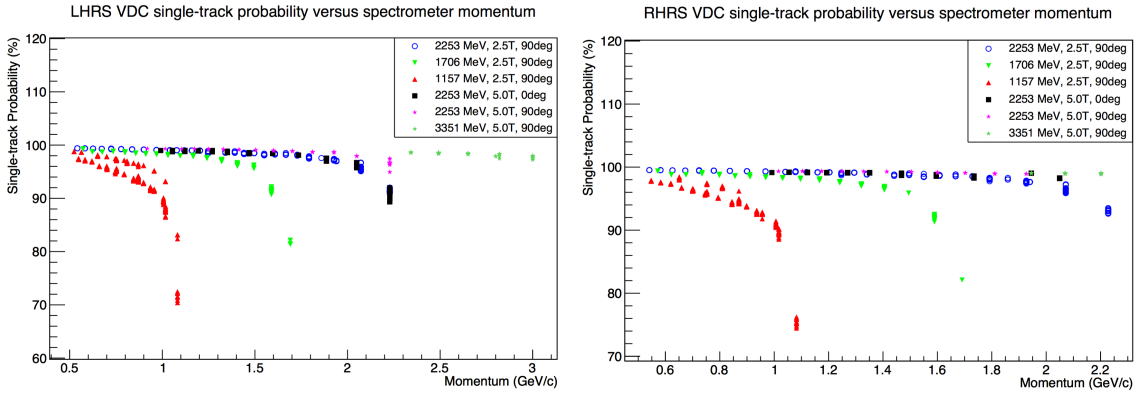

Figure 7-1: Probability of an event leaving only one track in the VDC. Plot reproduced from [139].

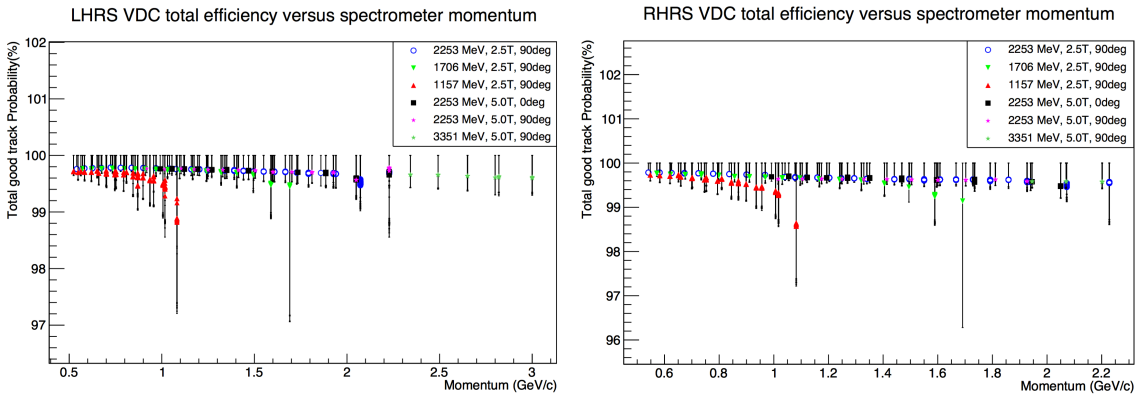

Figure 7-2: Total VDC efficiency. Plot reproduced from [139].

of the VDC efficiency reached $< 1\%$ for most kinematic settings. Figure 7-2 gives the total VDC efficiency with the uncertainty for both arms of HRS. For most of the kinematic settings, the VDC efficiency is approximately 100%. See Ref. [139] for more details of the multi-track efficiency analysis.

7.2.2 Particle Identification Efficiency

The Cherenkov detector and the electromagnetic calorimeter detectors of the HRS detector package are used for particle identification (PID). All particles with the correct momentum-to-charge ratio are selected by the spectrometer, which include electrons, pions, kaons and etc. To ensure a good electron sample, cuts were applied to the data to select a clean electron sample. In the kinematics of E08-027, the major contamination arises from the pions. The majority of pions can be removed with a cut on the Cherenkov, since pions cannot directly trigger this detector as we explained in Section 5.4.2. In practice, the gas Cherenkov cut is used together with two additional cuts: a cut on the first layer of the lead-glass calorimeter (first pion rejector on HRS-L or "pre-shower" on HRS-R) and a cut on the total energy deposited in the calorimeter. All three PID cuts are chosen to maximize the pion suppression while minimizing the removal of good electron events from the data sample.

The detector performance results for the Cherenkov detector and the calorimeters are discussed in details in Ref. [140], and are briefly summarized here. The gas Cherenkov cut works as a threshold cut on both arms, which is a constant cut for

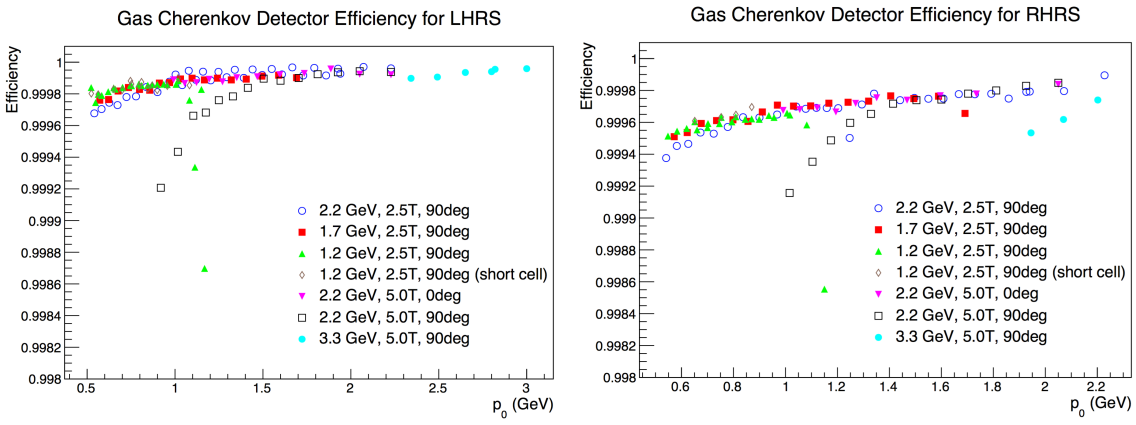

Figure 7-3: Detector efficiencies of the gas Cherenkov detectors. Plot reproduced from [140].

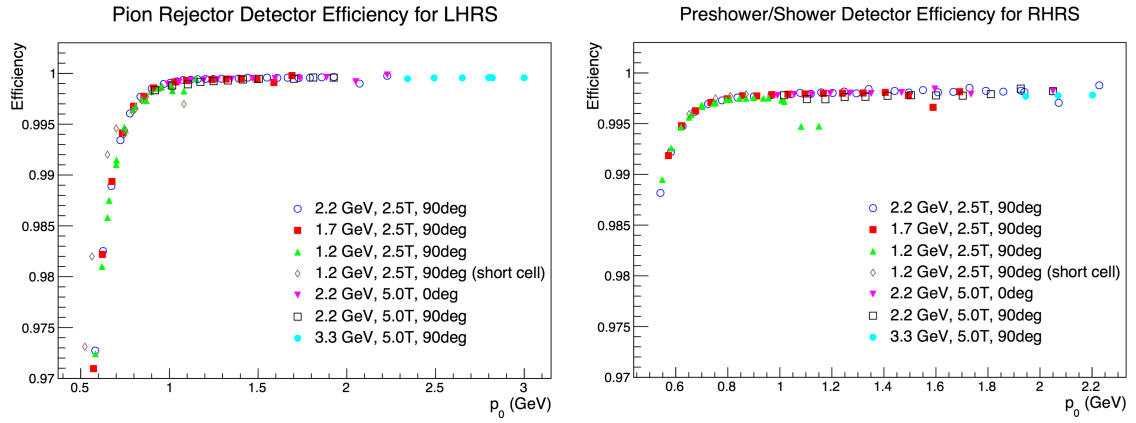

Figure 7-4: Detector efficiencies of the electromagnetic calorimeters. Plot reproduced from [140].

every kinematic setting. The calorimeter cuts are then chosen to keep the overall electron detection efficiency above 99%. A conservative cut is placed on the pre-shower for HRS-R (first layer of the calorimeters on HRS-R, see Section 5.4.2), and a separate cut is placed on the total deposited energy; these cuts are momentum dependent unlike the gas Cherenkov cuts. For HRS-L, the cut on the first layer does not need to be as conservative, since more energy is deposited in the first layer of the pion rejector which is thicker than the pre-shower in right arm.

The detector efficiencies of the gas Cherenkov detectors are shown in Figure 7-3. The efficiency of the gas Cherenkov detector for both arms of the HRS is found to be above 99.8% across the entire range of kinematics. Figure 7-4 shows the calorimeter

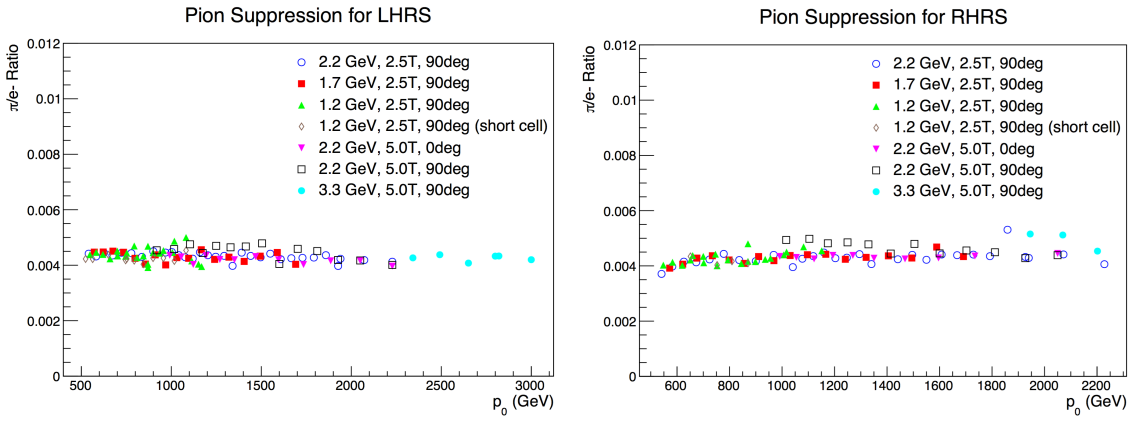

Figure 7-5: Residual pion contamination after PID cuts are applied. Plot reproduced from [140].

efficiencies. The detection efficiency of the pion rejectors in HRS-L is above 98%, and the efficiency of the pre-shower and shower in HRS-R is above 98.8% for all kinematic settings. These results indicate that the performance of the PID detectors is very good during the experiment. After PID cuts are applied, the level of residual pion contamination is very low, with $\pi/e < 0.0052$ for all kinematic settings on both arms of the HRS, as shown in Figure 7-5.

7.3 Packing Fraction Analysis

Ideally the target cell should be completely filled with solid ammonia. However, due to the size and shape of the ammonia beads, there is some space between the beads and this space is filled with liquid helium. The packing fraction is defined as the effective length of the ammonia divided by the length of the target cell. During the experiment, data is collected with the production NH_3 target and the dummy target which has been described in Section 5.3.2. These data are used to extract the packing fraction.

The normalized yield for each run is defined as:

$$Y = \frac{ps \cdot N_{\text{acc}}}{Q \cdot LT \cdot \eta_{\text{det}}}. \tag{7.11}$$

Here the definitions of each quantity are exactly the same as Eq. (7.4). Using the packing fraction p_f, the yield of a production run could be broken into contributions from each target material:

$$Y_{\text{target}} = Y_{\text{He}}^{\text{out}} + (1 - p_f)Y_{\text{He}}^{\text{cell}} + p_f Y_{\text{NH}_3}^{\text{cell}}, \tag{7.12}$$

where the $Y_{\text{He}}^{\text{cell}}$ is the yield of a target cell full of liquid helium, the $Y_{\text{NH}_3}^{\text{cell}}$ is the yield of a target cell filled fully with pure ammonia and the $Y_{\text{He}}^{\text{out}}$ is the yield from liquid helium inside the target nose, but outside the target cell.

The dummy target cell is identical to the ammonia cell except that it is filled with liquid helium but no NH_3 beads. Thus the contributions from the liquid helium can be obtained from the yield Y_{dummy} of a run with the dummy target. In reality, the data collected with dummy target also contains contributions from the aluminum target cell cap (See Section 5.3.2). However, the thickness of the target cell cap (0.018 mm) is very small so the contribution from aluminum is neglected in the packing fraction analysis [141]. The $Y_{\text{He}}^{\text{cell}}$ and $Y_{\text{He}}^{\text{out}}$ can then be expressed in terms of Y_{dummy}:

$$Y_{\text{He}}^{\text{cell}} = \left(\frac{L_{\text{cell}}}{L_{\text{total}}}\right) Y_{\text{dummy}}, \tag{7.13}$$

$$Y_{\text{He}}^{\text{out}} = \left(\frac{L_{\text{total}} - L_{\text{cell}}}{L_{\text{total}}}\right) Y_{\text{dummy}}, \tag{7.14}$$

where the L_{cell} is the length of the target cell and L_{total} is the effective total length of the target nose.

Thus the packing fraction can be expressed as:

$$p_f = \left(\frac{L_{\text{total}}}{L_{\text{cell}}}\right)\left(\frac{Y_{\text{target}}}{Y_{\text{dummy}}} - 1\right)\left(\frac{Y_{\text{NH}_3}^{\text{cell}}}{Y_{\text{He}}^{\text{cell}}} - 1\right)^{-1}. \tag{7.15}$$

It is not possible to obtain the quantity $Y_{\text{NH}_3}^{\text{cell}}$ from the data. However, the ratio $Y_{\text{NH}_3}^{\text{cell}}/Y_{\text{He}}^{\text{cell}}$ could be expressed in terms of the cross-sections since the yield can be expressed as:

$$Y \propto \sigma \frac{\rho \cdot L}{M}, \tag{7.16}$$

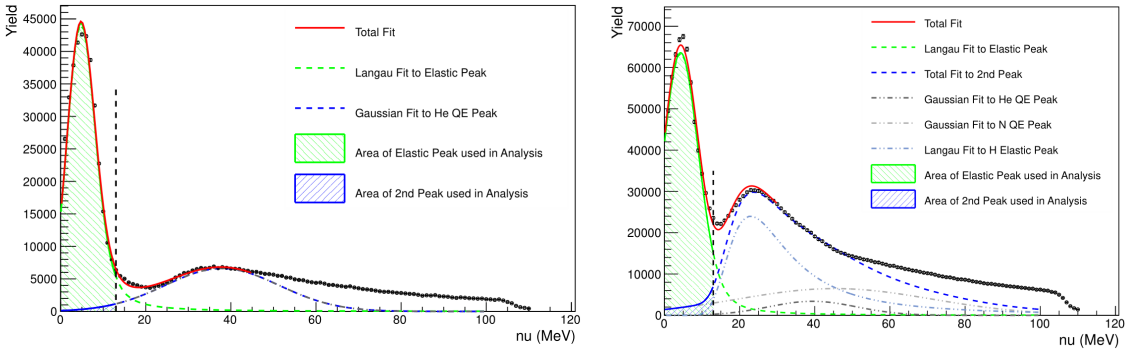

(a) Fit for dummy target. (b) Fit for production target.

Figure 7-6: An example of the fit of the elastic and quasi-elastic peak. Plot reproduced from [141].

where ρ, L and M are the mass density, length and the molar mass of the target material, respectively. The acceptance is ignored here since it cancels out in the cross-section ratio. Thus, Eq. (7.15) can be rewritten as:

$$p_f = \left(\frac{L_{\text{total}}}{L_{\text{cell}}}\right)\left(\frac{Y_{\text{target}}}{Y_{\text{dummy}}} - 1\right)\left(\frac{\sigma_{\text{N}}\frac{\rho_{\text{N}}}{M_{\text{N}}} + \sigma_{\text{H}}\frac{\rho_{\text{H}}}{M_{\text{H}}}}{\sigma_{\text{He}}\frac{\rho_{\text{He}}}{M_{\text{He}}}} - 1\right)^{-1}. \tag{7.17}$$

The packing fraction is extracted from elastic scattering data. The cross-sections σ_{H}, σ_{He} and σ_{N} are determined using elastic form factors from Ref. [142] and [143]. The yield ratio $Y_{\text{target}}/Y_{\text{dummy}}$ is obtained from elastic scattering data. The raw data are used to fit the elastic peaks of hydrogen, helium and nitrogen nuclei as shown in Figure 7-6. One major issue of the fit is the contamination from the quasi-elastic peak. Thus, both the elastic peak and the quasi-elastic peak of a nucleus in the target material need to be fit to match the total spectrum. A Landau-Gaussian convolution function is used to fit the elastic peak of a nucleus since the elastic peak has a radiative tail, whereas the quasi-elastic peak is fit with a Gaussian function.

For the dummy target, the helium elastic peak and the quasi-elastic peak are fit separately and matched with the total spectrum. However, the situation is more complicated for the production target. The spectrum contains five contributions from the nitrogen elastic peak, the helium elastic peak, the nitrogen quasi-elastic peak, the helium quasi-elastic peak and the hydrogen elastic peak. The relative contribution

Beam Energy	Field Strength	Field Angle	Material ID	Packing Fraction
2.254 GeV	2.5 T	90°	7	0.461±0.010
2.254 GeV	2.5 T	90°	8	0.704±0.012
1.710 GeV	2.5 T	90°	7	0.477±0.006
1.710 GeV	2.5 T	90°	8	0.468±0.009
1.157 GeV	2.5 T	90°	11	0.444±0.029
1.157 GeV	2.5 T	90°	12	0.456±0.030
1.157 GeV	2.5 T	90°	14	0.264±0.007
2.254 GeV	5.0 T	0°	17	0.507±0.009
2.254 GeV	5.0 T	0°	18	0.533±0.011
2.254 GeV	5.0 T	90°	19	0.605±0.026
2.254 GeV	5.0 T	90°	20	0.595±0.032

Table 7.1: Packing fraction results for each kinematic setting. Material 14 is used with a special target cell which is shorter than the normal ones. Table reproduced from [141].

from each material is determined with the help of the Quasi-Free-Scattering (QFS) model [144].

The packing fraction analysis is discussed in Ref. [141] in detail and the results are summarized in Table 7.1 for each kinematic setting. Since the target material need to be replaced due to radiation damage, we prepared a few samples of the material. The "Material ID" in the table is used to distinguish these samples. The average packing fraction of the target material is ≈0.5 with an uncertainty of $0.01 \sim 0.03$.

7.4 Dilution Analysis

The detected events from polarized electron scattering are diluted by the electrons scattered from the unpolarized material such as the nitrogen and helium nuclei in the target. Thus, the measured asymmetries need to be corrected by a factor f which is referred to as the dilution factor to retrieve the physics asymmetry as shown in Eq. (7.2).

If the yield of the electrons scattered by unpolarized materials is denoted as Y_{bg},

the raw asymmetry can be rewritten as:

$$A_{\text{raw}} = \frac{Y^+ - Y^-}{Y^+ + Y^- + Y_{\text{bg}}}. \tag{7.18}$$

The ammonia target used in this experiment contains ammonia beads, liquid helium and aluminum foil as caps, thus the Y_{bg} can be decomposed as:

$$Y_{\text{bg}} = Y_{\text{N}} + Y_{\text{He}} + Y_{\text{Al}}. \tag{7.19}$$

Comparing Eq. (7.2) and Eq. (7.18), the dilution factor can be expressed as:

$$f = 1 - \frac{Y_{\text{bg}}}{Y_{\text{target}}}, \tag{7.20}$$

where Y_{target} is the yield of a production run with the ammonia target. The difference between the Y_{target} here and Eq. (7.12) is that the contributions of aluminum caps are included in the dilution analysis.

In Eq. (7.16), we have already known that the yield of a given material is proportional to the corresponding cross-section, thus Y_{bg} can be rewritten as:

$$Y_{\text{bg}} = AN_A \left(\frac{\rho_{\text{NH}_3} L_{\text{cell}} p_f}{M_{\text{NH}_3}} \sigma_{\text{N}} + \frac{\rho_{\text{He}} (L_{\text{total}} - p_f L_{\text{cell}})}{M_{\text{He}}} \sigma_{\text{He}} + \frac{\rho_{\text{Al}} L_{\text{Al}}}{M_{\text{Al}}} \sigma_{\text{Al}} \right), \tag{7.21}$$

where p_f is the packing fraction as mentioned in Section 7.3, A is the acceptance factor and N_A is the Avogadro's number.

During the experiment, several different target materials were used to determine the unpolarized background contribution Y_{bg}. These targets included a dummy cell, which can be used to estimate the aluminum contribution, and a carbon target, which can be scaled using cross-section models to approximate the nitrogen contribution. Data were also collected with the pure liquid helium in the target nose which is referred to as the "empty" target to estimate the helium background. The yields for the empty target, the dummy target and the carbon target are denoted as Y_{empty}, Y_{dummy} and Y_{carbon}, respectively. These yields can be written in terms of the corresponding

materials:

$$Y_{\text{empty}} = AN_A \left(\frac{\rho_{\text{He}} L_{\text{total}}}{M_{\text{He}}} \sigma_{\text{He}} \right), \tag{7.22}$$

$$Y_{\text{dummy}} = AN_A \left(\frac{\rho_{\text{He}} L_{\text{total}}}{M_{\text{He}}} \sigma_{\text{He}} + \frac{\rho_{\text{Al}} L_{\text{Al}}}{M_{\text{Al}}} \sigma_{\text{Al}} \right), \tag{7.23}$$

$$Y_{\text{carbon}} = AN_A \left(\frac{\rho_{\text{He}} (L_{\text{total}} - L_{\text{C}})}{M_{\text{He}}} \sigma_{\text{He}} + \frac{\rho_{\text{C}} L_{\text{C}}}{M_{\text{C}}} \sigma_{\text{C}} \right), \tag{7.24}$$

where L_{C} is the length of the carbon target.

The Y_{Al} is extracted from the dummy target yield and the empty target yield:

$$Y_{\text{Al}} = Y_{\text{dummy}} - Y_{\text{empty}}, \tag{7.25}$$

and the Y_{He} is extracted from the empty target yield:

$$Y_{\text{He}} = \left(1 - \frac{L_{\text{cell}}}{L_{\text{total}}} p_f \right) Y_{\text{empty}}. \tag{7.26}$$

The carbon yield Y_{C} can be extracted from the carbon target yield and the empty target yield:

$$Y_{\text{C}} = Y_{\text{carbon}} - \frac{L_{\text{total}} - L_{\text{C}}}{L_{\text{total}}} Y_{\text{empty}}. \tag{7.27}$$

The Y_{N} is extracted from the carbon yield by scaling Eq. (7.27) with the cross-section ratio $\sigma_{\text{N}}/\sigma_{\text{C}}$. The model from Ref. [145] is used to calculate the cross-section ratio. Thus, the nitrogen contamination can be expressed as:

$$Y_{\text{N}} = \frac{\sigma_{\text{N}}}{\sigma_{\text{C}}} p_f \frac{\rho_{\text{NH}_3} L_{\text{cell}} M_{\text{C}}}{\rho_{\text{C}} L_{\text{C}} M_{\text{NH}_3}} \left(Y_{\text{carbon}} - \frac{L_{\text{total}} - L_{\text{C}}}{L_{\text{total}}} Y_{\text{empty}} \right). \tag{7.28}$$

The dilution factor can then be calculated via Eqs. (7.20) and (7.25) to (7.27).

Since the dilution study is still on-going, a preliminary dilution factor is extracted using the cross-sections instead of data. The model from Ref. [145] is used to calculate the cross-sections for various target materials. In terms of cross-sections, the dilution

factor can be expressed as:

$$f = \frac{3\,\dfrac{\rho_{\mathrm{NH_3}} L_{\mathrm{cell}}\, p_f}{M_{\mathrm{NH_3}}}\sigma_{\mathrm{H}}}{\dfrac{\rho_{\mathrm{NH_3}} L_{\mathrm{cell}}\, p_f}{M_{\mathrm{NH_3}}}(\sigma_{\mathrm{N}} + 3\sigma_{\mathrm{H}}) + \dfrac{\rho_{\mathrm{He}} L_{\mathrm{cell}}(1-p_f)}{M_{\mathrm{He}}}\sigma_{\mathrm{He}} + \dfrac{\rho_{\mathrm{Al}} L_{\mathrm{Al}}}{M_{\mathrm{Al}}}\sigma_{\mathrm{Al}}}. \tag{7.29}$$

The dilution factors calculated via Eq. (7.29) for each kinematic setting are shown in Figures 7-7 to 7-12. The packing fractions used in the calculation are taken from Table 7.1. Material 19 and 20 are also used in the $E_{\mathrm{beam}} = 3.350$ GeV setting. However, no packing fraction data were collected during this setting so the packing fractions from the kinematic setting with 2.253 GeV beam energy and 5.0 T transverse target field are used in the dilution factor calculation.

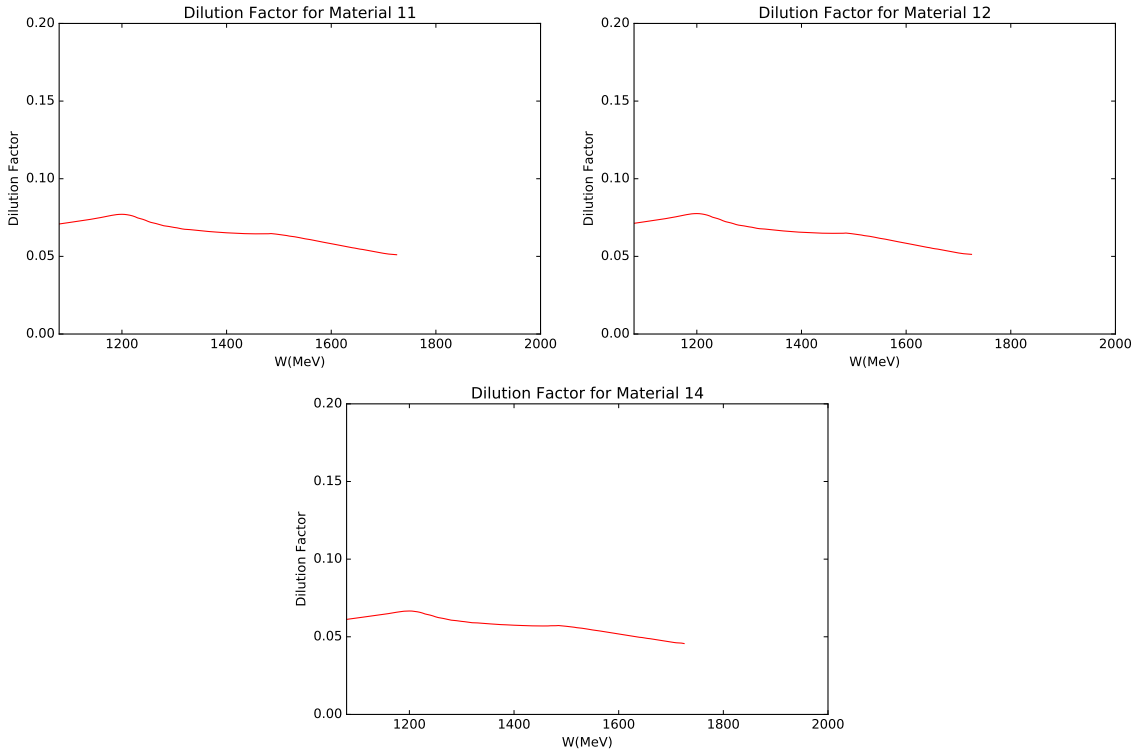

Figure 7-7: Preliminary dilution factors of the kinematic setting with 1.157 GeV beam energy and 2.5 T transverse target field.

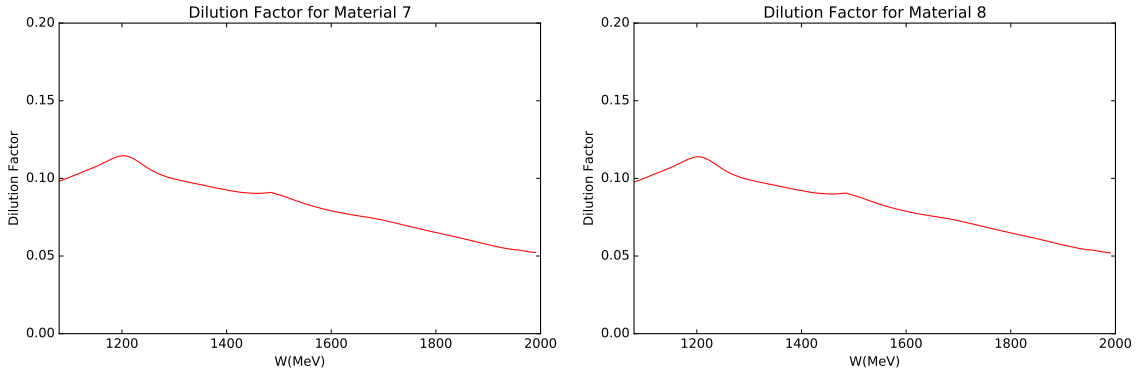

Figure 7-8: Preliminary dilution factors of the kinematic setting with 1.710 GeV beam energy and 2.5 T transverse target field.

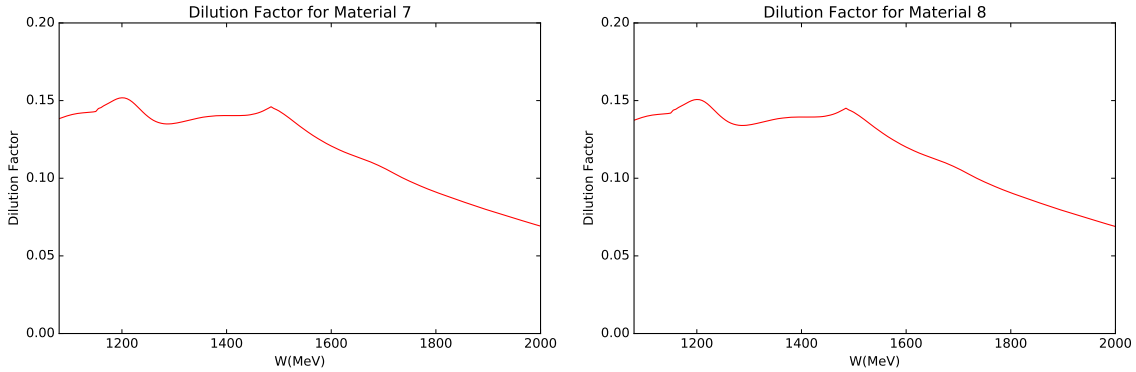

Figure 7-9: Preliminary dilution factors of the kinematic setting with 2.253 GeV beam energy and 2.5 T transverse target field.

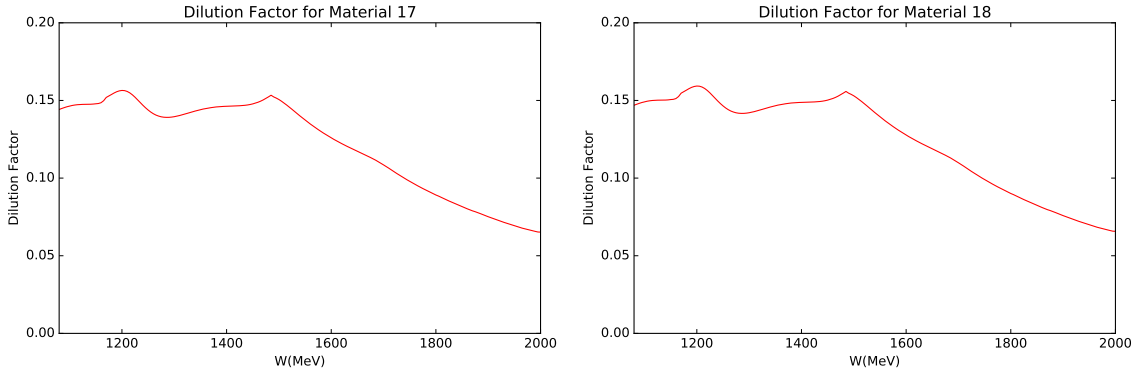

Figure 7-10: Preliminary dilution factors of the kinematic setting with 2.253 GeV beam energy and 5.0 T longitudinal target field.

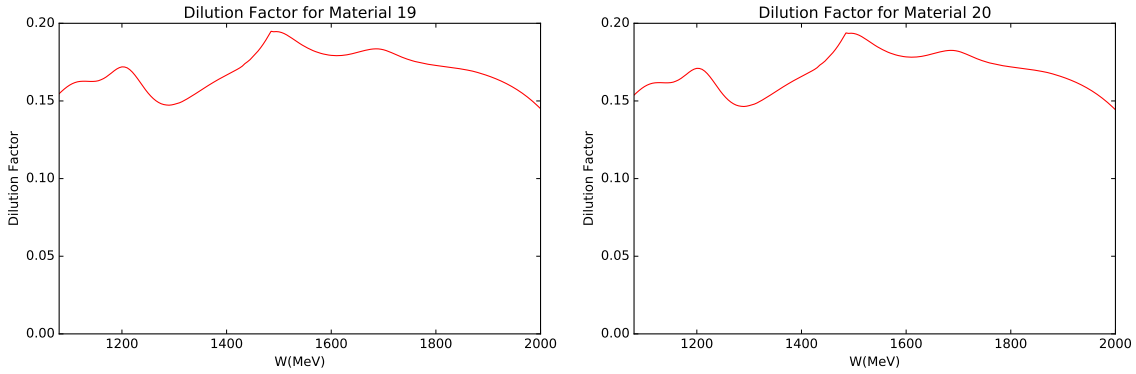

Figure 7-11: Preliminary dilution factors of the kinematic setting with 2.253 GeV beam energy and 5.0 T transverse target field.

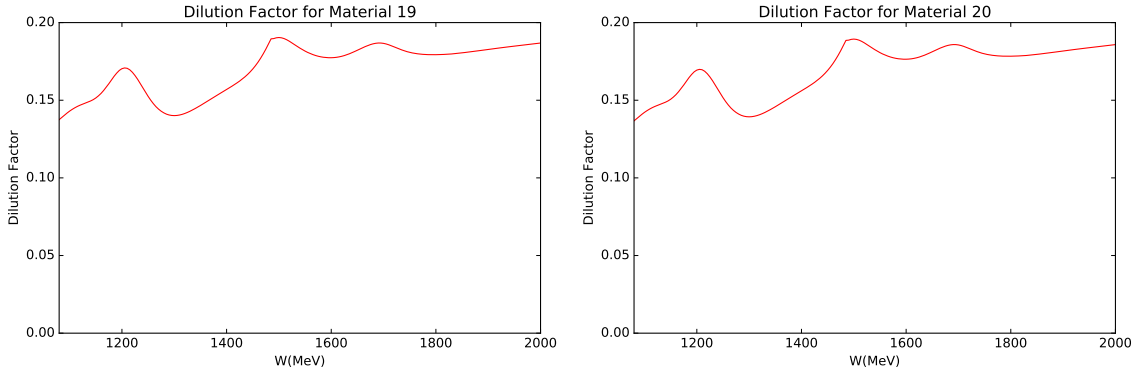

Figure 7-12: Preliminary dilution factors of the kinematic setting with 3.350 GeV beam energy and 5.0 T transverse target field.

Chapter 8

Results and Conclusions

In this chapter, preliminary results for the proton asymmetries and polarized cross-section differences are presented. The spin structure functions and their contributions to the spin polarizabilities are discussed as well. Only the L-HRS data with 1.710, 2.253 and 3.350 GeV beam energies are analyzed in this thesis. Future work towards final results are described in the end.

8.1 Asymmetry Results

Equations (7.3) and (7.4) can be used to extract the physics asymmetry. The beam current has been discussed in Section 5.2.2 and the livetime correction has been discussed in Section 5.4.2. The beam polarization and target polarization has been discussed in Section 5.2.4 and Section 5.3.3, respectively. The preliminary dilution factors have been given in Section 7.4. Thus, the physics asymmetries can be extracted. The results are shown in Figures 8-1 to 8-4.

The statistical uncertainties of the physics asymmetries are shown in the plots. If we assume the total event amount is $N \approx 2N^+ \approx 2N^-$, the absolute statistical uncertainty of the asymmetries is $\sim 1/\sqrt{N}$. This statement is valid because the fluctuations of the event amount $N^\pm$ follow the Poisson distribution, which are $\Delta N^\pm \equiv \sqrt{N^\pm}$ here. However, the DAQ event rate is reduced by applying a prescale factor ps when the raw trigger rate is high. In this case, the fluctuations of the event

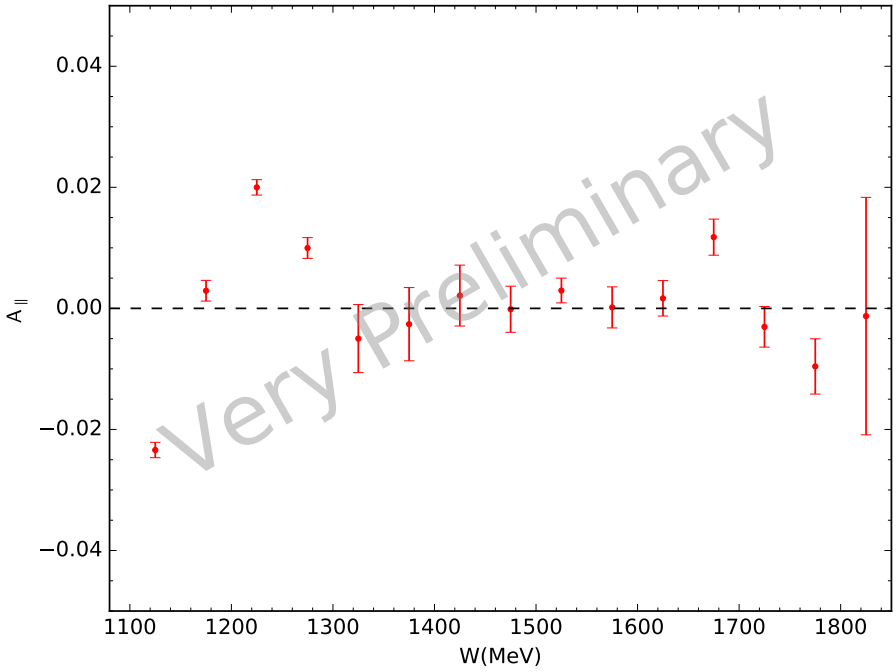

(a) Longitudinal configuration.

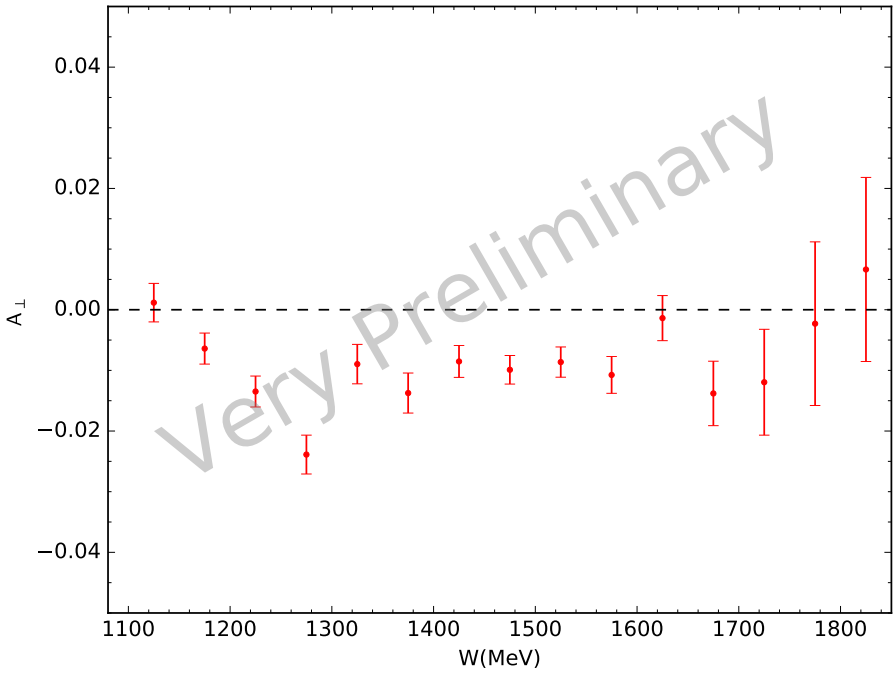

(b) Transverse configuration.

Figure 8-1: Physics asymmetries for the configurations with 2.253 GeV beam energy and 5.0 T target field. The uncertainties shown are only statistical.

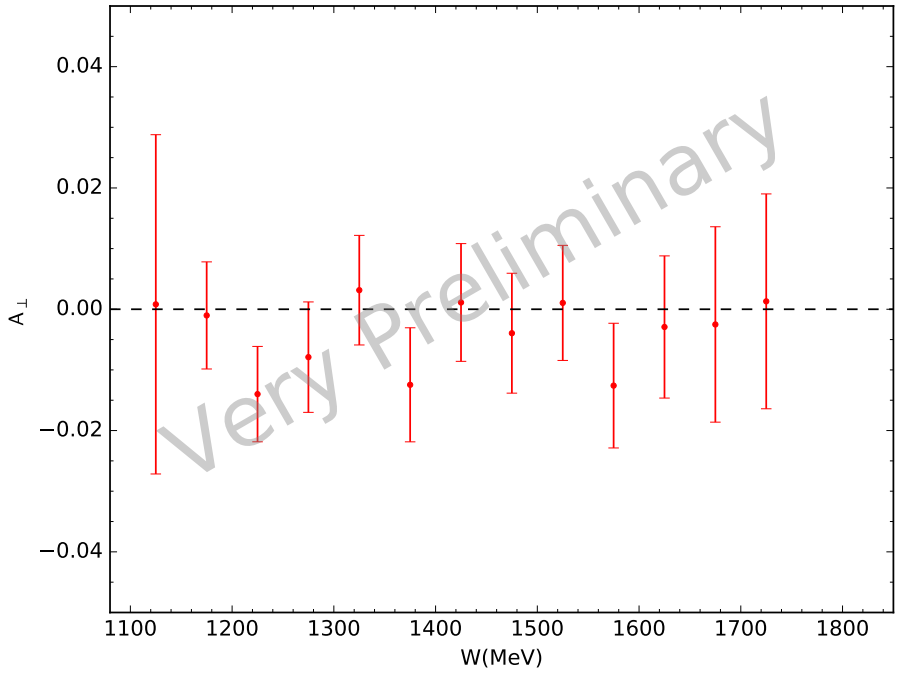

Figure 8-2: Physics asymmetries for the configurations with 1.710 GeV beam energy and 2.5 T transverse target field. The uncertainties shown are only statistical.

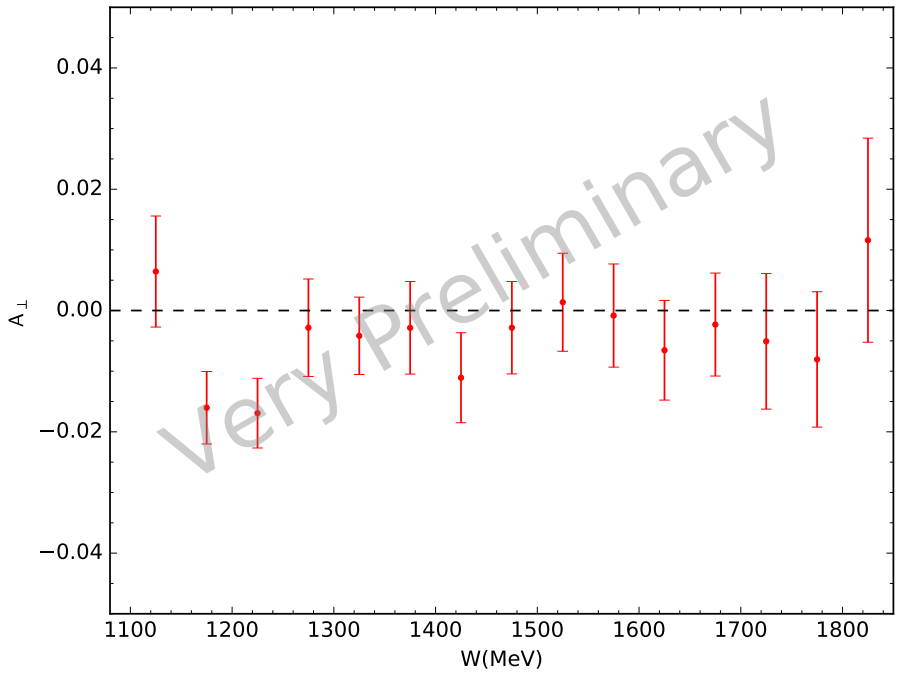

Figure 8-3: Physics asymmetries for the configurations with 2.253 GeV beam energy and 2.5 T transverse target field. The uncertainties shown are only statistical.

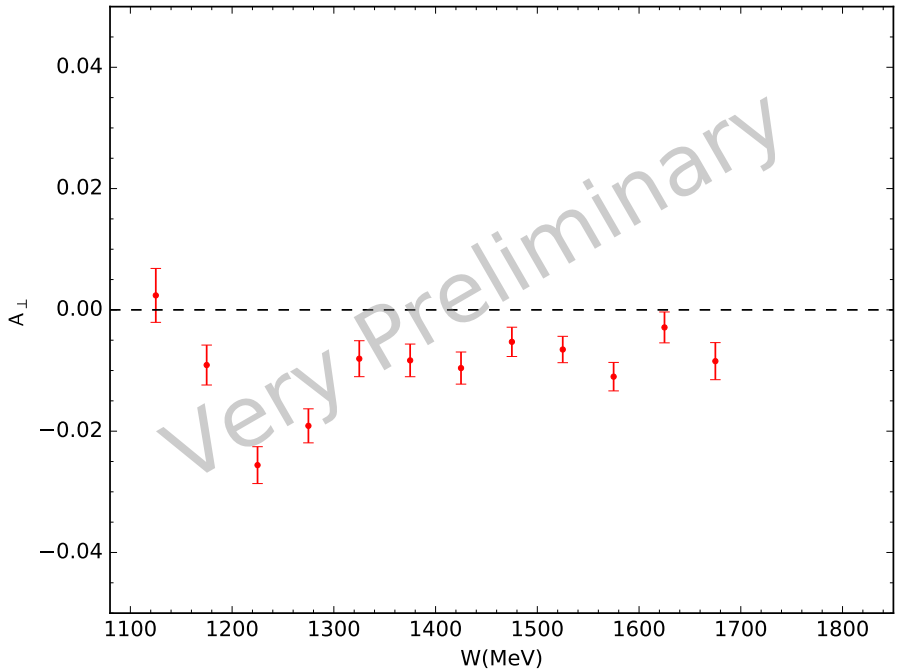

Figure 8-4: Physics asymmetries for the configurations with 3.350 GeV beam energy and 5.0 T transverse target field. The uncertainties shown are only statistical.

amount ΔN no longer follow the Poisson distribution, and need to be corrected by a factor S [128]:

$$S = \sqrt{1 - LT \cdot f_A(1 - \frac{1}{ps})}, \tag{8.1}$$

where LT is the livetime correction of the DAQ system and f_A is the acceptance correction which is defined as $f_A = N_{\text{accepted}}/N_{\text{total}}$. The statistical uncertainty can then be written as:

$$\delta A \simeq \frac{1}{2}\sqrt{\frac{S_+^2}{N_+} + \frac{S_-^2}{N_-}}. \tag{8.2}$$

During the experiment, the data is taken in "runs", each containing about 7 million events. Eq. (8.2) can be used to calculate the uncertainty for each run, and the final asymmetry must be combined using a statistically weighted average:

$$A = \frac{\sum_i A_i/\delta A_i^2}{\sum_i 1/\delta A_i^2}, \tag{8.3}$$

$$\delta A = \sqrt{\frac{1}{\sum_i 1/\delta A_i^2}}, \tag{8.4}$$

where A_i is the asymmetry calculated for the ith run, δA_i is the statistical uncertainty given by Eq. (8.2), and the summation is over all runs.

8.2 Radiative Corrections

The Feynman diagram shown in Figure 2-1 only considers the leading order process, which is known as the Born approximation. This is assumed for theoretical analyses of lepton-nucleon scattering. However, the data contains all of the high order effects which need to be corrected for the data to be compared with theoretical results. This correction is referred to as the radiative correction.

The radiative correction arises from several different sources. The virtual photon one-loop corrections are shown in Figure 8-5. It includes (a) the vacuum polarization correction where the virtual photon splits into an e^-/e^+ pair and acts as an electric dipole, (b) the vertex correction, (c)(d) the electron self-energy which contribute to the renormalization of the electron mass and (e)(f) the Bremsstrahlung radiation.

Diagrams (a), (b), (c) and (d) are considered to be relatively small compared to the contributions of the internal and external Bremsstrahlung. The internal Bremsstrahlung happens when the electron emits and re-absorbs a photon due to effect from the target nucleon's field, whereas the external Bremsstrahlung happens when the electron passes through the materials before or after the interaction. In addition to the Bremsstrahlung, energy can also be lost when an electron passes through the materials, due to ionization effect. The ionization energy loss is dependent on the radiation thickness of the material the electron passes through. The ionization energy loss is typically in the order of a few MeVs for the targets in this experiment.

The radiative corrections should be applied to the asymmetry and the cross-section results extracted from the data. For preliminary study, the asymmetry results from data were not radiatively corrected, but they are compared with radiative corrected model predictions. The Mainz online partial-wave analysis of meson electroproduction (MAID model) [147] is used to generate the polarized cross-section differences. The radiative effects are separated into the internal part and the external part for

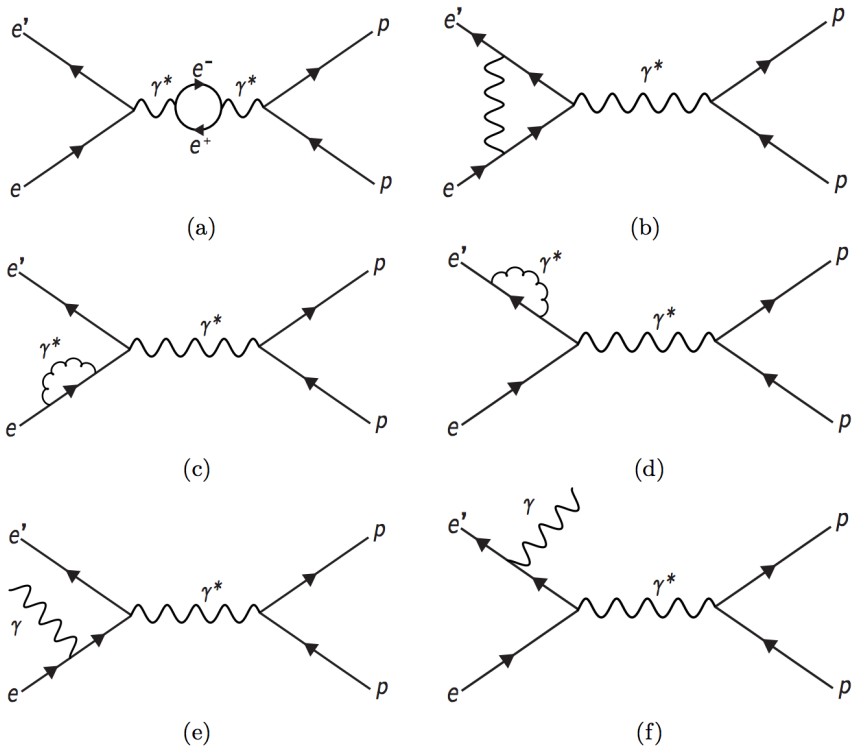

Figure 8-5: Diagrams for next-to-leading order corrections. Plot reproduced from [146].

convenience. The POLRAD formalism [148] is used to calculate the internal radiative effects. And the methods in Ref. [149] developed by Mo and Tsai is used to evaluate the external radiative effects.

The fits of P. Bosted to the inclusive inelastic electron scattering [145] are used to generate the unpolarized cross-sections, which also need to be corrected by the radiative effects. The radiative effects are calculated using the same formalism as the polarized cross-section differences with the fits of P. Bosted as input for both the internal and external corrections.

The elastic tail must also be considered since it becomes significant in the resonance region. The MASCARD code [150] is used to generate polarized elastic cross-sections. And the form factors from Mo and Tsai are used to calculate the radiative effects for both the polarized and unpolarized radiative effects.

To account for the actual kinematic coverage in the calculation, the data are used to provide a fit of the relation between the scattering angle and W for each kinematic

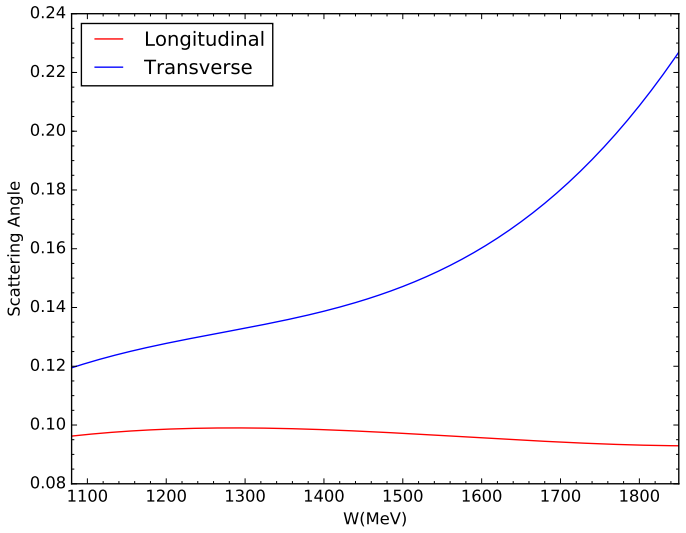

Figure 8-6: Relations between the scattering angle and W for the kinematic settings with 2.253 GeV beam energy and 5.0 T target field (longitudinal and transverse configuration).

setting, and the Q^2 can be determined with W and the scattering angle. The value of W and the Q^2, θ values from the fit are used in the model as inputs. Figure 8-6 shows the relations between W and the scattering angle. Only the two settings with 2.253 GeV beam energy and 5.0 T target field are shown in the figure as examples. The variation of the scattering angle is an effect of the target magnetic field. As shown in Figure 8-6, the variation is very small for the longitudinal configuration but for transverse configuration it is significant. The radiated and unradiated model predictions for the asymmetries are compared in Figure 8-7. Here only the two kinematic settings (longitudinal and transverse configurations) with 2.253 GeV beam energy and 5.0 T target field are shown as examples.

Figures 8-8 to 8-11 shows the comparison of the radiated model predictions with the physics asymmetries extracted in the previous section. There can be an uncertainty for the model prediction, which arises from several different sources. The fits of P. Bosted contribute a relative uncertainty of 5% [145] and the Mo and Tsai formalism contributes a relative uncertainty of 4% [149]. The MAID group does not provide the fit uncertainties since the fit uncertainty is unrealistically small in this case due to the large number of data points included in the fit. Thus, we will use the

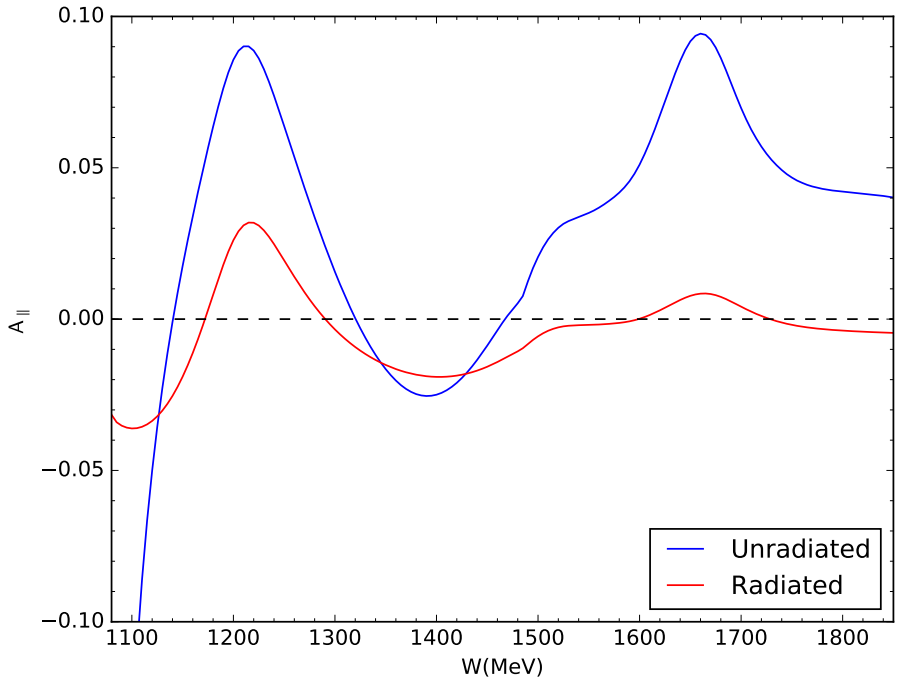

(a) Longitudinal configuration.

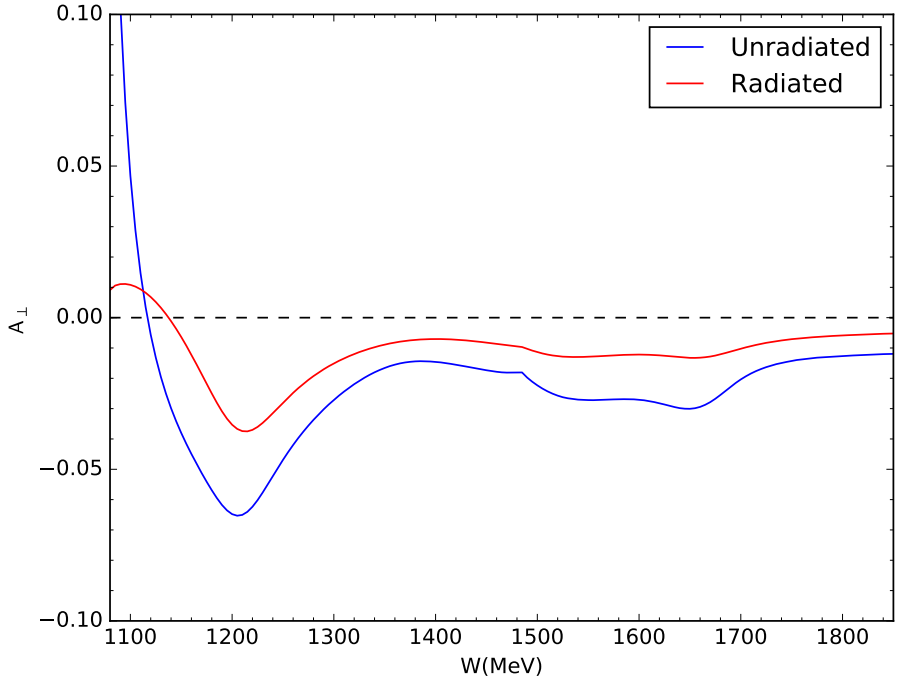

(b) Transverse configuration.

Figure 8-7: Comparison of the radiated and unradiated model predictions for the asymmetries of the kinematic setting with 2.253 GeV beam energy and 5.0 T target field.

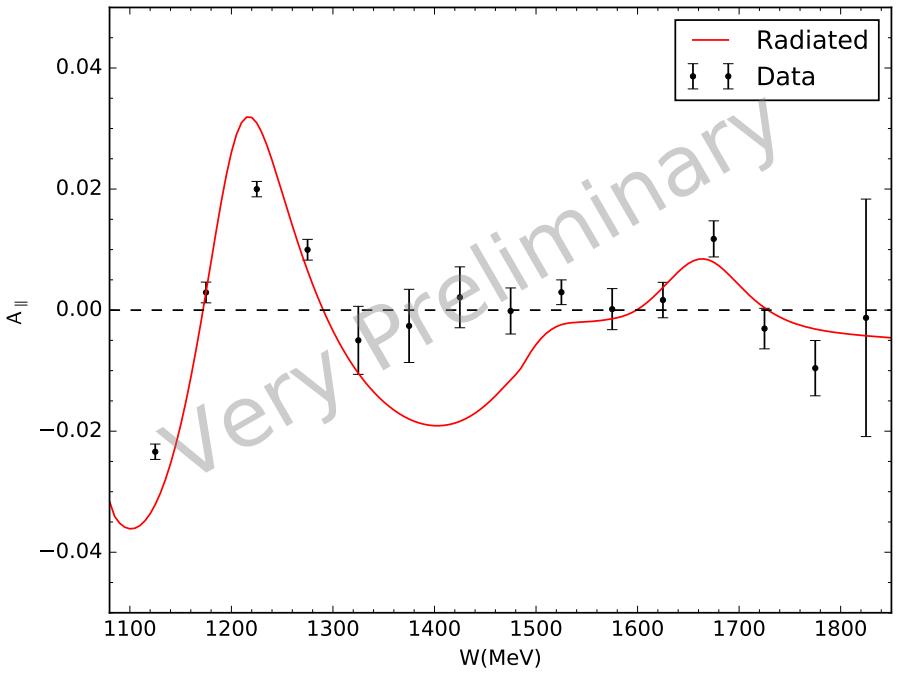

(a) Longitudinal configuration.

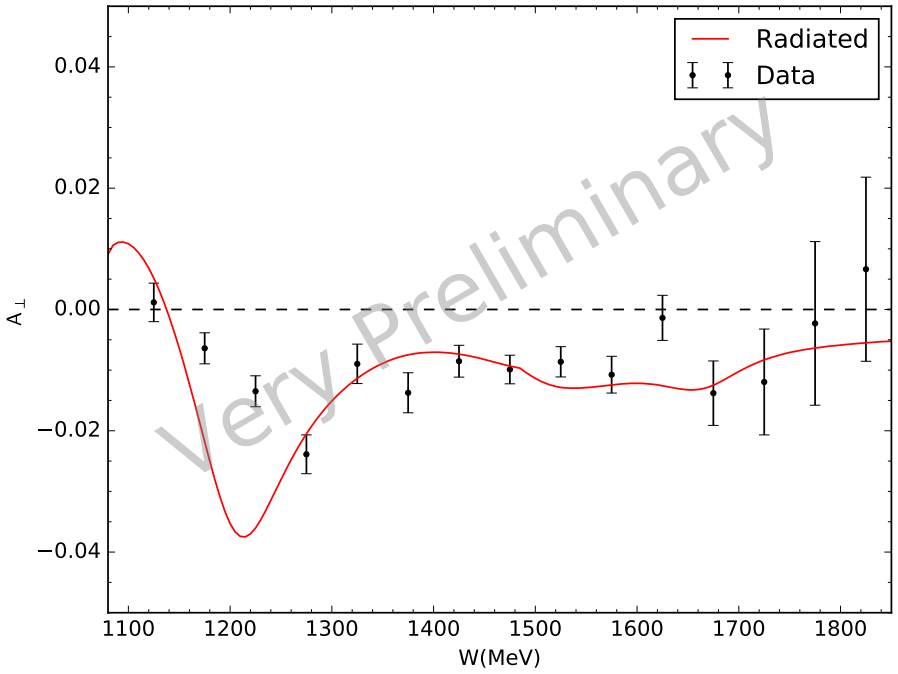

(b) Transverse configuration.

Figure 8-8: Comparison of the radiated model predictions with measured asymmetries for the kinematic settings with 2.253 GeV beam energy and 5.0 T target field (longitudinal and transverse configurations). Data are not radiatively corrected.

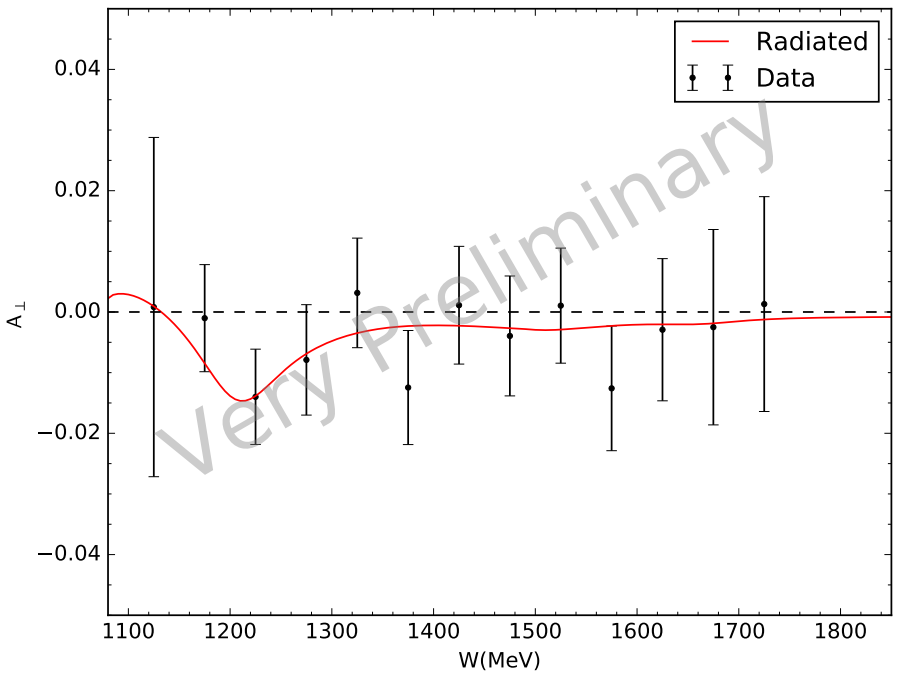

Figure 8-9: Comparison of the radiated model predictions with measured asymmetries for the kinematic settings with 1.710 GeV beam energy and 2.5 T transverse target field. Data are not radiatively corrected.

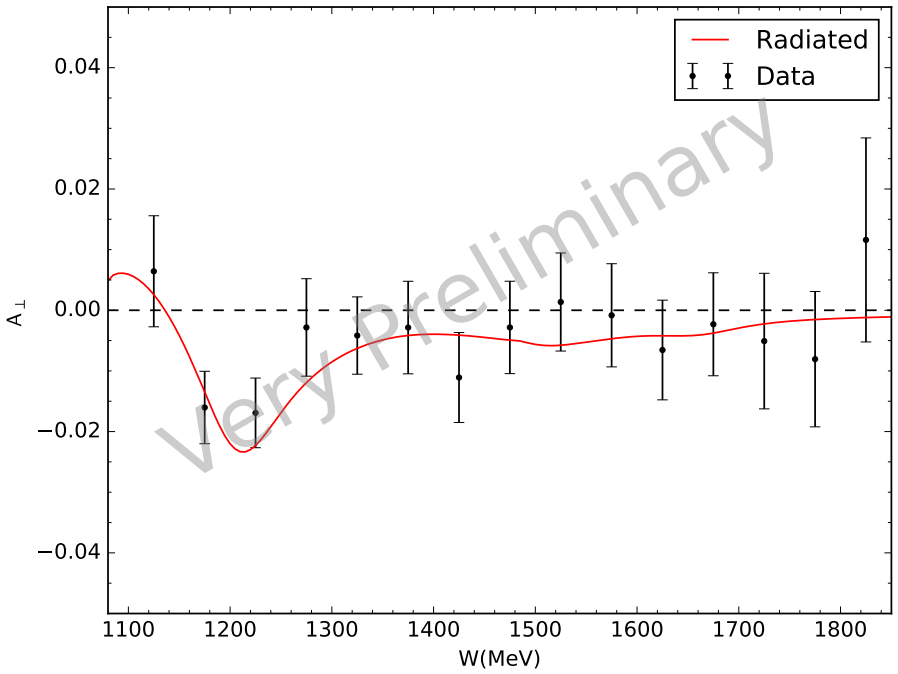

Figure 8-10: Comparison of the radiated model predictions with measured asymmetries for the kinematic settings with 2.253 GeV beam energy and 2.5 T transverse target field. Data are not radiatively corrected.

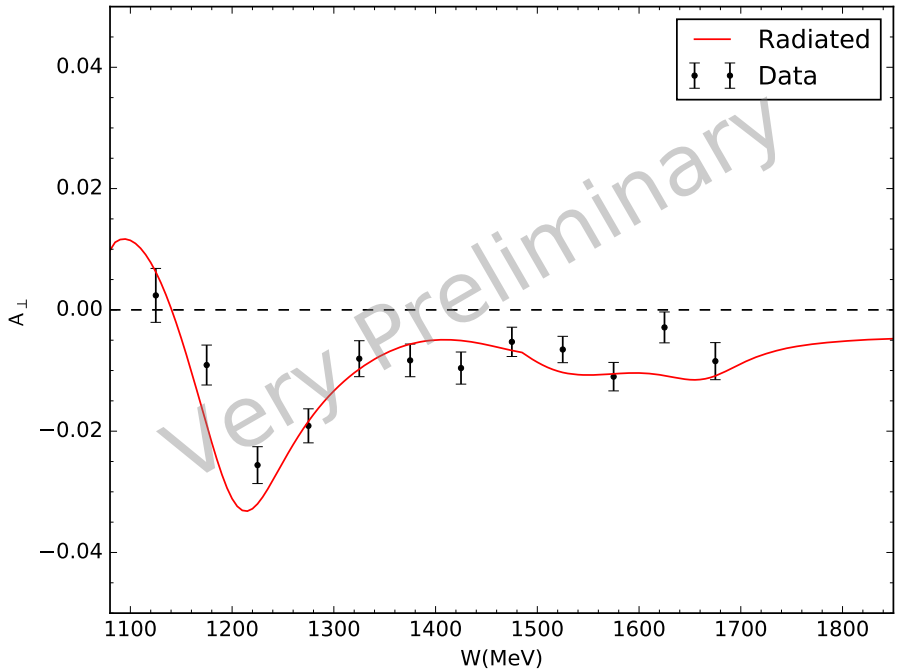

Figure 8-11: Comparison of the radiated model predictions with measured asymmetries for the kinematic settings with 3.350 GeV beam energy and 5.0 T transverse target field. Data are not radiatively corrected.

difference between the model prediction and our data as the uncertainty of the model when we calculate the cross-section differences in the next section. The acceptance effects also contribute to the uncertainty when we fit the relationship between W and the scattering angle with data. Since the acceptance analysis is still on-going, its contribution to the uncertainty of the model prediction has not been determined yet.

8.3 Polarized Cross-Section Differences

The polarized cross-section differences can be calculated via Eq. (7.7). The asymmetries $A_{\parallel,\perp}$ were presented in the previous section. Since the acceptance analysis is still on-going, the unpolarized cross-sections extracted from our data are not reliable yet. Thus, the fits of P. Bosted [145] are used for the unpolarized cross-section as inputs to Eq. (7.7) to extract $\Delta\sigma_{\parallel,\perp}$.

In order to extract the polarized structure functions, the cross-section differences need to be radiative corrected. The standard method to perform radiative correction

is to deconvolute the spectrum extracted from the data with the help of a simulation. In this thesis, we perform the radiative correction to the asymmetries in an alternate way. If we denote the radiated and unradiated model predictions of asymmetries by $A_{\rm rad}^{\rm model}$ and $A_{\rm unrad}^{\rm model}$ respectively, the difference between the radiated and unradiated models can be expressed as:

$$\Delta_{\rm RC}^{\rm model} = A_{\rm unrad}^{\rm model} - A_{\rm rad}^{\rm model}. \tag{8.5}$$

$\Delta_{\rm RC}^{\rm model}$ is taken as the radiative correction, and the asymmetries and the cross-section differences can be expressed as:

$$A_{\rm corrected} = A_{\rm uncorrected} - \Delta_{\rm RC}^{\rm model}, \tag{8.6}$$

$$\Delta\sigma_{\parallel,\perp}^{\rm corrected} = 2A_{\parallel,\perp}^{\rm corrected} \cdot \sigma_0^{\rm corrected}. \tag{8.7}$$

The radiative-corrected cross-section differences are shown in Figures 8-12 to 8-15. The radiated and unradiated model predictions of the cross-section differences are also shown in the figures for comparison. The error bars on each data point are statistical only.

The systematic uncertainty of these cross-section difference results has two major contributions: the systematic uncertainties of the asymmetries $A_{\parallel,\perp}$ and the unpolarized cross-sections σ_0. Since the unpolarized cross-sections are given by the fits of P. Bosted, the systematic uncertainties contributed by σ_0 are 5%. There are several different contributions to the systematic uncertainty of the asymmetry results. The dilution factors are calculated from the packing fraction with Eq. (7.29). The uncertainties of the packing fractions are listed in Table 7.1 and there is an additional $\approx$5% uncertainty to account for the fact that the dilution factors are extracted from calculated cross-sections using P. Bosted's fits. The uncertainties of the beam polarization and the target polarization are $\approx$1.7% and $\approx$1.2% respectively, which have been described in Chapter 5. The largest contribution to the uncertainty comes from the models we used to perform the radiative correction. As mentioned in Section 8.2,

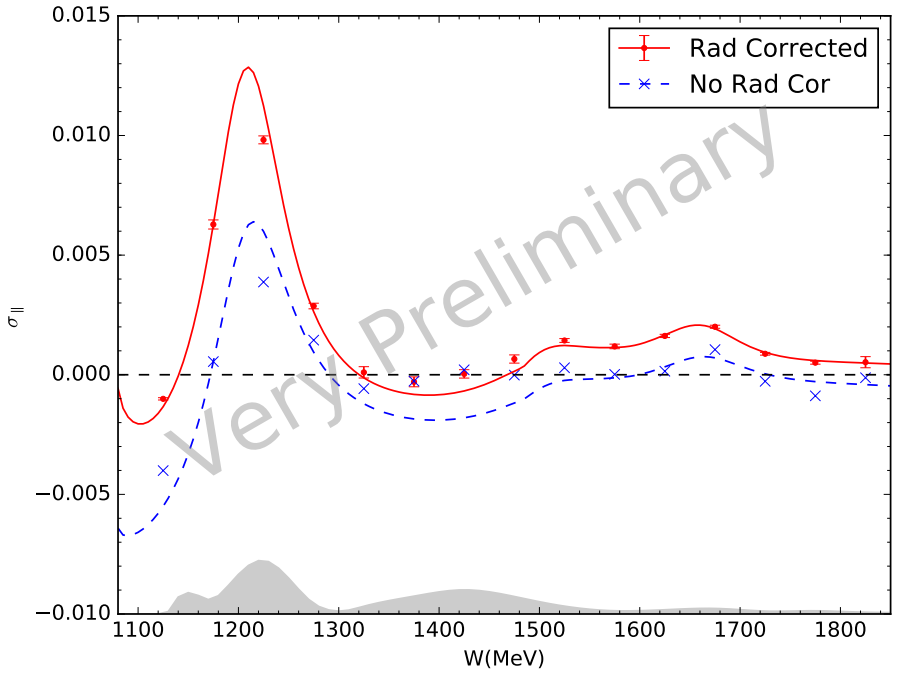

(a) Longitudinal configuration.

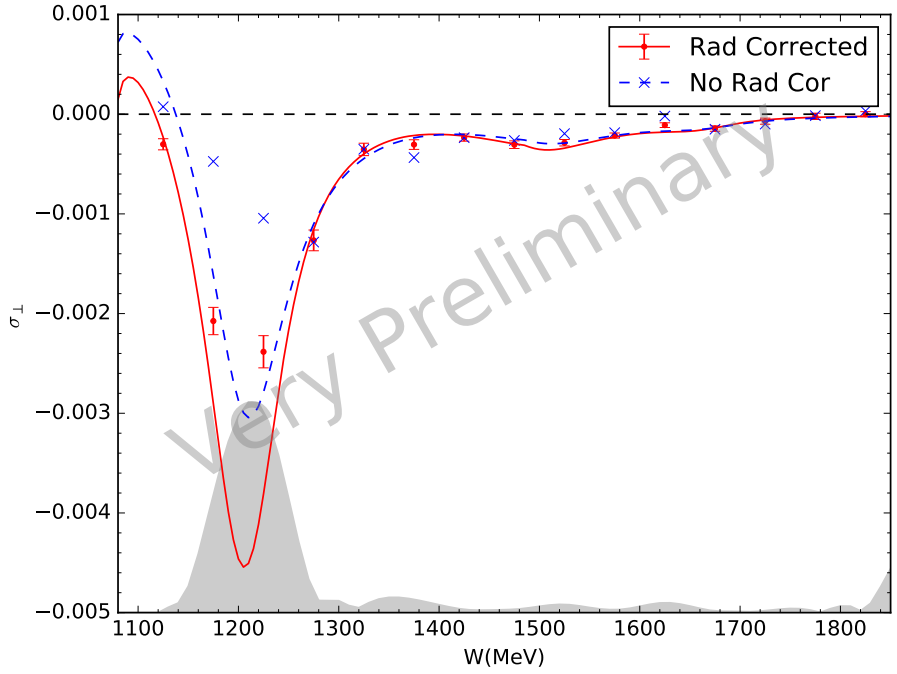

(b) Transverse configuration.

Figure 8-12: Comparison of the radiative corrected and uncorrected cross-section differences for the kinematic settings with 2.253 GeV beam energy and 5.0 T target field (longitudinal and transverse configurations). The error bars for the uncorrected data are not shown in this plot.

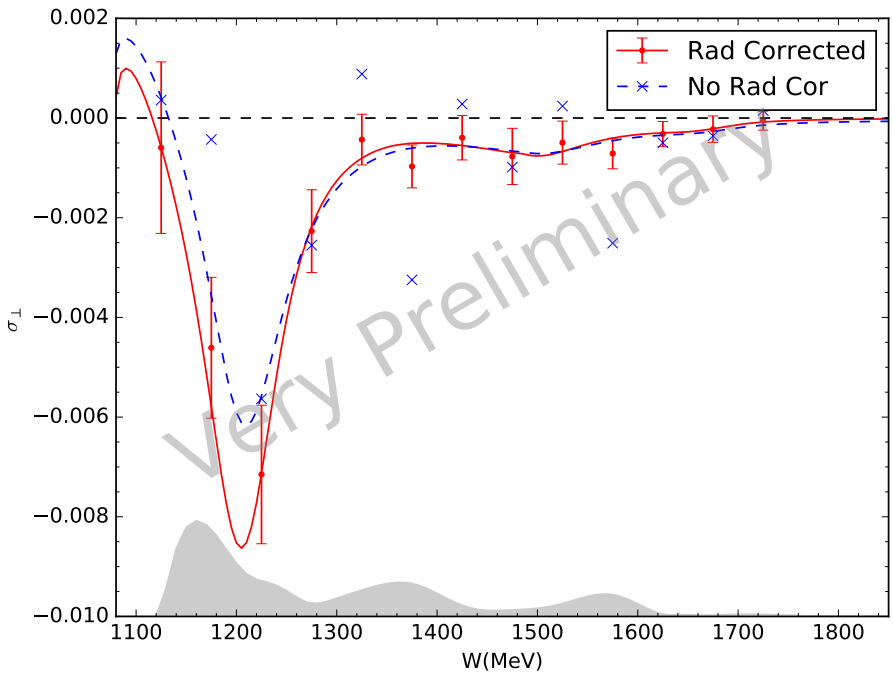

Figure 8-13: Comparison of the radiative corrected and uncorrected cross-section differences for the kinematic settings with 1.710 GeV beam energy and 2.5 T transverse target field. The error bars for the uncorrected data are not shown in this plot.

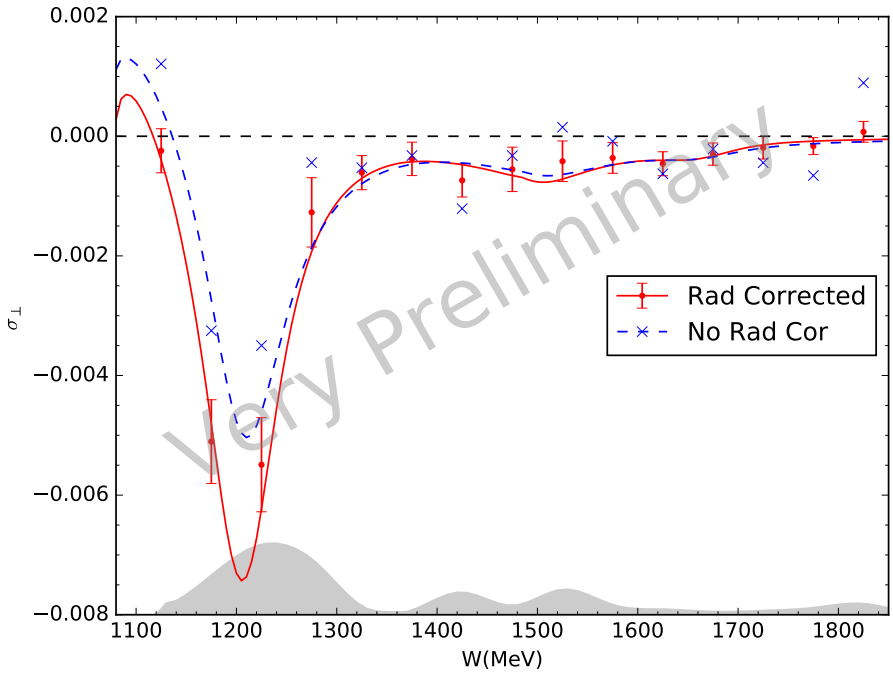

Figure 8-14: Comparison of the radiative corrected and uncorrected cross-section differences for the kinematic settings with 2.253 GeV beam energy and 2.5 T transverse target field. The error bars for the uncorrected data are not shown in this plot.

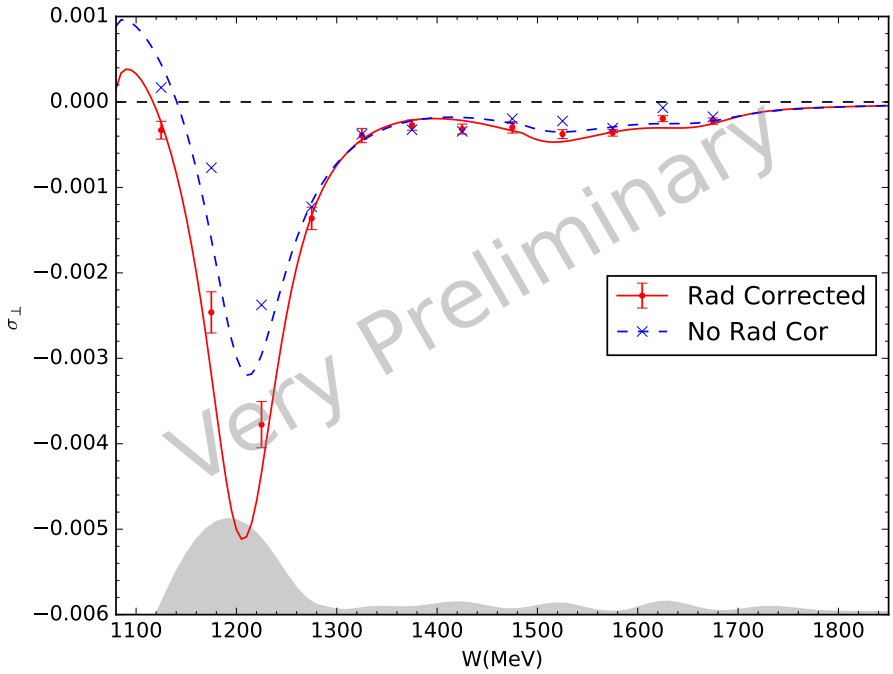

Figure 8-15: Comparison of the radiative corrected and uncorrected cross-section differences for the kinematic settings with 3.350 GeV beam energy and 5.0 T transverse target field. The error bars for the uncorrected data are not shown in this plot.

the difference between the MAID model and our data is taken as the uncertainty in the analysis. Thus, we could combine all of these contributions to estimate the systematic uncertainty of the cross-section differences. The estimations of the systematic uncertainty are shown as the grey bands in Figures 8-12 to 8-15.

8.4 Spin Structure Function g_2^p

In Section 2.2, we have derived the relationships between the polarized cross-section differences and the polarized structure functions Eqs. (2.30) and (2.31). Thus, the polarized structure functions g_1 and g_2 can be written in terms of the cross-section differences as:

$$g_1 = \frac{MQ^2}{4\alpha^2}\frac{y}{(1-y)(2-y)}\left[\Delta\sigma_{\parallel} + \tan\frac{\theta}{2}\Delta\sigma_{\perp}\right], \tag{8.8}$$

$$g_2 = \frac{MQ^2}{4\alpha^2}\frac{y^2}{2(1-y)(2-y)}\left[-\Delta\sigma_{\parallel} + \frac{1+(1-y)\cos\theta}{(1-y)\sin\theta}\Delta\sigma_{\perp}\right], \tag{8.9}$$

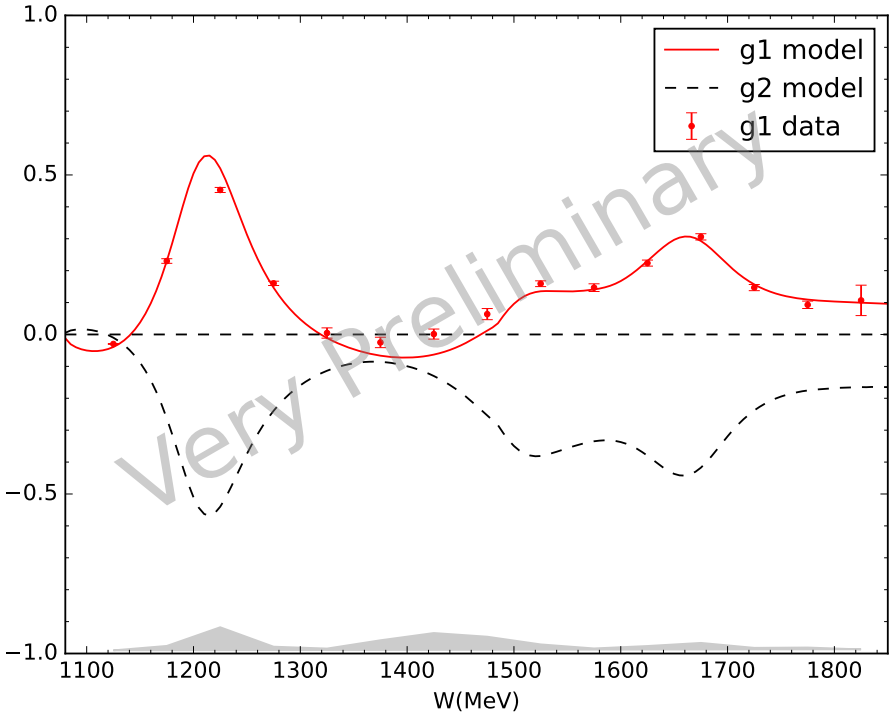

(a) Longitudinal configuration.

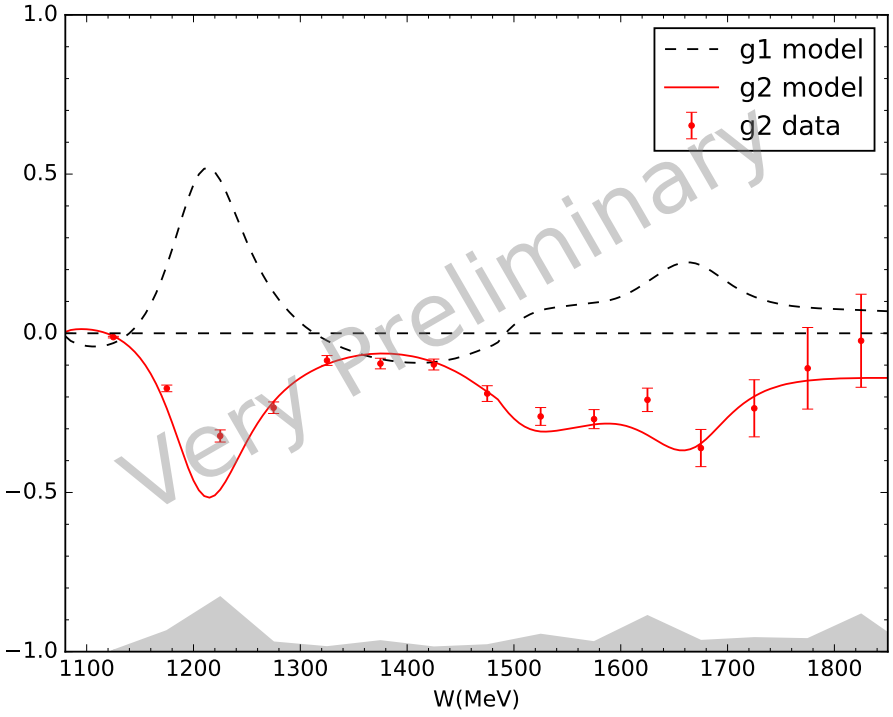

(b) Transverse configuration.

Figure 8-16: g_1 and g_2 results for the kinematic settings with 2.253 GeV beam energy and 5.0 T target field (longitudinal and transverse configurations). The error bars on each data point are statistical.

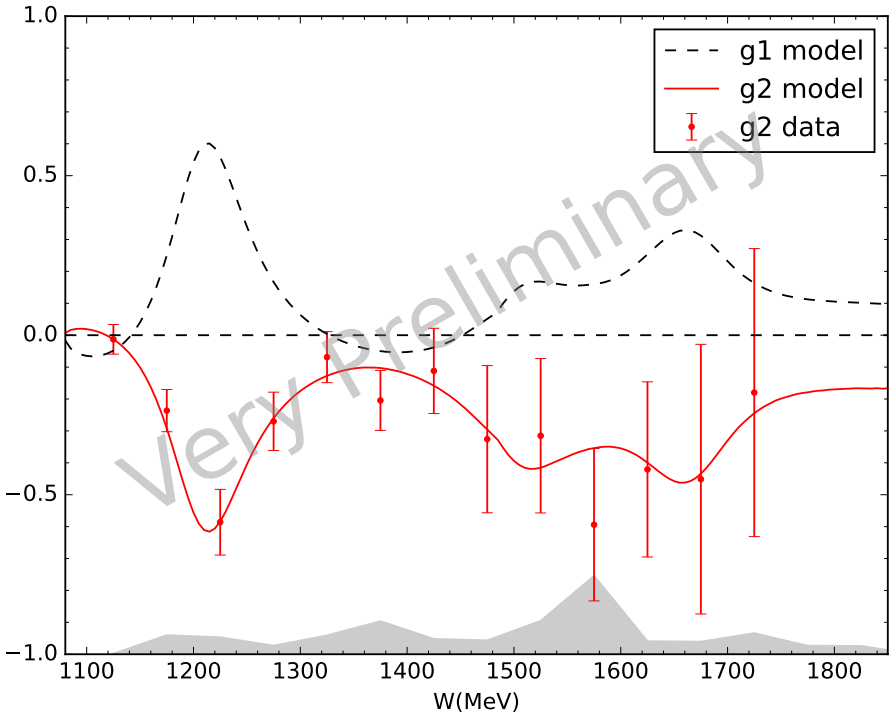

Figure 8-17: g_2 results for the kinematic settings with 1.710 GeV beam energy and 2.5 T target field. The error bars on each data point are statistical.

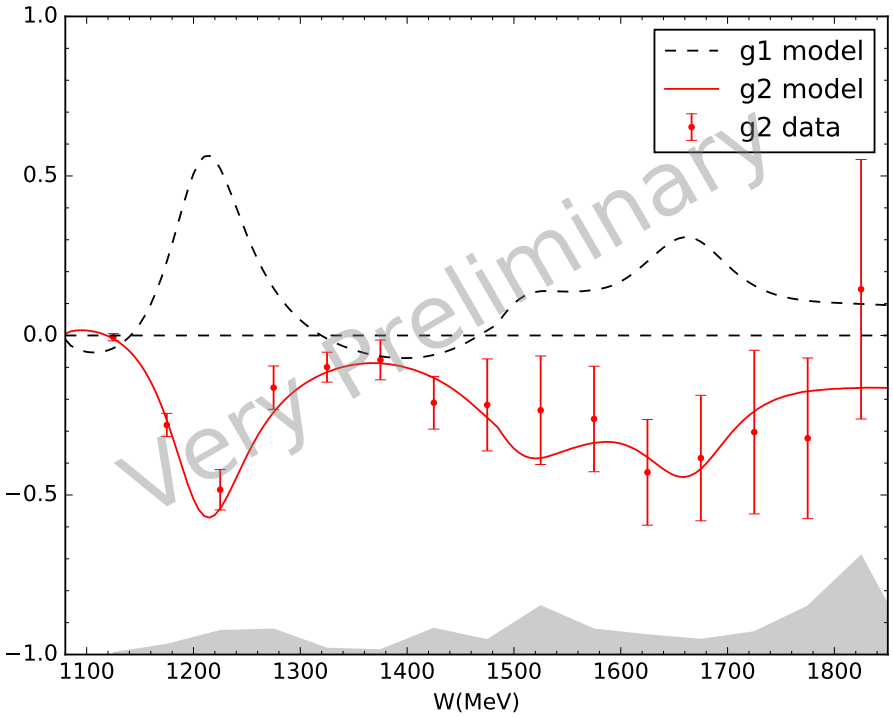

Figure 8-18: g_2 results for the kinematic settings with 2.253 GeV beam energy and 2.5 T target field. The error bars on each data point are statistical.

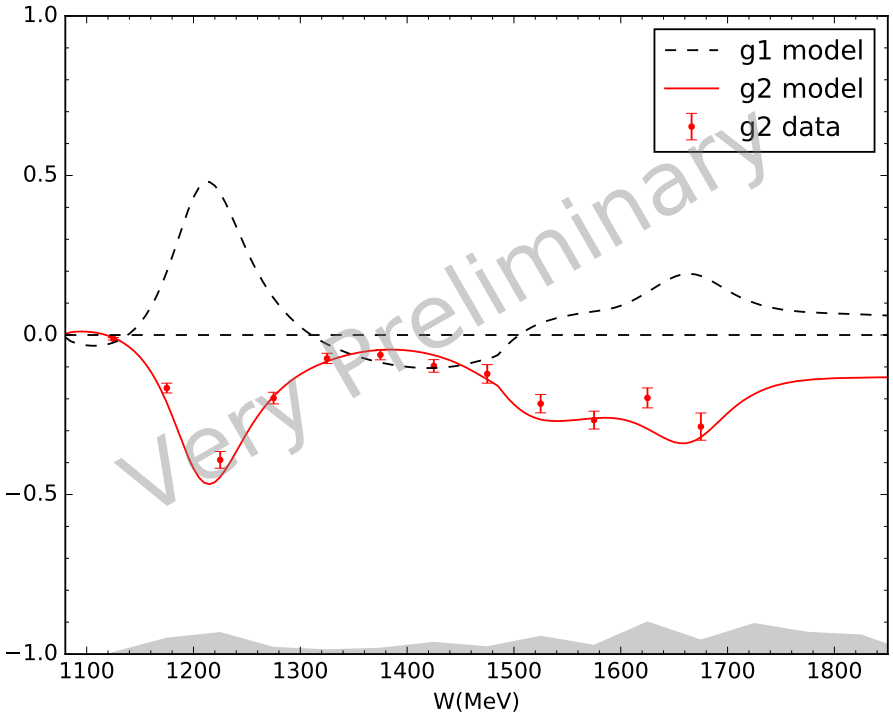

Figure 8-19: g_2 results for the kinematic settings with 3.350 GeV beam energy and 5.0 T target field. The error bars on each data point are statistical.

where $y = \nu/E$.

For the preliminary results presented here, the results on $\Delta\sigma_\perp$ from Section 8.2 were combined with model predictions of $\Delta\sigma_\parallel$ to extract g_1 and g_2 using Eqs. (8.8) and (8.9). In addition, as described in Section 8.2, the $\Delta\sigma_\perp$ results were obtained using asymmetries measured in E08-027 combined with model predictions for σ_0. For the final analysis to be carried out in the future, $\Delta\sigma_\parallel$ will be replaced by the data form Jefferson Lab EG4 and $\Delta\sigma_\perp$ itself will be extracted from E08-027, thus completely eliminating the use of model predictions. For the kinematic setting with 2.253 GeV beam energy and 5.0 T target field, although both $\Delta\sigma_\perp$ and $\Delta\sigma_\parallel$ were measured during the experiment, the kinematics of the longitudinal and transverse configurations are not the same as shown in Figure 8-6. Thus the model predictions for $\Delta\sigma_\parallel$ are also used in these settings. Results for g_1 and g_2 are shown in Figures 8-16 to 8-19. The systematic uncertainties are shown as the grey bands in the plots which contain the contributions from the systematic uncertainties of the transverse

cross-section differences discussed in the previous section.

8.5 Spin Polarizability δ_{LT}

As mentioned in Section 2.4.3, the generalized polarizabilities γ_0 and δ_{LT} are moments of g_1 and g_2, Eqs. (2.80) and (2.84). Using preliminary results for the spin structure functions presented in the previous section, we can calculate the integrand of γ_0 and δ_{LT}. These results are shown in Figs. 8-20 and 8-21, for γ_0 and δ_{LT}, respectively. Here only the two kinematic settings (longitudinal and transverse configurations) with 2.253 GeV beam energy and 5.0 T target field are shown as examples. The average Q^2 for this setting is $\approx$0.1 GeV^2. To evaluate δ_{LT} and γ_0 at this Q^2, the integrals in Eqs. (2.80) and (2.84) have to be carried out from $x = 0$ to the pion threshold, which is $x \approx 0.25$ for this setting. The unmeasured low x region will be evaluated using the g_2^{WW} calculated from g_1 models. However, we expect the contribution of this low x region to be suppressed due to the x^2 weighting in the integrals.

8.6 Conclusions and Future Work

The E08-027 collaboration successfully collected data for the first precision extraction of proton g_2 structure function in the Q^2 range of $0.02 \sim 0.2$ GeV^2. The preliminary data analysis presented in this thesis has demonstrated that g_2^p can be successfully extracted from E08-027 data, with the required precision for the calculation of γ_0, δ_{LT} for a stringent test of χPT predictions.

For preliminary results presented in this chapter, model predictions were used as inputs, for σ_0 in $\Delta\sigma_\perp$ and for $\Delta\sigma_\parallel$, to extract g_2 because the acceptance study of E08-027 has not been finalized. Once the acceptance study is finished, our data will be used to extract the unpolarized cross-sections σ_0 for each kinematic setting in place of the fits used here. In addition, the method for radiative correction in Section 8.3 relies on the radiated cross-section models and thus is not sufficiently accurate. This method will be updated with the standard deconvolution method.

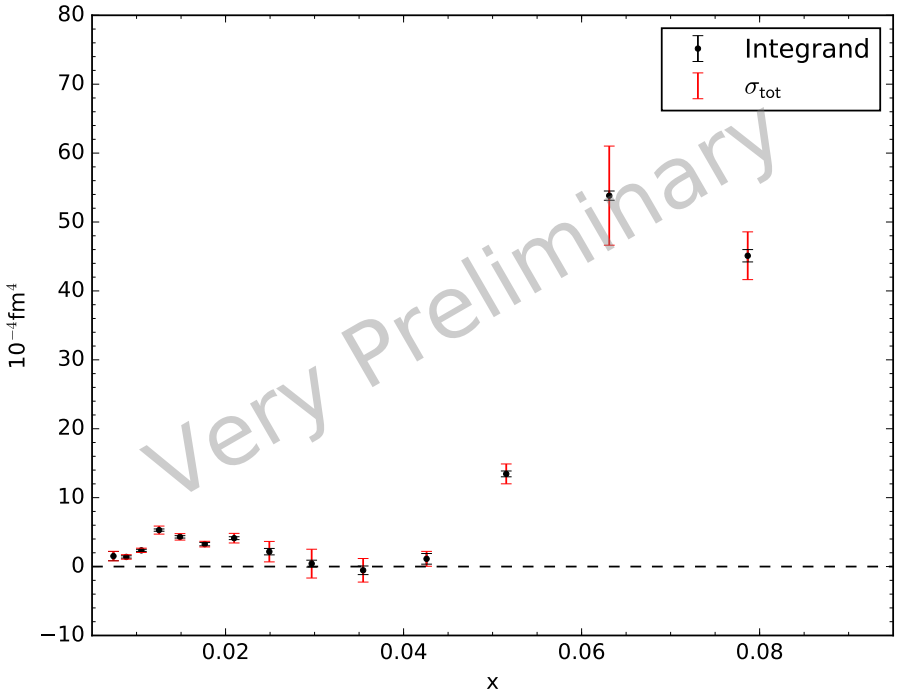

(a) Longitudinal configuration.

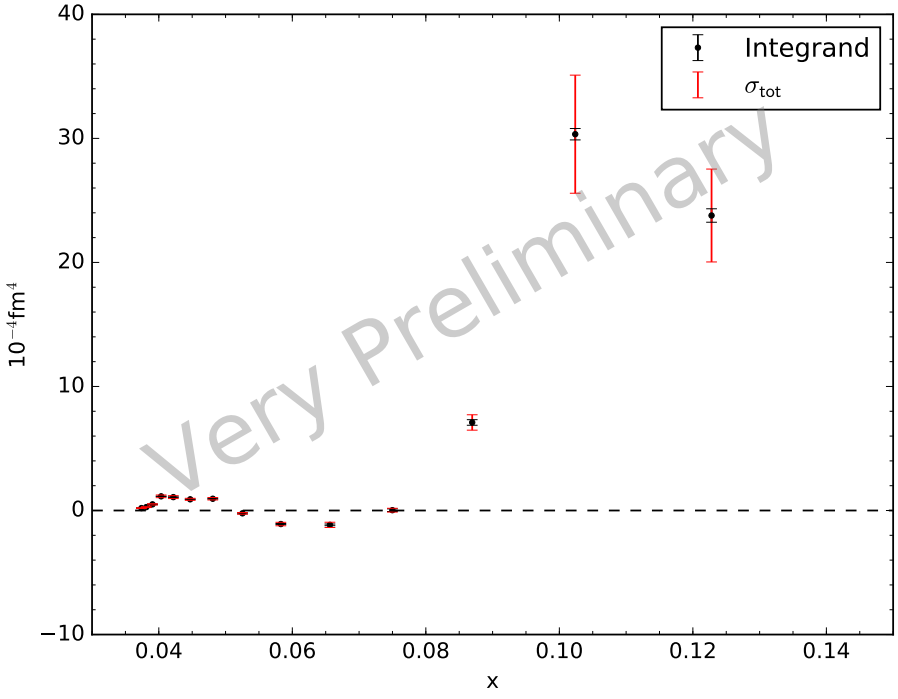

(b) Transverse configuration.

Figure 8-20: Preliminary results for the γ_0 integrand for the kinematic setting with 2.253 GeV beam energy and 5.0 T target field (longitudinal and transverse configurations). For this setting, the average Q^2 is $\approx$0.1 GeV^2. σ_{tot} is the total uncertainty.

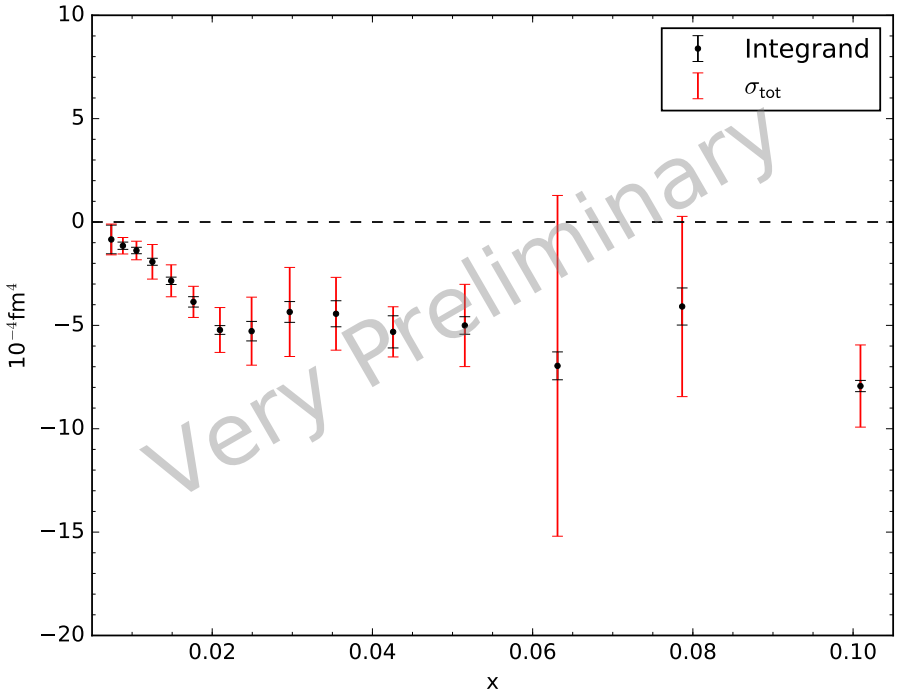

(a) Longitudinal configuration.

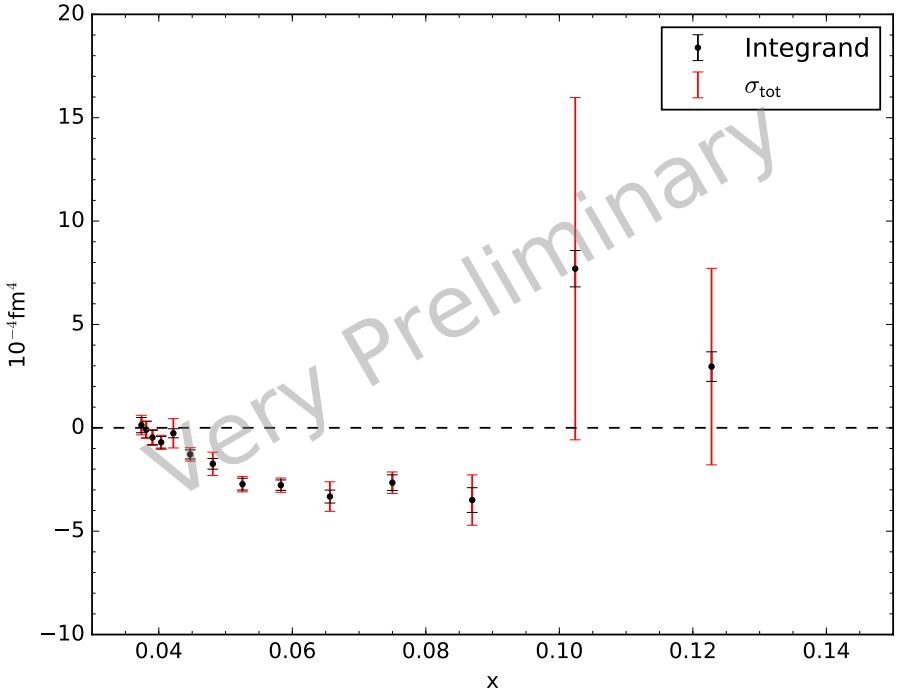

(b) Transverse configuration.

Figure 8-21: Preliminary results for the δ_{LT} integrand for the kinematic setting with 2.253 GeV beam energy and 5.0 T target field (longitudinal and transverse configurations). For this setting, the average Q^2 is $\approx$0.1 GeV^2. σ_{tot} is the total uncertainty.

From preliminary results on the polarized cross-section differences $\Delta\sigma_{\perp}$, we can conclude that the data agree well with model predictions obtained from the MAID model and P. Bosted's fits in the region of the Δ-resonance. However, the agreement for higher W is not as good. From Figure 8-7, we notice that the radiative effects are a large correction at high W, especially for the longitudinal configuration. This indicates that once we use our own data to extract the unpolarized cross-section and to perform the radiative correction, the agreement between calculation and data on $\Delta\sigma_{\perp,\parallel}$ may improve.

In Section 8.4, we used model predictions as inputs for $\Delta\sigma_{\parallel}$ since for most kinematics we measured only $\Delta\sigma_{\perp}$. The Jefferson Lab Hall B EG4 experiment measured $\Delta\sigma_{\parallel}$ in a similar kinematics range as this experiment. Thus, model predictions of $\Delta\sigma_{\parallel}$ will be replaced by data from EG4 once they finalize their analysis.

Once the studies mentioned above are done, the final results of the proton spin structure function g_2 will be extracted. These data will provide the first test of the BC sum rule for the proton at low Q^2. These data are also eagerly awaited to provide a benchmark test of the χPT predictions for the generalized spin polarizabilities γ_0 and δ_{LT}.

Appendix A

Helicity Decoder

In Section 5.1.2, we have discussed the helicity scheme of E08-027. During the experiment, the helicity scheme was determined by the Hall C QWEAK experiment with a high reversal rate at 960.02 Hz. The typical DAQ rate of E08-027 was $5 \sim 6$ kHz. The helicity decoder for QWEAK helicity scheme (THaQWEAKHelicity in the Hall A analyzer package) requires the DAQ rate to be lower than 100 Hz [130], thus this decoder could not be used in E08-027. A new helicity decoder was designed for E08-027. In this section, we will discuss the algorithm used by this new decoder and the test results. This section is also available as a technical note, Ref. [151].

A.1 Data Acquisition Setup

To calculate the asymmetry, each recorded event needs to be sorted by the helicity of the electron beam. The number of accepted events in each helicity state is normalized by the total charge from BCM and the DAQ live time with the same helicity. Thus, the BCM signal, the triggers (T1$\sim$T8) and L1A signal of Hall A DAQ need to be sorted by the beam helicity. In E08-027, these signals and the detected physical events are addressed as two different issues.

The helicity signals described in Section 5.1.2 are copied to three different electronics during E08-027. The helicity of the physical event is recorded by the trigger interface (TI). The TI has 12 state registers (TIR). Four of these registers are used to

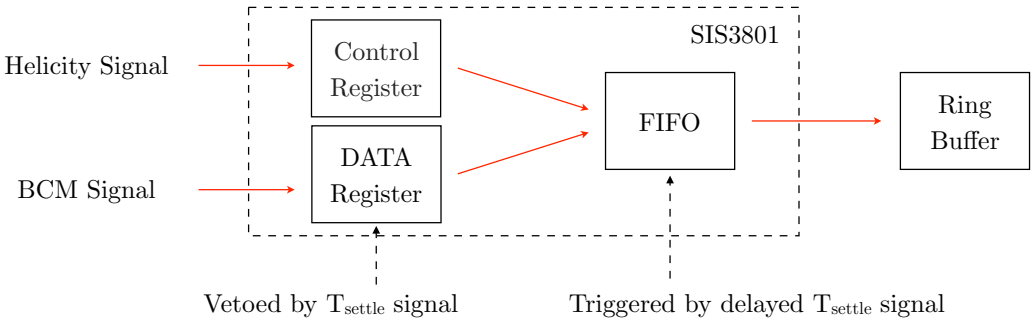

Figure A-1: Workflow of a SIS3801 scaler.

record all of the four helicity signals, Pattern Sync, Pair Sync, Delayed Helicity and T_{settle}, respectively (See Figure 5-3). The electronics setup is based on Ref. [152] and the recorded helicity is referred as TIR helicity in the rest of this section. Besides, decoding the TIR helicity requires timing information. The standard 103.7 kHz fast clock signal of Hall A was used to set a time-stamp for each physical event.

The BCM signals, triggers and L1A signals are all pulse signals. Helicity-gated SIS3801 scalers are used in the experiment to count these signals. Figure A-1 shows the workflow of a SIS3801 scaler. The scaler contains 32 data registers to count, 8 control registers and a FIFO (First-In-First-Out) data buffer. The data signals are sent to the data registers and the T_{settle} signal is sent to one of the control registers to make a veto gate. The data registers only count during the T_{stable} part of a helicity window. Once the counting of one helicity window is finished, the FIFO reads the counting results and save them temporarily. Two additional control registers are used to record the Delayed Helicity and Pattern Sync signals. The FIFO also reads these and records the helicity state of each helicity window.

However, the FIFO is not capable to store a large amount of data. A ring buffer, which is able to store the counting results of 1000 helicity windows, is set in the memory of the VME crate to keep the counting results. The ring buffer is read by the DAQ system every 50 physical events to reduce DAQ dead time. After each readout, the ring buffer is cleared for new counting results. With SIS3801 scalers, the helicity-gated counting results are saved to the raw data file marked with their helicity. The helicity recorded by the ring buffer is referred as ring buffer helicity hereafter.

A.2 Helicity Decoder

As mentioned in Section 5.1.2, the helicity recorded by the DAQ of experimental halls is delayed by 8 helicity windows compare to the actual helicity of the beam. In the accelerator injector, the beam helicity is determined by a pseudo-random generator which is shown in Figure A-2. Since the algorithm of this pseudo-random generator is well defined, the actual helicity can be extracted via the same pseudo-random algorithm. The idea is to read 30 continuous helicity quartets to retrieve the random seed, and use this seed to predict the reported helicity, i.e. the delayed helicity as well as the actual helicity. The prediction can be compared to the reported helicity of the first window of each pattern in the helicity sequence to make sure it is correct.

A.2.1 Predict Actual Ring Buffer Helicity

The ring buffer saves a full sequence of the helicity as mentioned in Appendix A.1. The sequence breaks only if no event was written during the time period of 1000 helicity windows that in our case is about a second. This is because the capacity of the ring buffer is 1000 helicity windows, and the newly coming data flush the old one out if the DAQ system does not read the ring buffer to clear it.

The method of decoding the ring buffer helicity is shown in Figure A-3. If the random seed is not set, the program reads the ring buffer helicity in sequence and

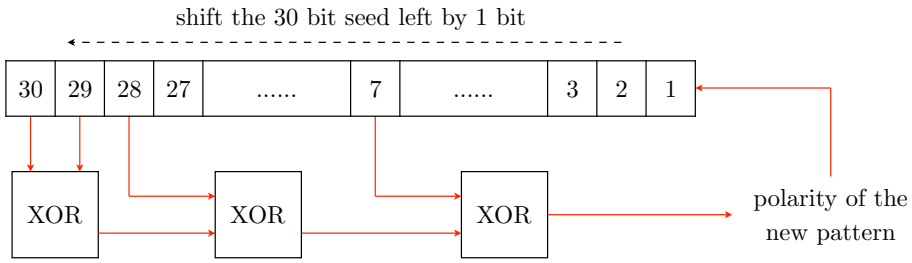

Figure A-2: The 30-bit shift register in the Helicity Control Board. The polarity of a new quartet is calculated by applying an XOR (exclusive disjunction) operation to the bit 30, bit 29, bit 28 and bit 7 of a 30-bit register. Then the register is left-shifted by one bit and the new bit 1 is set by the XOR result. The repeat length of this generator is $2^{30} - 1 = 1,073,741,823$ bits.

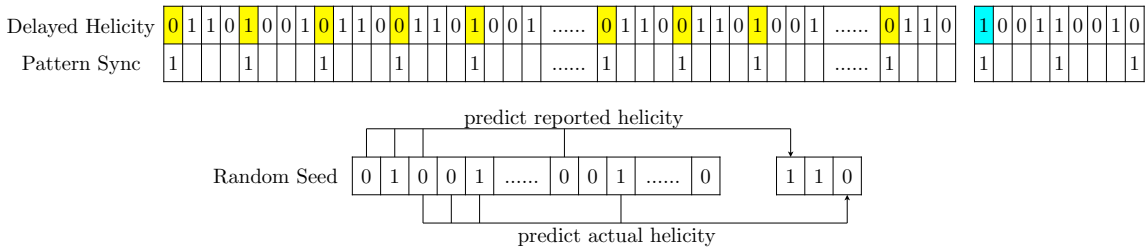

Figure A-3: Predict actual ring buffer helicity. The windows marked as yellow are used to generate the random seed. The seed is used to predict the reported helicity and the actual helicity of the newly coming window (marked as cyan), using the 30-bit shift register algorithm shown in Figure A-2. The actual helicity is behind the reported one by 2 quartets or 8 helicity windows. In this example, the reported helicity of the cyan window is 1 but the actual helicity is 0.

selects out the windows with Pattern Sync 1. The helicities of these windows are appended to the random seed. The seed is used to predict the reported helicity and the actual helicity of the next helicity pattern once all 30 bits are collected. For a Quartet pattern ("$+--+$" or "$-++-$"), only the helicity of the first window needs to be predicted by the seed, because the helicities of the second and the third windows of the quartet are always opposite to the first window and the helicity of the forth window is always equal to the first one. After prediction of all four windows in one quartet, the random seed is left-shifted by one bit and the new bit 1 is set with the reported helicity of the first window of the predicted pattern. The prediction is verified with the reported helicity sequence. If the prediction does not agree with the reported value for any reason, all windows in this quartet are marked as bad and the 30-bit random seed is reset immediately and generate again.

A.2.2 Predict Actual TIR Helicity

For TIR helicity, the decoding algorithm is still based on the prediction method. However, it is possible that several raw events are saved in one helicity window, or no physical event is saved during several helicity windows. Figure A-4 shows an example of TIR helicity. It does not show any obvious pattern, which makes the decoding more difficult. It is critical to find a method to locate each event in the helicity sequence before any prediction can be proceed. Since the helicity windows all have identical

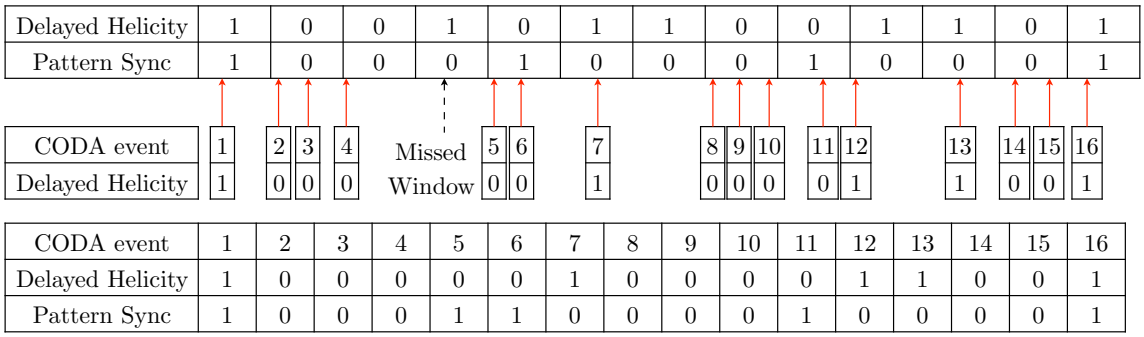

Figure A-4: An example of the TIR helicity. The sequence on the top is the normal helicity sequence. The physical event stream at the bottom shows how the TIR helicity breaks the normal helicity sequence.

time length, it is possible to identify each raw event in the helicity sequence if they are labeled by some kind of time-stamp. The standard 103.9 kHz fast clock signal of Hall A was used to set the time-stamp during the experiment. The clock signal is counted by an ungated scaler (which means it is not helicity gated), and read by the DAQ system for each event. The helicity reversal frequency is 960.02 Hz in the experiment, so the time length of each window is about $T_{\rm w} = 103900 \div 960.02 \approx 108.2$ scaler counts. Some of the TIR event may be saved during the $T_{\rm settle}$ part of a helicity window. These events were excluded from the decoding process and marked as "unstable" by the decoder.

The first step to decode the TIR helicity is still to generate the random seed. For convenience, the helicity windows with Pattern Sync 1 are referred as Pattern Sync windows hereafter. Any events in these Pattern Sync windows are also referred as Pattern Sync events. The helicity of Pattern Sync events is used to generate the random seed, however, there are 3 different situations for the TIR helicity:

1. The event is the first event of a Pattern Sync window, and no Pattern Sync window is missed before this event. In this case, the helicity of this event should be appended to the random seed.

2. The event is the second (or third, ...) event of a Pattern Sync window. In this case it is ignored because the first event of this window has been appended to the random seed.

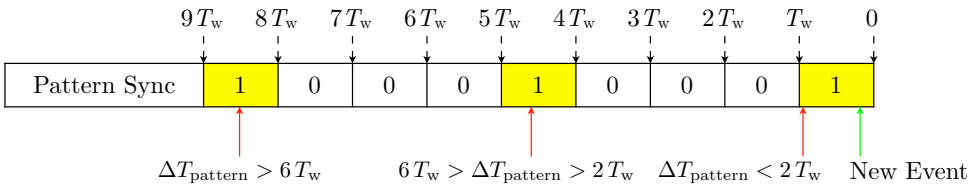

Figure A-5: Thresholds on $\Delta T_{\text{pattern}}$ to determine whether a Pattern Sync window is missed or not if the new event is a Pattern Sync event. Here T_{w} is the time length of a helicity window in unit of scaler counts. The red arrows are different possibilities of the previous event. Yellow backgrounds indicate the possible range of $\Delta T_{\text{pattern}}$, and the thresholds are set in between these ranges to avoid any possible error due to scaler fluctuation.

3. The event is the first event of a Pattern Sync window, but one or more Pattern Sync windows are missed before this event. In this case, all existed 30 bits of the random seed are reset.

In the decoder, a time interval $\Delta T_{\text{pattern}}$ is calculated to determine these 3 situations. Assuming the time-stamp of the current event is T and the previous Pattern Sync event is $T^{\text{last}}_{\text{pattern}}$, $\Delta T_{\text{pattern}}$ can be expressed as $\Delta T_{\text{pattern}} = T - T^{\text{last}}_{\text{pattern}}$. Figure A-5 shows the restrictions on $\Delta T_{\text{pattern}}$ for these 3 situations. If $\Delta T_{\text{pattern}} < 2\,T_{\text{w}}$, the previous Pattern Sync event and the new one are in the same window, and it is case 1 described above. If $\Delta T_{\text{pattern}} > 6\,T_{\text{w}}$, at least one Pattern Sync window is missed, and this is case 3. Notice that the possible value of $\Delta T_{\text{pattern}}$ are $0 \sim 1\,T_{\text{w}}$, $3 \sim 5\,T_{\text{w}}$, $7 \sim 9\,T_{\text{w}}$ or etc. The restrictions are chosen to be just inbetween two ranges to avoid any possible error due to the scaler fluctuation.

Once the random seed is generated, the second step is to predict the reported and the actual helicity for each event with the seed. Since the random seed needs to be left-shifted by 1 bit whenever a helicity quartet is finished, it is critical to determine n, the number of missed Pattern Sync windows. Besides $\Delta T_{\text{pattern}}$, another time interval ΔT is used to determine n. Assuming the time-stamp of the previous event is T^{last}, ΔT can be expressed as $\Delta T = T - T^{\text{last}}$. The random seed must be left-shifted by n bits before making the helicity prediction as described below. When shifting, the new bits are always calculated with the algorithm in Figure A-2. Due to the particularity of the Pattern Sync event, three different situations need to be considered separately:

1. Both the new event and its previous event are Pattern Sync events. In this case, the restrictions on $\Delta T_{\text{pattern}}$ shown in Figure A-5 still works. If $\Delta T_{\text{pattern}} < 2\,T_{\text{w}}$, the new event is in the same window of the previous one. The same random seed is used to predict the actual helicity. If $(4\times n+2)\,T_{\text{w}} < \Delta T_{\text{pattern}} < (4\times n+6)\,T_{\text{w}}$, n Pattern Sync windows are missed (n can be 0). The random seed is left-shifted by n bits, then the prediction for the new event is made. After the prediction, the seed is left-shifted by 1 bit to prepare for the next prediction.

2. The new event is a Pattern Sync event but its previous event is not. In this case, the time interval ΔT is used to determine n, the number of missed Pattern Sync windows, as $n = \text{int}[\Delta T/(4\,T_{\text{w}})]$. The random seed is left-shifted by n bits, then the prediction for the new event is made. After the prediction, the seed is left-shifted by 1 bit to prepare for the next prediction.

3. The new event is not a Pattern Sync event. In this case, the time interval $\Delta T_{\text{pattern}}$ is used to determine n as $n = \text{int}[\Delta T_{\text{pattern}}/(4\,T_{\text{w}})]$. The random seed is left-shifted by n bits, then the prediction for the new event is made. But in this case, the prediction only tells the actual helicity of the first window in the Quartet pattern to which the new event belongs to. The actual helicity of this particular event can be determined according to its Pattern Sync, Pair Sync and the reported helicity value, as shown in Table A.1. Unlike cases 1 and 2,

Prediction of the First Window is +				Prediction of the First Window is −			
Reported Helicity	Pattern Sync	Pair Sync	Actual Helicity	Reported Helicity	Pattern Sync	Pair Sync	Actual Helicity
1	1	1	+	1	1	1	−
0	0	0	−	0	0	0	+
0	0	1	−	0	0	1	+
1	0	0	+	1	0	0	−
0	1	1	+	0	1	1	−
1	0	0	−	1	0	0	+
1	0	1	−	1	0	1	+
0	0	0	+	0	0	0	−

Table A.1: Find the actual helicity of a event according to its reported helicity and Pair Sync value.

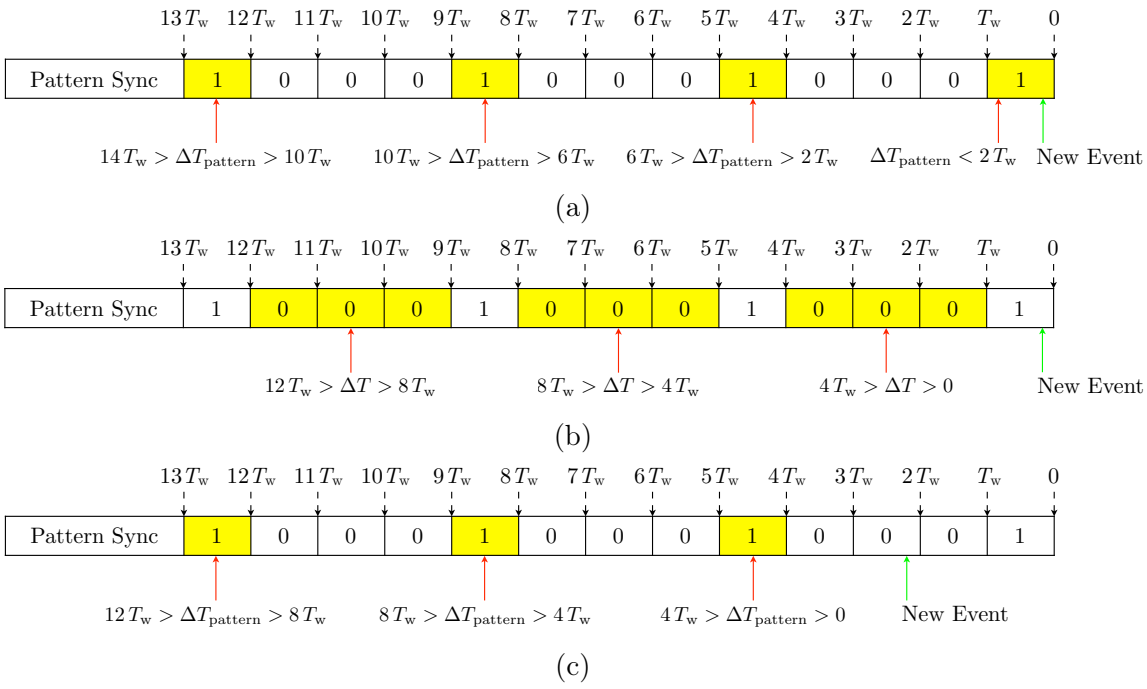

Figure A-6: Thresholds to determine the number of missed Pattern Sync windows: (a) Both the new event and its previous event are Pattern Sync events; (b) The new event is a Pattern Sync event but its previous event is not one; (c) The new event is not a Pattern Sync event. Yellow backgrounds indicate all possible time ranges for the previous event. And the thresholds are chosen in between the possible ranges of ΔT and $\Delta T_{\text{pattern}}$.

the seed does not need to be left-shifted after the prediction, but the $T^{\text{last}}_{\text{pattern}}$ need to be increased by $n \times 4\,T_w$ in case the next event is still not a Pattern Sync event.

Figure A-6 illustrates the thresholds on ΔT and $\Delta T_{\text{pattern}}$ to determine n for these 3 situations. The prediction of the reported helicity of each event is checked with the reported helicity written in the raw data file. If the prediction fails, all events in this quartet are marked as bad. The 30-bit random seed is reset and regenerated.

Due to the fluctuation of the scaler, the time interval ΔT and $\Delta T_{\text{pattern}}$ may not always satisfy the thresholds described and in Figure A-6. The excluded T_{settle} events are used to calibrate T^{last} and $T^{\text{last}}_{\text{pattern}}$ since the time length of helicity windows is fixed. As shown in Figure A-7, a T_{settle} event which is right before a Pattern Sync window is selected for calibration. Assuming the time-stamp of this T_{settle} event is

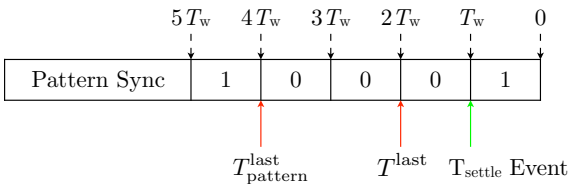

Figure A-7: Calibrate $T^{\rm last}$ and $T^{\rm last}_{\rm pattern}$ with $\rm T_{settle}$ events.

T, the $T^{\rm last}$ is set to $T - T_{\rm w}$ and the $T^{\rm last}_{\rm pattern}$ is set to $T - 3\,T_{\rm w}$. Once calibrated, $T^{\rm last}$ and $T^{\rm last}_{\rm pattern}$ are not used to store the time stamp of previous events any more. The values of $T^{\rm last}$ and $T^{\rm last}_{\rm pattern}$ are increased by $n \times 4\,T_{\rm w}$ if n patterns are finished during the prediction. And any qualified $\rm T_{settle}$ events are used to recalibrate their values. The fluctuation of ΔT and $\Delta T_{\rm pattern}$ is reduced by at least half if calculated with calibrated $T^{\rm last}$ and $T^{\rm last}_{\rm pattern}$, the number of missed Pattern Sync windows can be determined more accurately, and the fail rate of the helicity prediction is reduced.

A.2.3 Align TIR Helicity with Ring Buffer Helicity

The purpose to align TIR helicity with ring buffer helicity is to insert the helicity-gated informations into the physical data stream. As mentioned in Figure A-2, the helicity random seed repeats every 2^{30}-1 bits, thus it never repeats repeats during one particular run, which is usually hour-long. Therefore the random seed can be used as the "fingerprint" to do this alignment.

Before alignment, the quality of the prediction result is checked to avoid false asymmetry. If the actual helicity of a event is not predictable due to some error, events in the same helicity quartet are also marked as bad during the checking. For the ring buffer helicity, the BCM information is used to determine beam trips. The data taken during the beam trip and within 30 helicity quartets before and after the beam trip is excluded from the data analysis to prevent any systematic error.

Figure A-8 shows an example of the alignment. Here BCM is selected as an example of the helicity-gated data. For each helicity quartet in the ring buffer helicity, two BCM values C_+ and C_- are calculated for + and − helicity. The random seed saved for this pattern is compared with all the random seeds saved in the TIR helicity.

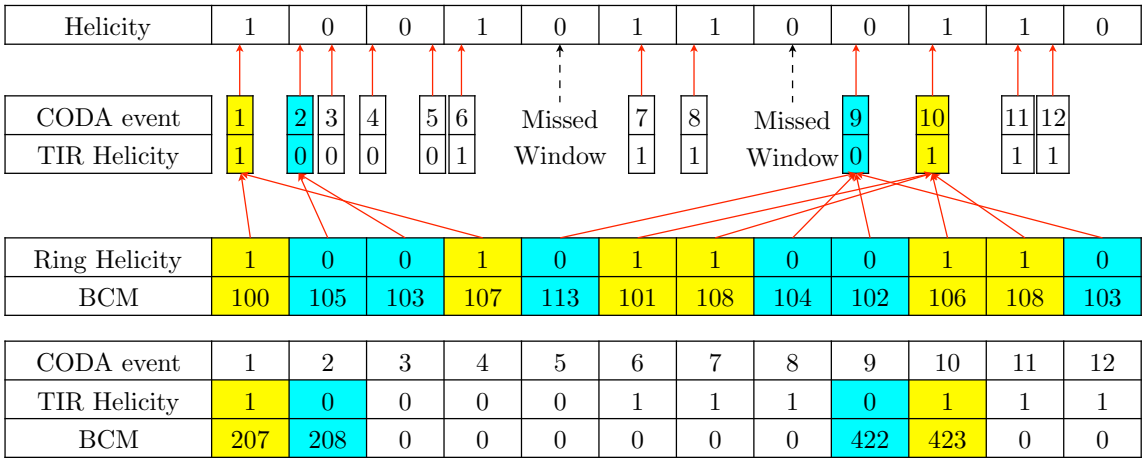

Figure A-8: Align TIR helicity with ring buffer helicity. Take BCM as an example of the helicity-gated data. The second quartet in the helicity sequence missed two 0 helicity windows, so the BCM values of this pattern is added to the values of the next quartet to be saved in the physical event stream.

If a matching pattern is found and the pattern contains at least one event with + helicity and one event with − helicity, C_+ is saved to the first event with + helicity and C_- is saved to the first event with − helicity. If no pattern matches, C_+ and C_- is added to the BCM values of the next helicity quartet in the ring buffer helicity. This method preserves the most helicity-gated data in the physical event stream so they can be used in helicity-related calculation.

A.3 Test with Charge Asymmetry

The helicity decoder is tested with beam charge asymmetry during the experiment. The beam charge asymmetry A_Q can be expressed as:

$$A_Q = \frac{Q_+ - Q_-}{Q_+ + Q_-}. \tag{A.1}$$

Here $Q_\pm$ are the beam charge with helicity ± 1. The beam charge asymmetry can be adjusted in the injector. For the test, beam with large charge asymmetry is required from the injector and is measured with HRS DAQ (SIS3801 scaler), Hall A Møller DAQ and Hall C DAQ simultaneously. The Møller DAQ and Hall C DAQ are used as

reference of this test. The results of the test are listed in Table A.2. The calculation result of the new helicity decoder agrees well with the Møller DAQ and Hall C DAQ, indicating our new decoder can be used for the analysis.

ID	Left HRS	Right HRS	Moller	Hall C
1	-0.91%	-0.91%	-0.92%	-0.91%
2	-0.56%	-0.56%	-0.56%	-0.56%
3	-0.092%	-0.095%	-0.090%	-0.094%

Table A.2: Beam charge asymmetry test with different DAQs.

Appendix B

Uncertainty Estimation for Target Field Map

E08-027 uses a 2.5 Tesla (5.0 T in some configurations) magnetic field to polarize the ammonia target. The map of this magnetic field is used to trace the trajectory of the out-going electrons and to reconstruct the kinematics. The uncertainty of the field map is an important contribution to the final uncertainty of the kinematics. The target field is generated by a pair of super-conducting Helmholtz coils and the field map of these coils is calculated directly from the Biot-Savart law. To estimate the uncertainty of the calculation, measurements of the target field were performed during the experiment. In this section we will summarize the measurement and give an estimation for the uncertainty of the field map.

B.1 Target Field Measurement

The Hall effect is commonly used to measure magnetic field. It is difficult to place a Hall probe inside the target chamber so the field is measured at several different positions on the surface of the target chamber. As shown in Fig. B-1, an aluminum block is used to keep a single-axis Hall probe perpendicular to the surface of the target chamber. The sensitive direction of the probe is the axial direction so it measures the $\hat{r}$-component of the target field in a cylindrical coordinate system. The origin

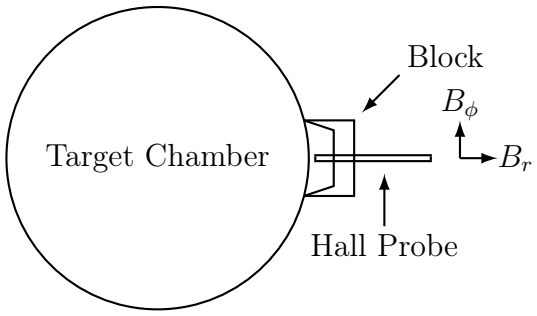

Figure B-1: Setup for target field mapping, showing the radial-direction Hall probe, the aluminum block and the target chamber. The azimuth-direction Hall probe, which was installed in the same aluminum block, is not shown in this figure.

of this coordinate system is the target center and the $\hat{z}$ is vertical up. Another Hall probe is also installed in the holder with the sensitive direction pointing to the azimuth direction to measure the $\hat{\phi}$-component of the target field. The position of each measuring point is surveyed in the HCS (See Section 6.1.1 for the definition of HCS). Once the coordinates are known, the theoretical values of B_r and B_ϕ for each measuring point can be interpolated from the field map and compare with data.

The readout of the Hall probes need to be calibrated first since the sensitive direction of the probe may not align to the radial direction and azimuth direction perfectly. Mechanical errors can arise from the installation of the Hall probe into the aluminum holder, and cause some space deviation between the actual sensitive point of the probe and surveyed coordinates of the measuring point. Thus, the probe is considered to have five degrees of freedom: a space offset (r_0, ϕ_0, h_0) with respect to the measuring point and an angle deviation (θ, ϕ), where θ is the polar angle with respect to the local $\hat{r}$ direction, and ϕ is the corresponding azimuthal angle. The readout of the probes should be projected to the actual $\hat{r}$ and $\hat{\phi}$ direction to extract the measured values of B_r and B_ϕ. However, the space offset (r_0, ϕ_0, h_0) and the

Probe	r_0/mm	ϕ_0/rad	h_0/mm	θ/rad	ϕ/rad
r	10.74	0.1351	0.00	0.0983	3.5197
ϕ	16.17	0.1351	-4.01	1.5032	3.1346

Table B.1: Fit result for the space offset and angle deviation of the Hall probes. r_0, ϕ_0, h_0 are in the cylindrical coordinate system of the target chamber. θ and ϕ are polar and azimuthal angles with respect to the local $\hat{r}$ direction.

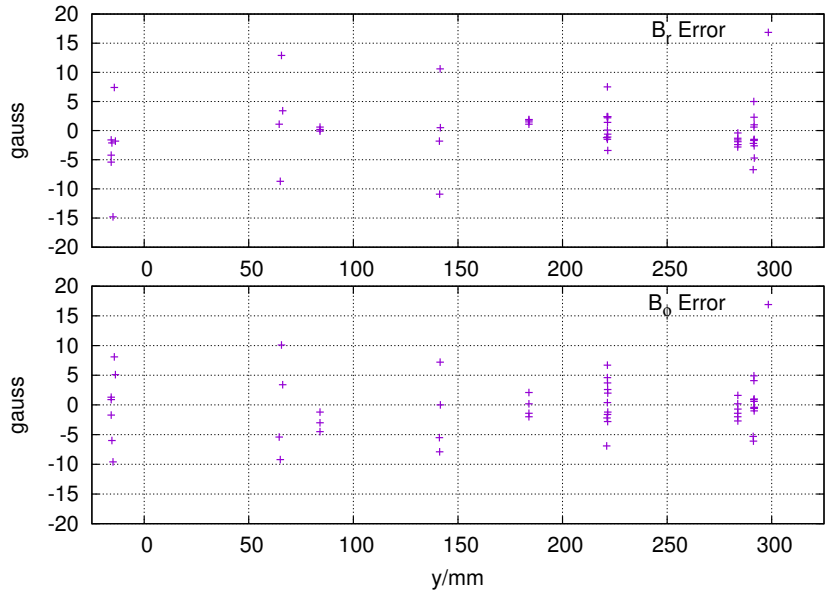

Figure B-2: The differences between the measured field and the map. The horizontal axis is the y coordinates of the measured points in the HCS.

angle deviation (θ, ϕ) of the probe is very difficult to measure without destroying the probe. Thus, the probe readout is used to fit B_r and B_ϕ. In the fit, (r_0, ϕ_0, h_0) and (θ, ϕ) are treated as free parameters to minimize the difference between the theoretical values of B_r and B_ϕ and their measured values. The fit result is shown in Table B.1. Once the parameters are fixed by the fit, the measured values of B_r and B_ϕ and their theoretical values are listed in Table B.2. Figure B-2 shows the differences between the measured value and the theoretical value from the field map. The average deviation between the measurement and the field map is 4.7 gauss for B_r and 4.4 gauss for B_ϕ.

ID	x (mm)	y (mm)	z (mm)	B_r^{data}	B_r^{map}	B_r^{error}	B_ϕ^{data}	B_ϕ^{map}	B_ϕ^{error}
1	414.08	283.78	-242.54	-433.0	-432.6	-0.4	-460.8	-462.4	1.6
2	386.75	283.78	-284.15	-486.8	-485.2	-1.6	-430.5	-429.1	-1.4
3	355.26	283.77	-322.71	-534.5	-531.7	-2.8	-389.1	-389.3	0.2
4	319.94	283.78	-357.79	-572.4	-571.1	-1.3	-346.5	-344.5	-2.0
5	281.17	283.78	-389.02	-605.5	-603.1	-2.4	-299.1	-296.4	-2.7
6	239.38	283.79	-416.07	-629.4	-627.5	-1.9	-246.8	-246.1	-0.7

continued on next page

continued from previous page

ID	x/mm	y/mm	z/mm	B_r^{data}	B_r^{map}	B_r^{error}	B_ϕ^{data}	B_ϕ^{map}	B_ϕ^{error}
7	413.92	183.93	-242.65	-720.9	-722.4	1.5	-599.2	-597.2	-2.0
8	386.58	183.92	-284.25	-812.1	-813.2	1.1	-553.8	-552.4	-1.4
9	355.08	183.92	-322.80	-889.1	-890.9	1.8	-498.1	-498.3	0.2
10	319.75	183.92	-357.87	-952.2	-954.1	1.9	-436.3	-438.4	2.1
11	413.76	84.08	-242.75	-1004.0	-1004.2	0.2	-707.7	-703.2	-4.5
12	386.41	84.07	-284.35	-1128.8	-1129.4	0.6	-649.5	-646.5	-3.0
13	354.90	84.07	-322.89	-1232.3	-1232.2	-0.1	-579.9	-578.7	-1.2
14	413.60	-15.77	-242.86	-1108.2	-1106.6	-1.6	-732.2	-730.5	-1.7
15	386.24	-15.78	-284.45	-1247.6	-1243.4	-4.2	-668.9	-669.8	0.9
16	354.72	-15.78	-322.98	-1359.4	-1354.0	-5.4	-596.3	-597.6	1.3
17	210.61	221.61	-431.32	-896.8	-893.4	-3.4	-248.0	-250.0	2.0
18	164.78	221.57	-450.84	-910.4	-909.8	-0.6	-194.0	-191.2	-2.8
19	117.17	221.54	-465.51	-918.7	-917.6	-1.1	-130.2	-132.8	2.6
20	68.30	221.51	-475.15	-915.9	-917.3	1.4	-75.9	-74.3	-1.6
21	18.69	221.49	-479.67	-906.7	-908.9	2.2	-11.5	-15.2	3.7
22	-31.12	221.46	-479.03	-892.3	-892.4	0.1	49.5	44.9	4.6
23	-80.59	221.43	-473.22	-868.7	-867.2	-1.5	107.0	106.6	0.4
24	210.61	291.67	-431.36	-614.8	-610.1	-4.7	-208.3	-207.9	-0.4
25	164.78	291.63	-450.87	-623.8	-622.3	-1.5	-157.8	-157.2	-0.6
26	117.17	291.60	-465.53	-630.5	-627.9	-2.6	-107.0	-106.0	-1.0
27	68.30	291.57	-475.17	-628.8	-627.2	-1.6	-55.0	-54.5	-0.5
28	18.69	291.54	-479.68	-617.8	-620.1	2.3	-1.9	-2.5	0.6
29	-31.12	291.52	-479.03	-606.1	-606.7	0.6	54.3	50.2	4.1
30	-80.60	291.49	-473.21	-588.4	-586.7	-1.7	108.3	103.4	4.9
31	-142.22	291.61	-458.45	-549.9	-550.9	1.0	172.7	171.7	1.0
32	-229.55	291.45	-421.51	-472.6	-477.6	5.0	273.2	272.3	0.9
33	-315.51	291.28	-361.60	-372.0	-369.8	-2.2	365.1	371.2	-6.1
34	-371.09	291.13	-304.21	-281.5	-274.8	-6.7	424.0	429.3	-5.3
35	-142.04	221.61	-458.52	-818.3	-820.7	2.4	185.9	187.1	-1.2
36	-229.39	221.45	-421.63	-712.9	-720.4	7.5	316.8	310.1	6.7
37	-315.38	221.28	-361.77	-562.0	-564.4	2.4	432.9	435.1	-2.2
38	-370.99	221.13	-304.40	-422.9	-421.7	-1.2	501.7	508.6	-6.9
39	-141.83	141.61	-458.61	-1148.9	-1149.4	0.5	196.3	196.3	0.0
40	-229.21	141.45	-421.76	-1013.6	-1024.2	10.6	350.3	343.1	7.2
41	-315.23	141.28	-361.95	-824.5	-813.6	-10.9	491.6	499.5	-7.9
42	-370.88	141.13	-304.62	-612.3	-610.5	-1.8	586.8	592.3	-5.5
43	-141.84	66.23	-458.62	-1385.2	-1388.6	3.4	202.5	199.1	3.4
44	-229.07	65.67	-421.87	-1238.9	-1251.8	12.9	371.0	360.9	10.1
45	-314.99	65.04	-362.22	-1015.3	-1006.6	-8.7	530.2	539.4	-9.2

continued on next page

continued from previous page									
ID	x/mm	y/mm	z/mm	B_r^{data}	B_r^{map}	B_r^{error}	B_ϕ^{data}	B_ϕ^{map}	B_ϕ^{error}
46	-370.60	64.55	-305.04	-757.9	-759.0	1.1	641.6	647.0	-5.4
47	-141.67	-13.74	-458.69	-1472.7	-1470.9	-1.8	205.9	200.8	5.1
48	-228.93	-14.30	-421.98	-1321.8	-1329.2	7.4	374.2	366.1	8.1
49	-314.88	-14.93	-362.38	-1086.4	-1071.6	-14.8	540.3	549.9	-9.6
50	-370.51	-15.42	-305.23	-810.6	-808.5	-2.1	654.8	660.8	-6.0

Table B.2: Comparison between the measured field and the field map. The x, y and z coordinates of the measured points are in the HCS. The unit of fields is gauss.

B.2 Uncertainty Estimation

The deviations between the measured fields and the field map are shown in Table B.2. The deviation is in average approximately 5 gauss around the target chamber. However, in calculating these results, it was assumed that the calibration of the orientation of the Hall probes is accurate. Since this is difficult to verify with real measurements, this assumption may not be true. The influence of the orientation of the Hall probes to the uncertainty of the measured field can be estimated by adding an uncertainty of certain value to the polar angle of the probes and recalculate the average deviations between the measured fields and the predicted values from the field map. Two situations have been tested to estimate the uncertainty. In the first situation, the polar angle of the probes is increased by 10 mrad, and the average deviations were found to increase to 6.71 gauss for B_r and 10.18 gauss for B_ϕ. In the second situation, the polar angle of the probes is decreased by 10 mrad, and the average deviations were found to increase to 6.67 gauss for B_r and 10.17 gauss for B_ϕ. So it is safe for us to conclude that the uncertainty of this measurement is less than 12 gauss and the relative uncertainty is 1.2% (the average field strength around the target chamber is ≈1000 gauss).

The angle deflection of a charged particle in a static magnetic field can be expressed by:

$$\Delta\theta = \frac{q}{mv}\int_L \vec{B} \times \mathrm{d}\vec{l}. \tag{B.1}$$

Here the integration is along the trajectory of the particle and the integrand is referred

as the $B\,\mathrm{d}l$ of the trajectory. Thus, the uncertainty of the target field need to be propagated to the integration of $B\,\mathrm{d}l$ to give its contribution to the uncertainty of the kinematics variables. The uncertainty of the target field outside the target chamber has been estimated above. During the experiment, the field strength at the target center is monitored by the NMR method. The relative uncertainty of this method is less than 0.1%. The uncertainty of the target field in the other region of the target chamber is not known, so an interpolation between 0.1% and 1.2% was used when applying Eq. (B.1). A simulation package was used to calculate the integrated $B\,\mathrm{d}l$. With a 2.5 T transverse target field, the integrated $B\,\mathrm{d}l$ is 6.682×10^{-1} T·m, and the uncertainty is 5.682×10^{-3} T·m, the relative uncertainty is 0.85%. Thus, the contribution of the uncertainty of the target field map to the scattering angle is about 0.85%.

Bibliography

[1] M. Breidenbach, J. I. Friedman, H. W. Kendall and *et al.*, Phys. Rev. Lett. **23**, 935 (1969).

[2] W. Gerlach and O. Stern, Z. Phys. **9**, 349 (1922).

[3] M. J. Alguard *et al.*, Phys. Rev. Lett. **51**, 1135 (1983).

[4] J. Ashman *et al.*, EMC, Phys. Lett. B **206**, 364 (1988).

[5] S. Kuhn, J. P. Chen, and E. Leader, Prog. Part. Nucl. Phys. **63**, 1 (2009).

[6] A. Camsonne, J. P. Chen, D. Crabb and K. Slifer (spokespersons) *et al.*, *A Measurement of g_2^p and the Longitudinal-Transverse Spin Polarizability*, Jefferson Lab Experiment E08-027 (2008).

[7] M. Amarian *et al.*, E94010 Collaboration, Phys. Rev. Lett. **89**, 242301 (2002).

[8] M. Amarian *et al.*, E94010 Collaboration, Phys. Rev. Lett. **92**, 022301 (2004).

[9] M. Amarian *et al.*, E94010 Collaboration, Phys. Rev. Lett. **93**, 152301 (2004).

[10] F. R. Wesselmann *et al.*, RSS Collaboration, Phys. Rev. Lett. **98**, 132003 (2007).

[11] R. Fatemi *et al.*, CLAS Collaboration, Phys. Rev. Lett. **91**, 222002 (2003).

[12] J. Yun *et al.*, CLAS Collaboration, Phys. Rev. C **67**, 055204 (2003).

[13] A. Deur *et al.*, Phys. Rev. Lett. **93**, 212001 (2004).

[14] K. V. Dharmawardane *et al.*, Phys. Rev. B **641**, 11 (2006).

[15] J. P. Chen, A. Deur, and Z. E. Meziani, Mod. Phys. Lett. A **20**, 2745 (2005).

[16] F. Halzen and A. D. Martin, *Quarks and Leptons: An Introductory Course in Modern Particle Physics* (John Wiley & Sons, 1984).

[17] E. Leader and E. Predazzi, *An Introduction to Gauge Theories and Modern Particle Physics* (Cambridge University Press, 1996).

[18] A. W. Thomas and W. Weise, *The Structure of the Nucleon* (Wiley-Vch, Berlin, 2001).

[19] M. Anselmino, A. Efremov, and E. Leader, Phys. Rep. **261**, 1 (1995).

[20] J. D. Bjorken and E. A. Paschos, Phys. Rev. **185**, 1975 (1969).

[21] H. W. Kendall, Rev. Mod. Phys. **63**, 597 (1991).

[22] R. P. Feynman, Phys. Rev. Lett. **23**, 1415 (1969).

[23] C. G. Callan, Jr. and D. J. Gross, Phys. Rev. Lett. **22**, 156 (1969).

[24] K.A. Olive *et al.*, Particle Data Group, Chin. Phys. C **38**, 090001 (2014).

[25] V. N. Gribov and L. N. Lipatov, Sov. J. Nucl. Phys. **15**, 438 (1972).

[26] Y. L. Dokshitzer, Sov. Phys. JETP **46**, 641 (1977).

[27] G. Altarelli and G. Parisi, Nucl. Phys. B **126**, 298 (1977).

[28] D. Drechsel and L. Tiator, Annu. Rev. Nucl. Part. Sci. **54**, 69 (2004).

[29] L. N. Hand, Phys. Rev. **129**, 1834 (1963).

[30] F. J. Gilman, Phys. Rev. **167**, 1365 (1968).

[31] D. Drechsel, S. S. Kamalov, and L. Tiator, Phys. Rev. D **63**, 114010 (2001).

[32] D. Drechsel, B. Pasquini, and M. Vanderhaeghen, Phys. Rept. **378**, 99 (2003).

[33] F. E. Low, Phys. Rev. **96**, 1428 (1954).

[34] M. Gell-Mann and M. L. Goldberger, Phys. Rev. **96**, 1433 (1954).

[35] A. M. Baldin, Nucl. Phys. **18**, 310 (1960).

[36] L. I. Lapidus, Sov. Phys. JETP **16**, 964 (1963).

[37] S. Gerasimov, Sov. J. Nucl. Phys. **2**, 430 (1966).

[38] S. D. Drell and A. C. Hearn, Phys. Rev. Lett. **16**, 908 (1966).

[39] M. Gell-Mann, M. L. Goldberger, and W. E. Thirring, Phys. Rev. **95**, 1612 (1954).

[40] J. D. Bjorken, Phys. Rev. **148**, 1467 (1966).

[41] J. D. Bjorken, Phys. Rev. D **1**, 1376 (1970).

[42] S. A. Larin and J. A. M. Vermaseren, Phys. Lett. B **259**, 345 (1991).

[43] P. L. Anthony *et al.*, E155 Collaboration, Phys. Lett. B **493**, 19 (2000).

[44] H. Burkhardt and W. N. Cottingham, Ann. Phys. **563**, 453 (1970).

[45] W. Marciano and H. Pagels, Phys. Rept. **36**, 137 (1978).

[46] S. Scherer, Adv. Nucl. Phys. **27**, 277 (2003).

[47] C. Vafa and E. Witten, Nucl. Phys. B **234**, 173 (1984).

[48] J. Goldstone, Nuovo Cim. **19**, 154 (1961).

[49] J. Goldstone, A. Salam, and S. Weinberg, Phys. Rev. **127**, 965 (1962).

[50] S. Weinberg, Physica A **96**, 327 (1979).

[51] J. Gasser and H. Leutwyler, Annals. Phys. **158**, 142 (1984).

[52] J. Gasser and H. Leutwyler, Phys. Lett. B **250**, 465 (1985).

[53] V. Bernard, N. Kaiser, J. Kambor, and U. G. Meissner, Nucl. Phys. B **388**, 315 (1992).

[54] V. Bernard, N. Kaiser, and U. G. Meissner, Phys. Rev. D **48**, 3062 (1993).

[55] E. Jenkins and A. V. Manohar, Phys. Lett. B **255**, 558 (1991).

[56] E. Jenkins and A. V. Manohar, Phys. Lett. B **259**, 353 (1991).

[57] P. J. Ellis and H. B. Tan, Phys. Rev. C **57**, 3356 (1998).

[58] T. Becher and H. Leutwyler, Eur. Phys. J. C **9**, 643 (1999).

[59] X. D. Ji, C. W. Kao, and J. Osborne, Phys. Lett. B **472**, 1 (2000).

[60] V. Bernard, T. R. Hemmert, and U. G. Meissner, Phys. Lett. B **545**, 105 (2002).

[61] C. W. Kao, T. Spitzenberg, and M. Vanderhaeghen, Phys. Rev. D **67**, 016001 (2003).

[62] V. Bernard, T. R. Hemmert, and U. G. Meissner, Phys. Rev. D **67**, 076008 (2003).

[63] T. R. Hemmert, B. R. Holstein, and J. Kambor, J. Phys. G **24**, 1831 (1998).

[64] G. Kubis and U. G. Meissner, Nucl. Phys. A **679**, 698 (2001).

[65] K. G. Wilson, Phys. Rev. **179**, 1499 (1969).

[66] A. V. Manohar, arXiv:hep-ph/9204208 (1992).

[67] R. L. Jaffe and X. D. Ji, Phys. Rev. D **43**, 724 (1991).

[68] R. L. Jaffe, Comments Nucl. Part. Phys. **19**, 239 (1990).

[69] V. Barone and P. G. Ratcliffe, *Transverse Spin Physics* (World Scientific, Singapore, 2003).

[70] S. Wandzura and F. Wilczek, Phys. Lett. B **72**, 195 (1977).

[71] K. J. Slifer, Ph.D. thesis, Temple University (2004).

[72] P. L. Anthony *et al.*, Phys. Rev. D **54**, 6620 (1996).

[73] D. Adams *et al.*, Phys. Rev. D **56**, 5330 (1997).

[74] P. L. Anthony *et al.*, E155x Collaboration, Phys. Lett. B **553**, 18 (2003).

[75] K. Abe *et al.*, E143 Collaboration, Phys. Rev. D **58**, 112003 (1998).

[76] M. Stratmann, Z. Phys. C Part. Fields **60**, 763 (1993).

[77] X. Song, Phys. Rev. D **54**, 1955 (1996).

[78] H. Weigel and L. Gamberg, Nucl. Phys. A **680**, 48 (2001).

[79] M. Wakamatsu, Phys. Lett. B **487**, 118 (2000).

[80] K. Kramer *et al.*, Phys. Rev. Lett. **95**, 142002 (2005).

[81] X. Zheng *et al.*, Jefferson Lab Hall A Collaboration, Phys. Rev. C **70**, 065207 (2004).

[82] V. Olmos de Leon *et al.*, Eur. Phys. J. A **10**, 207 (2001).

[83] J. Tonnison *et al.*, Phys. Rev. Lett. **80**, 4382 (1998).

[84] J. Ahrens *et al.*, GDH and A2 Collaborations, Phys. Rev. Lett. **87**, 022003 (2001).

[85] H. Dutz *et al.*, GDH Collaboration, Phys. Rev. Lett. **91**, 192001 (2003).

[86] Y. Prok *et al.*, CLAS Collaboration, Phys. Lett. B **672**, 12 (2009).

[87] V. Bernard, E. Epelbaum, H. Krebs, and U. G. Meissner, Phys. Rev. D **87**, 054032 (2013).

[88] V. Lensky, J. M. Alarcon, and V. Pascalutsa, Phys. Rev. C **90**, 055202 (2014).

[89] J. P. Chen, Int. J. Mod. Phys. E **19**, 1893 (2010).

[90] V. Nazaryan, C. E. Carlson, and K. A. Griffioen, Phys. Rev. Lett. **96**, 163001 (2006).

[91] J. Arrington, D. Day, R. Gilman, D. Higinbotham, G. Ron, A. Sarty (spokespersons) *et al.*, *Measurement of the Proton Elastic Form Factor Ratio at Low* Q^2, Jefferson Lab Experiment E08-007 (2008).

[92] C. K. Iddings, Phys. Rev. **138**, B446 (1965).

[93] R. N. Faustov and A. P. Martynenko, Eur. Phys. J. C **24**, 281 (2002).

[94] M. Battaglieri, A. Deur, R. D. Vita and M. Ripani (spokespersons) *et al.*, *The GDH Sum Rule with Nearly Real Photons and the Proton g_1 Structure Function at Low Momentum Transfer*, Jefferson Lab Experiment E03-006 (2003).

[95] J. Alcorn *et al.*, Nucl. Instr. Meth. Phys. Res. A **522**, 294 (2004).

[96] V. Sulkosky, Ph.D. thesis, The College of William and Mary (2007).

[97] F. Gross, J. Phys. Conf. Ser. **299**, 012001 (2011).

[98] R. Flood, S. Higgins and R. Suleiman, *Helicity Control Board User's Guide*, Jefferson Lab (2010).

[99] J. Hansknecht, *Injector Laser Table Element Definitions*, Technical Note, Jefferson Lab (2007).

[100] X. Zheng, Ph.D. thesis, Massachusetts Institute of Technology (2002).

[101] http://hallaweb.jlab.org/equipment/beam/energy/arc_web.html.

[102] J. C. Denard, A. Saha, and G. Laveissiere, in *Proceedings of the 2001 Particle Accelerator Conference* (2001), p. 2326.

[103] J. Musson, *Functional Description of Algorithms Used in Digital Receivers*, Technical Note, Jefferson Lab (2012).

[104] M. Bevins, in *Proceedings of the 2005 Particle Accelerator Conference* (2005), p. 3819.

[105] *G2P ELog Entry 173*, https://hallaweb.jlab.org/dvcslog/g2p/173.

[106] http://hallaweb.jlab.org/equipment/beam/absol_beam.html.

[107] http://hallaweb.jlab.org/experiment/LEDEX/camsonne/webpage_calorimeter/page_principale.html.

[108] P. Zhu, *Beam Charge Measurement for g2p Experiment*, E08-027 Technical Note, Jefferson Lab (2015).

[109] W. Barry, Nucl. Instr. Meth. Phys. Res. A **301**, 407 (1991).

[110] P. Piot, *Evaluation and Correction of Nonlinear Effects in FNPL Beam Position Monitors*, Technical Note, FNAL (2005).

[111] C. Yan, P. Adderley, D. Barker *et al.*, Nucl. Instr. Meth. Phys. Res. A **365**, 261 (1995).

[112] P. Zhu, *Beam Position Reconstruction for g2p Experiment in Hall A at Jefferson Lab*, E08-027 Technical Note, Jefferson Lab (2014).

[113] http://hallaweb.jlab.org/equipment/moller/.

[114] *Møller Measurements for E08-027 (g2p) and E08-007*, http://hallaweb.jlab.org/equipment/moller/e08-027.html.

[115] C. Yan, *Hall C Polarized Target Raster System Upgrade*, Technical Note, Jefferson Lab (2005).

[116] A. W. Overhauser, Phys. Rev. **92**, 411 (1953).

[117] C. D. Jeffries, Phys. Rev. **106**, 164 (1957).

[118] J. Pierce *et al.*, Nucl. Instrum. Meth. A **738**, 54 (2014).

[119] D. G. Crabb and W. Meyer, Annu. Rev. Nucl. Part. Sci. **47**, 67 (1997).

[120] M. Goldman, J. Magn. Reson. **17**, 393 (1975).

[121] T. Badman, *Proton Polarization Studies and Uncertainty Analysis for E08-027*, E08-027 Technical Note, Jefferson Lab (2013).

[122] K. G. Fissum *et al.*, Nucl. Instr. Meth. Phys. Res. A **474**, 108 (2001).

[123] R. Zielinski, *Determining the Trigger Efficiency for E08-027*, E08-027 Technical Note, Jefferson Lab (2014).

[124] W. R. Leo, *Techniques for Nuclear and Particle Physics Experiments: A How-to Approach* (Springer-Verlag, 1994).

[125] M. Iodice *et al.*, Nucl. Instr. Meth. Phys. Res. A **411**, 223 (1998).

[126] V. Sulkosky, *Spectrometer Optics Calibration for E97-110*, E97-110 Technical Note, Jefferson Lab (2005).

[127] N. K. Liyanage, *Optics Calibration of the Hall A High Resolution Spectrometers Using the New Optimizer*, Technical Note, Jefferson Lab (2002).

[128] Y. Qiang, Ph.D. thesis, Massachusetts Institute of Technology (2007).

[129] N. K. Liyanage, K. Saenboonruang, and R. Michaels, Q^2 *Measurement for PREX*, E06-002 Technical Note, Jefferson Lab (2011).

[130] O. Hansen, *Hall A C++ Analyzer Documentation*, http://hallaweb.jlab.org/podd/doc/.

[131] *ESPACE User's Guide*, http://hallaweb.jlab.org/espace/docs.html.

[132] *ROOT User's Guide*, https://root.cern.ch/guides/users-guide/.

[133] J. Liu, *Radiation Effects in Simulation*, E08-027 Technical Note, Jefferson Lab (2015).

[134] *Survey Report A1453*, https://www.jlab.org/accel/survalign/documents/dthalla.htm.

[135] *Survey Report A1465*, https://www.jlab.org/accel/survalign/documents/dthalla.htm.

[136] P. Zhu *et al.*, Nucl. Instr. Meth. Phys. Res. A **808**, 1 (2016).

[137] M. Huang, *Central Scattering Angle Measurement*, E08-027 Technical Note, Jefferson Lab (2014).

[138] https://hallaweb.jlab.org/wiki/index.php?title=G2p_optics.

[139] J. Liu, *VDC Multi-track Efficiency Study for E08-027*, E08-027 Technical Note, Jefferson Lab (2013).

[140] M. Cummings, *Efficiency Studies and PID Cut Optimization for E08-027*, E08-027 Technical Note, Jefferson Lab (2013).

[141] M. Cummings, *Packing Fraction Analysis for E08-027*, E08-027 Technical Note, Jefferson Lab (2015).

[142] S. Venkat, J. Arrington, G. A. Miller, and X. H. Zhan, Phys. Rev. C **83**, 015203 (2011).

[143] C. W. D. Jager, H. D. Vries, and C. D. Vries, At. Data Nucl. Data Tables **14**, 479 (1974).

[144] J. W. Lightbody, Jr. and J. S. O'Connell, Comput. Phys. **2**, 57 (1988).

[145] P. E. Bosted and M. E. Christy, Phys. Rev. C **77**, 065206 (2008).

[146] R. Zielinski, *Unpolarized Radiative Corrections*, E08-027 Technical Note, Jefferson Lab (2014).

[147] D. Drechsel, S. S. Kamalov, and L. Tiator, Eur. Phys. J. A **34**, 69 (2007).

[148] I. Akushevich *et al.*, Comput. Phys. Commun. **104**, 201 (1997).

[149] L. W. Mo and Y. S. Tsai, Rev. Mod. Phys. **41**, 205 (1969).

[150] A. Afanasev, I. Akushevich, and N. Merenkov, Phys. Rev. D **64**, 113009 (2001).

[151] C. Gu, *Helicity Decoder for E08-027*, E08-027 Technical Note, Jefferson Lab (2014).

[152] R. Michaels, *Schematic of Electronics for Helicity Info in Hall A HRS during QWEAK*, Technical Note, Jefferson Lab (2010).